PACIFIC EARTHQUAKE ENGINEERING
RESEARCH CENTER

Campbell-Bozorgnia NGA Ground Motion Relations for the Geometric Mean Horizontal Component of Peak and Spectral Ground Motion Parameters

Kenneth W. Campbell
EQECAT, Inc.
Beaverton, Oregon

and

Yousef Bozorgnia
Pacific Earthquake Engineering Research Center
University of California, Berkeley

PEER 2007/02
MAY 2007

Technical Report Documentation Page

1. Report No.	2. Government Accession No.	3. Recipient's Catalog No.
PEER 2007/02		

4. Title and Subtitle	5. Report Date
Campbell-Bozorgnia NGA Ground Motion Relations for the Geometric Mean Horizontal Component of Peak and Spectral Ground Motion Parameters.	May 2007
	6. Performing Organization Code

7. Author(s)	8. Performing Organization Report No.
Kenneth W. Campbell and Yousef Bozorgnia	UCB/PEER 2007/02

9. Performing Organization Name and Address	10. Work Unit No. (TRAIS)
Pacific Earthquake Engineering Research Center 325 Davis Hall MC 1792 University of California Berkeley, CA 94720	
	11. Contract or Grant No. 65A0058

12. Sponsoring Agency Name and Address	13. Type of Report and Period Covered
California Department of Transportation Engineering Service Center 1801 30th St., West Building MS-9 Sacramento, CA 95807	Technical report through June 2006
	14. Sponsoring Agency Code 06681

15. Supplementary Notes

This study was sponsored by the Pacific Earthquake Engineering Research Center's Program of Applied Earthquake Engineering Research of Lifelines Systems supported by the California Department of Transportation, the California Energy Commission, and the Pacific Gas and Electric Company.

16. Abstract

We present a new empirical ground motion model, commonly referred to as an attenuation relationship, which we developed as part of the PEER Next Generation Attenuation of Ground Motion (NGA) Project. Using a common database of worldwide strong motion recordings, we selected a subset of ground motion data and predictor variables that we believed were appropriate for use in developing our model. Consistent with the requirements of the PEER NGA Project, we developed both a median and aleatory uncertainty model for peak ground acceleration (PGA), peak ground velocity (PGV), peak ground displacement (PGD), and response spectral acceleration (PSA) and displacement (SD) for oscillator periods ranging from 0.01–10.0 s, magnitudes ranging from 4.0–8.0, and distances ranging from 0–200 km. We consider these models to be valid for use in the western United States and in other similar tectonically active regions of shallow crustal faulting worldwide. A comparison of our NGA model with our previous ground motion models (Campbell, 1997; Campbell and Bozorgnia, 1994, 2003) showed that the biggest differences in these models occur for sites located at small-to-moderate distances from large-magnitude earthquakes or near reverse faults with surface rupture, where the NGA model predicts lower ground motion, and for sites located on the hanging wall of dipping strike-slip and normal faults, where the NGA model predicts higher ground motion. We also found that the standard deviation is no longer a direct function of magnitude, which increases aleatory uncertainty for large-magnitude earthquakes and decreases it for small-magnitude earthquakes for stiff sites, compared to our previous models. However, the dependence of the standard deviation on nonlinear site effects in our new model can lead to less aleatory uncertainty for soft sites even at large magnitudes as compared to our previous models.

17. Key Words	18. Distribution Statement
NGA, ground motion, attenuation, near source, response spectra, site amplification, hanging wall, basin response	Unlimited

19. Security Classif. (of this report)	20. Security Classif. (of this page)	21. No. of Pages	22. Price
Unclassified	Unclassified	246	

Campbell-Bozorgnia NGA Ground Motion Relations for the Geometric Mean Horizontal Component of Peak and Spectral Ground Motion Parameters

Kenneth W. Campbell
EQECAT, Inc.
Beaverton, Oregon

and

Yousef Bozorgnia
Pacific Earthquake Engineering Research Center
University of California, Berkeley

PEER Report 2007/02
Pacific Earthquake Engineering Research Center
College of Engineering
University of California, Berkeley

May 2007

ABSTRACT

We present a new empirical ground motion model, commonly referred to as an attenuation relationship, which we developed as part of the PEER Next Generation Attenuation of Ground Motion (NGA) Project. Using a common database of worldwide strong motion recordings, we selected a subset of ground motion data and predictor variables that we believed were appropriate for use in developing our model. Consistent with the requirements of the PEER NGA Project, we developed both a median and aleatory uncertainty model for peak ground acceleration (PGA), peak ground velocity (PGV), peak ground displacement (PGD), and response spectral acceleration (PSA) and displacement (SD) for oscillator periods ranging from 0.01–10.0 s, magnitudes ranging from 4.0–8.0, and distances ranging from 0–200 km. We consider these models to be valid for use in the western United States and in other similar tectonically active regions of shallow crustal faulting worldwide. A comparison of our NGA model with our previous ground motion models (Campbell, 1997, 2000, 2001; Campbell and Bozorgnia, 1994, 2003a, 2003b, 2003c, 2004) showed that the biggest differences in these models occur for sites located at small-to-moderate distances from large-magnitude earthquakes or near reverse faults with surface rupture, where the NGA model predicts lower ground motion, and for sites located on the hanging wall of dipping strike-slip and normal faults, where the NGA model predicts higher ground motion. We also found that the standard deviation is no longer a direct function of magnitude, which increases aleatory uncertainty for large-magnitude earthquakes and decreases it for small-magnitude earthquakes for stiff sites, compared to our previous models. However, the dependence of the standard deviation on nonlinear site effects in our new model can lead to less aleatory uncertainty for soft sites even at large magnitudes as compared to our previous models.

ACKNOWLEDGMENTS

This study was sponsored by the Pacific Earthquake Engineering Research Center's Program of Applied Earthquake Engineering Research of Lifelines Systems supported by the California Department of Transportation, the California Energy Commission, and the Pacific Gas and Electric Company.

This work made use of the Earthquake Engineering Research Centers Shared Facilities supported by the National Science Foundation, under award number EEC-9701568 through the Pacific Earthquake Engineering Research (PEER) Center. Any opinions, findings, and conclusions or recommendations expressed in this material are those of the authors and do not necessarily reflect those of the National Science Foundation.

We would like to thank all of the NGA model developers and supporting researchers for their assistance and lively discussions throughout the project. We would especially like to thank Norm Abrahamson, Dave Boore, Brian Chiou, Ed Idriss, Walt Silva, and Bob Youngs for their many constructive comments during the many interaction meetings that were held throughout the project; and Maury Power, Tom Shantz, and Cliff Roblee for their dedicated efforts in managing the project. We would also like to thank Steve Day, Walt Silva, Paul Somerville, and Paul Spudich for providing us with ground motion simulation and analysis results that assisted us in developing our model.

CONTENTS

ABSTRACT ..... **iii**

ACKNOWLEDGMENTS ..... **iv**

TABLE OF CONTENTS ..... **v**

LIST OF FIGURES ..... **ix**

LIST OF TABLES ..... **xi**

1 INTRODUCTION **1**

1.1 Scope of the PEER NGA Project 1

1.2 Objectives of the PEER NGA Project 2

2 STRONG MOTION DATABASE **5**

3 GROUND MOTION MODEL **9**

3.1 Empirical Ground Motion Model 10

3.1.1 Strong Motion Parameter 10

3.1.2 Median Ground Motion Model 11

3.1.3 Aleatory Uncertainty Model 13

3.1.4 Regression Results 17

3.2 Justification of Functional Forms 18

3.2.1 Magnitude Term 18

3.2.2 Distance Term 20

3.2.3 Style-of-Faulting Term 21

3.2.4 Hanging-Wall Term 23

3.2.5 Shallow Site Response Term 24

3.2.6 Deep Site Response Term 25

3.3 Treatment of Missing Values 26

4 ALTERNATIVE HORIZONTAL COMPONENTS **39**

4.1 Geometric Mean 39

4.2 Arbitrary Horizontal Component 40

4.3 Maximum Horizontal Component 41

4.4 Maximum Rotated Horizontal Component 42

4.5 Strike-Normal Horizontal Component 42
4.6 Calculation from Geometric Mean 44

5 EVALUATION OF ALTERNATIVE PREDICTOR VARIABLES 53

5.1 Distance Measures 53
5.2 Sediment Depth Parameters 54
5.3 Source Parameters 54
5.4 Depth to Top of Rupture 57
5.5 Rake Angle 58
5.6 Dip Angle 58

6 GUIDANCE TO USERS 61

6.1 General Limits of Applicability 61
6.1.1 Magnitude 62
6.1.2 Distance 62
6.1.3 Shear-Wave Velocity 62
6.1.4 Sediment Depth 63
6.1.5 Depth to Top of Rupture 63
6.1.6 Dip Angle 64
6.1.7 Tectonic Regime 64
6.2 Estimating Rock PGA 64
6.3 Estimating Unknown Predictor Variables 65
6.3.1 Magnitude and Distance 65
6.3.2 Shear-Wave Velocity 65
6.3.3 Style of Faulting and Dip Angle 66
6.3.4 Depth to Top of Rupture 66
6.3.5 Sediment Depth 67
6.4 Estimating Epistemic Uncertainty 67
6.5 Estimating Spectral Displacement and PGD 68
6.5.1 Spectral Displacement 69
6.5.2 Peak Ground Displacement (PGD) 71
6.6 Use in the National Seismic Hazard Mapping Project 73

7 MODEL EVALUATION 79

7.1 Example Calculations 79

7.2 Scaling with Predictor Variables 80

7.2.1 Median Model 80

7.2.2 Aleatory Uncertainty Model 81

7.2.3 Median Response Spectra 81

7.3 Comparison with Previous Models 81

REFERENCES 113

APPENDIX A: SUMMARY OF STRONG MOTION DATABASE USED IN THE ANALYSIS A-1

APPENDIX B: RESPONSE TO QUESTIONS BY THE U.S. GEOLOGICAL SURVEY (USGS) AND CALIFORNIA GEOLOGICAL SURVEY (CGS) B-1

LIST OF FIGURES

Fig. 2.1 Distribution of recordings with respect to earthquake magnitude and rupture distance....7

Fig. 3.1 Dependence of inter-event residuals on earthquake magnitude....30

Fig. 3.2 Dependence of intra-event residuals on earthquake magnitude....31

Fig. 3.3 Dependence of intra-event residuals on rupture distance....32

Fig. 3.4 Dependence of inter-event residuals on depth to top of rupture....33

Fig. 3.5 Dependence of inter-event residuals on rake angle and style of faulting for strike-slip (SS), normal (NM), and reverse (RV) faults....34

Fig. 3.6 Dependence of intra-event residuals on hanging-wall factor....35

Fig. 3.7 Dependence of intra-event residuals on 30-m shear-wave velocity....36

Fig. 3.8 Dependence of intra-event residuals on rock PGA....37

Fig. 4.1 Ratios of alternative horizontal components to new geometric mean....51

Fig. 5.1 Comparison of relationships between aspect ratio and earthquake magnitude....59

Fig. 5.2 Dependence of inter-event residuals on dip angle....60

Fig. 6.1 Dependence of spectral displacement on magnitude for strike-slip faulting, $R_{RUP} = 0$, and $Z_{2.5} = 2.0$ km....78

Fig. 7.1 Ground motion scaling with rupture distance....89

Fig. 7.2 Ground motion scaling with earthquake magnitude....90

Fig. 7.3 Ground motion scaling with style of faulting and hanging-wall/footwall site locations for $\mathbf{M} = 7.0$....91

Fig. 7.4 Shallow site amplification scaling with rock PGA....92

Fig. 7.5 NEHRP site coefficient F_a scaling with PGA on NEHRP BC site conditions....93

Fig. 7.6 NEHRP site coefficient F_v scaling with PGA on NEHRP BC site conditions....94

Fig. 7.7 Deep site amplification scaling with depth to 2.5 km velocity horizon....95

Fig. 7.8 Total standard deviation scaling with rock PGA....96

Fig. 7.9 Standard deviation scaling with oscillator period for $\mathbf{M} = 7.0$ and $R_{RUP} = 10$ km....97

Fig. 7.10 Spectral acceleration scaling with rupture distance....98

Fig. 7.11 Spectral acceleration scaling with earthquake magnitude....99

Fig. 7.12 Spectral acceleration scaling with style of faulting, hanging-wall/footwall site locations, and rupture depth for $\mathbf{M} = 6.5$ and $R_{RUP} = 5$ km 100

Fig. 7.13 Spectral acceleration scaling with shallow site conditions for $R_{RUP} = 10$ km 101

Fig. 7.14 Spectral acceleration scaling with sediment depth for $\mathbf{M} = 7.0$, $R_{RUP} = 10$ km, and NEHRP D site conditions 102

Fig. 7.15 Comparison of ground motion scaling with rupture distance between CB-NGA and CB03 and C97 (PGV) ground motion models for NEHRP BC site conditions ...103

Fig. 7.16 Comparison of ground motion scaling with earthquake magnitude between CB-NGA and CB03 and C97 (PGV) ground motion models for NEHRP BC site conditions 104

Fig. 7.17 Comparison of spectral acceleration scaling with rupture distance between CB-NGA and CB03 ground motion models for NEHRP BC site conditions 105

Fig. 7.18 Comparison of spectral acceleration scaling with earthquake magnitude between CB-NGA and CB03 ground motion models for NEHRP BC site conditions 106

Fig. 7.19 Comparison of spectral acceleration scaling with rupture distance between CB-NGA and CB03 ground motion models for NEHRP D site conditions 107

Fig. 7.20 Comparison of spectral acceleration scaling with earthquake magnitude between CB-NGA and CB03 ground motion models for NEHRP D site conditions 108

Fig. 7.21 Comparison of spectral acceleration scaling with style of faulting, hanging-wall/ footwall site locations, and rupture depth between CB-NGA and CB03 ground motion models for reverse faults, $\mathbf{M} = 6.5$, $R_{RUP} = 5$ km, and $\delta = 45°$ 109

Fig. 7.22 Comparison of spectral acceleration scaling with style of faulting and hanging-wall/footwall site locations between CB-NGA and CB03 ground motion models for normal and strike-slip faults, $\mathbf{M} = 6.5$, $R_{RUP} = 5$ km, and $\delta = 45°$ 110

Fig. 7.23 Comparison of total standard deviations between CB-NGA and CB03 and C97 (PGV) ground motion models for NEHRP BC site conditions and $R_{RUP} = 0$ 111

Fig. 7.24 Comparison of total standard deviations between CB-NGA and CB03 and C97 (PGV) ground motion models for NEHRP B, C, D, and E site conditions and $R_{RUP} = 0$ 112

LIST OF TABLES

Table 3.1 Coefficients for CB-NGA median ground motion model 28

Table 3.2 Standard deviations and correlation coefficients for CB-NGA aleatory uncertainty model 29

Table 4.1 Ratio between geometric mean of as-recorded horizontal components and new geometric mean averaged over all magnitudes and distances 46

Table 4.2 Ratio between maximum and minimum horizontal components and geometric mean averaged over all magnitudes and distances 47

Table 4.3 Ratio between maximum horizontal and maximum rotated horizontal components and geometric mean averaged over all magnitudes and distances 48

Table 4.4 Ratio between strike-normal and strike-parallel horizontal components and geometric mean averaged over all magnitudes and distances 49

Table 4.5 Median ratio between strike-normal and strike-parallel horizontal components and geometric mean for $\mathbf{M} \geq 6.5$ and four distance bins 50

Table 6.1 Incremental values of median ground motion in epistemic uncertainty model 76

Table 6.2 Comparison of near-fault estimates of PGD 76

Table 6.3 Comparison of far-field estimates of PGD 77

Table 7.1 Example calculations for 90°-dipping strike-slip fault 84

Table 7.2 Example calculations for hanging wall of 45°-dipping reverse fault 86

Table 7.3 Parameter values used for strike-slip faulting scenario given in Table 7.1 88

Table 7.4 Parameter values used for reverse-faulting scenario given in Table 7.2 88

1 Introduction

1.1 SCOPE OF THE PEER NGA PROJECT

The PEER Next Generation of Ground Motion Attenuation Project (the "PEER NGA Project") is a research initiative conducted by the Pacific Earthquake Engineering Research Center Lifelines Program in partnership with the U.S. Geological Survey (USGS), the Southern California Earthquake Center (SCEC), and the Pacific Gas and Electric Company (PG&E). According to Power et al. (2006), the objective of the PEER NGA Project is to develop updated empirical ground motion models (attenuation relationships) through a comprehensive and highly interactive research program. The model development was supported by other project components that included: (1) development of an updated and expanded PEER database of recorded ground motions, (2) supporting research projects to provide constraints on the selected functional forms of the ground motion models, and (3) interactions throughout the development process to provide input and reviews from both the scientific research community and the engineering user community. An overview of the PEER NGA Project components, process, and products is presented in Power et al. (2006). The PEER NGA database is available at http://peer.berkeley.edu/nga/index.html.

Under the auspices of the PEER NGA Project, updated empirical ground motion models were developed for shallow crustal earthquakes for use in the western United States through a comprehensive and highly interactive research program that involved the following components: (1) development of separate sets of ground motion models by five teams (the "developers"); (2) development of an updated and expanded PEER ground motion database to provide the recorded ground motion data and the supporting metadata on the causative earthquakes, source-to-site travel paths, and local site conditions needed by the developers for their empirical regression

analyses; (3) a number of supporting research projects, including theoretical simulations of rock motions, soil site response, and basin response, to provide an improved scientific basis for evaluating functional forms and determining constraints on the ground motion models; and (4) a series of workshops, working group meetings, developer meetings, and external review that provided input into and review of the project results by both the scientific research community and the engineering user community.

1.2 OBJECTIVES OF THE PEER NGA PROJECT

Developers of five pre-existing and widely used empirical ground motion models participated in the concurrent development of the NGA models. These developers, along with references to their pre-existing models, are as follows: (1) Abrahamson and Silva (2007) updating Abrahamson and Silva (1997), (2) Boore and Atkinson (2007) updating Boore et al. (1997), (3) Campbell and Bozorgnia (this report) updating Campbell (1997, 2000, 2001) and Campbell and Bozorgnia (1994, 2003a, 2003b, 2003c, 2004), (4) Chiou and Youngs (2007) updating Sadigh et al. (1993; 1997), and (5) Idriss (2007) updating Idriss (1991).

To meet the needs of earthquake engineering design practice, all NGA models were required to be applicable to the following conditions (Power et al., 2006): (1) they should include the ground motion parameters of peak ground acceleration, velocity, and displacement (PGA, PGV, PGD) and 5%-damped elastic pseudo-absolute response spectral acceleration (PSA) for a minimum set of periods ranging from 0–10 s; (2) they should model the average horizontal motion as well as motions in the strike-normal (SN) and strike-parallel (SP) directions, although this latter requirement was eventually postponed to a later phase of the project; (3) they should be valid for shallow crustal earthquakes with strike-slip, reverse, and normal mechanisms in the western United States; (4) they should be valid for moment magnitudes ranging from 5.0–8.5; (5) they should be valid for distances ranging from 0–200 km; and (6) they should incorporate a commonly used site classification scheme, such as that defined in the National Earthquake Hazard Reduction Program (NEHRP) (e.g., BSSC, 2004).

The main technical issues that were addressed in the NGA model development and supporting research included: (1) rupture-directivity effects, although this was eventually postponed to a later phase of the project; (2) the effects of polarization of near-field motion in

terms of strike-normal and strike-parallel effects, although this too was eventually postponed to a later phase of the project; (3) footwall and hanging-wall effects for dipping faults; (4) style-of-faulting effects, including strike-slip, reverse, and normal mechanisms; (5) depth of faulting, especially potential differences between buried and surface rupture; (6) source effects, such as static stress drop, rupture area, and aspect ratio; (6) site amplification effects relative to a reference "rock" site condition; (7) 3-D sedimentary basin amplification effects; (8) uncertainties in predictor variables; (9) treatment of missing values of predictor variables; and (10) dependencies of standard errors on magnitude, distance, and soil type.

The remainder of this report summarizes the development of the Campbell-Bozorgnia NGA empirical ground motion model (EGMM), hereafter referred to as the CB-NGA model.

2 Strong Motion Database

The database used for this study was a subset of the PEER strong motion database that was updated as part of the PEER NGA Project. This database can be downloaded from the PEER website at http://peer.berkeley.edu/nga/index.html. The database includes strong motion recordings intended to represent free-field site conditions (e.g., large buildings were excluded). However, we applied additional criteria for deciding whether a recording should be used. For example, recordings from this database were used if they met the following general criteria: (1) the earthquake was within the shallow continental lithosphere (crust) in a region considered to be tectonically active; (2) the recording was at or near ground level with no known embedment effects; (3) the earthquake had enough recordings to reliably represent the mean ground motion, although this criterion was relaxed for larger earthquakes in order to retain these important recordings; and (4) the earthquake or recording was considered to be reliable (see below for earthquakes and recordings that were excluded because of reliability issues).

To ensure that the ground motion predictions represented as closely as possible the above criteria, for purposes of our analysis we excluded from the PEER database: (1) recordings having only one horizontal component or only a vertical component, which precluded us from calculating the geometric mean of the two horizontal components; (2) recording sites having no measured or estimated 30-m shear-wave velocity, which precluded us from modeling shallow site effects; (3) earthquakes having no rake angle, focal mechanism, or plunge (dip) of the maximum compressive stress (*P*) and minimum compressive stress (*T*) axes, which precluded us from modeling style-of-faulting effects; (4) earthquakes having the hypocenter or a significant amount of the fault rupture located in the lower crust, in an oceanic plate, or in a stable continental region, which was not consistent with the desired tectonic regime; (5) the Lamont Doherty Geologic Observatory recordings from the 1999 Düzce, Turkey, earthquake, which we considered to be unreliable because of their very unusual spectral shapes; (6) recordings from

instruments designated quality "D" from the 1999 Chi-Chi, Taiwan, earthquake according to the quality designation of Lee et al. (2001), which we considered to be unreliable because of their poor quality; (7) an aftershock located in the immediate vicinity of the inferred main-shock rupture plane, which we considered potentially to have below-average stress drops, but not an event "triggered" by the main shock (e.g., the 1992 Big Bear earthquake), which we considered to have a similar stress regime as the main shock; (8) an earthquake considered to be poorly recorded, which we defined as an earthquake with (a) $\mathbf{M} < 5.0$ and $N < 5$, (b) $5.0 \le \mathbf{M} < 6.0$ and $N < 3$, or (c) $6.0 \le \mathbf{M} < 7.0$, $R_{RUP} > 60$ km and $N < 2$, where $\mathbf{M}$ is moment magnitude and N is the number of recordings (note that singly recorded earthquakes with $\mathbf{M} \ge 7.0$ and $R_{RUP} \le 60$ km were retained because of their significance); (9) a recording site considered not representative of free-field conditions, which we defined as an instrument located (a) in the basement of a building, (b) below the ground surface, or (c) on a dam, except an abutment, other than the Pacoima Dam upper-left abutment which has well-documented topographic effects; and (10) recordings from the Tarzana Cedar Hill Nursery, which has been shown to exhibit strong topographic effects.

A list of the selected earthquakes and recording sites used in the development of the CB-NGA model is given in Appendix A. This list contains 1561 recordings from 64 earthquakes. The distribution of the recordings with respect to magnitude and distance is shown in Figure 2.1.

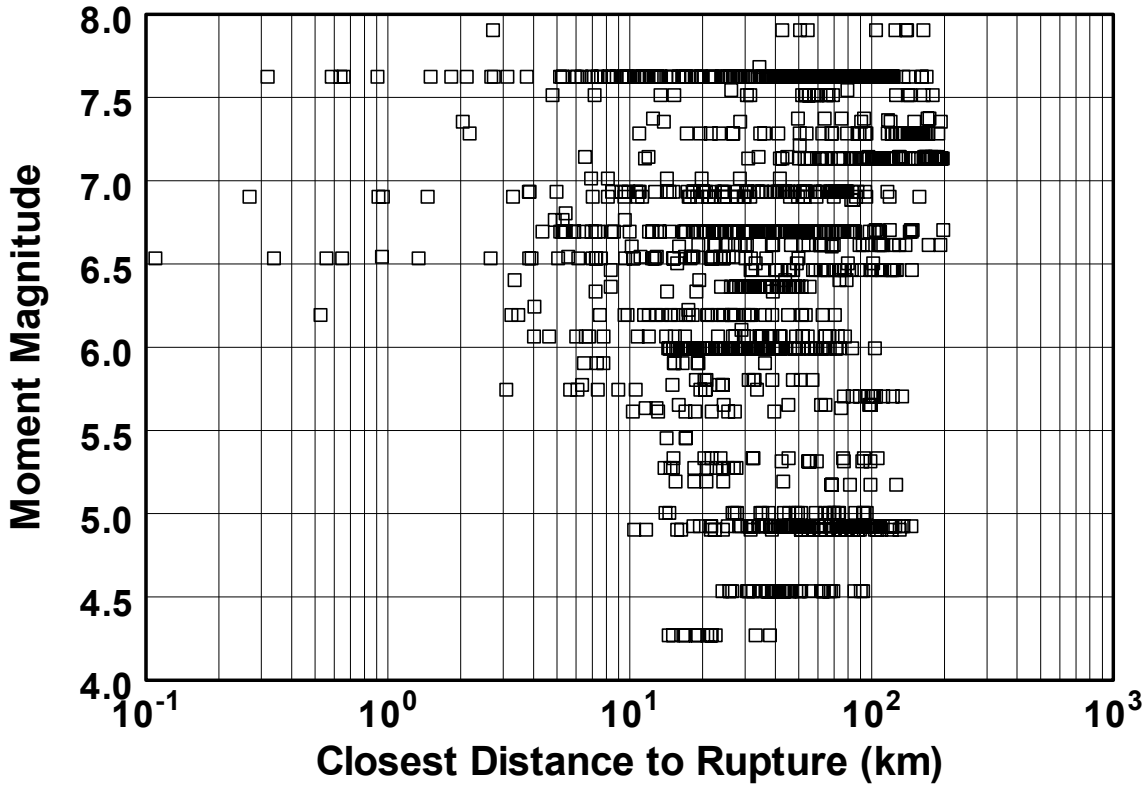

Fig. 2.1 Distribution of recordings with respect to earthquake magnitude and rupture distance.

3 Ground Motion Model

The functional forms used to develop the CB-NGA model were developed or confirmed using classical data exploration techniques, such as analysis of residuals. Candidate functional forms were developed or selected through numerous iterations to capture the observed trends in the recorded ground motion data. The final functional forms included those developed by ourselves, those taken from the literature, those derived from theoretical studies, and those proposed by the other developers during the numerous interaction meetings that were held throughout the PEER NGA Project. Final forms were chosen based on (1) their simplicity, although this was not an overriding factor; (2) their sound seismological basis; (3) their unbiased residuals; and (4) their ability to be extrapolated to values of magnitude, distance, and other predictor variables that are important to engineering applications, such as probabilistic seismic hazard analysis (PSHA). Item 4 was the most difficult to meet, because the data did not always allow the functional forms of some predictor variables to be developed empirically. For such cases, theoretical constraints were used to define these functional forms based on the supporting studies conducted as part of the PEER NGA Project.

During the development of the functional forms, the regression analysis was performed in two stages using a subset of oscillator periods and the two-step regression procedure of Boore et al. (1993) and Joyner and Boore (1993) except that each step used nonlinear rather than linear regression analysis. In Stage 1, all of those mathematical terms involving individual recordings (so-called intra-event terms) were fit by the method of nonlinear least squares using all of the selected recordings, in which each earthquake was forced to have a zero mean residual by including an inter-event term, or regression coefficient, for each earthquake. These terms included f_{dis}, f_{hng}, f_{site}, and f_{sed} in the CB-NGA model given below. In Stage 2, all of those functional forms involving the earthquake source were fit using the method of weighted least squares and the inter-event terms from Stage 1 as the database, in which each inter-event term

was assigned a weight that was inversely proportional to its variance from Stage 1. These terms included f_{mag} and f_{flt} in the CB-NGA model given below. This two-step analysis allowed us to decouple the intra-event and inter-event terms, which made the regression analysis much more stable and allowed us to independently evaluate and model magnitude-scaling effects at large magnitudes. Once the functional forms of all of the mathematical terms were established, the final regression analysis was performed for the entire range of oscillator periods using random-effects regression analysis (Abrahamson and Youngs, 1992).

3.1 EMPIRICAL GROUND MOTION MODEL

This section summarizes the CB-NGA empirical ground motion model (EGMM). Subsections include the definition of the strong motion parameter used in the model, the functional form of the median ground motion model, the functional form of the aleatory uncertainty model, and the model results.

3.1.1 Strong Motion Parameter

The strong motion component used in the CB-NGA model is not the traditional geometric mean of the two horizontal components that has been used in previous models. Previously, the geometric mean was calculated as the square root of the product (or, alternatively, the mean of the logarithms) of the peak ground motion parameters of the two as-recorded orthogonal horizontal components. This geometric mean, which we refer to as the geometric mean of the as-recorded horizontal component, is dependent on the orientation of the sensors as installed in the field. This means that the ground motion measure could differ for the same 3-D wave field depending on the orientation of the sensors. This dependence on sensor orientation is most pronounced for strongly correlated ground motion, which often occurs at oscillator periods of one second and longer.

The PEER NGA Project opted to use an alternative definition of the ground motion measure that is independent of sensor orientation. It is based on a set of geometric means computed from the as-recorded orthogonal horizontal motions after rotating them through a non-redundant angle of 90° (Boore et al., 2006). A single period-independent rotation is used, in

which the angle is chosen that minimizes the spread of the rotation-dependent geometric means over the usable range of oscillator periods. Period-independence ensures that the proper correlation between spectral ordinates is maintained. There is a distribution of geometric means to choose from using this approach (one for each of the 90 discrete rotation angles). The PEER NGA Project selected the 50th-percentile, or what is called GMRotI50 by Boore et al. (2006), as being the most appropriate for engineering use. We refer to GMRotI50 simply as the geometric mean throughout this report unless it is important to distinguish it from the geometric mean of the as-recorded horizontal components, in which case we refer to it as the geometric mean of the rotated horizontal components.

Boore et al. (2006) used the entire PEER strong motion database to compare the new geometric mean with the old geometric mean and showed that it is systematically larger than the previous one, but only by a small amount (less than 3% on average). We made this same comparison for our selected NGA database and found the two to differ by no more than 2% and generally by less than 1% (see Section 4.1). We also carried out a regression analysis on the as-recorded component of the geometric mean database and found that the regression results were very close to those reported in this chapter (Bozorgnia et al., 2006). The theoretical advantage of the new measure is that it removes sensor orientation as a contributor to aleatory uncertainty. Instead, this latter component of uncertainty is explicitly added back when an estimate of the arbitrary horizontal component (Baker and Cornell, 2006), or what some refer to as the randomly oriented horizontal component, of ground motion is required (see Sections 3.4.1 and 4.1).

The strong motion parameters addressed in this study are peak ground acceleration (PGA), peak ground velocity (PGV), peak ground displacement (PGD), and 5%-damped elastic pseudo-absolute acceleration response spectra (PSA) at 21 oscillator periods ranging from 0.01–10.0 s. The specific oscillator periods included in the CB-NGA model are 0.01, 0.02, 0.03, 0.05, 0.075, 0.1, 0.15, 0.2, 0.25, 0.3, 0.4, 0.5, 0.75, 1.0, 1.5, 2.0, 3.0, 4.0, 5.0, 7.5, and 10.0 s.

3.1.2 Median Ground Motion Model

The CB-NGA median ground motion model is given by the general equation

$$\widehat{\ln Y} = f_{mag} + f_{dis} + f_{flt} + f_{hng} + f_{site} + f_{sed} \tag{3.1}$$

where the magnitude term is given by

$$f_{mag} = \begin{cases} c_0 + c_1\mathbf{M}; & \mathbf{M} \le 5.5 \\ c_0 + c_1\mathbf{M} + c_2(\mathbf{M} - 5.5); & 5.5 < \mathbf{M} \le 6.5 \\ c_0 + c_1\mathbf{M} + c_2(\mathbf{M} - 5.5) + c_3(\mathbf{M} - 6.5); & \mathbf{M} > 6.5 \end{cases}, \tag{3.2}$$

the distance term is given by

$$f_{dis} = (c_4 + c_5\mathbf{M}) \ln\left(\sqrt{R_{RUP}^2 + c_6^2}\right), \tag{3.3}$$

the style-of-faulting term is given by

$$f_{flt} = c_7 F_{RV} f_{flt,Z} + c_8 F_{NM}, \tag{3.4}$$

$$f_{flt,Z} = \begin{cases} Z_{TOR}; & Z_{TOR} < 1 \\ 1; & Z_{TOR} \ge 1 \end{cases}, \tag{3.5}$$

the hanging-wall term is given by

$$f_{hng} = c_9 f_{hng,R} f_{hng,M} f_{hng,Z} f_{hng,\delta}, \tag{3.6}$$

$$f_{hng,R} = \begin{cases} 1; & R_{JB} = 0 \\ \left[\max\left(R_{RUP}, \sqrt{R_{JB}^2 + 1}\right) - R_{JB}\right] \Big/ \max\left(R_{RUP}, \sqrt{R_{JB}^2 + 1}\right); & R_{JB} > 0, Z_{TOR} < 1 \\ (R_{RUP} - R_{JB}) / R_{RUP}; & R_{JB} > 0, Z_{TOR} \ge 1 \end{cases}, \tag{3.7}$$

$$f_{hng,M} = \begin{cases} 0; & \mathbf{M} \le 6.0 \\ 2(\mathbf{M} - 6.0); & 6.0 < \mathbf{M} < 6.5 \\ 1; & \mathbf{M} \ge 6.5 \end{cases}, \tag{3.8}$$

$$f_{hng,Z} = \begin{cases} 0; & Z_{TOR} \ge 20 \\ (20 - Z_{TOR}) / 20; & 0 \le Z_{TOR} < 20 \end{cases}, \tag{3.9}$$

$$f_{hng,\delta} = \begin{cases} 1; & \delta \le 70 \\ (90 - \delta) / 20; & \delta > 70 \end{cases}, \tag{3.10}$$

the shallow site response term is given by

$$f_{site} = \begin{cases} c_{10}\ln\left(\dfrac{V_{S30}}{k_1}\right) + k_2\left\{\ln\left[A_{1100} + c\left(\dfrac{V_{S30}}{k_1}\right)^n\right] - \ln\left[A_{1100} + c\right]\right\}; & V_{S30} < k_1 \\ (c_{10} + k_2 n)\ln\left(\dfrac{V_{S30}}{k_1}\right); & k_1 \le V_{S30} < 1100, \\ (c_{10} + k_2 n)\ln\left(\dfrac{1100}{k_1}\right); & V_{S30} \ge 1100 \end{cases} \quad (3.11)$$

and the deep site response term is given by

$$f_{sed} = \begin{cases} c_{11}(Z_{2.5} - 1); & Z_{2.5} < 1 \\ 0; & 1 \le Z_{2.5} \le 3. \\ c_{12}k_3 e^{-0.75}\left[1 - e^{-0.25(Z_{2.5}-3)}\right]; & Z_{2.5} > 3 \end{cases} \quad (3.12)$$

In the above equations, $\widehat{\ln Y}$ is the natural logarithm of the median value of PGA (g), PGV (cm/s), PGD (cm), or PSA (g) defined in terms of the new geometric mean measure GMRotI50; **M** is moment magnitude; R_{RUP} (km) is closest distance to the coseismic rupture plane; R_{JB} (km) is closest distance to the surface projection of the coseismic rupture plane (so-called Joyner-Boore distance); F_{RV} is an indicator variable representing reverse and reverse-oblique faulting, where $F_{RV} = 1$ for $30° < \lambda < 150°$ and $F_{RV} = 0$ otherwise, and λ is rake angle, defined as the average angle of slip measured in the plane of rupture between the strike direction and the slip vector (e.g., Lay and Wallace, 1995); F_{NM} is an indicator variable representing normal and normal-oblique faulting, where $F_{NM} = 1$ for $-150° < \lambda < -30°$ and $F_{NM} = 0$ otherwise; Z_{TOR} (km) is depth to the top of the coseismic rupture plane; δ (°) is average dip of the rupture plane; V_{S30} (m/s) is average shear-wave velocity in the top 30 m of the site profile; A_{1100} (g) is the value of PGA on rock with $V_{S30} = 1100$ m/s; $Z_{2.5}$ (km) is depth to the 2.5 km/s shear-wave velocity horizon (sediment depth); $c = 1.88$ and $n = 1.18$ are period-independent, theoretically constrained model coefficients; k_i are period-dependent, theoretically constrained model coefficients; and c_i are empirically derived model coefficients.

3.1.3 Aleatory Uncertainty Model

The CB-NGA aleatory uncertainty model is given by the general random effects equation

$$\ln Y_{ij} = \widehat{\ln Y_{ij}} + \eta_i + \varepsilon_{ij} \quad (3.13)$$

where η_i is the random effect (otherwise known as the inter-event variation or source term) for the *i*th earthquake, and $\widehat{\ln Y}_{ij}$, $\ln Y_{ij}$ and ε_{ij} are the median estimate, the observed value, and the intra-event variation of the *j*th recording for the *i*th earthquake, respectively. The η_i and ε_{ij} are assumed to be independent normally distributed variates with variances τ^2 and σ^2.

In order to evaluate the validity of our median ground motion model, it is useful to relate η_i and ε_{ij} to the total model residual, defined as the difference between the observed and predicted value of $\ln Y$. Given this definition of a residual, the total model residual from Equation (3.13) is calculated as

$$r_{ij} = \eta_i + \varepsilon_{ij} = \ln Y_{ij} - \widehat{\ln Y_{ij}} \tag{3.14}$$

from which the inter-event and intra-event residuals are defined by the equations (Abrahamson and Youngs, 1992)

$$r_i^{[\text{inter}]} = \eta_i = \frac{\tau^2 \sum_{j=1}^{N_i} r_{ij}}{N_i \tau^2 + \sigma^2} \tag{3.15}$$

$$r_{ij}^{[\text{intra}]} = \varepsilon_{ij} = r_{ij} - r_i^{[\text{inter}]} \tag{3.16}$$

where N_i is the number of recordings of the *i*th earthquake. Note that in the random effects model, the proportion of the total residual that is attributed to an event is given by the ratio $\tau^2 / (N_i \tau^2 + \sigma^2)$.

In this section we present an alternative formulation to the calculation of aleatory uncertainty that arises from the explicit incorporation of nonlinear site effects in the median ground motion model (Abrahamson and Silva, 2007). As rock PGA increases, the nonlinear behavior of relatively soft sites (i.e., sites with $V_{S30} < k_1$ in the CB-NGA model) will cause a diminution in site response at short periods, which can actually result in de-amplification in some cases. As rock PGA decreases, the more linear behavior of these soft sites will cause an increase in site response. This self-compensating behavior reduces the variability of PGA and short-period PSA on soft sites that are subjected to relatively large ground motion as compared to hard sites or to soft sites that are subjected to relatively low ground motion. These effects are especially significant for NEHRP site classes D and E.

The total aleatory standard deviation of the geometric mean is given by the equation

$$\sigma_T = \sqrt{\sigma^2 + \tau^2} \tag{3.17}$$

The intra-event and inter-event variances in Equation (3.17) are defined by the relationships

$$\sigma^2 = \sigma_{\ln Y}^2 + \alpha^2 \sigma_{\ln A_{1100B}}^2 + 2\alpha\rho_\sigma \sigma_{\ln Y_B} \sigma_{\ln A_{1100B}} \tag{3.18}$$

$$\tau^2 = \tau_{\ln Y}^2 + \alpha^2 \tau_{\ln A_{1100}}^2 + 2\alpha\rho_\tau \tau_{\ln Y} \tau_{\ln A_{1100}} \tag{3.19}$$

where $\sigma_{\ln Y}$ and $\sigma_{\ln A_{1100}}$ are the intra-event standard deviations of $\ln Y$ and $\ln A_{1100}$ ($\ln \text{PGA}$) from the regression analysis (i.e., the standard errors of regression), $\tau_{\ln Y}$ and $\tau_{\ln A_{1100}}$ are the inter-event standard deviations of $\ln Y$ and $\ln A_{1100}$ from the regression analysis; $\sigma_{\ln Y_B}$ is the intra-event standard deviation of $\ln Y$ on rock ($V_{S30} = 1100$ m/s) at the base of the site profile; $\sigma_{\ln A_{1100B}}$ is the intra-event standard deviation of $\ln A_{1100}$ at the base of the site profile; ρ_σ and ρ_τ are the correlation coefficients between the intra-event and inter-event residuals of $\ln Y$ and $\ln A_{1100}$; and α is the rate of change (modeled correlation) between the shallow site response term f_{site} and $\ln A_{1100}$. For all intents and purposes, $\sigma_{\ln Y}$, $\sigma_{\ln A_{1100B}}$, $\tau_{\ln Y}$ and $\tau_{\ln A_{1100}}$ can be assumed to represent the aleatory uncertainty in the linear site response of ground motion because of the dominance of such recordings in the database.

The intra-event variances of $\ln Y$ and $\ln A_{1100}$ at the base of the site profile are given by the equations

$$\sigma_{\ln Y_B}^2 = \sigma_{\ln Y}^2 - \sigma_{\ln AMP}^2 \tag{3.20}$$

$$\sigma_{\ln A_{1100B}}^2 = \sigma_{\ln A_{1100}}^2 - \sigma_{\ln AMP}^2 \tag{3.21}$$

where $\sigma_{\ln AMP}$ is the standard deviation of the linear part of the shallow site response term f_{site}. According to W. Silva (personal communication, 2007), $\sigma_{\ln AMP} \approx 0.3$ for all oscillator periods, based on the site response analyses reported by Silva (2005). The inter-event variances of $\ln Y$ and $\ln A_{1100}$ are not reduced by the value of $\sigma_{\ln AMP}^2$, since this latter variance is considered to represent only intra-event aleatory uncertainty in the properties of the shallow site profile.

The rate of change (modeled correlation) between the shallow site response term and rock PGA is given by the partial derivative

$$\alpha = \frac{\partial f_{site}}{\partial \ln A_{1100}} = \begin{cases} k_2 A_{1100} \left\{ \left[A_{1100} + c\left(\dfrac{V_{S30}}{k_1} \right)^n \right]^{-1} - \left[A_{1100} + c \right]^{-1} \right\} & V_{S30} < k_1 \\ 0 & V_{S30} \geq k_1 \end{cases} \tag{3.22}$$

Choi and Stewart (2005) also found a dependence of the intra-event standard deviation on V_{S30}. They found that softer sites tended to have lower standard deviations than stiffer sites.

Since these authors did not include ground motion amplitude as a parameter in their aleatory uncertainty model, the difference in the standard deviations that they found might be due, at least in part, to the nonlinear site effects embodied in Equations (3.18) to (3.22). We investigated this by binning our intra-event residuals into V_{S30} ranges representing NEHRP site classes C ($V_{S30} = 360 - 760$ m/s) and D ($V_{S30} = 180 - 360$ m/s) and by performing a hypothesis test to see if the differences in the mean residuals for PGA and PSA at periods of 0.2, 1.0, and 3.0 s were statistically significant. We found that the mean residuals for each of the velocity bins were not significantly different from zero (no bias) and that the residual standard deviations of each of the bins were within about 0.03 of each other (an insignificant difference). Therefore, we did not find it necessary to make the standard deviations of the linear ground motion predictions dependent on the value of V_{S30}.

We did find both a slight positive bias in the mean residuals and a larger difference in the residual standard deviations between bins when we included only those sites with measured values of V_{S30}. The differences in the standard deviations were generally consistent with the results of Choi and Stewart (2005), who only used sites with measured values of V_{S30}. The bias in the mean residuals suggests that ground motion amplitudes might be underpredicted by the CB-NGA model by as much as 10% at some oscillator periods. However, further study is needed before we would recommend adjusting our model for possible differences in the predicted amplitudes of ground motion between sites with estimated and measured values of V_{S30}, particularly since there is likely to be a correlation between sites with measured shear-wave velocities and recordings with relatively high levels of ground motion, due to the engineering significance of such recordings.

It is important to note that intra-event and inter-event standard deviations were not found to be a significant function of magnitude as has been the case in many past studies. The previously observed dependence of aleatory variability on magnitude by us (Campbell and Bozorgnia, 1994, 2003a, 2003b, 2003c, 2004) and other researchers might largely have been an artifact of the use of poorly recorded events near the upper- and lower-magnitude limits of the data range. The larger number of events and high-quality recordings for both small- and large-magnitude earthquakes in the present study has allowed us to adopt more restrictive selection criteria, especially with respect to the minimum number of recordings for small-magnitude earthquakes, which has significantly improved the analysis and reduced the inter-event and intra-

event variability of these events. The increase in the number of well-recorded earthquakes at large magnitudes has resulted in a better, albeit somewhat increased, estimate of intra-event variability for such events. Our findings are consistent with those of Choi and Stewart (2005) who, in a careful investigation of the residuals of several empirical ground motion models, did not find compelling evidence for either a magnitude-dependent or distant-dependent inter-event or intra-event standard deviation, once the dependence on V_{S30} was taken into account.

The relatively large variability of ground motion close to the 2004 (**M** 6.0) Parkfield earthquake led Shakal et al. (2006) to suggest that a distance-dependent standard deviation may be important to consider when predicting ground motion close to faults. The PGA from this earthquake within a few kilometers of the surface trace of the causative fault ranged from around 0.13*g* to over 1.8*g*, depending on where the recording was located. Upon further investigation, we found that the standard deviation associated with the Parkfield recordings, although larger at close distances, was not larger than that predicted by the CB-NGA model and, therefore, we do not believe that this uncertainty should be increased at short distances. What is evident from the Parkfield earthquake is that the recordings that were located within the relatively wide San Andreas fault zone had very low accelerations and velocities compared to those located just outside of this zone. Pitarka et al. (2006) attributed this to the relatively low shear-wave velocity and relatively high attenuation in the fault gouge within this zone.

3.1.4 Regression Results

The median ground motion model coefficients determined in this study for PGA, PGV, PGD, and PSA at the 21 oscillator periods ranging from 0.01–10.0 s are listed in Table 3.1. The aleatory standard deviations and correlation coefficients are listed in Table 3.2. Note that the constants $c = 1.88$ and $n = 1.18$ are the same for all oscillator periods, as indicated in the footnote to Table 3.1. Also note that there are some combinations of parameter values for which the calculated value of PSA at $T < 0.2$ s falls below the value of PSA at $T = 0.01$ s (PGA). Since this is an artifact of the regression analysis and is not physically possible given the definition of pseudo-absolute acceleration, the calculated value of PSA should be set equal to the value of PSA at $T = 0.01$ s when this situation occurs.

3.2 JUSTIFICATION OF FUNCTIONAL FORMS

This section presents justification for the selected functional forms in the median ground motion model. Subsections include a discussion of the magnitude term, the distance term, the style-of-faulting term, the hanging-wall term, the shallow site response term, and the deep site response term. Plots of residuals versus each of the predictor variables included in the model are used to confirm the validity of each of these terms. Plots are shown for PGA, PGV, and PSA at periods of 0.2, 1.0, 3.0, and 10.0 s. Note that a positive residual indicates underprediction by our model and a negative residual indicates overprediction by our model.

3.2.1 Magnitude Term

The trilinear functional form used to model f_{mag} was derived from an analysis of residuals. This functional form was used to model the observed decrease in the degree of magnitude scaling with increasing magnitude at short distances, commonly known as saturation (Campbell, 1981), using a piecewise linear function rather than the more commonly used quadratic function. The piecewise linear scaling model for $\mathbf{M} > 6.5$ allows greater control of large-magnitude scaling and, unlike the quadratic scaling model, decouples this scaling from that of smaller magnitudes, allowing more flexibility in determining how ground motions scale with the size of an earthquake. Stochastic simulations demonstrated that the trilinear model was able to fit the magnitude-scaling characteristics of ground motion just as well as the quadratic model over the magnitude range of interest in this study.

The regression analysis using the trilinear magnitude term produced a tendency for oversaturation at the shorter periods of ground motion for large magnitudes and short distances. This behavior, which had been noted in previous studies, but not considered to be reliable, was reinforced by some recent well-recorded large-magnitude earthquakes, including the 1999 (**M** 7.5) Kocaeli earthquake in Turkey, the 1999 (**M** 7.6) Chi-Chi earthquake in Taiwan, and the 2002 (**M** 7.9) Denali earthquake in Alaska. Although some seismologists believe that such a reduction in short-period ground motion is possible for very large earthquakes (e.g., Schmedes and Archuleta, 2007), this behavior was not found to be statistically significant because of the limited number of near-source recordings from large earthquakes.

Other functional forms were either found to be too difficult to constrain empirically (e.g., the hyperbolic tangent function used by Campbell, 1997, 2000, 2001) or could not be reliably extrapolated to magnitudes as large as **M** 8.5 (e.g., the quadratic function used by many other investigators) as required by the PEER NGA Project. It is interesting to note that in our previous spectral acceleration model (Campbell and Bozorgnia, 2003a, 2003b, 2003c, 2004), we found it necessary to force magnitude saturation at all periods in order to make the regression analysis converge. In the CB-NGA model, this constraint was not necessary nor was it warranted at moderate-to-long periods.

During review of the NGA models, one of the reviewers was concerned that many of the large earthquakes in the PEER database had ground motions that were biased low because of a potentially biased distribution of recordings with respect to tectonic environment, source-site azimuth, and the location of large asperities. He did, however, support the notion that short-period ground motion should "saturate" with magnitude near the fault. This was later verified by Frankel (2007) using broadband ground motion simulations of extended fault sources. Halldorsson and Papageorgiou (2005) also found a breakdown in self-similar magnitude scaling of high-frequency ground motion from worldwide "interplate" earthquakes above **M** 6.3, which caused them to add a parameter to significantly decrease high-frequency magnitude scaling at large magnitudes in their specific barrier model. They attributed this deviation to a decrease in "effective" source area and/or irregularities in the rupture kinematics. This supports the Hanks and Bakun (2002) finding that the rupture area of shallow continental earthquakes is less dependent on magnitude above about **M** 6.7, which they attributed to a breakdown in self-similar magnitude scaling after coseismic rupture extends the full width of the seismogenic zone, consistent with the *L* (length) rupture model of Scholz (1982). Douglas (2002) also found empirical evidence in support of the *L*-model's inferred near-source magnitude-scaling characteristics for PGA and PGV. Schmedes and Archuleta (2007) used kinematic ground motion simulations of a strike-slip fault with large aspect ratio (length/width) to show that PGV increases to a maximum at a critical epicentral distance and then decreases to an asymptotic level beyond a critical distance along the fault related to the rupture width. Di Toro et al. (2006) gave a possible physical reason for a breakdown in self similarity. They concluded from investigations of exhumed faults and from laboratory experiments in granitoids (tonalities) that dynamic shear resistance becomes low at 10 km depths when coseismic slip exceeds around 1 m

due to friction-induced melting on the fault surface. According to Wells and Coppersmith (1994), 1 m of displacement corresponds to an earthquake of approximately **M** 6.7–6.9.

The observations noted above could possibly be interpreted as possible evidence for oversaturation of ground motion with magnitude. However, considering the weak statistical evidence for oversaturation in our analyses, the general support of the USGS and other seismologists that short-period ground motion can saturate, and the lack of scientific consensus in support of oversaturation, we conservatively decided to constrain f_{mag} to remain constant (i.e., saturate) at $\mathbf{M} > 6.5$ and $R_{RUP} = 0$ when oversaturation was predicted by the regression analysis. This constraint was equivalent to setting $c_3 = -c_1 - c_2 - c_5 \ln(c_6)$ in Equation (3.2).

Jack Boatwright of the USGS (written communication, 2005) developed a simple seismological model that showed that the far-field magnitude-scaling coefficient of $\log \mathrm{PGA}$ and $\log \mathrm{SA}$ at short periods for earthquakes of $\mathbf{M} > 6.7$, where ground motion can be expected to saturate with magnitude at close distances, should be less than about $0.38\,\Delta\mathbf{M}$. Converting our large-magnitude-scaling coefficient (c_3) from a natural to a common logarithm, we get a far-field ($R_{RUP} = 200$ km) magnitude-scaling coefficient of about $0.25\,\Delta\mathbf{M}$ for $\log \mathrm{PGA}$ and $\log \mathrm{SA}$ at $T = 0.2$ s, where our model saturates. Our model does not predict near-source magnitude saturation at moderate-to-long spectral periods, but if we assume saturation, we get a far-field magnitude-scaling coefficient of about $0.29\,\Delta\mathbf{M}$ for $\log \mathrm{SA}$ at $T = 1.0$ and 3.0 s, very similar to that at shorter periods. All of these magnitude-scaling coefficients satisfy the upper-bound threshold suggested from Boatwright's simple seismological model. Figures 3.1 and 3.2 show the dependence of inter-event and intra-event residuals on magnitude. In these and all subsequent figures, plots labeled SA refer to the pseudo-absolute acceleration parameter PSA.

3.2.2 Distance Term

Our previous model (Campbell and Bozorgnia, 1994, 2003a, 2003b, 2003c, 2004), which was developed for distances of 60 km and less, had a constant rate of attenuation with magnitude. Since the PEER NGA Project required that the ground motion predictions be valid to distances of 200 km, we found it was important to add a magnitude-dependent geometrical attenuation term to f_{dis}, similar to that used by Abrahamson and Silva (1997), in order to fit both small- and large-magnitude recordings. Another advantage of the Abrahamson-Silva functional form over

our old functional form is that it transfers the magnitude-dependent attenuation term from inside the square-root term in Equation (3.3) to outside this term, which made the nonlinear regression analysis more stable.

Jack Boatwright of the USGS (written communication, 2005) developed a simple seismological model that showed that the magnitude-dependent geometrical attenuation coefficient (c_5) should be less than 0.17. We obtained a value close to this in our regression analysis, but the coefficient varied randomly with period. As a result, we chose to set $c_5 = 0.17$ in our final model. The magnitude-independent rate of attenuation predicted by f_{dis}, represented by the coefficient c_4 in the CB-NGA model, includes the effects of anelastic as well as geometrical attenuation. For this reason, we predict higher overall geometrical attenuation rates than the values of –1 for a point-source (**M** 5.0) and –0.5 for an infinitely long fault (**M** 8.0) predicted by Boatwright's simple seismological model. For these same magnitudes, we get values of about –1.3 and –0.8 for PGA and PSA at $T = 0.2$ s and –1.2 and –0.6 for PSA at $T = 1.0$ and 3.0 s, which, as expected, are consistently higher than the theoretical values for geometrical attenuation alone.

Frankel (2007) used broadband ground-motion simulations of extended fault sources to show that the distance decay of response spectral ordinates was consistent with the functional form of the CB-NGA model for magnitudes of 6.5 and 7.5 and distances ranging from about 2–100 km. Figure 3.3 shows the dependence of intra-event residuals on distance.

3.2.3 Style-of-Faulting Term

The functional form used to model f_{flt} was determined from an analysis of residuals. It introduces a new parameter (Z_{TOR}) that represents whether or not coseismic rupture extends to the surface. This new parameter was found to be important for modeling reverse-faulting events. Ground motions were found to be significantly higher for reverse faults when rupture did not propagate to the surface no matter whether this rupture was on a blind thrust fault or on a fault with previous surface rupture. When rupture broke to the surface or to very shallow depths, ground motions for reverse faults were found to be comparable on average to those for strike-slip faults. Some strike-slip ruptures with partial or weak surface expression also appeared to have higher-than-average ground motions (e.g., the 1995 Kobe, Japan, earthquake), but there were

many counter examples in the database. Some of these discrepancies could be due to the ambiguity in identifying coseismic surface rupture for strike-slip events. As a result, we decided that additional study would be needed to resolve these discrepancies before it was possible to consider Z_{TOR} as a parameter for strike-slip faulting.

Somerville and Pitarka (2006) give both empirical and theoretical evidence to support their conclusions that ground motions from earthquakes that break the ground surface are weaker than those from buried events. Dynamic rupture simulations show that if a weak zone exists at shallow depths, rupture of the shallow part of the fault will be controlled by velocity strengthening, with larger slip weakening distance, larger fracture energy, larger energy absorption from the crack tip, lower rupture velocity, and lower slip velocity than at greater depths on the fault. These properties lead to lower ground motions for surface faulting than for buried faulting. The field and laboratory results of Di Toro et al. (2006) also indicate that this phenomenon might extend to intermediate depths as well due to melting on the fault surface during large coseismic slip. If this were true, we possibly could expect this phenomenon to occur for all earthquakes of large enough slip (about 1 m according to Di Toro et al.). However, this phenomenon is interrelated with magnitude-scaling effects (see Section 3.2.1), so it might be that the presence of a weak shallow layer adds to this effect for surface-rupturing earthquakes.

The model coefficient for normal faulting was found to be only marginally significant at shorter periods, but significant at longer periods. We were concerned that the long-period effects were due to systematic differences in sediment depth, since many of these events occurred in a geological and tectonic environment that might be associated with shallow depths to hard rock (e.g., Italy and Greece). This seems to be corroborated by Ambraseys et al. (2005), who found that strike-slip and normal-faulting ground motions from similar regions in Europe and the Middle East had similar spectral amplitudes at moderate-to-long periods. As a result, we constrained the relatively small normal-faulting factor (F_{NM}) found at short periods (–12%) to go to zero at longer periods.

Figure 3.4 shows the dependence of inter-event residuals on depth to top of rupture. Figure 3.5 shows the dependence of inter-event residuals on rake angle, with vertical grey lines showing the model we used for partitioning rake angle in terms of strike-slip (SS), reverse (RV), and normal (NM) faulting mechanisms.

3.2.4 Hanging-Wall Term

The functional form used to model f_{hng} was determined from an analysis of residuals with additional constraints to limit its range of applicability. The functional form for $f_{hng,R}$, the term used to model the distance-dependence of f_{hng}, is our modified version of the hanging-wall term originally suggested by Chiou and Youngs (2007). In our version, we force hanging-wall effects to have a smooth transition between the hanging wall and the footwall, even at small values of Z_{TOR}, which avoids an abrupt drop in the predicted ground motion as one crosses the fault trace from the hanging wall to the footwall. The original Chiou-Youngs model only smoothed out the transition from the hanging wall to the footwall when the fault was buried. In its preliminary review of the NGA models for PEER, the USGS pointed out that there is very little data to support such an abrupt drop from the hanging wall to the footwall over what can amount to only a few meters distance, and that providing a smooth transition from the hanging wall to the footwall would allow for some uncertainty in the location of the actual fault trace. We also included the additional terms $f_{hng,M}$, $f_{hng,Z}$, and $f_{hng,\delta}$ to phase out hanging-wall effects at small magnitudes, large rupture depths, and large rupture dips, where the residuals suggested that these effects are either negligible or cannot be resolved with the data.

Unlike our previous model, we have included hanging-wall effects for normal-faulting earthquakes in our current NGA model. Although the statistical evidence for hanging-wall effects for normal faults is weak in our regression analysis, we found that it was consistent with the better-constrained hanging-wall effects for reverse faults. Furthermore, Jim Brune (personal communication, 2006) has noted that hanging-wall effects similar to those for reverse faults have been observed in foam rubber modeling of normal-faulting earthquakes in laboratory experiments and is consistent with the limited amount of precarious rock observations on the hanging wall of normal faults with documented historical and Holocene rupture in the basin and range province of the United States. Also, in a recent study on broadband simulations of ground motion in the basin and range, Collins et al. (2006) found a hanging-wall factor for normal-faulting earthquakes that is similar to the one we found empirically for reverse-faulting earthquakes. It should be noted that, unlike a reverse fault, the hanging wall of a normal fault will typically lie beneath the range front valley where most of the population is located (e.g., Reno, Nevada, and Salt Lake City, Utah).

No single predictor variable can be used to represent the hanging-wall term. Instead, Figure 3.6 shows the dependence of intra-event residuals on the hanging-wall factor. This factor is defined as the product of $f_{hng,R}$, $f_{hng,M}$, $f_{hng,Z}$ and $f_{hng,\delta}$ in Equation (3.6).

3.2.5 Shallow Site Response Term

The linear part of the functional form used to model f_{site} is similar to that originally proposed by Boore et al. (1994) and Borcherdt (1994) and later adopted by Boore et al. (1997) and Choi and Stewart (2005), among others. One difference from these earlier studies is that we hold the site term to be constant to the term for $V_{S30} = 1100$ m/s when site velocities are greater than this value. This constraint was imposed based on an analysis of residuals that indicated that ground motion at long periods and high values of V_{S30} were underpredicted when this constraint was not applied. This constraint should have probably been applied at a smaller value of V_{S30} at long periods, but that would have complicated the use of the nonlinear site term (i.e., the limiting value of V_{S30} would have been less than k_1 for some oscillator periods). Since there are only a limited number of recordings with site velocities greater than 1100 m/s, we believe that a more refined constraint is unwarranted at this time.

The nonlinear part of the site term was constrained from theoretical studies conducted as part of the PEER NGA Project, since the empirical data were insufficient to constrain the complex nonlinear behavior of the softer soils. After including the linear part of f_{site} in the model, the residuals clearly exhibited a bias when plotted against rock PGA (A_{1100}), consistent with the nonlinear behavior of PGA and PSA at shorter periods. However, because of the relatively small number of recordings, the residuals alone could not be used to determine how this behavior varied with V_{S30}, ground motion amplitude, and oscillator period. Instead, a nonlinear site response model developed by Walling and Abrahamson (2006), based on 1-D equivalent-linear site response simulations conducted by Silva (2005), was used to constrain the functional form and the nonlinear model coefficients k_1, k_2, n, and c in Equation (3.11). This approach is supported by Kwok and Stewart (2006) who found that theoretical site factors from 1-D equivalent-linear site response analyses were able to capture the average effects of soil nonlinearity when used in conjunction with empirical ground motion models to estimate a reference rock spectrum.

The linear behavior of the CB-NGA model was calibrated by empirically fitting c_{10} in the regression analysis. This explicit incorporation of nonlinear site effects is believed to be superior to the approach used in our previous models (Campbell and Bozorgnia, 1994, 2003a, 2003b, 2003c, 2004; Campbell, 1997, 2000, 2001), which implicitly modeled these effects by making the near-source attenuation term a function of site conditions.

Walling and Abrahamson (2006) developed two sets of nonlinear model coefficients, one set representing dynamic soil properties (i.e., strain-dependent shear modulus reduction and damping curves) developed by EPRI (1993) and another set representing dynamic soil properties developed by Silva et al. (1999), which they refer to as the peninsular range or PEN curves. Neither our residuals nor the empirical site factors compiled by Power et al. (2004) could distinguish between these two alternative models, although a slightly lower aleatory standard deviation favored the PEN model. On the advice of Walt Silva, we selected the PEN model because it represents a wider range of regional site conditions than the EPRI model.

Figure 3.7 shows the dependence of intra-event residuals on 30-m shear-wave velocity and rock PGA. Vertical lines on this plot show the partitioning of V_{S30} into the five NEHRP site classes (BSSC, 2004). Figure 3.8 shows the dependence of intra-event residuals on rock PGA.

3.2.6 Deep Site Response Term

The functional form used to model f_{sed} has two parts: (1) a term to model 3-D basin effects for $Z_{2.5} > 3.0$ km and (2) a term to model shallow-sediment effects for $Z_{2.5} < 1.0$ km. We modeled the basin term from theoretical studies conducted as part of the PEER NGA Project. We modeled the shallow sediment term based on an analysis of residuals. The residuals after including f_{site} clearly indicated that long-period ground motion increased with sediment depth up to around $Z_{2.5} = 1.0$ km, leveled off, then increased again at $Z_{2.5} > 3.0$ km. We surmise that the observed decrease in long-period ground motion for sites with shallow sediment depths might be the result of relatively lower long-period site amplification effects compared to sites with deep sediment depths and the same values of V_{S30}. We found that the data were sufficient to empirically constrain this trend.

The trend for $Z_{2.5} > 3.0$ km, which is due presumably to 3-D basin effects, was based on too few data to empirically determine how these effects could be extrapolated with sediment

depth and oscillator period. Instead, this trend was constrained using the sediment depth model developed by Day et al. (2006) for $Z_{1.5}$ and later by Day (personal communication, 2006) for $Z_{2.5}$ from theoretical ground motion simulations of the 3-D response of the Los Angeles, San Gabriel, and San Fernando basins in southern California. These authors also found that ground motions scaled strongly with depth between depths of 1.0 and 3.0 km, whereas we did not find any trend in the residuals over this depth range. We believe that this scaling is apparently accounted for by other parameters in our model (most likely V_{S30}). For example, it is below a depth of 3.0 km that we find a strong correlation between $Z_{2.5}$ and V_{S30} in the PEER database. It is also possible that the ground motion simulations are dominated by 1-D effects at depths shallower than about 3.0 km, which are adequately modeled by f_{site}.

Day et al.'s model was developed for oscillator periods of 2.0 s and greater, but these authors developed relationships for their model coefficients which allowed us to extrapolate them to shorter periods. In order to remove any bias that this extrapolation might cause, we included an additional model coefficient (c_{12}) in Equation (3.12) to empirically adjust the theoretical model coefficient k_3 (Day et al.'s a_2 coefficient). This additional coefficient was found to increase from about one half for PGA to around unity for PSA at longer periods. Once c_{12} obtained unity in the regression analysis, it was constrained to unity at longer periods. Because the Day et al. model was applied only at large sediment depth, their first term (involving their a_1 coefficient) was found to be negligible and was dropped from our deep site response term.

The finite value of c_{12} at short periods causes the CB-NGA model to predict some (albeit weak) amplification at these periods. Although counter-intuitive to many seismologists' expectations, these results are generally consistent with the empirical results of Campbell (1997, 2000, 2001) and Field (2000), although Campbell did not find any significant amplification at oscillator periods of less than 0.5 s. Figure 3.9 shows the dependence of intra-event residuals on sediment depth.

3.3 TREATMENT OF MISSING VALUES

When predictor variables for selected recordings were missing from the PEER database, they were either estimated or the regression analysis involving the terms that contained those

variables was performed using only those recordings for which the values were available. These recordings were still used in the regression analyses that involved other predictor variables, for which these missing values were not an issue. Sediment depth ($Z_{2.5}$) was the only predictor variable that had missing values and no available estimates to substitute. There were two predictor variables (R_{RUP} and V_{S30}) for which missing values were replaced with estimated values. When direct measurements of V_{S30} for California sites were missing, estimates were provided by Wills and Clahan (2005) using statistical relationships between V_{S30} and geologic units. When direct measurements of V_{S30} for Taiwan sites were missing, Brian Chiou (written communication, 2006) provided estimates of V_{S30} using relationships among V_{S30}, site elevation, and generalized geologic site categories.

The 1992 (**M** 6.5) Big Bear earthquake was the only $\mathbf{M} \geq 6.0$ event in our database that was missing values for R_{RUP}. In this case, we used the values for R_{SEIS} from our previous model. Because the depth to the top of rupture was around 3.0 km, the two distance measures could be considered equivalent. For those selected events with $\mathbf{M} < 6.0$, we used hypocentral distance as an estimate of R_{RUP} because of their relatively small source dimensions.

Table 3.1 Coefficients for CB-NGA median ground motion model.

T	c_0	c_1	c_2	c_3	c_4	c_5	c_6	c_7	c_8	c_9	c_{10}	c_{11}	c_{12}	k_1	k_2	k_3
0.010	-1.715	0.500	-0.530	-0.262	-2.118	0.170	5.60	0.280	-0.120	0.490	1.058	0.040	0.610	865	-1.186	1.839
0.020	-1.680	0.500	-0.530	-0.262	-2.123	0.170	5.60	0.280	-0.120	0.490	1.102	0.040	0.610	865	-1.219	1.840
0.030	-1.552	0.500	-0.530	-0.262	-2.145	0.170	5.60	0.280	-0.120	0.490	1.174	0.040	0.610	908	-1.273	1.841
0.050	-1.209	0.500	-0.530	-0.267	-2.199	0.170	5.74	0.280	-0.120	0.490	1.272	0.040	0.610	1054	-1.346	1.843
0.075	-0.657	0.500	-0.530	-0.302	-2.277	0.170	7.09	0.280	-0.120	0.490	1.438	0.040	0.610	1086	-1.471	1.845
0.10	-0.314	0.500	-0.530	-0.324	-2.318	0.170	8.05	0.280	-0.099	0.490	1.604	0.040	0.610	1032	-1.624	1.847
0.15	-0.133	0.500	-0.530	-0.339	-2.309	0.170	8.79	0.280	-0.048	0.490	1.928	0.040	0.610	878	-1.931	1.852
0.20	-0.486	0.500	-0.446	-0.398	-2.220	0.170	7.60	0.280	-0.012	0.490	2.194	0.040	0.610	748	-2.188	1.856
0.25	-0.890	0.500	-0.362	-0.458	-2.146	0.170	6.58	0.280	0.000	0.490	2.351	0.040	0.700	654	-2.381	1.861
0.30	-1.171	0.500	-0.294	-0.511	-2.095	0.170	6.04	0.280	0.000	0.490	2.460	0.040	0.750	587	-2.518	1.865
0.40	-1.466	0.500	-0.186	-0.592	-2.066	0.170	5.30	0.280	0.000	0.490	2.587	0.040	0.850	503	-2.657	1.874
0.50	-2.569	0.656	-0.304	-0.536	-2.041	0.170	4.73	0.280	0.000	0.490	2.544	0.040	0.883	457	-2.669	1.883
0.75	-4.844	0.972	-0.578	-0.406	-2.000	0.170	4.00	0.280	0.000	0.490	2.133	0.077	1.000	410	-2.401	1.906
1.0	-6.406	1.196	-0.772	-0.314	-2.000	0.170	4.00	0.255	0.000	0.490	1.571	0.150	1.000	400	-1.955	1.929
1.5	-8.692	1.513	-1.046	-0.185	-2.000	0.170	4.00	0.161	0.000	0.490	0.406	0.253	1.000	400	-1.025	1.974
2.0	-9.701	1.600	-0.978	-0.236	-2.000	0.170	4.00	0.094	0.000	0.371	-0.456	0.300	1.000	400	-0.299	2.019
3.0	-10.556	1.600	-0.638	-0.491	-2.000	0.170	4.00	0.000	0.000	0.154	-0.820	0.300	1.000	400	0.000	2.110
4.0	-11.212	1.600	-0.316	-0.770	-2.000	0.170	4.00	0.000	0.000	0.000	-0.820	0.300	1.000	400	0.000	2.200
5.0	-11.684	1.600	-0.070	-0.986	-2.000	0.170	4.00	0.000	0.000	0.000	-0.820	0.300	1.000	400	0.000	2.291
7.5	-12.505	1.600	-0.070	-0.656	-2.000	0.170	4.00	0.000	0.000	0.000	-0.820	0.300	1.000	400	0.000	2.517
10.0	-13.087	1.600	-0.070	-0.422	-2.000	0.170	4.00	0.000	0.000	0.000	-0.820	0.300	1.000	400	0.000	2.744
PGA	-1.715	0.500	-0.530	-0.262	-2.118	0.170	5.60	0.280	-0.120	0.490	1.058	0.040	0.610	865	-1.186	1.839
PGV	0.954	0.696	-0.309	-0.019	-2.016	0.170	4.00	0.245	0.000	0.358	1.694	0.092	1.000	400	-1.955	1.929
PGD	-5.270	1.600	-0.070	0.000	-2.000	0.170	4.00	0.000	0.000	0.000	-0.820	0.300	1.000	400	0.000	2.744

Note: $c = 1.88$ and $n = 1.18$ for all periods; PGA and PSA have units of g; PGV and PGD have units of cm/s and cm, respectively.

Table 3.2 Standard deviations and correlation coefficients for CB-NGA aleatory uncertainty model.

Period T (s)	Standard Deviation			σ_T for $V_{S30} \geq k_1$ [3]		Correlation Coeff.	
	$\sigma_{\ln Y}$	$\tau_{\ln Y}$	σ_c	Geometric Mean[1]	Arbitrary Comp.[2]	ρ_σ	ρ_τ
0.010	0.478	0.219	0.166	0.526	0.551	1.000	1.000
0.020	0.480	0.219	0.166	0.528	0.553	0.999	0.994
0.030	0.489	0.235	0.165	0.543	0.567	0.989	0.979
0.050	0.510	0.258	0.162	0.572	0.594	0.963	0.927
0.075	0.520	0.292	0.158	0.596	0.617	0.922	0.880
0.10	0.531	0.286	0.170	0.603	0.627	0.898	0.871
0.15	0.532	0.280	0.180	0.601	0.628	0.890	0.885
0.20	0.534	0.249	0.186	0.589	0.618	0.871	0.913
0.25	0.534	0.240	0.191	0.585	0.616	0.852	0.873
0.30	0.544	0.215	0.198	0.585	0.618	0.831	0.848
0.40	0.541	0.217	0.206	0.583	0.618	0.785	0.756
0.50	0.550	0.214	0.208	0.590	0.626	0.735	0.631
0.75	0.568	0.227	0.221	0.612	0.650	0.628	0.442
1.0	0.568	0.255	0.225	0.623	0.662	0.534	0.290
1.5	0.564	0.296	0.222	0.637	0.675	0.411	0.290
2.0	0.571	0.296	0.226	0.643	0.682	0.331	0.290
3.0	0.558	0.326	0.229	0.646	0.686	0.289	0.290
4.0	0.576	0.297	0.237	0.648	0.690	0.261	0.290
5.0	0.601	0.359	0.237	0.700	0.739	0.200	0.290
7.5	0.628	0.428	0.271	0.760	0.807	0.174	0.290
10.0	0.667	0.485	0.290	0.825	0.874	0.174	0.290
PGA	0.478	0.219	0.166	0.526	0.551	1.000	1.000
PGV	0.484	0.203	0.190	0.525	0.558	0.691	0.538
PGD	0.667	0.485	0.290	0.825	0.874	0.174	0.290

[1] Geometric mean defined as GMRotI50 by Boore et al. (2006).

[2] Arbitrary horizontal component of Baker and Cornell (2006); also known as randomly oriented component.

[3] See Equations (3.14)–(3.19) for the calculation of σ_T for $V_{S30} < k_1$.

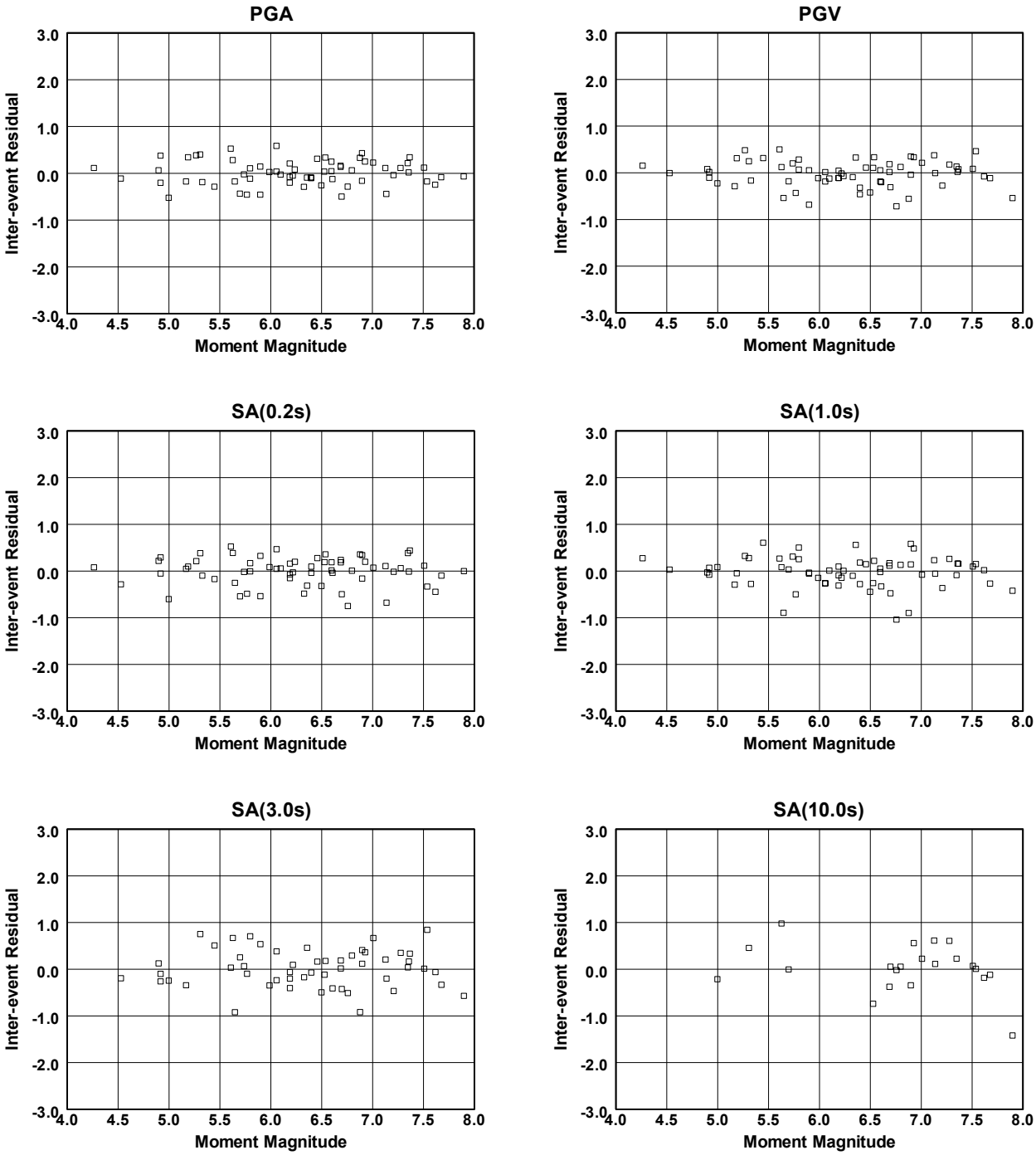

Fig. 3.1 Dependence of inter-event residuals on earthquake magnitude.

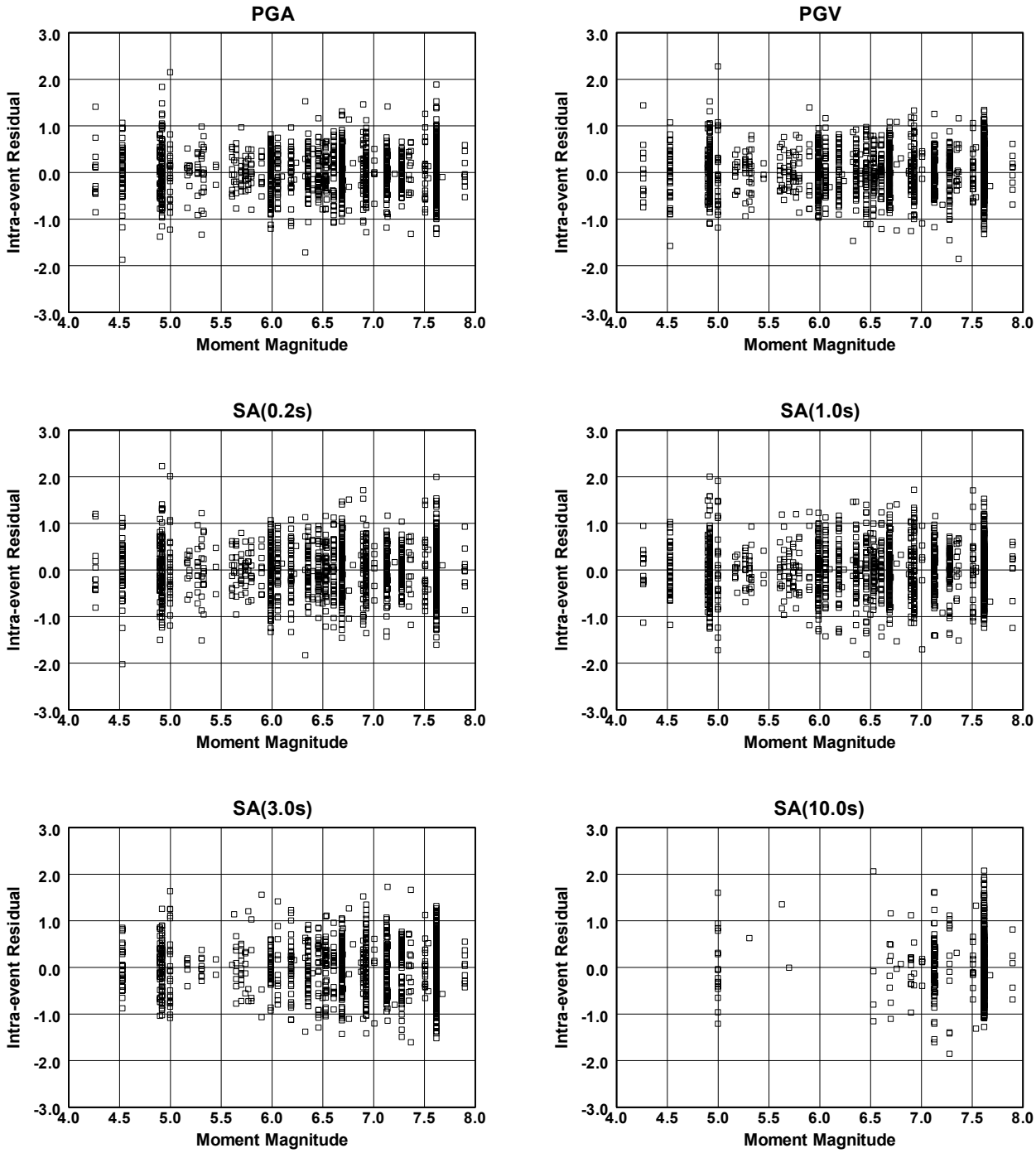

Fig. 3.2 Dependence of intra-event residuals on earthquake magnitude.

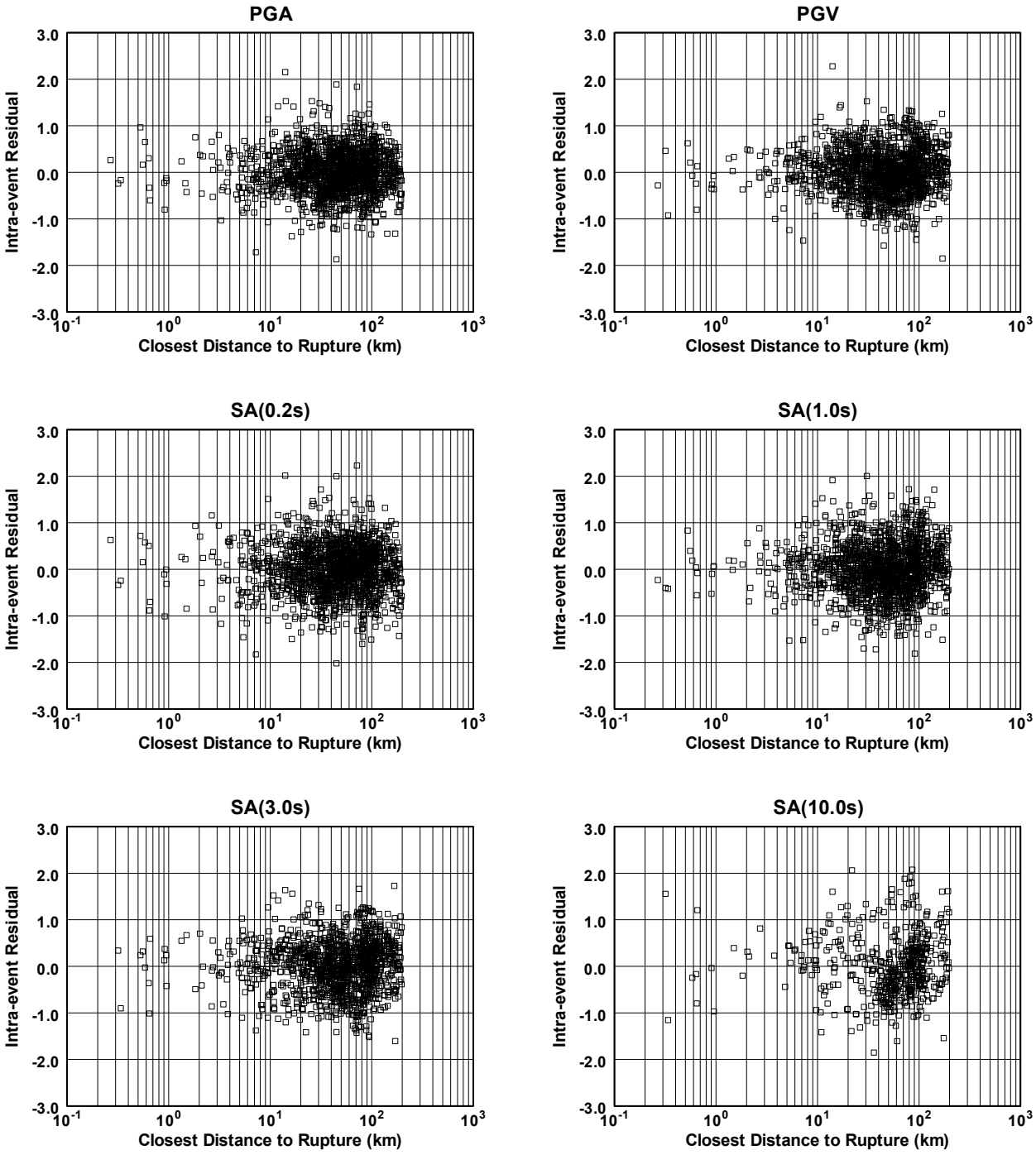

Fig. 3.3 Dependence of intra-event residuals on rupture distance.

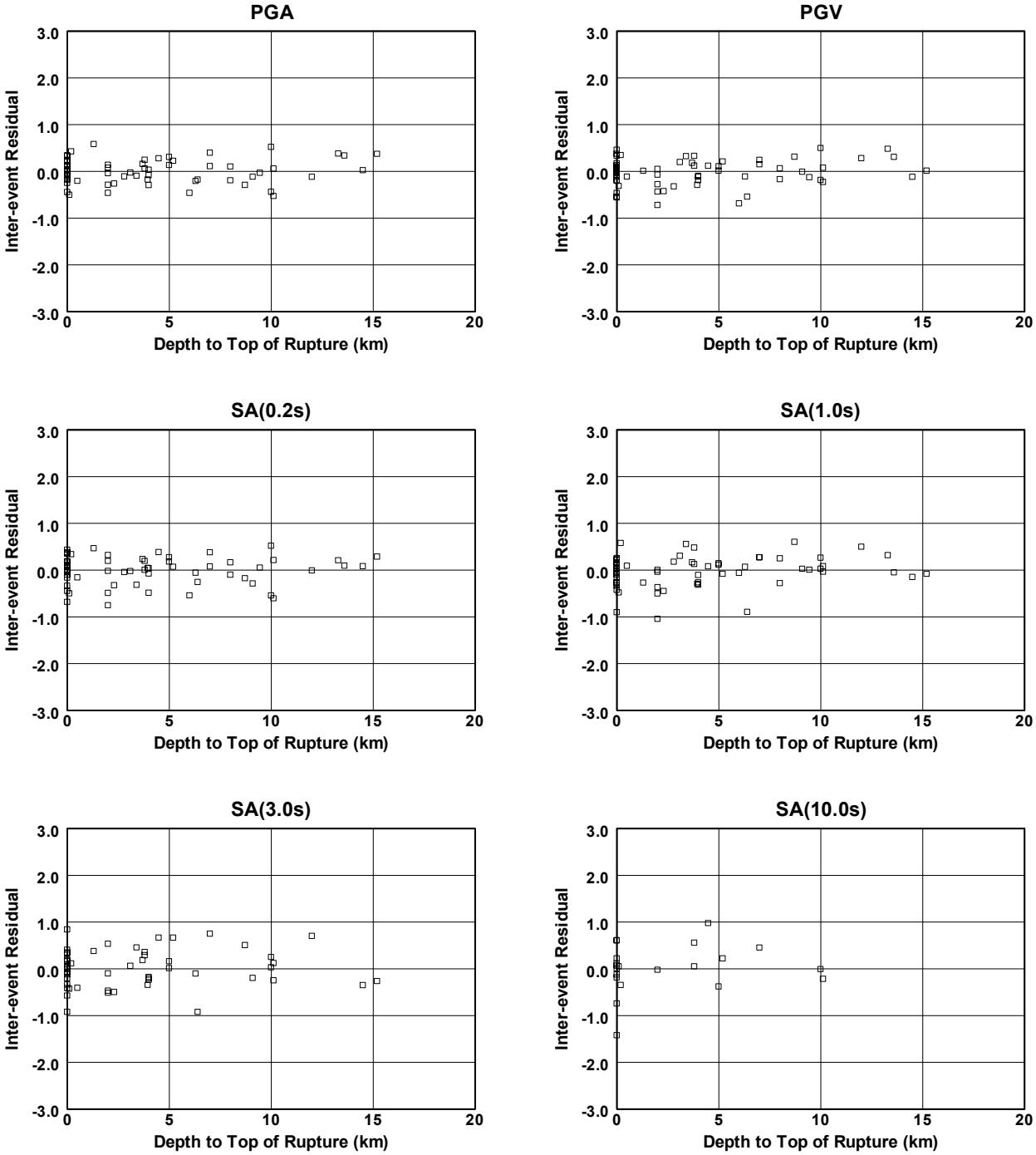

Fig. 3.4 Dependence of inter-event residuals on depth to top of rupture.

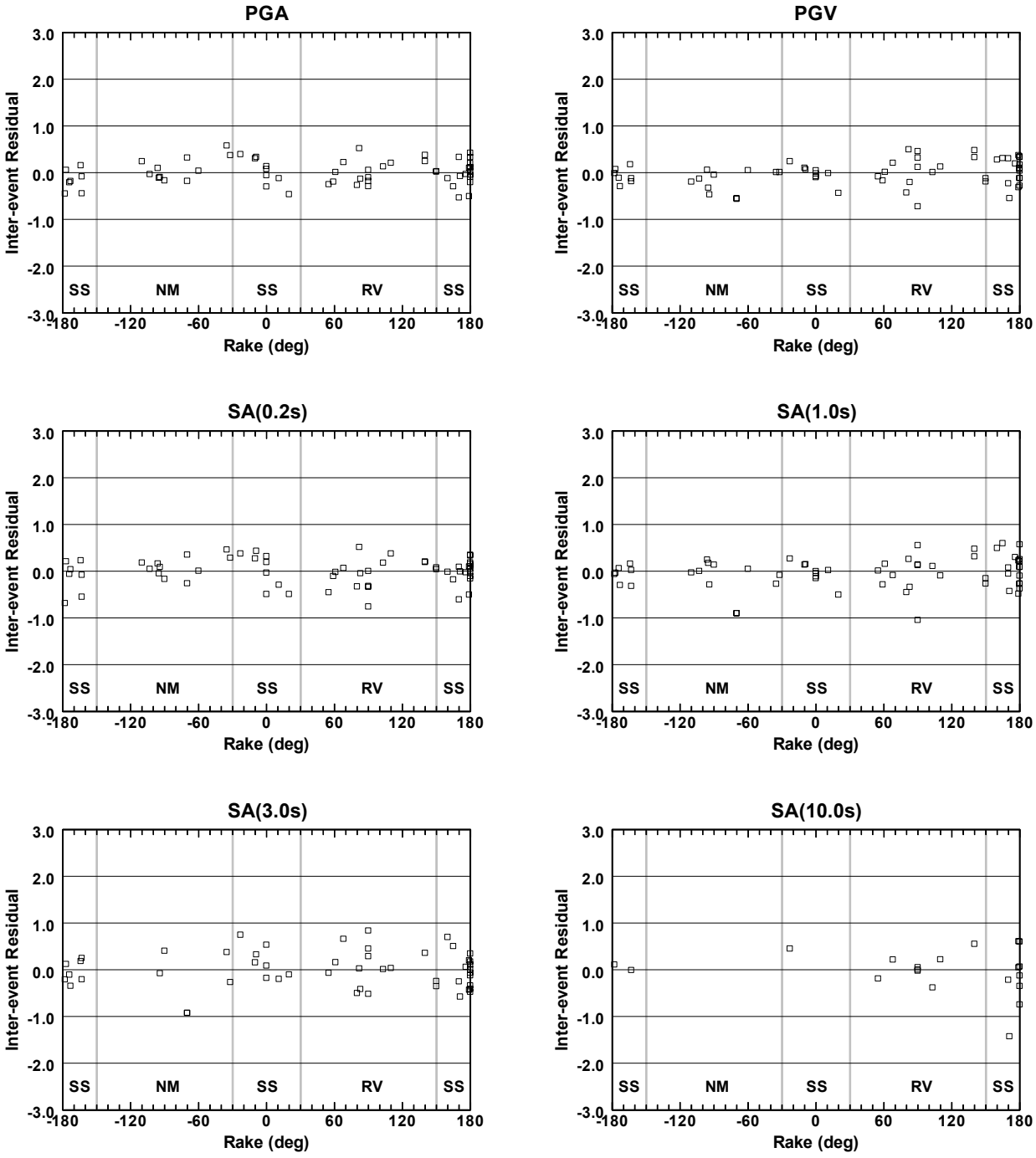

Fig. 3.5 Dependence of inter-event residuals on rake angle and style of faulting for strike-slip (SS), normal (NM), and reverse (RV) faults.

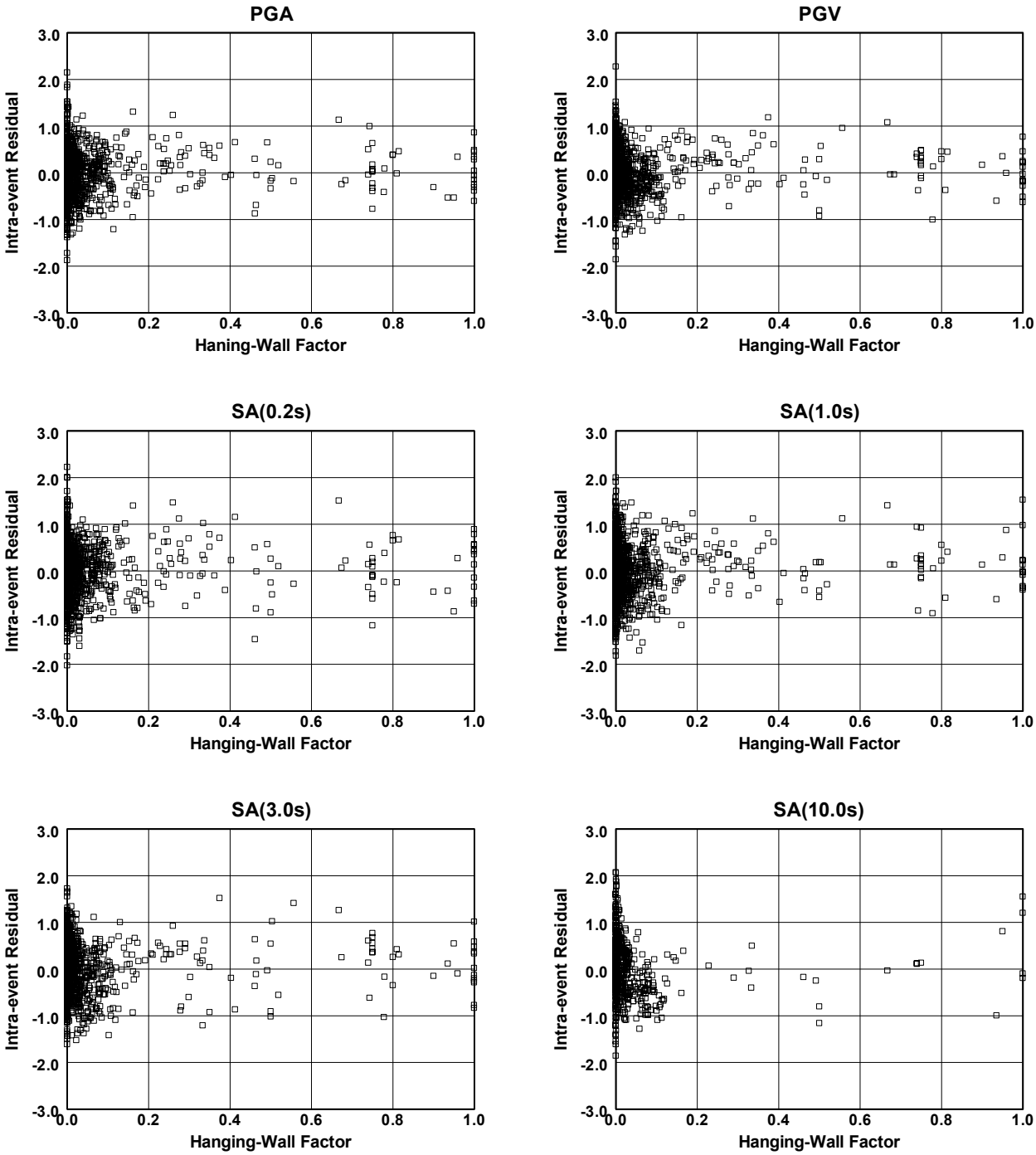

Fig. 3.6 Dependence of intra-event residuals on hanging-wall factor.

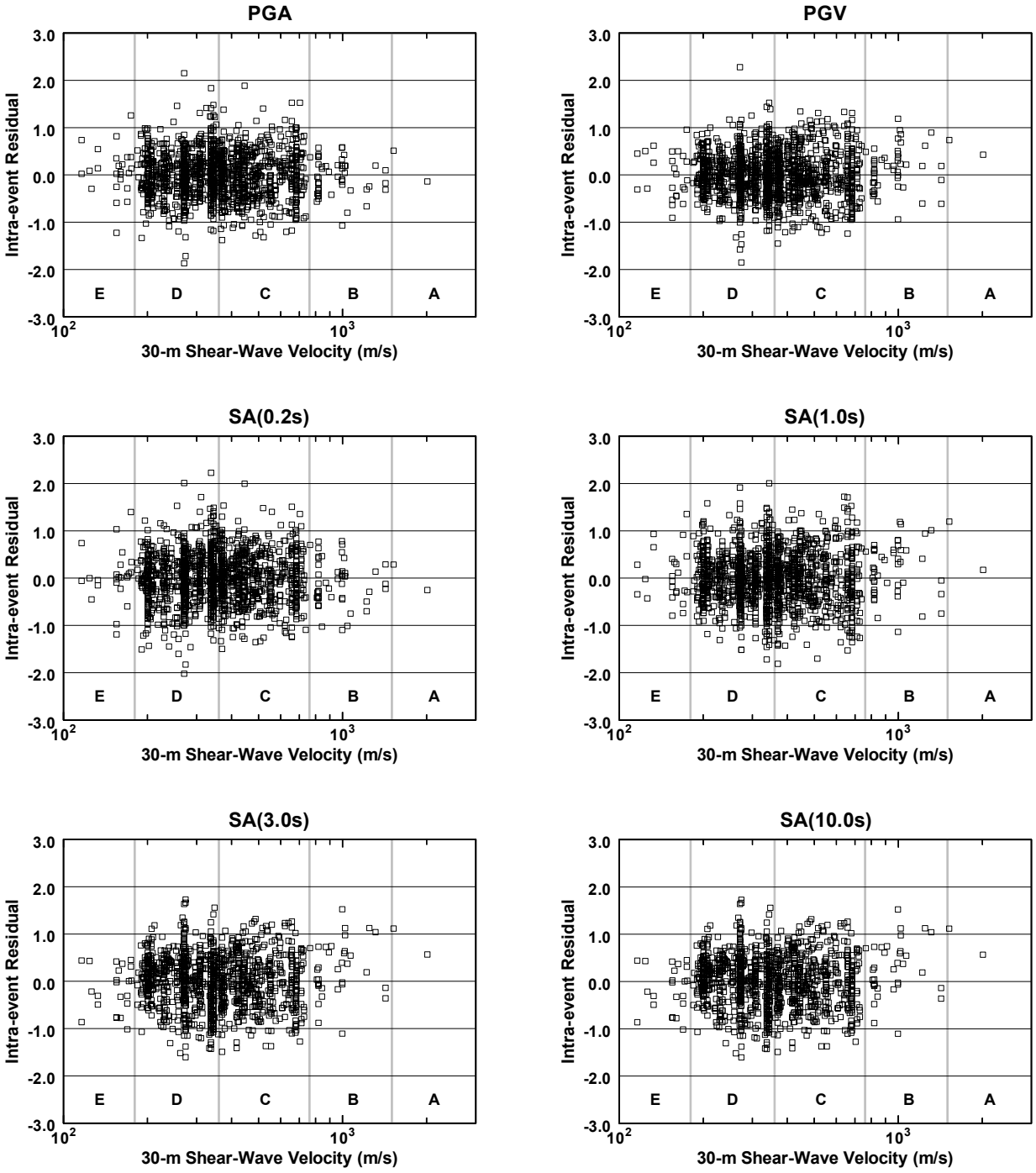

Fig. 3.7 Dependence of intra-event residuals on 30-m shear-wave velocity.

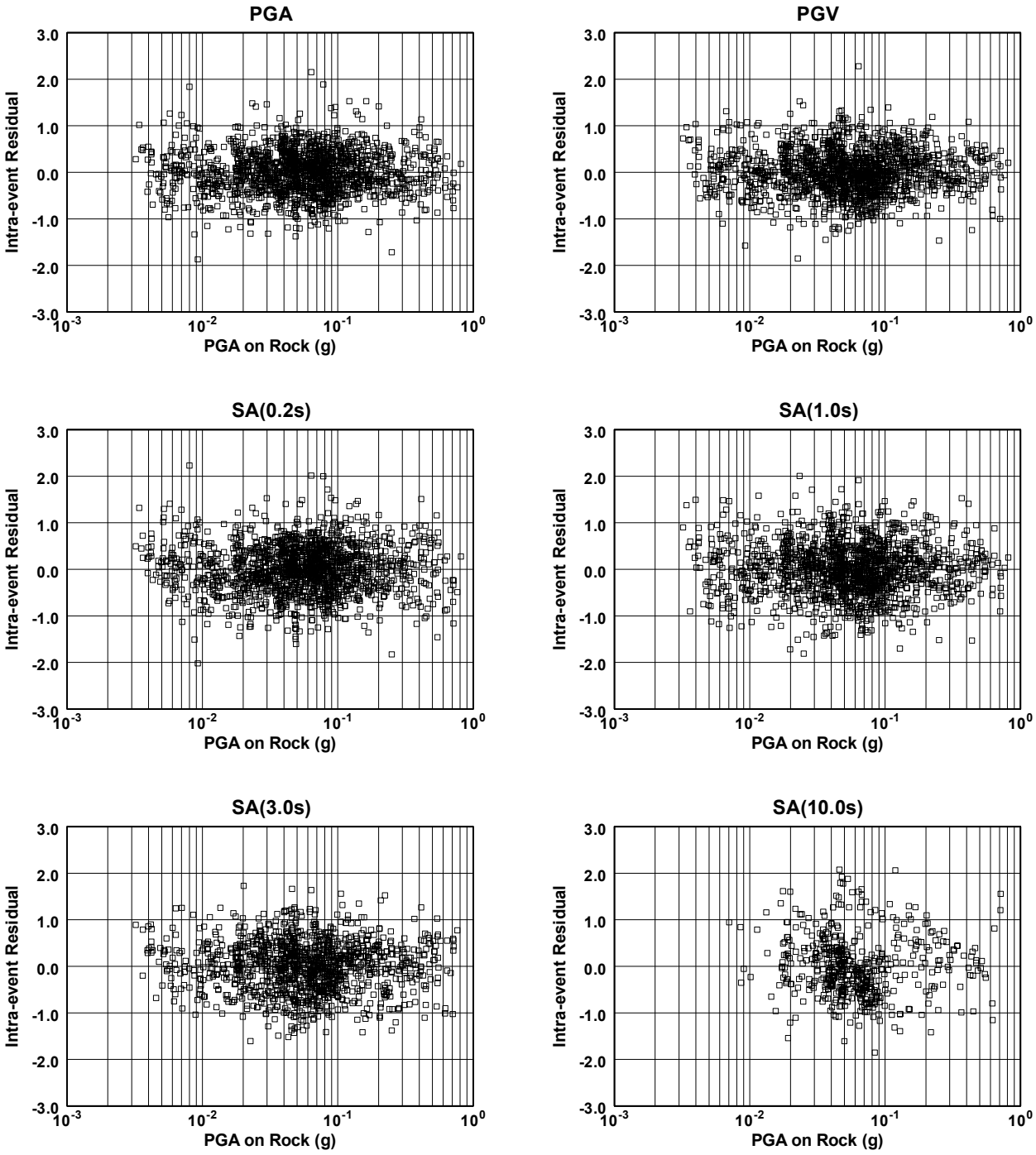

Fig. 3.8 Dependence of intra-event residuals on rock PGA.

4 Alternative Horizontal Components

During the course of the PEER NGA Project, we had an opportunity to ask several structural engineers what strong motion components besides the geometric mean and the arbitrary horizontal component addressed in Section 3.1.1 would be of interest. In response, they expressed interest in the vertical component and in the horizontal component(s) that could be considered to represent the largest horizontal ground motion. The vertical component will be investigated in a subsequent NGA project and will not be discussed here. However, in order to investigate which horizontal component might correspond to the largest ground motion, we used our selected NGA database, the one we used to develop our NGA model, to analyze several alternative horizontal components in addition to the geometric mean, referred to here as the arbitrary horizontal component, the maximum horizontal component, the maximum rotated horizontal component, and the strike-normal horizontal component. For completeness, we also analyzed the minimum horizontal component and the strike-parallel horizontal component. We also provide statistics between the new geometric mean (GMRotI50) and the geometric mean used in past studies.

4.1 GEOMETRIC MEAN

The definition of the geometric mean used in the PEER NGA Project (GMRotI50) and that used in past studies was discussed in Section 3.1.1. In this section we provide the actual statistics between these two ground motion measures. To determine how the old geometric mean differs from the new geometric mean, we calculated its logarithmic ratio with respect to the new geometric mean and averaged it over all recordings (i.e., over all magnitudes and distances). From this logarithmic ratio we calculated a mean, maximum, minimum, and standard deviation for each oscillator period. The results of this analysis are summarized in Table 4.1. Figure 4.1

shows a plot of these ratios with respect to oscillator period, where the vertical bar represents the median plus and minus one standard deviation.

Table 4.1 shows that the exponential of the mean logarithmic ratio (median ratio) of the old geometric mean is generally constant with oscillator period at a value of about 0.99. The standard deviation in natural log units increases only slightly from 0.07 to 0.11 over this same period range. The median ratio and the standard deviation for PGV is 0.99 and 0.08, respectively. However, the minimum and maximum median ratios for a given period indicate that the difference between these two geometric means can be large for individual recordings. We also carried out an independent regression analysis on the geometric mean of two as-recorded horizontal components as part of a study on inelastic response spectra and found that the median results are very close to the median results on the new geometric mean (GMRotI50) presented in this report (Bozorgnia et al., 2006).

4.2 ARBITRARY HORIZONTAL COMPONENT

We define the arbitrary horizontal component as the expected value of the peak amplitude from the two as-recorded orthogonal horizontal traces (Baker and Cornell, 2006). Although this expected value (taken with respect to its logarithm) is identical to the geometric mean of the as-recorded horizontal components and virtually identical to the geometric mean of the rotated horizontal component (Table 4.1), its standard deviation is not. Baker and Cornell (2006) pointed out that many engineering applications require a probabilistic estimate of the arbitrary horizontal component, not the geometric mean. In such a case, even though no adjustment of the median is required, the larger standard deviation associated with the arbitrary horizontal component will lead to a larger probabilistic estimate of ground motion.

Boore (2005) showed that the aleatory variance of the arbitrary horizontal component, which he called the component-to-component variability, can be calculated from the equation

$$\sigma_c^2 = \frac{1}{4N}\sum_{j=1}^{N}(\ln Y_{1j} - \ln Y_{2j})^2 \tag{4.1}$$

where the subscripts 1 and 2 refer to the two individual horizontal components of the recording from which the geometric mean was calculated, j is an index representing the recording number, and N is the total number of recordings. We used this equation to calculate the values of σ_c

associated with the selected NGA database we used to develop our NGA model. These values are summarized in Table 3.2. The total standard deviation corresponding to this component as calculated from Equation (4.3) is also shown in this table for comparison with that of the geometric mean.

4.3 MAXIMUM HORIZONTAL COMPONENT

We define the maximum and minimum horizontal components of ground motion as the largest and smallest peak amplitudes of the two as-recorded orthogonal horizontal acceleration traces. To determine how these components differ from the geometric mean, we calculated their logarithmic ratios with respect to the geometric mean and averaged them over all recordings (i.e., over all magnitudes and distances). From these logarithmic ratios we calculated a mean, maximum, minimum, and standard deviation for each oscillator period. The results of this analysis are summarized in Table 4.2. Figure 4.1 shows a plot of the ratios for the maximum horizontal component with respect to oscillator period, where the vertical bar represents the median plus and minus one standard deviation. As with all of the analyses in this chapter, these calculations were carried out using the selected NGA database we used to develop our NGA model.

Table 4.2 shows that the exponential of the mean logarithmic ratio (median ratio) of the maximum horizontal component generally increases with oscillator period from a value of 1.12 at short periods to 1.23 at long periods. The standard deviation in natural log units generally increases from 0.10 to 0.14 over this same period range. The median ratio and the standard deviation for PGV is 1.15 and 0.12, respectively. The median ratio of the minimum horizontal component generally decreases with period from a value of 0.89 at short periods to 0.78 at long periods. Its standard deviation generally increases from 0.16 to 0.26 over this same period range. The median ratio and standard deviation for PGV is 0.85 and 0.16, respectively. These results are very similar to those found by Beyer and Bommer (2006) using a somewhat different database for oscillator periods ranging up to 5.0 s, the longest period investigated by these authors.

4.4 MAXIMUM ROTATED HORIZONTAL COMPONENT

The maximum rotated horizontal component of ground motion is defined as the largest peak amplitude of a suite of orthogonal horizontal acceleration traces that have been rotated through a non-redundant angle of 90°. This can be considered a worst-case scenario for the peak ground motion averaged over all magnitudes and distances. This component was not available for our NGA database, but considering that our median ratios for the maximum arbitrary horizontal component were very similar to those of Beyer and Bommer (2006), we believe that the ratios for the maximum rotated horizontal component found by these authors can serve as a good representation of the ratios we would expect from our database. Beyer and Bommer calculated the logarithmic ratio of this component with respect to the geometric mean and averaged it over all recordings (i.e., over all magnitudes and distances) as we did for the maximum horizontal component. From these logarithmic ratios, they calculated a mean and standard deviation for each oscillator period. These results are summarized in Table 4.3, where they are compared to our results for the maximum horizontal component from Table 4.1. Figure 4.1 shows a plot of the ratios for the maximum rotated horizontal component with respect to oscillator period, where the vertical bar represents the median plus and minus one standard deviation.

Table 4.3 shows that the median ratio of the maximum rotated horizontal component generally increases with oscillator period from a value of 1.20 at short periods to 1.34 at long periods (in this case to an oscillator period of 5.0 s). The standard deviation in natural log units generally increases from 0.09 to 0.14 over this same period range. While the standard deviations are similar to those found for the maximum horizontal component, the median ratios are found to be as much as 12% larger on average.

4.5 STRIKE-NORMAL HORIZONTAL COMPONENT

The strike-normal (SN) and strike-parallel (SP) horizontal components of ground motion are defined as the peak amplitudes of the two orthogonal horizontal components after rotating them to azimuths that are normal to and parallel to the strike of the rupture plane. To determine how these components differ from the geometric mean, we calculated their logarithmic ratios with respect to the geometric mean and averaged them over all recordings (i.e., over all magnitudes

and distances). From these logarithmic ratios we calculated a mean, maximum, minimum, and standard deviation for each oscillator period. The results are summarized in Table 4.4. Figure 4.1 shows a plot of the ratios for the SN component with respect to oscillator period, where the vertical bar represents the median plus and minus one standard deviation.

Table 4.4 shows that on average the median ratios of the SN and SP components are within a few percent of the geometric mean, except at the longest periods, where the SN component is 5% higher and the SP component is 8% lower than the geometric mean. The standard deviation in natural log units generally increases from 0.15 at short periods to 0.30 at long periods for the SN component and from 0.15 at short periods to 0.37 at long periods for the SP component. These results are similar to those of Beyer and Bommer (2006). The standard deviations at short periods are about the same as those for the minimum horizontal component, but those at long periods are much larger. The biggest difference between these components and the maximum and minimum horizontal components is in their extreme values. At long periods, the largest median ratios reach values as high as 6.9 and 6.1 for the SN and SP components, respectively, whereas the largest ratios for the maximum and minimum horizontal components do not exceed values of 1.8 and 1.3, respectively. The extreme values are relatively constant at around 1.6–1.8 up to an oscillator period of 3.0 s, after which they steadily increase to their maxima at 10.0 s.

The larger dispersion and larger extreme values of the SN and SP components at long periods no doubt reflect the relatively strong azimuthal dependence of these components that results from source directivity. The near unity median ratios for these two components indicates that on average (i.e., averaged over all magnitudes and distances) neither of them show a strong tendency to be the largest horizontal component. However, this changes at small distances, large magnitudes, and long periods where empirical source directivity effects have been shown to become important (e.g., Howard et al., 2005; Spudich et al., 2004; Spudich and Chiou, 2006; Somerville et al., 1997). Rowshandel (2006) also found directivity effects to be important at long periods, but did not investigate their dependence on magnitude and distance. For conditions most conducive to directivity, all of these authors have shown that the long-period SN component of PSA can be more than a factor of two higher than the geometric mean for a site located in the forward-directivity direction.

We investigated the potential impact of magnitude and distance on the SN and SP components in our NGA database by repeating our analysis for earthquakes with $\mathbf{M} \geq 6.5$ and recordings with $R_{RUP} < 5$ km, $5 \leq R_{RUP} < 10$ km, $10 \leq R_{RUP} < 20$ km, and $R_{RUP} \geq 20$ km. These results are summarized in Table 4.5. Figure 4.1 shows a plot of the ratios for the SN component ($\mathbf{M} \geq 6.5$, $R_{RUP} < 5$ km) with respect to oscillator period, where the vertical bar represents the median plus and minus one standard deviation. The most significant effects are found for the shortest distance bin, where the median ratio for the SN component generally increases from a value of 1.06 at short periods to 1.24 at long periods and the median ratio for the SP component generally decreases from 0.88 at short periods to 0.67 at long periods. The biggest effect is for oscillator periods greater than 1.0 s. Although these effects are not trivial, they raise the question of why we are not seeing larger ratios. We believe that there are at least three reasons for this: (1) we are not including the potential effects of directivity on the geometric mean ground motion, (2) we include all source-site azimuths and are, therefore, averaging over forward- and backward-directivity directions, which Somerville et al. (1997), Spudich et al. (2004), and Rowshandel (2006) have found to have counteracting effects, and (3) we are combining recordings from strike-slip and reverse earthquakes, whereas Howard et al. (2005) found that maximum forward- directivity effects from reverse faults are not necessarily closely aligned with the SN component. These effects are complicated and require more research. Therefore, the explicit inclusion of directivity effects will be addressed in a future NGA project.

4.6 CALCULATION FROM GEOMETRIC MEAN

There are two adjustments that need to be made to the CB-NGA model in order to use it to estimate one of the alternative strong motion components (designated Y_{Comp}) discussed in the previous sections. The first adjustment is to the median model and is given by the equation

$$\ln Y_{Comp} = \widehat{\ln Y} + \ln Y_{Comp/GM} \tag{4.2}$$

where $\widehat{\ln Y}$ is the median estimate of the geometric mean from Equation (3.1) and $\ln Y_{Comp/GM}$ is the median estimate of the ratio of Y_{Comp} to the geometric mean given in Table 3.2 and in Tables 4.1–4.4. Note that the median ratio of the arbitrary horizontal component is unity (i.e., $\ln Y_{Comp/GM} = 0$) so that no adjustment is necessary.

The second adjustment is to the aleatory uncertainty model and is given by the equation

$$\sigma_{Comp} = \sqrt{\sigma_T^2 + \sigma_{Comp/GM}^2} \tag{4.3}$$

where σ_T is the total standard deviation of the geometric mean given in Equation (3.14) and $\sigma_{Comp/GM}$ is the standard deviation of the logarithmic ratio of Y_{Comp} to the geometric mean given in Table 3.2 and in Tables 4.1–4.4. The standard deviation of the arbitrary horizontal component (σ_{Comp}) listed in Table 3.2 was calculated in this manner from Equation (4.3) by setting $\sigma_{Comp/GM} = \sigma_c$.

Table 4.1 Ratio between geometric mean of as-recorded horizontal components and new geometric mean averaged over all magnitudes and distances.

Period T (s)	Geometric Mean of As-Recorded Horizontal Components			
	Median[1]	Max.	Min.	σ_{Comp} [2]
0.010	0.988	1.207	0.158	0.073
0.020	0.988	1.177	0.158	0.073
0.030	0.989	1.190	0.142	0.074
0.050	0.990	1.230	0.133	0.076
0.075	0.992	1.233	0.120	0.079
0.10	0.990	1.212	0.101	0.085
0.15	0.992	1.305	0.093	0.089
0.20	0.990	1.286	0.107	0.089
0.25	0.989	1.242	0.155	0.083
0.30	0.989	1.238	0.172	0.084
0.40	0.990	1.348	0.173	0.086
0.50	0.991	1.301	0.273	0.079
0.75	0.985	1.319	0.363	0.082
1.0	0.989	1.350	0.509	0.082
1.5	0.986	1.280	0.663	0.080
2.0	0.988	1.314	0.598	0.082
3.0	0.985	1.237	0.675	0.081
4.0	0.989	1.258	0.524	0.085
5.0	0.989	1.298	0.615	0.089
7.5	0.988	1.272	0.560	0.097
10.0	0.981	1.276	0.433	0.107
PGA	0.988	1.207	0.158	0.073
PGV	0.988	1.304	0.622	0..078
PGD	0.981	1.276	0.433	0.107

[1] Median is calculated as the exponential of the mean logarithmic ratio.
[2] Standard deviation is calculated with respect to logarithmic ratio in natural log units.

Table 4.2 Ratio between maximum and minimum horizontal components and geometric mean averaged over all magnitudes and distances.

Period	Maximum Horizontal Component				Minimum Horizontal Component			
T (s)	Median[1]	Max.	Min.	σ_{Comp} [2]	Median[1]	Max.	Min.	σ_{Comp} [2]
0.010	1.117	1.686	0.848	0.098	0.874	1.105	0.015	0.160
0.020	1.118	1.692	0.845	0.098	0.874	1.105	0.015	0.159
0.030	1.116	1.696	0.833	0.098	0.876	1.141	0.012	0.161
0.050	1.114	1.663	0.855	0.095	0.879	1.140	0.011	0.163
0.075	1.113	1.663	0.846	0.095	0.885	1.219	0.009	0.165
0.10	1.117	1.700	0.812	0.104	0.877	1.188	0.006	0.179
0.15	1.129	1.669	0.853	0.105	0.871	1.253	0.005	0.191
0.20	1.133	1.689	0.830	0.109	0.864	1.245	0.007	0.192
0.25	1.140	1.813	0.813	0.113	0.858	1.214	0.014	0.183
0.30	1.147	1.734	0.817	0.114	0.852	1.228	0.018	0.189
0.40	1.154	1.865	0.825	0.118	0.849	1.316	0.018	0.196
0.50	1.160	1.973	0.816	0.121	0.847	1.275	0.046	0.186
0.75	1.168	1.777	0.828	0.123	0.832	1.254	0.081	0.196
1.0	1.179	1.720	0.806	0.124	0.830	1.289	0.165	0.194
1.5	1.174	1.774	0.837	0.123	0.829	1.195	0.298	0.190
2.0	1.179	1.785	0.801	0.122	0.828	1.245	0.254	0.197
3.0	1.179	1.738	0.804	0.122	0.823	1.213	0.307	0.197
4.0	1.193	1.744	0.857	0.117	0.820	1.219	0.170	0.209
5.0	1.191	1.781	0.871	0.120	0.822	1.197	0.251	0.213
7.5	1.225	1.821	0.868	0.121	0.797	1.245	0.185	0.242
10.0	1.233	1.770	0.883	0.136	0.781	1.251	0.118	0.260
PGA	1.117	1.686	0.848	0.098	0.874	1.105	0.015	0.160
PGV	1.145	1.697	0.791	0.119	0.853	1.204	0.266	0.164
PGD	1.233	1.770	0.883	0.136	0.781	1.251	0.118	0.260

[1] Median is calculated as the exponential of the mean logarithmic ratio.
[2] Standard deviation is calculated with respect to logarithmic ratio in natural log units.

Table 4.3 Ratio between maximum horizontal and maximum rotated horizontal components and geometric mean averaged over all magnitudes and distances.

Period T (s)	Maximum Horizontal Component		Maximum Rotated Component[1]	
	Median[2]	σ_{Comp} [3]	Median[2]	σ_{Comp} [3]
0.010	1.117	0.098	1.211	0.104
0.020	1.118	0.098	1.213	0.101
0.030	1.116	0.098	1.209	0.101
0.050	1.114	0.095	1.199	0.099
0.075	1.113	0.095	1.203	0.093
0.10	1.117	0.104	1.207	0.099
0.15	1.129	0.105	1.227	0.108
0.20	1.133	0.109	1.241	0.111
0.25	1.140	0.113	1.254	0.120
0.30	1.147	0.114	1.259	0.122
0.40	1.154	0.118	1.265	0.127
0.50	1.160	0.121	1.279	0.131
0.75	1.168	0.123	1.287	0.138
1.0	1.179	0.124	1.307	0.136
1.5	1.174	0.123	1.302	0.128
2.0	1.179	0.122	1.303	0.136
3.0	1.179	0.122	1.304	0.134
4.0	1.193	0.117	1.321	0.134
5.0	1.191	0.120	1.335	0.136
PGA	1.117	0.098	1.211	0.104

[1] From Beyer and Bommer (2006).
[2] Median is calculated as the exponential of the mean logarithmic ratio.
[3] Standard deviation is calculated with respect to logarithmic ratio in natural log units.

Table 4.4 Ratio between strike-normal and strike-parallel horizontal components and geometric mean averaged over all magnitudes and distances.

Period	Strike-Normal Component				Strike-Parallel Component			
T (s)	Median[1]	Max.	Min.	σ_{Comp} [2]	Median[1]	Max.	Min.	σ_{Comp} [2]
0.010	0.980	1.569	0.415	0.163	0.993	1.770	0.408	0.160
0.020	0.981	1.569	0.414	0.163	0.994	1.767	0.405	0.160
0.030	0.982	1.572	0.412	0.157	0.995	1.806	0.421	0.157
0.050	0.983	1.569	0.410	0.155	0.994	1.631	0.480	0.153
0.075	0.987	1.540	0.421	0.152	0.994	1.521	0.513	0.151
0.10	0.993	1.584	0.464	0.163	0.990	1.745	0.460	0.162
0.15	0.990	1.727	0.303	0.180	0.995	1.628	0.366	0.172
0.20	0.992	1.883	0.346	0.187	0.991	1.640	0.354	0.185
0.25	0.986	1.719	0.253	0.196	0.998	1.750	0.384	0.189
0.30	0.985	2.075	0.281	0.207	0.995	1.655	0.385	0.202
0.40	0.981	1.699	0.349	0.215	0.998	1.859	0.356	0.211
0.50	0.974	1.808	0.330	0.220	1.004	1.728	0.311	0.216
0.75	0.974	1.729	0.286	0.238	1.000	1.738	0.348	0.228
1.0	0.980	1.712	0.315	0.248	0.994	1.733	0.364	0.234
1.5	0.986	1.750	0.266	0.247	0.980	1.797	0.330	0.247
2.0	0.991	1.738	0.216	0.255	0.978	1.740	0.227	0.253
3.0	0.965	1.651	0.273	0.257	1.001	1.745	0.340	0.245
4.0	0.965	2.163	0.235	0.276	0.994	2.821	0.313	0.268
5.0	0.954	3.638	0.217	0.302	0.984	3.444	0.237	0.306
7.5	0.999	5.142	0.207	0.298	0.943	5.838	0.150	0.355
10.0	1.056	6.914	0.268	0.290	0.919	6.111	0.165	0.370
PGA	0.980	1.569	0.415	0.163	0.993	1.770	0.408	0.160

[1] Median is calculated as the exponential of the mean logarithmic ratio.
[2] Standard deviation is calculated with respect to logarithmic ratio in natural log units.

Table 4.5 Median ratio between strike-normal and strike-parallel horizontal components and geometric mean for $M \geq 6.5$ and four distance bins.

Period	Strike-Normal Component				Strike-Parallel Component			
T (s)	0–5	5–10	10–20	20–200	0–5	5–10	10–20	20–200
0.010	1.057	1.026	1.007	0.983	0.876	0.943	0.965	0.993
0.020	1.058	1.028	1.007	0.984	0.883	0.939	0.965	0.994
0.030	1.071	1.022	1.008	0.983	0.893	0.950	0.967	0.994
0.050	1.086	1.028	1.015	0.985	0.892	0.944	0.970	0.995
0.075	1.087	1.056	1.011	0.982	0.904	0.933	0.976	0.993
0.10	1.053	1.022	1.007	0.979	0.929	0.958	0.977	1.002
0.15	1.035	1.023	1.010	0.982	0.917	1.002	0.985	1.005
0.20	1.061	0.978	1.019	0.986	0.893	0.987	0.964	0.998
0.25	1.067	1.011	1.013	0.990	0.880	0.983	0.985	0.992
0.30	1.068	1.030	1.005	0.989	0.935	0.937	1.015	0.992
0.40	1.069	1.103	0.992	0.984	0.904	0.891	1.000	0.998
0.50	1.041	1.052	1.001	0.993	0.952	0.919	0.969	0.993
0.75	1.053	1.053	1.001	0.989	0.892	0.908	0.964	0.993
1.0	1.101	1.054	1.007	0.995	0.837	0.938	0.961	0.992
1.5	1.163	1.053	1.019	0.974	0.784	0.970	0.966	1.003
2.0	1.142	1.032	1.007	0.956	0.763	0.951	0.963	1.019
3.0	1.183	1.075	1.039	0.989	0.745	0.884	0.958	0.982
4.0	1.241	1.056	1.011	0.986	0.689	0.887	0.982	0.981
5.0	1.234	1.034	0.969	0.972	0.668	0.898	1.019	0.972
7.5	1.179	1.004	0.925	0.921	0.811	0.962	1.041	1.016
10.0	1.221	1.011	0.883	0.906	0.723	1.028	1.117	1.070
PGA	1.057	1.026	1.007	0.983	0.876	0.943	0.965	0.993

Note: All distances are in kilometers.

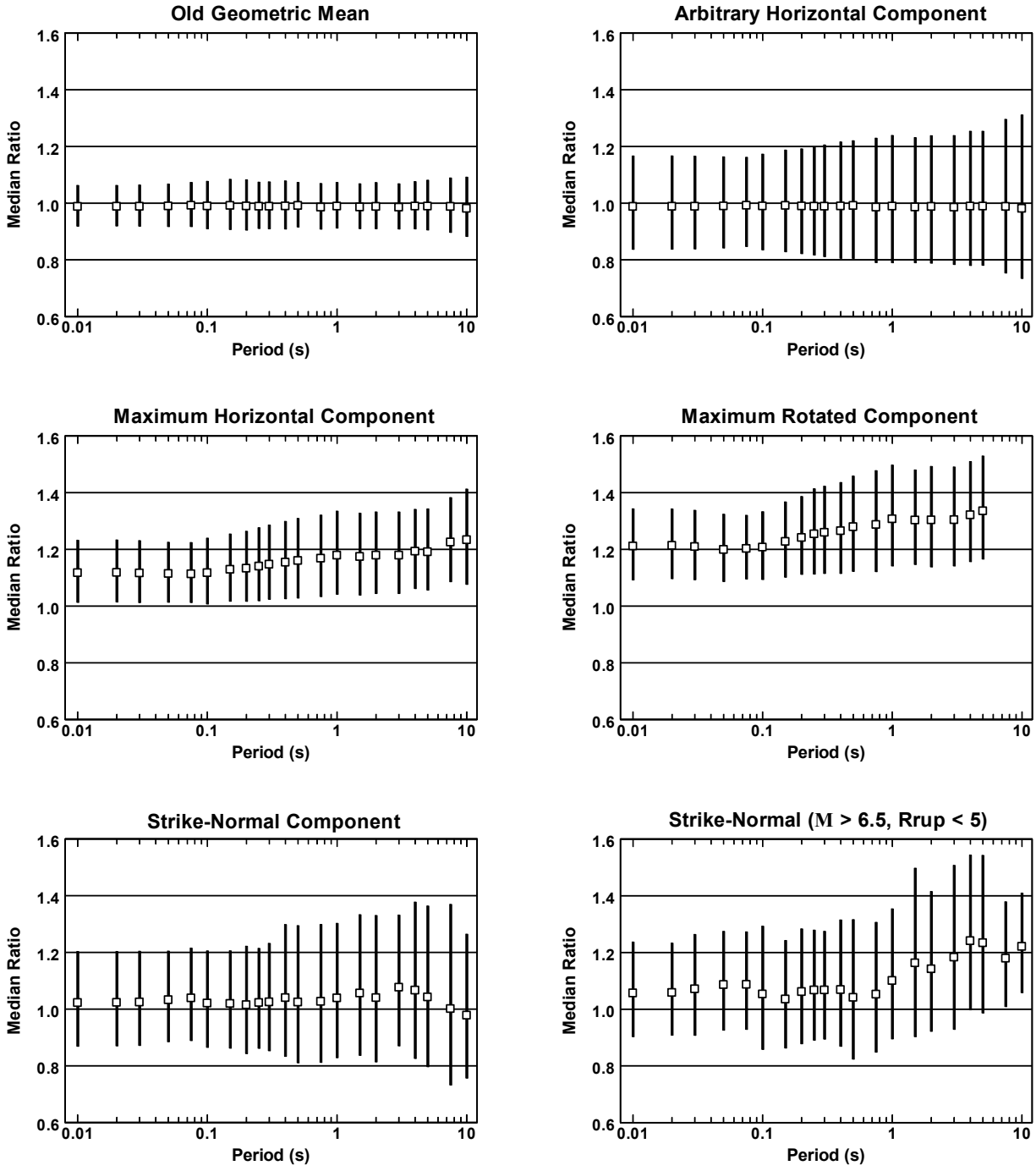

Fig. 4.1 Ratios of alternative horizontal components to new geometric mean.

5 Evaluation of Alternative Predictor Variables

The PEER NGA database contains dozens of predictor (independent) variables, many of which have not previously been available to the developers of empirical ground motion models. They were included in the database based on the advice of the NGA Working Groups and the developers. We began our selection process by first selecting parameters that had been found to be important from past studies. These parameters included moment magnitude (**M**), one or more of the fault distance measures (R_{JB}, R_{RUP}, R_{SEIS}), indicator variables for style of faulting (F_{RV} and F_{NM}), hanging-wall parameters (derived from the distance measures R_{RUP} and R_{JB}), 30-m shear-wave velocity (V_{S30}), and one or more of the sediment depth parameters ($Z_{1.0}$, $Z_{1.5}$, $Z_{2.5}$). We also evaluated and identified several other parameters that had not been used in previous studies, based on an analysis of residuals and the results of similar analyses conducted by the other developers. Based on this evaluation, we selected one additional predictor variable, the depth to the top of coseismic rupture (Z_{TOR}), to include in our model. We also used this evaluation to help select and modify the functional forms used in the CB-NGA model, as discussed in Chapter 3.

5.1 DISTANCE MEASURES

At first we intended to evaluate all three distance measures in order to select which one might be best for modeling near-source attenuation. However, the Campbell distance measure (R_{SEIS}), which had been used in our previous model (Campbell and Bozorgnia, 1994, 2003a, 2003b, 2003c, 2004), was not available for many earthquakes until late in the project. Therefore, in its absence, we selected rupture distance (R_{RUP}) as our preferred distance measure with the intent that we would look at the other distance measures at a latter date. However, because of the time-consuming process of finding appropriate functional forms and in evaluating the relatively large

number of potential predictor variables that were made available to us, we did not have a chance to evaluate these other distance measures and continued to use R_{RUP}.

5.2 SEDIMENT DEPTH PARAMETERS

We evaluated all three of the sediment depth parameters that were provided in the PEER database. In the preliminary two-stage regression analyses, this was done after including the shallow site response term f_{site} in the empirical ground motion model in order to capture any sediment depth effects that were not accounted for by V_{S30}. These parameters represented depths to the 1.0, 1.5 and 2.5 km/s shear-wave velocity horizon, referred to as $Z_{1.0}$, $Z_{1.5}$ and $Z_{2.5}$, respectively. We found that $Z_{1.0}$ showed the least correlation with the residuals at all sediment depths that were clearly visible for the other sediment depth parameters. The parameters $Z_{1.5}$ and $Z_{2.5}$ showed equally good correlation with the residuals at large sediment depths, but $Z_{2.5}$ clearly exhibited the strongest correlation with the residuals at shallow sediment depths. As a result, we used $Z_{2.5}$ as the best overall parameter to represent both the shallow ($Z_{2.5} < 1.0$ km) and deep ($Z_{2.5} > 3.0$ km) sediment depth effects.

We note that there is some degree of uncertainty in using f_{dep} for $Z_{2.5} > 3.0$ km outside of the Los Angeles area for which it was theoretically developed (Day, 2005; Day et al., 2005). Since sediment depths were only available for the Los Angeles, Imperial Valley, and San Francisco areas, we also caution the user in the use of f_{dep} for even shallow sediment depths for areas outside of these regions. Regional differences were mitigated somewhat by the inclusion of c_{12} in the regression analysis, which was based on recordings in both the Los Angeles and San Francisco areas. Empirical relationships between $Z_{2.5}$ and the other sediment depth parameters are provided in Section 6.3.5.

5.3 SOURCE PARAMETERS

We spent the greatest amount of time exploring parameters that could explain and model the reduced degree of magnitude scaling that we observed in the inter-event residuals for $\mathbf{M} > 6.5$. This scaling is critical because it determines how the CB-NGA model extrapolates to the larger magnitudes of greatest interest in engineering. We plotted the inter-event residuals against

several source and fault parameters, including geologic slip rate, static stress drop, rupture area, depth to top of coseismic rupture, and aspect ratio. Aspect ratio (*AR*) is defined as the ratio of rupture length to rupture width. We introduced *AR* to the other developers as a possible parameter for quantifying the observed change in magnitude scaling at large magnitudes based on the study by Hanks and Bakun (2002), who found a bilinear relationship between **M** and the logarithm of rupture area for large continental strike-slip earthquakes. They found that for earthquakes with $\mathbf{M} \geq 6.7$ rupture area scales with magnitude consistent with the *L*-model of Scholz (1982). Douglas (2002) also showed empirically that the near-source magnitude-scaling characteristics of PGA and PGV were consistent with the *L*-model. Since this model assumes that rupture width (*W*) is constant, Douglas's result implies that ground motion should scale differently for large *AR*. Schmedes and Archuleta (2007) came to a similar conclusion based on kinematic simulations of large strike-slip earthquakes.

Residual plots indicated that the inter-event terms were only weakly correlated with geologic slip rate, static stress drop, and rupture area. Although we did not perform a statistical test, the large scatter and weak trends exhibited by these plots led us to conclude that these parameters would not be good predictors of the change in magnitude scaling that was observed at large magnitudes, nor could they explain why some earthquakes had higher inter-event terms than others. However, we did find that the inter-event terms were strongly correlated with aspect ratio, at least for $AR > 2$. Increasing values of *AR* were clearly found to correspond to decreasing inter-event terms and, therefore, to lower amplitudes of PGA and short-period PSA. Based on this observation, we tentatively adopted *AR* as a parameter in our model to explain the change in magnitude scaling for $AR > 2$ and $\mathbf{M} > 6.5$ for strike-slip faulting. However, this approach was later abandoned after further study led us to question the values of *AR* in the PEER database.

In order to test the reliability of *AR* as a predictor variable, we developed several plots that compared the values of *AR* in the PEER NGA database with those inferred from: (1) characteristic earthquakes of similar magnitude in the seismic source model developed for the 2002 National Seismic Hazard Mapping Project (NSHMP) (Frankel et al., 2002; Cao et al., 2003) and (2) from several commonly used magnitude versus rupture area relationships (e.g., Wells and Coppersmith, 1994; Hanks and Bakun, 2002; WGCEP, 2003). One of these plots for Type A faults in California is shown in Figure 5.1, where the solid black squares are the aspect

ratios from the NGA database, and the open symbols are the aspect ratios from the NSHMP fault database for northern California (diamonds) and southern California (triangles). The magnitude rupture area relationships of Wells and Coppersmith (1994), Hanks and Bakun (2002), and WGCEP (2003), which was developed by Bill Ellsworth in 2002, are identified as WC94, HB02 and EL02, respectively, in these plots. These relationships were evaluated for a maximum fault width of 15 km and for a minimum aspect ratio of 1.5.

The plots of *AR* versus magnitude indicated that the aspect ratios from the PEER database were systematically lower than those inferred from both the 2002 NSHMP seismic source model and the selected magnitude-area relationships for $\mathbf{M} > 7.0$ strike-slip events. Based on these results, we concluded that there might be either a bias in the values of *AR* in the PEER database or an inconsistency in the way that rupture dimensions were being estimated in the PEER database and the existing magnitude-area relationships. This latter concern was confirmed for the 2002 Denali earthquake (**M** 7.9), which was later found to have an aspect ratio that was at least twice that given in the PEER database (Rowe et al., 2004). We found that such a discrepancy could lead to a significant underprediction of ground motion for large earthquakes when values of *AR* from the 2002 NSHMP source model were used with a ground motion model that had been developed from values of *AR* in the PEER NGA database.

Although we still believe that *AR* shows great promise in explaining the reduced degree of magnitude scaling at large magnitudes (e.g., Douglas, 2002; Schmedes and Archuleta, 2007), we concluded that it was premature to use it in our model until the above-noted discrepancies in the *AR* values could be resolved. Instead, we prefer for the time being to adopt the alternative trilinear magnitude-scaling model discussed in the Chapter 3, which we believe does not suffer from this same discrepancy and indirectly takes into account the observed effects of *AR*. We also note that earthquakes with large *AR* tend to be associated with large surface displacements, so that our buried reverse-faulting term that predicts relatively lower short-period ground motions for events with surface faulting inherently takes into account the possible effects of *AR*.

We note that shortly before this report was written, the aspect ratio in the PEER strong motion database for the Denali earthquake was significantly increased by decreasing the rupture width from 30 to 15 km, more consistent with estimates of seismogenic rupture width based largely on seismicity constraints (e.g., Rowe et al., 2004). Unfortunately, this change came too late for us to reconsider using *AR* as a predictor variable in the CB-NGA model. Besides, Figure

5.1 indicates that other earthquakes in the PEER database in all likelihood suffer from the same discrepancy, so that our general observation is still valid.

5.4 DEPTH TO TOP OF RUPTURE

An analysis of residuals also indicated that the inter-event terms for reverse faulting were strongly dependent on whether there was coseismic surface rupture (i.e., whether $Z_{TOR} > 0$). When rupture propagated to the surface, the inter-event terms for reverse faults were found to be similar to those for strike-slip faults. When coseismic rupture was buried, the inter-event terms and, thus, the ground motion for reverse faults were found to be significantly higher than those for strike-slip faults. There is a hint that there also might be a difference in the inter-event terms for strike-slip faults with and without coseismic surface rupture. Such a difference would appear to be supported by Bouchon et al. (2006), who after analyzing the Bam recording from the shallow, predominantly strike-slip 2003 Bam (Iran) earthquake, concluded that the lack of significant surface rupture during this event might have been related to the extremely high rupture velocity, which they estimated to be equivalent to the Rayleigh-wave speed (i.e., 92% of the shear-wave speed). These authors also note that rupture velocities approaching the Raleigh-wave speed produce larger ground motions.

Unfortunately, the relationship between surface rupture and ground motion amplitude for strike-slip faults is masked by large scatter and significant inconsistencies by whether, in fact, the observed rupture was coseismic, triggered, or post-seismic. The 1995 Kobe earthquake is a good example of this inconsistency. That part of the Kobe rupture on Awaji Island was clearly visible at the surface, whereas that part beneath the city of Kobe was buried. The earthquake was flagged as having coseismic surface rupture in the PEER database, because of the surface rupture on Awaji Island, even though most of the strong motion recordings were closer to that part of the rupture that was buried. Because of this, we concluded that it would be impossible to model the potential effect of coseismic surface rupture for strike-slip faults until a more careful review of this parameter could be performed for the strike-slip events in the PEER database.

5.5 RAKE ANGLE

Rather than use indicator variables defined in terms of rake angle to represent the style of faulting, we plotted the Stage 1 residuals directly in terms of rake angle to see if it were possible to use this angle directly. While we could see clear clusters of relatively high and relatively low residuals that corresponded with the rake angle bins used to define the indicator variables, there was no apparent continuous trend that could be modeled. As a result, we decided to continue our use of indicator variables. The analysis did confirm the reasonableness of the rake angle bins that had been used to define the style-of-faulting categories in the PEER database. Furthermore, our classification of earthquakes as strike slip, reverse, and normal using these rake angle bins was found to be identical to that used by Boore and Atkinson (2007) using an alternative classification based on the plunge (dip) of the maximum compressive stress (*P*) and minimum compressive stress (*T*) axes. In their scheme, based on a proposal by Zoback (1992), strike-slip faulting is defined as an event with a *P* and *T* axis plunge less than or equal to 40°, reverse faulting is defined as an event with a *T* axis plunge greater than 40°, and normal faulting is defined as an event with a *P* axis plunge greater than 40°.

5.6 DIP ANGLE

We found a weak, but significant, trend of increasing ground motion with the average dip of the rupture plane for both reverse and strike-slip faults, but we were not convinced that this trend could be justified scientifically after discussing it with several seismologists. Figure 5.2 shows the dependence of inter-event residuals on rupture dip. There is a suggestion that inter-event residuals are biased high (an underprediction by the model) for rupture dips greater than 0 and less than about 75°. However, because this trend could not be explained seismologically, we did not include rupture dip as a parameter in the CB-NGA model at this time other than as a filter to phase out hanging-wall effects for steeply dipping faults. We will reconsider it in the future when there is more seismological consensus on its effects.

The strongest argument in favor of including rupture dip as a predictor variable was for reverse faults, where the inter-event terms implied that ground motion amplitude systematically increases with increasing rupture dip and, presumably, higher normal stresses on the rupture

plane. However, when we included dip as a parameter for reverse faults, we found that it led to the prediction of smaller ground motion for shallow-dipping, surface-rupturing reverse faults than for strike-slip faults, which we thought might be biased by our inability to distinguish between buried and surface-rupturing strike-slip faults in the current PEER database. The potential impact of rupture dip should be a topic of future research.

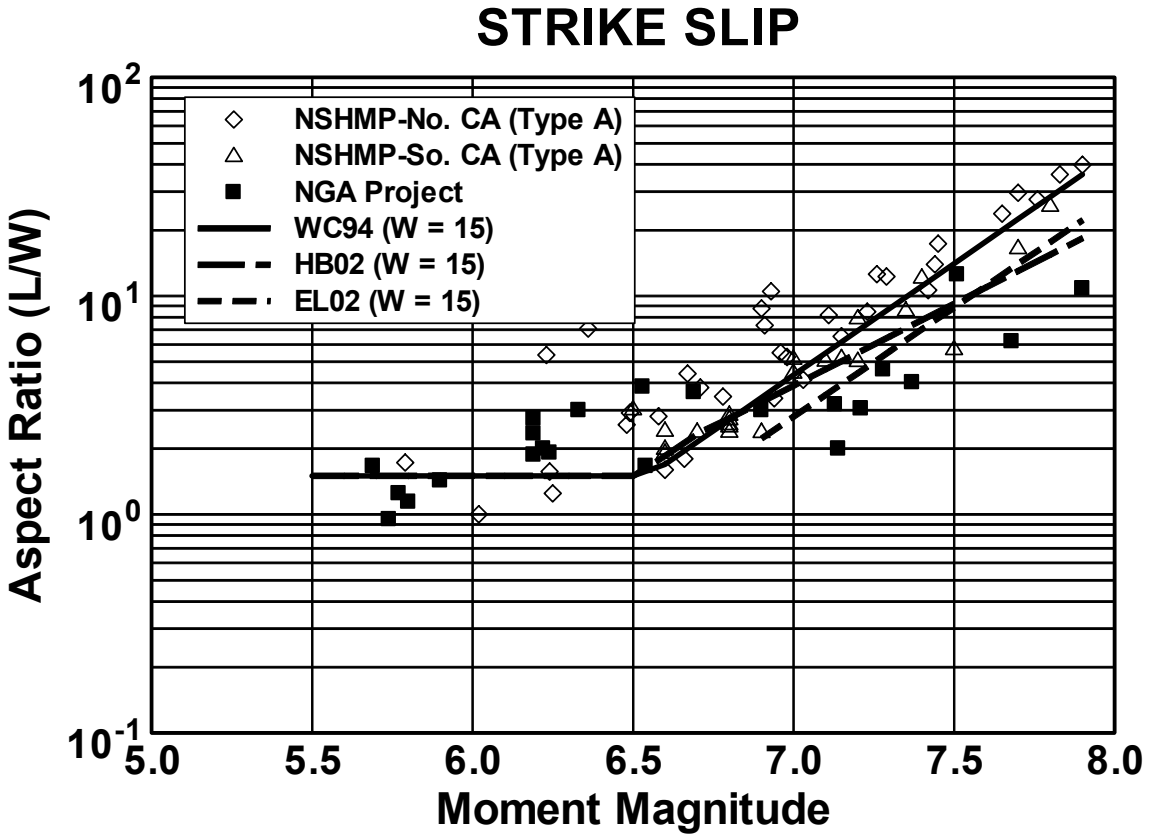

Fig. 5.1 Comparison of relationships between aspect ratio and earthquake magnitude.

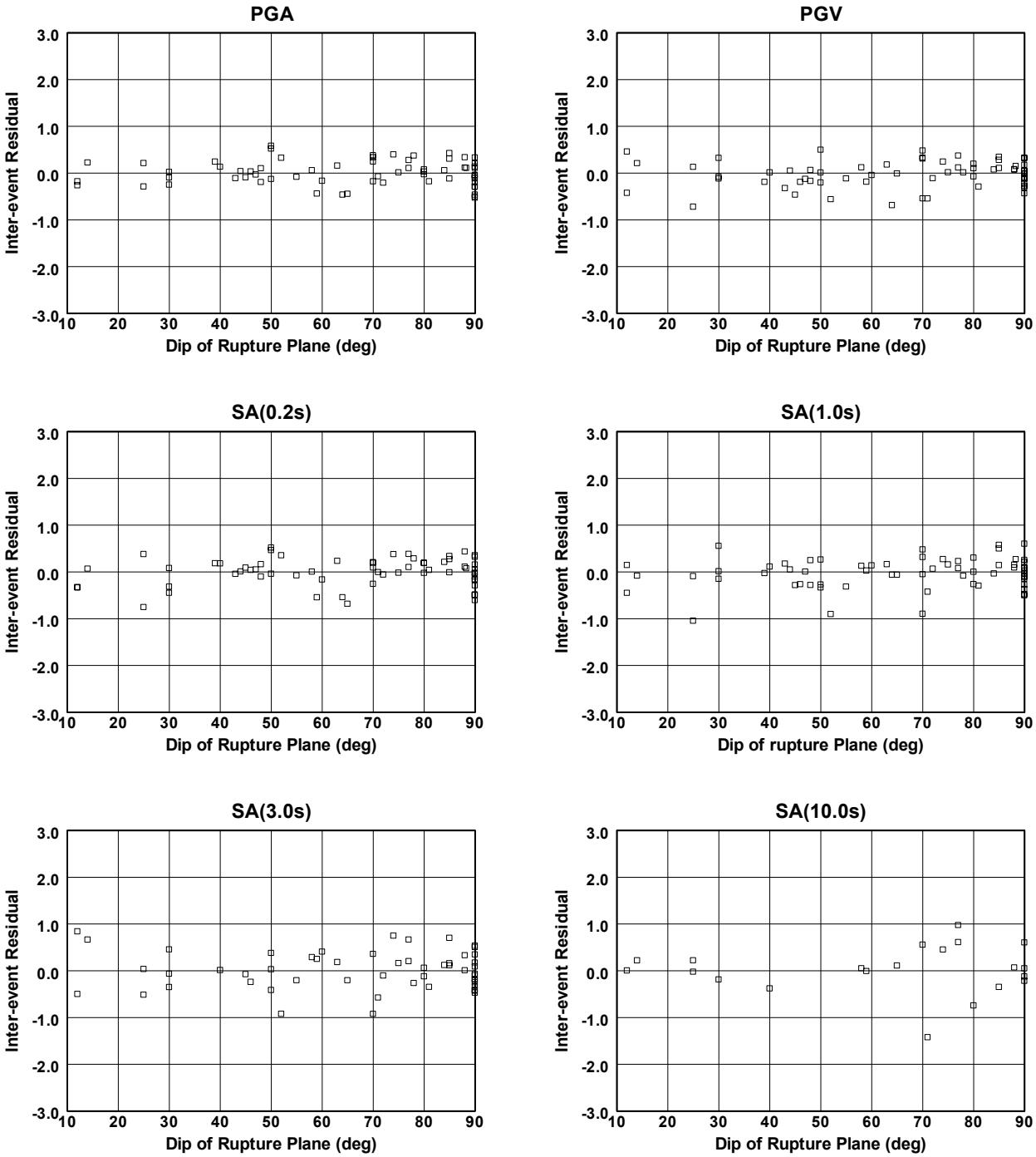

Fig. 5.2 Dependence of inter-event residuals on dip angle.

6 Guidance to Users

Because of the relatively complex nature of the CB-NGA functional forms and because of the inclusion of many new predictor variables, this chapter presents guidelines to users on how to evaluate the model for engineering applications. Covered topics include general limits of applicability, calculating PGA on rock, accounting for unknown predictor variables, estimating epistemic uncertainty, estimating spectral displacement and PGD, and use in the National Seismic Hazard Mapping Project (NSHMP).

6.1 GENERAL LIMITS OF APPLICABILITY

Generally speaking, the CB-NGA model is considered to be valid for shallow continental earthquakes occurring in worldwide active tectonic regimes for which the following conditions apply: (1) $\mathbf{M} > 4.0$; (2) $\mathbf{M} < 8.5$ for strike-slip faulting, 8.0 for reverse faulting, and 7.5 for normal faulting; (3) $R_{RUP} = 0 - 200$ km; (4) $V_{S30} = 150 - 1500$ m/s, corresponding to NEHRP site classes B, C, D and E; (4) $Z_{2.5} = 0 - 10$ km; (5) $Z_{TOR} = 0 - 15$ km; and (6) $\delta = 15 - 90°$.

Practically speaking, the CB-NGA model is not uniformly valid over the entire range of predictor variables listed above. Statistical prediction errors are smallest for parameter values near their mean and increase as these values diverge from this mean (e.g., see Campbell, 2004). These errors can become very large when the model is extrapolated beyond the data limits of the predictor variable and should be used with caution under such conditions. The applicable range of some predictor variables have been extended beyond the limits of the data when the model has been constrained theoretically.

6.1.1 Magnitude

The upper-magnitude limits for strike-slip and reverse faulting are dictated by the requirements of the PEER NGA Project. The largest magnitudes for each of these faulting categories were 0.3–0.6 magnitude units smaller than these limits. Although not a requirement by the PEER NGA Project, we have recommended a similar extrapolation for normal faulting. We believe that such an extrapolation can be justified because of the careful selection of an appropriate magnitude-scaling term. Nonetheless, any extrapolation is associated with additional epistemic uncertainty (see discussion below). The lower-magnitude limit is about 0.3 magnitude units below the smallest magnitude used in the analysis.

6.1.2 Distance

The distance limit of 200 km was also dictated by the PEER NGA Project. The rate of attenuation out to this distance is reasonably well constrained, except at the smaller magnitudes where data are only complete to 100–150 km. Careful selection of an appropriate attenuation term allows extrapolation, even for the smaller magnitudes, out to 200 km, although it is unlikely that such distant earthquakes will have much impact on the results of a seismic hazard analysis. Because both geometrical and anelastic attenuation is modeled by a pseudo-geometrical attenuation term, there might be a tendency to overestimate ground motion beyond about 100 km, especially at the smaller magnitudes. This overprediction at small magnitudes is exacerbated by the tendency to selectively process only those strong motion recordings with relatively high ground motion amplitudes at moderate-to-large distances.

6.1.3 Shear-Wave Velocity

Even though our selected NGA database included a limited number of recording sites with $V_{S30} < 180$ m/s, such soft-soil sites or even sites with higher velocities might have other conditions (e.g., shallow Bay Mud over rock) that make site response more complicated than our simple nonlinear soil model would predict. For that reason, we caution the use of the CB-NGA model for NEHRP site class E sites. Furthermore, the 1-D equivalent-linear simulations that

were used to derive the nonlinear soil model become unreliable at shear strains in excess of about 1%. However, if neither of these conditions exists, the model might be valid for $V_{S30} < 180$ m/s because of its theoretical basis and the lack of any significant bias in the intra-event residuals (Fig. 3.7). Otherwise, we recommend that a site response analysis be conducted. There is only one recording site in our database that would be classified as a NEHRP site class A site, which is insufficient to determine whether the model can be extrapolated beyond $V_{S30} > 1500$ m/s. Note also that even though the shallow site response term is held constant for $V_{S30} > 1100$ m/s, there is still a tendency for the CB-NGA model to underestimate ground motion for oscillator periods greater than 1.0 s for NEHRP site class B sites. The shallow site response term included in our model is intended to provide an approximate empirical estimate of site response. We strongly recommend that a site-specific study be conducted for important engineering applications.

6.1.4 Sediment Depth

The sediment depth limit used in the 3-D basin response analyses that formed the basis for our sediment depth term for $Z_{2.5} > 3.0$ km was about 6 km. However, the model might be valid beyond this depth limit (up to about 10 km) because of its theoretical basis. It is possible, although improbable, that the value of V_{S30} could be inconsistent with the value of $Z_{2.5}$ for very shallow sediment depths. There are two cases where this might occur: (1) when V_{S30} is extrapolated to values exceeding 2500 m/s, in which case $Z_{2.5} = 0$ and (2) when $Z_{2.5}$ becomes very small, in which case V_{S30} must be large enough to adequately represent the top 30 m of the soil column. This first case should never occur based on our recommendation that the model should not be extrapolated beyond $V_{S30} = 1500$ m/s. For small values of both V_{S30} and $Z_{2.5}$, it is possible that a site resonance condition will occur, which is not predicted by our model. In this case, we strongly recommended that a site-specific site response analysis be conducted.

6.1.5 Depth to Top of Rupture

The 15 km limit for the depth to top of rupture is based on an analysis of residuals that showed that the inter-event residuals were generally unbiased out to this depth (Fig. 3.4). The inter-event residuals suggested that our model might underpredict ground motion at short-to-mid periods for

$Z_{TOR} > 13$ km, but the data are insufficient to establish a trend. Therefore, until we can acquire additional deep earthquake data to better constrain this possible depth dependence, we recommend that the CB-NGA model should not be used for rupture depths greater than about 15 km. By any definition, this depth limit constrains the modeled earthquakes to occur in the shallow lithosphere (crust).

6.1.6 Dip Angle

The dip of the rupture plane is used only to determine when hanging-wall effects are phased out at $\delta > 70°$. The broader range of dip angles is given to represent the range of values used in the analysis.

6.1.7 Tectonic Regime

Even if an earthquake is shallow, there is some uncertainty in deciding whether an earthquake is located within the continental lithosphere. Continental means that the earthquake must occur within continental crust rather than oceanic crust. Earthquakes that occur on land or on the continental shelf and have focal depths of less than about 25 km can generally be considered to occur within continental lithosphere. There is also some uncertainty in deciding if a region can be considered an active tectonic regime. A general rule of thumb is that a region can be classified as active if it is not otherwise identified as a Stable Continental Region or SCR (e.g., Johnston, 1996; Campbell, 2004), although regional studies should be used to confirm this.

6.2 ESTIMATING ROCK PGA

It might appear at first that the shallow site response term given by Equation (3.11) is non-unique, because it requires an estimate of rock PGA (A_{1100}). However, in no case does the model coefficient k_1, the threshold value of V_{S30} at which f_{site} becomes linear, exceed the 1100 m/s value used to define rock PGA. Therefore, rock PGA can be calculated using only the second (linear) term in Equation (3.11), which does not require an estimate of A_{1100}. This estimate can then be substituted back into f_{site} for purposes of calculating ground motion, including PGA,

when $V_{S30} < k_1$. Consistent with the way that the CB-NGA aleatory uncertainty model was developed, the median estimate of A_{1100} should be used to estimate ground motion on other site conditions even if this estimate is for a level of aleatory uncertainty larger or smaller than the median.

6.3 ESTIMATING UNKNOWN PREDICTOR VARIABLES

There will be instances in which the user will not know the value of one or more of the predictor variables. Simply substituting a default value for such a parameter can lead to biased results and an underestimation of uncertainty. The more rigorous approach is to estimate or assume reasonable estimates for the mean values of these parameters, assign them subjective weights, and model them as additional epistemic uncertainty (e.g., using a logic tree). If a parameter is estimated from a model rather than from data, it also might be associated with additional aleatory uncertainty. The determination of whether parameter estimates are subject to aleatory or epistemic uncertainty is beyond the scope of this report and is left to the user. However, some guidance on the selection and estimation of unknown or uncertain predictor variables is provided below.

6.3.1 Magnitude and Distance

If **M** or R_{RUP} are unknown, these parameters can be estimated from other magnitude and distance measures (e.g., Scherbaum et al., 2004). However, it is preferable to directly include in the seismic hazard analysis one or more 3-D models of the potential rupture planes of the relevant seismic sources in order to properly account for epistemic and aleatory uncertainty in the estimated distances and, for reverse faults, to take into account potential hanging-wall effects.

6.3.2 Shear-Wave Velocity

If V_{S30} is unknown, it can be estimated from the NEHRP site class (BSSC, 2004; Campbell, 2004; Bozorgnia and Campbell, 2004) or from the geological unit associated with the site, either using correlations developed during development of the PEER database (NGA, 2005; Wills and

Clahan, 2005) or other correlations available in the literature (Wills and Silva, 1998; Wills et al., 2000). If NEHRP site classes are used, we recommend that either the boundary values or the geometric mean of the boundary values of V_{S30} be used because of the logarithmic relationship between site amplification and V_{S30}. Our recommended values of V_{S30} for NEHRP site classes E, DE, D, CD, C, BC, and B are 150, 180, 255, 360, 525, 760, and 1070 m/s, respectively.

6.3.3 Style of Faulting and Dip Angle

If style of faulting or rupture dip is unknown, weights should be assigned to alternative estimates of the predictor variables F_{RV}, F_{NM}, and δ based on the orientation and dip of the proposed rupture plane and its relationship to the regional tectonic stress regime.

6.3.4 Depth to Top of Rupture

If the depth to the top of coseismic rupture (Z_{TOR}) is unknown, its aleatory distribution can be estimated probabilistically using the approach of Youngs et al. (2003). If that approach is considered to be too complicated, a simpler empirical approach can be used in which the likelihood of surface rupture is probabilistically estimated using the logistic regression model of Wells and Coppersmith (1993). In this approach, the probability of principal surface rupture is given by the equation

$$P(\text{slip}) = \frac{e^{f_{slip}}}{1+e^{f_{slip}}} \tag{6.1}$$

where

$$f_{slip} = -12.51 + 2.053\,\mathbf{M} \tag{6.2}$$

This probability can then be used to weight two alternative logic-tree branches that define whether or not surface rupture occurs. For the branch where surface rupture is assumed to occur, the user should set $f_{flt,Z} = 0$ in Equation (3.5). For the branch where surface rupture is not assumed to occur, the user should set $f_{flt,Z} = 1$ in this equation. In either case, the user should conservatively set $f_{hng,Z} = 1$ in Equation (3.9), since the actual value of Z_{TOR} is unknown. If the more rigorous approach of Youngs et al. (2003) is used, a distribution of Z_{TOR} values will be simulated and $f_{flt,Z}$ and $f_{hng,Z}$ should be set accordingly.

6.3.5 Sediment Depth

If the depth to the 2.5 km/s velocity horizon is unknown, it can be estimated from one of the other sediment depth parameters, if known, using the following relationships developed using data from the PEER database:

$$Z_{2.5} = 0.519 + 3.595 Z_{1.0}; \quad \sigma_Z = 0.711 \tag{6.3}$$

$$Z_{2.5} = 0.636 + 1.549 Z_{1.5}; \quad \sigma_Z = 0.864 \tag{6.4}$$

where all depths are in kilometers.

However, if none of these depths are known, sediment depth is the only parameter that could possibly be assigned a default value unless it is known or expected that it is either less than 1.0 km or greater than 3.0 km. If sediment depth effects are not expected to be important, V_{S30} alone can serve as a reasonable representative of both shallow and deep site response, and $Z_{2.5}$ can be set to a default value of 2 km (actually any value between 1 and 3 km). If sediment depth effects are expected to be important, then reasonable alternative values for $Z_{2.5}$ and their associated weights should be used to evaluate this parameter.

6.4 ESTIMATING EPISTEMIC UNCERTAINTY

Although magnitude saturation of short-period ground motion at short distances limits the median predicted value of near-source ground motion at large magnitudes, these predictions are based on a limited number of recordings. As a result, there is additional epistemic uncertainty in the near-source median predictions that might not be adequately captured by the use of multiple empirical ground motion models. Modeling this additional epistemic uncertainty is a current topic of research. We intend to use bootstrapping methods to evaluate epistemic uncertainty in the predicted ground motion from our model once this research is completed.

We recommend that the current practice of exclusively using multiple ground motion models to model epistemic uncertainty in predicted ground motion should be abandoned. A preliminary comparison of the NGA models indicates that there are ranges of magnitude and distance, and probably other parameters as well, for which there is very little variability between these relationships. We believe that such implied “agreement” is not representative of a lack of uncertainty, but rather an artifact of using a limited number of models to estimate ground motion.

We recommend that the user consider developing a separate epistemic uncertainty model that represents the true uncertainty in the ground motion estimates from these relationships. Such models should consider the additional epistemic uncertainties discussed above. Specific guidance on modeling epistemic uncertainty is available in Budnitz et al. (1997) and Bommer et al. (2005). However, if the user does not want to develop an independent epistemic uncertainty model, we recommend using the model proposed by the USGS for use in the 2007 update of the National Seismic Hazard Maps (NSHMP, 2007), where epistemic uncertainty is based on the number of earthquakes in a series of magnitude-distance bins in the NGA databases used by two of the developers. This model is given by the equation

$$\ln Y_{unc} = \widehat{\ln Y} \pm \Delta\widehat{\ln Y} \tag{6.5}$$

where $\ln Y_{unc}$ is the predicted value of $\ln Y$ incorporating epistemic uncertainty, $\widehat{\ln Y}$ is the median ground motion predicted from Equation (3.1), and $\Delta\widehat{\ln Y}$ is an incremental value of median ground motion intended to represent approximately one standard deviation of the epistemic probability ground motion distribution. The unmodified median prediction is given a weight of 0.630, and the lower- and upper-bound median predictions are each given a weight of 0.185. The epistemic uncertainty given by this model is applied in addition to the inherent uncertainty in the use of multiple ground motion models and to the aleatory uncertainty model given in Section 3.1.3. The tentative values of $\Delta\widehat{\ln Y}$ recommended by the USGS are listed in Table 6.1. The final values will be published in the final version of NSHMP (2007).

6.5 ESTIMATING SPECTRAL DISPLACEMENT AND PGD

A surge in the design and construction of high-rise condominium buildings and base-isolated structures in the last few years has brought about a renewed interest in the prediction of long-period spectral displacement and PGD. Both of these parameters represent oscillator periods that have been largely ignored by the developers of ground motion models in the past or, if not ignored, have not been properly constrained either empirically or theoretically. It is for this reason that the PEER NGA Project required the developers to provide models for PGD and spectral acceleration out to periods of 10 s. In this section, we provide some guidance and justification for the PGD and long-period PSA components of the CB-NGA model.

6.5.1 Spectral Displacement

The number of recordings in our NGA database that have oscillator periods within the useable bandwidth fall off significantly for oscillator periods exceeding a few seconds. At $T = 10$ s only 506 of the original 1561 selected recordings and 21 of the original 64 selected earthquakes remain, covering magnitudes in the range $6.5 \le \mathbf{M} \le 7.9$. Nearly 70% of these remaining recordings come from the Chi-Chi earthquake. Therefore, as mentioned previously, we used a simple seismological model (Atkinson and Silva, 2000) to help constrain our $\mathbf{M} < 6.5$ magnitude-scaling term at long periods. The question addressed below is whether these constraints and the empirical constraints at larger magnitudes produce reasonable estimates of 5%-damped spectral displacement (SD). An example of the spectral displacements predicted by the CB-NGA model is shown in Figure 6.1.

Faccioli et al. (2004) collected digital recordings from Europe, Japan, and Taiwan that they considered to be valid up to oscillator periods of 10 s. Their Figure 2 gives plots of the average and plus-one standard deviation SD that were derived from these recordings for three magnitude bins and two distance bins. We compared this figure with our Figure 6.1 and found that their empirically derived spectral shapes and inferred magnitude scaling are very similar to those predicted from the CB-NGA model for NEHRP site class D. This is consistent with their predominant use of recordings from soil sites, which are subject to strong amplification at long periods. For example, our model predicts over two times higher spectral ordinates at $T = 10$ s for NEHRP site class D site conditions as compared to BC site conditions.

Faccioli et al. (2004) also show that the theoretical estimate of SD at $T = 10$ s calculated from a simple one-sided displacement pulse in the time domain is equal to PGD for spectra that have become independent of period at long periods. This is a fundamental property of a viscously damped single-degree-of-freedom system and can be shown mathematically from the equation of motion to occur at $T \to \infty$ (e.g., Hudson, 1979). Figure 12 of Faccioli et al. predicts that this limit actually occurs at a period that is about six times the half duration of the one-sided displacement pulse, or three times the period of the corresponding two-sided velocity pulse, and is relatively independent of the shape of this pulse. These authors also show that the relationship of Somerville (2003) relating the duration of the strike-normal forward-directivity velocity pulse to magnitude, when used with their theoretical model, closely matches the average displacement

spectra from the digital recordings out to a distance of 30 km. The Somerville relationship is given by the equation

$$\log 2t_0 = -3.17 + 0.5\mathbf{M} \tag{6.6}$$

where t_0 (s) is the half duration of the one-sided displacement pulse.

Since the above equation represents the duration of a directivity pulse, it likely provides a lower bound to the corner period at which the displacement spectra should become independent of magnitude. In order to get a more representative range of possible corner periods, we also look to the values predicted from the Atkinson and Silva (1997, 2000) two-corner and Brune (1970, 1972) one-corner source models. The longer-period corner for the Atkinson and Silva two-corner source model is given by the equation

$$\log T_0 = -2.18 + 0.5\mathbf{M} \tag{6.7}$$

where T_0 (s) is the corner period. The corner period for the Brune source model (e.g., Boore, 2003) can be represented by the equation

$$\log T_0 = -2.55 + 0.5\mathbf{M} \tag{6.8}$$

for $\beta_s = 3.5$ km/s, $\Delta\sigma = 100$ bars, and seismic moment (dyne-cm) defined by the equation $\log M_0 = 1.5\mathbf{M} + 16.05$, based on the western North America source model proposed by Campbell (2003).

Both the empirical and theoretical displacement spectra given by Faccioli et al. (2004) indicate that the midpoint of the range over which the displacement spectra roll over to a constant value is equal to about $3t_0$. Substituting this value into Equation (6.6) and evaluating the corner periods given by Equations (6.7) and (6.8), results in the following range of periods at which SD might be expected to become independent of period: 0.3–2.1 s for $\mathbf{M} = 5.0$, 1.0–6.6 s for $\mathbf{M} = 6.0$, 3.2–21 s for $\mathbf{M} = 7.0$, and 10–66 s for $\mathbf{M} = 8.0$. These estimates suggest that SD should become independent of period for $T < 10$ s and $\mathbf{M} < 6.5$, as predicted by the CB-NGA model.

Based on the above discussion, we believe that the CB-NGA model does provide a reasonable representation of the amplitude and shape of the long-period displacement spectrum based on both empirical and theoretical considerations. Additional verification is given in the discussion on PGD and its relationship to SD in the next section. Nonetheless, the user should use discretion when using this model to estimate spectral acceleration, velocity, and displacement for $T > 5.0$ s until further empirical and theoretical verification becomes available.

6.5.2 Peak Ground Displacement

Empirical estimates of PGD are notoriously unreliable because of their sensitivity to long-period noise, low-pass filter parameters, and accelerogram processing errors. Nonetheless, we provide model coefficients for PGD in Table 3-1 based on a mathematical relationship between long-period oscillator response and PGD. The resulting PGD ground motion model is intended for evaluation purposes only at this time and should not be used for engineering design until further empirical and theoretical verification becomes available.

Faciolli et al (2004) show both empirically and theoretically that for displacement spectra that have attained a constant value independent of period at $T = 10$ s, the value of SD at this oscillator (SD_{10}) is a reasonable approximation to PGD. This is a fundamental property of a viscously damped single-degree-of-freedom system and can be shown mathematically from the equation of motion to occur at $T \to \infty$ (e.g., Hudson, 1979). This behavior is achieved in the CB-NGA model for earthquakes of $\mathbf{M} < 7$. Therefore, the prediction of SD_{10} at these magnitudes can be used potentially as an estimate of PGD. However, for larger events, where SD_{10} has not obtained a constant value, we need to adjust the predicted value of SD_{10} in order to be able to obtain an estimate of PGD. We do this by (1) comparing our model's near-fault magnitude-scaling properties with scaling relationships between fault-rupture displacement and magnitude and (2) comparing our model's far-field magnitude-scaling properties with simple seismological theory.

Consistent with the finding of Faccioli et al. (2004), Tom Heaton of Caltech (personal communication, 2006) suggested that near-source PGD and SD at long periods should scale with fault slip. According to the empirical relationships of Wells and Coppersmith (1994), fault slip scales as $10^{b\mathbf{M}}$, where $b = 0.69$ for the average value of fault-rupture displacement (*AD*) and $b = 0.82$ for the maximum value of fault-rupture displacement (*MD*) for magnitudes in the range $5.6 \le \mathbf{M} \le 8.1$. Averaging these two estimates of *b* gives a magnitude-scaling coefficient for fault-rupture displacement (*D*) of $b = 0.76$. This value is nearly identical to the $\mathbf{M} < 6.5$ magnitude-scaling coefficient for SD_{10} in our model once we set $R_{RUP} = 0$ to represent a near-fault location and convert our scaling coefficient to a common logarithm by dividing by $\ln(10)$.

Wells and Coppersmith (1994) found empirically that *D* and fault-rupture length (*L*) have similar magnitude-scaling characteristics. Hanks and Bakun (2002) used this property, which is

consistent with the *L*-model of Scholz (1982), to justify their empirically revised revision of the Wells and Coppersmith magnitude rupture area (*A*) relationship for $\mathbf{M} \geq 6.7$. The *L*-model also predicts that once rupture has reached the full width of the fault, which can be expected to occur at $\mathbf{M} \geq 6.7$ for large strike-slip earthquakes, *A* should scale with *L*. We used the observation that *D*, *L,* and *A* all have about the same value of *b* to infer a magnitude-scaling coefficient for spectral displacement at large magnitudes where SD_{10} has not yet attained a constant value in the CB-NGA model. Hanks and Bakun found that $b = 0.75$ in their revised *A* vs. **M** relationship for $\mathbf{M} \geq 6.7$. That value is virtually identical to the value we found for SD_{10} at $\mathbf{M} < 6.5$ ($b = 0.77$). This implies that we can set our large earthquake magnitude-scaling coefficient to match our small earthquake magnitude-scaling coefficient for purposes of deriving a ground motion model for PGD from the model for SD_{10} at large magnitudes. This is equivalent to setting $c_3 = c_2$ in Equation (3.2).

If we further assume that *D* is a reasonable proxy for PGD near the fault, we can use the magnitude-scaling relationships of Wells and Coppersmith (1994) to compare estimates of *AD* and *MD* with our estimates of PGD from SD_{10} after setting $c_3 = c_2$ in Equation (3.2). The predicted value of PGD from the CB-NGA model represents an average over the rupture plane, which is expected to be closer to the value of *AD* rather than *MD*. Wells and Coppersmith show that *AD* is on average 0.5 times the value of *MD*. Therefore, if we assume $AD = 0.5\,MD$, take the geometric mean of *AD* from the two Wells and Coppersmith magnitude-scaling relationships, correct for the average partitioning of the displacement into its spatial components, and evaluate the predicted median value of SD_{10} from our model for $V_{S30} = 620$ m/s (generic rock) and $R_{RUP} = 0$ (near-fault conditions), we get the comparison shown in Table 6.2 between the value of PGD estimated from geologic observations of fault-rupture displacement and the near-fault value of PGD inferred from the adjusted CB-NGA model for SD_{10}. This table gives predictions from the CB-NGA model both with and without setting $c_3 = c_2$, identified by the terms *adjusted* and *unadjusted* in the table. The adjusted model is the one we propose to use to estimate PGD.

The comparison in Table 6.2 shows that the near-fault predictions of PGD derived from the adjusted ground motion model for SD_{10} are consistent with geologic estimates of fault-rupture displacement. The adjustment accounts for the observation that SD_{10} is still increasing and has not yet attained its asymptotic value of PGD for $\mathbf{M} > 7$. The evaluation of our model for generic rock site conditions is somewhat arbitrary. Generic rock was selected as an average

estimate of the likely site conditions for which observations of *AD* and *MD* were made. Softer or harder site conditions would lead to estimates of spectral acceleration that are higher or lower than those obtained for generic rock. However, the magnitude scaling would remain the same.

Another check of the reasonableness of our proposed PGD model is to compare it with the far-field magnitude scaling of PGD inferred from simple seismological theory. Faccioli et al. (2004) show that the far-field value of PGD estimated from a Brune omega-square source spectrum (Brune 1970, 1972) can be related to moment magnitude by the equation

$$\log \mathrm{PGD} = -4.46 + \frac{1}{3}\log \Delta\sigma + \mathbf{M} - \log R_{HYP} \tag{6.9}$$

where PGD (cm) is maximum displacement, $\Delta\sigma$ (MPa) is stress drop, and R_{HYP} (km) is hypocentral distance. If we evaluate this equation for $\Delta\sigma = 2$ MPa and $R_{HYP} = 100$ km (far-field conditions) and evaluate our SD_{10} model for $R_{RUP} = 100$ km (far-field conditions) and $V_{S30} = 620$ m/s (generic rock), we obtain the comparison shown in Table 6.3 between the far-field value of PGD estimated from simple seismological theory and the far-field value of PGD inferred from the CB-NGA model for SD_{10}. This table gives predictions from the CB-NGA model both with and without setting $c_3 = c_2$, identified by the terms *adjusted* and *unadjusted* in the table. The adjusted model is the one we propose to use to estimate PGD.

The comparison in Table 6.3 shows that the far-field predictions of PGD derived from the adjusted ground motion model for SD_{10} are consistent with estimates based on simple seismological theory. The 2 MPa stress drop was chosen to make the comparison as close as possible, but it is not an unreasonable value considering that observed values range between 1 and 10 MPa and that it falls within a factor of 1.5 of the often-quoted average of 3 MPa (Hanks and Bakun, 2002). The evaluation of the CB-NGA model for generic rock site conditions is consistent with the near-fault predictions given above. The good agreement of the two estimates over the magnitude range $5.0 \le \mathbf{M} \le 8.5$ is the direct result of the agreement of the far-field magnitude-scaling coefficients from the Brune and CB-NGA models (i.e., $b = 1.0$).

6.6 USE IN THE NATIONAL SEISMIC HAZARD MAPPING PROJECT

The USGS National Seismic Hazard Mapping Project (NSHMP) is currently in the process of revising the national seismic hazard maps for release in September 2007. Because the empirical

ground motion models that the USGS used in the 2002 maps for the western United States were revised as part of the PEER NGA Project, the USGS convened an independent expert panel in September 2006 to review the NGA models together with their supporting documentation. This included the documentation that the developers provided in response to USGS and California Geological Survey (CGS) questions prior to the panel's review (Appendix B). The panel was asked to make recommendations on if and how the NGA models should be implemented in the NSHMP. One of the items evaluated by the panel was whether any weight should be given to each developer's previous ground motion model or whether there was sufficient scientific bases and documentation to give the new models 100% weight. The panel, referred to as the "Tiger Team" by the USGS, found sufficient documentation and justification to recommend that our NGA model should be considered to supersede our previous model (Campbell and Bozorgnia, 2003a, 2003b, 2003c, 2004) in the 2007 revision of the National Seismic Hazard Maps and should be given a relative weight of 100% compared to our previous model.

As pointed out by the Tiger Team, the main issues that the USGS faced in implementing the CB-NGA model have to do with the difficulty in predicting the depth to the top of coseismic rupture (Z_{TOR}) and the depth of the sedimentary column ($Z_{2.5}$). Neither of these predictor variables can be reliably estimated on a national or even regional scale. As a result, the USGS asked us to recommend how to implement our model when these parameters were unknown. We recommended that $Z_{2.5}$ should be set equal to 2.0 km consistent with the general guidelines given in Section 6.3.5, recognizing that this depth was not needed for a relatively wide range of parameter values (i.e., for $1.0 \le Z_{2.5} \le 3.0$ km). We recommended that a probability distribution of rupture depths (or as a minimum the more simplified empirical approach for estimating rupture depths) described in Section 6.3.4 should be used to account for the epistemic uncertainty associated with Z_{TOR}, recognizing that this is an important new parameter that significantly impacts estimated ground motion for surface-rupturing earthquakes on reverse faults. As this report was being written, the USGS had not yet decided exactly how the CB-NGA model would be evaluated in terms of the new predictor variables.

We believe that the USGS and CGS questions and our answers referred to above are relevant to all users, since they provide additional insights into the reasons behind some of the critical decisions we made in the course of constructing the CB-NGA model as well as some important aspects of our model that would otherwise go unnoticed. Of particular interest are the

many residual plots that we produced that further demonstrated the validity and robustness of our model. Our response to these questions as they specifically relate to our model is provided in Appendix B. In all of the residual plots in Appendix B, inter-event and intra-event residuals are defined by the equations given in Section 3.2. Since the sum of the intra-event and inter-event residuals are very nearly zero, we interchangeably use the term inter-event residual and source term in the discussion in Appendix B.

It should be noted that the residuals given in Appendix B are defined in terms of the version of the regression equation (after smoothing the coefficients) that predicted oversaturation. We believe that these unadjusted residuals are a better representation of the behavior of the model than are the residuals after we constrain the model to saturate when it predicts oversaturation. Constraining the model to saturate always increases the ground motion and, therefore, will always cause a bias in $\widehat{\ln Y}$ by an amount equal to $(c_3 - c_3')\mathbf{M}$, where c_3' is the model coefficient c_3 after constraining the model to saturate. As a result, we do not believe that we should add to this bias by biasing the residuals as well for purposes of answering the USGS and CGS questions. In those plots where we want to emphasize this bias, we also show an adjusted baseline that is calculated by subtracting the bias from the original zero baseline.

Table 6.1 Incremental values of median ground motion in epistemic uncertainty model.

M	R_{RUP} (km)	$\Delta\widehat{\ln Y}$
5.0 – 5.9	≤10	0.375
5.0 – 5.9	10 – 30	0.210
5.0 – 5.9	≥30	0.245
6.0 – 6.9	≤10	0.230
6.0 – 6.9	10 – 30	0.225
6.0 – 6.9	≥30	0.230
≥7.0	≤10	0.400
≥7.0	10 – 30	0.360
≥7.0	≥30	0.310

Table 6.2 Comparison of near-fault estimates of PGD.

M	Estimated PGD from fault-rupture displacement (m)	Estimated near-fault PGD from CB-NGA model (m)	
		Unadjusted	Adjusted
5.0	0.02	0.02	0.02
5.5	0.04	0.04	0.04
6.0	0.10	0.10	0.10
6.5	0.24	0.24	0.24
7.0	0.58	0.46	0.57
7.5	1.39	0.91	1.39
8.0	3.32	1.78	3.35
8.5	7.91	3.48	8.10

Table 6.3 Comparison of far-field estimates of PGD.

M	Estimated PGD from seismological theory (cm)	Estimated far-field PGD from 10 s spectral displacement (cm)	
		Unadjusted	Adjusted
5.0	0.04	0.04	0.04
5.5	0.14	0.13	0.13
6.0	0.44	0.42	0.42
6.5	1.38	1.33	1.33
7.0	4.37	3.42	4.23
7.5	13.81	8.81	13.43
8.0	43.69	22.67	42.69
8.5	138.15	58.35	135.70

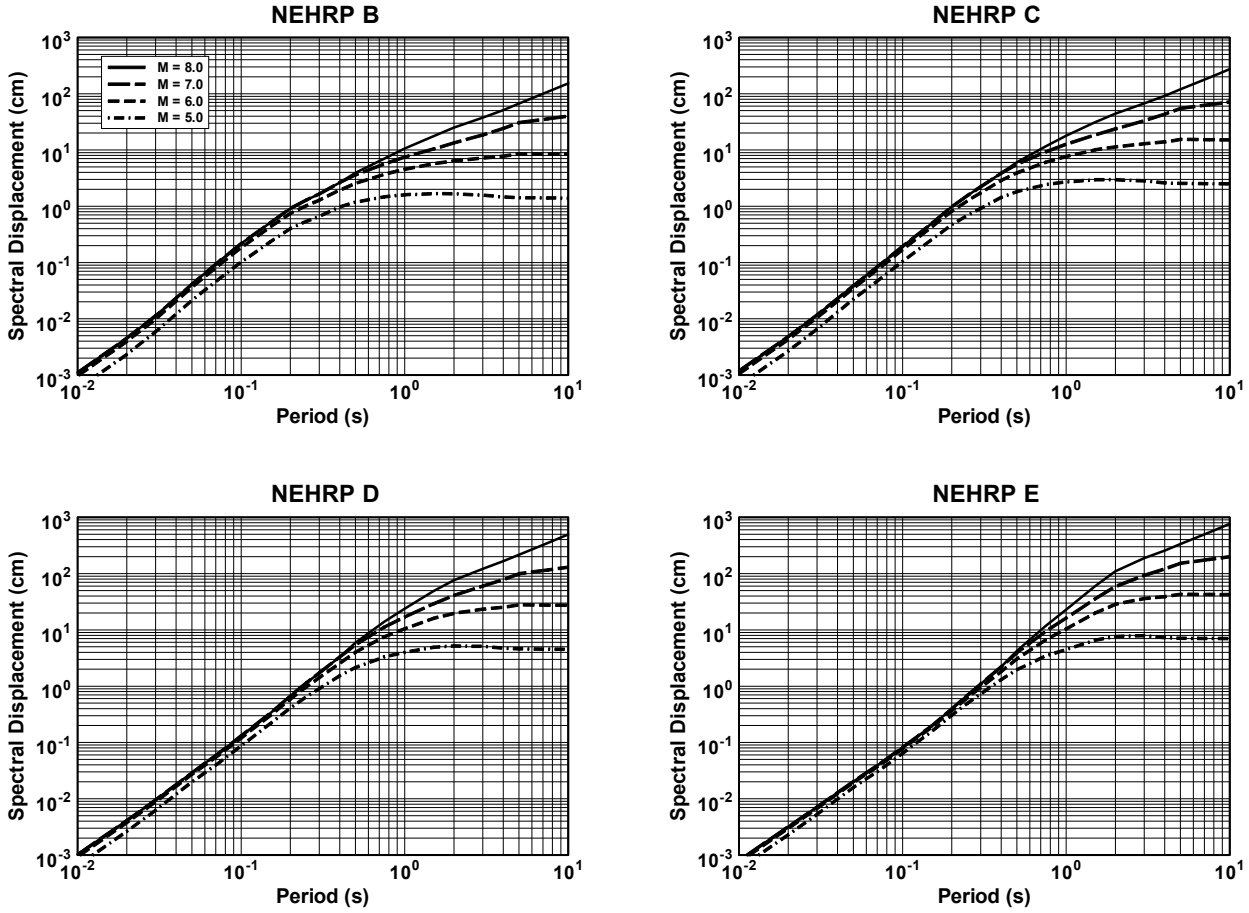

Fig. 6.1 Dependence of spectral displacement on magnitude for strike-slip faulting, $R_{RUP} = 0$, and $Z_{2.5} = 2.0$ km.

7 Model Evaluation

In this chapter, we present example calculations that allow the user to review the ground motion values predicted by the CB-NGA model and to verify their own implementation of the model. We also present a series of plots that show the predicted ground motion scales with the predictor variables and compare the CB-NGA predictions with our previous model.

7.1 EXAMPLE CALCULATIONS

Tables 7.1 and 7.2 give example calculations for PGA (i.e., $T = 0.01$ s), PGV, and PSA at oscillator periods of 0.2, 1.0, and 3.0 s to assist in verifying the implementation of the CB-NGA model presented in this report. Also included in these tables are estimates of PGV from our 1997 model (Campbell, 1997, 2000, 2001) and estimates of PGA and PSA from our 2003 model (Campbell and Bozorgnia, 2003a, 2003b, 2003c, 2004). These models are identified as CB-NGA, C97 and CB03, respectively, in these tables. Tables 7.1 and 7.2 give ground motions for strike-slip and reverse faulting, respectively.

Ground motion estimates in Tables 7.1 and 7.2 are given for moment magnitudes of 5.0 and 7.0. The depth to the top of the coseismic rupture was assumed to be 5.0 km for the $\mathbf{M} = 5.0$ scenario and zero for the $\mathbf{M} = 7.0$ scenario. For the reverse-faulting scenario, the calculation points are located on the hanging wall (HW) of a 45°-dipping fault and are, therefore, subject to hanging-wall effects. The dip of the rupture plane of the strike-slip scenario is assumed to be 90°. For both scenarios, the calculation points are located along a line perpendicular to the strike of the fault. The rupture width (i.e., the down-dip extent of rupture) was calculated from the rupture area assuming $W = \sqrt{A}$, where the rupture area was calculated from the equation (Wells and Coppersmith, 1994)

$$\log A = (\mathbf{M} - 4.07) / 0.98 \tag{7.1}$$

where A has units of square kilometers. If the calculated value of W exceeded the assumed seismogenic width of the fault, it was set equal to this width. The maximum depth of the seismogenic rupture zone was assumed to be 15 km. The depth to the top of the seismogenic rupture zone (for purposes of calculating R_{SEIS}) was taken as the minimum of the depth to the top of rupture or 3.0 km. A summary of the values of the parameters used to develop Tables 7.1 and 7.2 are listed in Tables 7.3 and 7.4, respectively. Note that the Campbell (1997, 2000, 2001) model was evaluated for generic rock and adjusted to NEHRP BC site conditions using the site factor for one-second PSA given by Campbell and Bozorgnia (2003a, 2003b, 2003c, 2004).

7.2 SCALING WITH PREDICTOR VARIABLES

In this section we give a series of plots that demonstrate how the CB-NGA median ground motion, aleatory uncertainty, and median spectra models scale with the predictor variables included in the models. Unless otherwise noted, the models are evaluated for strike-slip faulting, $Z_{TOR} = 0$, $V_{S30} = 760$ m/s (NEHRP BC site conditions), and $Z_{2.5} = 2.0$ km.

7.2.1 Median Model

All of the plots for the CB-NGA median ground motion model show scaling relations for six ground motion parameters: PGA, PGV, and PSA at oscillator periods of 0.2, 1.0, 3.0, and 10.0 s. PGA is equivalent to PSA at $T = 0.01$ s. Scaling of ground motion with rupture distance (R_{RUP}) is given in Figure 7.1. Scaling of ground motion with magnitude (**M**) is given in Figure 7.2. Scaling of ground motion with near-source distance showing the effects of style-of-faulting, hanging wall, and footwall is given in Figure 7.3. Scaling of shallow site amplification (f_{site}) with rock PGA (A_{1100}) for NEHRP B ($V_{S30} = 1070$ m/s), C ($V_{S30} = 525$ m/s), D ($V_{S30} = 255$ m/s), and E ($V_{S30} = 150$ m/s) site conditions is given in Figure 7.4. Scaling of NEHRP short-period site coefficient F_a (evaluated for $T = 0.2$ s) for NEHRP site classes C, D, and E with PGA for NEHRP BC site conditions is given in Figure 7.5. Scaling of NEHRP mid-period site coefficient F_v for NEHRP site classes C, D, and E with PGA on NEHRP BC site conditions is given in Figure 7.6. Finally, scaling of deep site amplification (f_{sed}) with sediment depth ($Z_{2.5}$) is given in Figure 7.7. Figures 7.5 and 7.6 also show, for comparison, the NEHRP site coefficients F_a

and F_v given in the NEHRP *Provisions* (BSSC, 2004) as well as those estimated by Choi and Stewart (2005) based on the ground motion models of Abrahamson and Silva (1997), Campbell and Bozorgnia (2003a, 2003b, 2003c, 2004), and Sadigh et al. (1997).

7.2.2 Aleatory Uncertainty Model

We present two sets of plots for the CB-NGA aleatory uncertainty model. The dependence of the total standard deviation (σ_T) on rock PGA (A_{1100}) is given in Figure 7.8. The dependence of all of the standard deviation measures (σ, τ, σ_c, σ_T, and σ_{Comp}) on oscillator period is given in Figure 7.9. In this case *Comp* represents the arbitrary horizontal component as defined in Chapter 4 of this report.

7.2.3 Median Response Spectra

Plots of median response spectra (PSA) are used to demonstrate the scaling of spectral amplitude and spectral shape with magnitude, distance, and site conditions. Scaling of PSA with rupture distance (R_{RUP}) is given in Figure 7.10. Scaling of PSA with magnitude (**M**) is given in Figure 7.11. Scaling of PSA with style of faulting and rupture depth is given in Figure 7.12 for sites located on the hanging wall (HW) and footwall (FW) of a 45°-dipping fault. Scaling of PSA with NEHRP site class is given in Figure 7.13. Scaling of PSA with sediment depth ($Z_{2.5}$) for NEHRP D site conditions is given in Figure 7.14. Finally, scaling of near-source spectral displacement (SD) with magnitude for NEHRP site classes B, C, D, and E is given in Figure 6.1

7.3 COMPARISON WITH PREVIOUS MODELS

In this section, we compare the predictions from our new model, identified as CB-NGA, with those from our previous models, identified as CB03 (Campbell and Bozorgnia, 2003a, 2003b, 2003c, 2004) and C97 (Campbell, 1997, 2000, 2001). The C97 model is used to evaluate PGV, which was not included as a parameter in the CB03 model. Unless otherwise noted, we evaluated all of the ground motion models using the parameter values given in Table 7.4, with the exception that we set $Z_{TOR} = 0$ for all magnitudes in the CB-NGA model, and we set

$F_{RV} = 0.5$ and $F_{TH} = 0.5$ to represent generic reverse faulting in the CB03 model. We evaluated the CB03 model for NEHRP D site conditions by setting $S_{VFS} = 0$, $S_{SR} = 0$, and $S_{FR} = 0$. Some of the comparisons have been shown to distances of 200 km even though the CB03 and C97 models were developed using data to 60 km, and we have recommended that they not be used for distances greater than 100 km. We do this because many users do not place constraints on empirical ground motion models when using them in a probabilistic seismic hazard analysis (PSHA), regardless of the author's recommendations.

Figures 7.15 and 7.16 show comparisons of ground motion scaling with rupture distance and earthquake magnitude for PGA, PGV, and PSA at oscillator periods of 0.2, 0.5, 1.0, and 3.0 s. The next six figures show comparisons of spectral scaling with (1) rupture distance for NEHRP BC site conditions (Fig. 7.17); (2) earthquake magnitude for NEHRP BC site conditions (Fig. 7.18); (3) rupture distance for NEHRP D site conditions (Fig. 7.19); (4) earthquake magnitude for NEHRP D site conditions (Fig. 7.20); (5) style of faulting, hanging wall/footwall site locations, and rupture depth for reverse faults (Fig. 7.21), and (6) style of faulting and hanging-wall/footwall site locations for normal and strike-slip faults (Fig. 7.22). The next two figures show comparisons of the total standard deviation for $R_{RUP} = 0$ and either NEHRP BC site conditions (Fig. 7.23) or NEHRP B, C, D, and E site conditions (Fig. 7.24). These latter comparisons are given as a function of magnitude, as this is the most common form of the CB03 and C97 aleatory uncertainty models used in practice.

Figures 7.15–7.20 show that the differences between our NGA and previous ground motion models are generally small, within the range of magnitudes and distances common to both databases (i.e., $\mathbf{M} = 5.0–6.5$ and $R_{RUP} = 10–60$ km) for NEHRP BC and NEHRP D site conditions. The biggest differences occur at smaller and larger magnitudes, where data were previously sparse or nonexistent. This is most apparent at intermediate distances from large-magnitude earthquakes, where the new functional form predicts a greater rate of attenuation and, therefore, a lower level of ground motion than the previous functional forms. These differences are largely due to us forcing saturation at $R_{SEIS} = 0$ for all ground motion parameters, regardless of the oscillator period, while at the same time constraining the rate of attenuation to be independent of magnitude in our previous models. The biggest difference is for PGV, where the more complete PEER database and new functional form has resulted in magnitude and distance scaling characteristics that are more similar to those found at longer periods than before. The

new functional form is supported both empirically by the additional strong motion recordings from $\mathbf{M} \geq 7.0$ earthquakes in the PEER database and theoretically by the broadband ground motion simulation results of Frankel (2007).

Figure 7.21 shows that the difference between our NGA and CB03 response spectral predictions are relatively small for a site located on the footwall (FW) or hanging wall (HW) of a surface-rupturing reverse fault at a distance of 5 km from a major earthquake. However, our NGA model predicts higher short-period spectral acceleration when such an event is buried (i.e., does not have surface rupture), since our previous model did not distinguish between reverse-faulting earthquakes with surface and buried fault rupture.

Figure 7.22 shows the same comparison as in Figure 7.21 except for normal and strike-slip faults. In this case, there is no distinction between earthquakes with surface or buried rupture in our new model. Now our NGA model predicts significantly higher ground motion than the CB03 model at short and mid periods, because of the inclusion of hanging-wall effects. This represents a worst-case scenario for strike-slip faults, which will typically have much steeper rupture planes than used in this comparison. Our NGA model predicts that hanging-wall effects phase out for dip angles greater than 70°.

Figure 7.23 shows that in all cases the total standard deviation from the CB-NGA model for NEHRP BC site conditions is smaller at small magnitudes and larger at large magnitudes as compared to those of the CB03 and C97 models. This transition from smaller to larger standard deviation occurs between magnitudes of 5.0 and 6.0, depending on the ground motion parameter. Figure 7.24 shows that the difference in standard deviation is strongly dependent on NEHRP site class. At short periods, where the standard deviation is a strong function of V_{S30} and A_{1100} (rock PGA), the total standard deviation of the CB-NGA model for the softer sites can be smaller than that of the CB03 and C97 models at large magnitudes. The upward curvature observed in the CB-NGA values at small magnitudes is due to the smaller value of A_{1100} at these magnitudes. The comparison in Figure 7.24 is much different for other distances and site locations. For example, at large distances, the CB-NGA curves coalesce to look like the curves in Figure 7.23. For sites on the hanging wall of a reverse fault, the higher ground motion in the CB-NGA model leads to a greater separation of the curves.

Table 7.1 Example calculations for 90°-dipping strike-slip fault.

R_{RUP} (km)	**M** = 5.0				**M** = 7.0			
	R_{JB}	R_{SEIS}	PSA, 0.01s (*g*)		R_{JB}	R_{SEIS}	PSA, 0.01s (*g*)	
			CB-NGA	CB03			CB-NGA	CB03
1	—	—	—	—	1.0	3.2	0.4742	0.4988
3	—	—	—	—	3.0	4.2	0.4292	0.4672
5	0.0	5.0	0.1752	0.1995	5.0	5.8	0.3691	0.4149
10	8.7	10.0	0.1031	0.1017	10.0	10.4	0.2513	0.2923
15	14.1	15.0	0.0677	0.0669	15.0	15.3	0.1852	0.2130
30	29.6	30.0	0.0300	0.0323	30.0	30.1	0.1025	0.1113
50	49.7	50.0	0.0159	0.0188	50.0	50.1	0.0647	0.0659
100	99.9	100.0	0.0067	0.0090	100.0	100.0	0.0342	0.0319
200	199.9	200.0	0.0028	0.0043	200.0	200.0	0.0180	0.0153
R_{RUP} (km)	R_{JB}	R_{SEIS}	PSA, 0.2s (*g*)		R_{JB}	R_{SEIS}	PSA, 0.2s (*g*)	
			CB-NGA	CB03			CB-NGA	CB03
1	—	—	—	—	1.0	3.2	1.0429	0.8900
3	—	—	—	—	3.0	4.2	0.9765	0.8601
5	0.0	5.0	0.3616	0.4758	5.0	5.8	0.8743	0.8040
10	8.7	10.0	0.2325	0.2491	10.0	10.4	0.6271	0.6328
15	14.1	15.0	0.1559	0.1613	15.0	15.3	0.4643	0.4872
30	29.6	30.0	0.0676	0.0741	30.0	30.1	0.2477	0.2613
50	49.7	50.0	0.0345	0.0413	50.0	50.1	0.1494	0.1514
100	99.9	100.0	0.0135	0.0186	100.0	100.0	0.0738	0.0695
200	199.9	200.0	0.0052	0.0084	200.0	200.0	0.0362	0.0314
R_{RUP} (km)	R_{JB}	R_{SEIS}	PSA, 1.0s (*g*)		R_{JB}	R_{SEIS}	PSA, 1.0s (*g*)	
			CB-NGA	CB03			CB-NGA	CB03
1	—	—	—	—	1.0	3.2	0.3795	0.4521
3	—	—	—	—	3.0	4.2	0.3247	0.4165
5	0.0	5.0	0.0481	0.0405	5.0	5.8	0.2657	0.3619
10	8.7	10.0	0.0265	0.0208	10.0	10.4	0.1744	0.2487
15	14.1	15.0	0.0174	0.0141	15.0	15.3	0.1297	0.1819
30	29.6	30.0	0.0081	0.0072	30.0	30.1	0.0755	0.0988
50	49.7	50.0	0.0045	0.0044	50.0	50.1	0.0502	0.0610
100	99.9	100.0	0.0020	0.0023	100.0	100.0	0.0287	0.0315
200	199.9	200.0	0.0009	0.0012	200.0	200.0	0.0164	0.0162

Table 7.1—*Continued*

R_{RUP} (km)	**M** = 5.0				**M** = 7.0			
	R_{JB}	R_{SEIS}	PSA, 3.0s (*g*)		R_{JB}	R_{SEIS}	PSA, 3.0s (*g*)	
			CB-NGA	CB03			CB-NGA	CB03
1	—	—	—	—	1.0	3.2	0.1073	0.1607
3	—	—	—	—	3.0	4.2	0.0918	0.1443
5	0.0	5.0	0.00542	0.00498	5.0	5.8	0.0751	0.1214
10	8.7	10.0	0.00298	0.00256	10.0	10.4	0.0493	0.0795
15	14.1	15.0	0.00196	0.00173	15.0	15.3	0.0367	0.0571
30	29.6	30.0	0.00091	0.00089	30.0	30.1	0.0213	0.0306
50	49.7	50.0	0.00051	0.00054	50.0	50.1	0.0142	0.0188
100	99.9	100.0	0.00023	0.00028	100.0	100.0	0.0081	0.0097
200	199.9	200.0	0.00010	0.00014	200.0	200.0	0.0046	0.0050
R_{RUP} (km)	R_{JB}	R_{SEIS}	PGV (cm/s)		R_{JB}	R_{SEIS}	PGV (cm/s)	
			CB-NGA	C97			CB-NGA	C97
1	—	—	—	—	1.0	3.2	44.234	34.677
3	—	—	—	—	3.0	4.2	37.721	32.437
5	0.0	5.0	6.525	9.075	5.0	5.8	30.750	29.409
10	8.7	10.0	3.558	3.708	10.0	10.4	20.013	22.427
15	14.1	15.0	2.323	2.122	15.0	15.3	14.796	16.960
30	29.6	30.0	1.067	0.829	30.0	30.1	8.524	8.457
50	49.7	50.0	0.592	0.420	50.0	50.1	5.616	4.435
100	99.9	100.0	0.264	0.164	100.0	100.0	3.174	1.654
200	199.9	200.0	0.118	0.058	200.0	200.0	1.791	0.515

Table 7.2 Example calculations for hanging wall of 45°-dipping reverse fault.

R_{RUP} (km)	**M** = 5.0				**M** = 7.0			
	R_{JB}	R_{SEIS}	PSA, 0.01s (*g*)		R_{JB}	R_{SEIS}	PSA, 0.01s (*g*)	
			CB-NGA	CB03			CB-NGA	CB03
1	—	—	—	—	0.0	3.4	0.7615	0.8191
3	—	—	—	—	0.0	3.2	0.6899	0.8216
5	0.0	5.0	0.2308	0.2834	0.0	5.0	0.5940	0.7892
10	7.0	10.0	0.1360	0.1444	0.0	10.0	0.4058	0.6187
15	13.2	15.0	0.0893	0.0951	6.2	15.0	0.2458	0.3079
30	29.1	30.0	0.0396	0.0459	26.0	30.0	0.1093	0.1586
50	49.5	50.0	0.0210	0.0267	47.7	50.0	0.0661	0.0938
100	99.7	100.0	0.0088	0.0128	98.9	100.0	0.0344	0.0453
200	199.9	200.0	0.0037	0.0061	199.4	200.0	0.0181	0.0217
R_{RUP} (km)	R_{JB}	R_{SEIS}	PSA, 0.2s (*g*)		R_{JB}	R_{SEIS}	PSA, 0.2s (*g*)	
			CB-NGA	CB03			CB-NGA	CB03
1	—	—	—	—	0.0	3.4	1.7023	1.4571
3	—	—	—	—	0.0	3.2	1.5940	1.4527
5	0.0	5.0	0.4785	0.6698	0.0	5.0	1.4271	1.4778
10	7.0	10.0	0.3076	0.3506	0.0	10.0	1.0236	1.3183
15	13.2	15.0	0.2062	0.2271	6.2	15.0	0.6190	0.6964
30	29.1	30.0	0.0894	0.1043	26.0	30.0	0.2644	0.3691
50	49.5	50.0	0.0456	0.0581	47.7	50.0	0.1528	0.2136
100	99.7	100.0	0.0179	0.0262	98.9	100.0	0.0742	0.0979
200	199.9	200.0	0.0069	0.0118	199.4	200.0	0.0363	0.0442
R_{RUP} (km)	R_{JB}	R_{SEIS}	PSA, 1.0s (*g*)		R_{JB}	R_{SEIS}	PSA, 1.0s (*g*)	
			CB-NGA	CB03			CB-NGA	CB03
1	—	—	—	—	0.0	3.4	0.6195	0.7032
3	—	—	—	—	0.0	3.2	0.5299	0.7093
5	0.0	5.0	0.0621	0.0569	0.0	5.0	0.4337	0.6492
10	7.0	10.0	0.0342	0.0292	0.0	10.0	0.2846	0.4756
15	13.2	15.0	0.0224	0.0198	6.2	15.0	0.1729	0.2594
30	29.1	30.0	0.0104	0.0101	26.0	30.0	0.0806	0.1389
50	49.5	50.0	0.0058	0.0062	47.7	50.0	0.0513	0.0858
100	99.7	100.0	0.0026	0.0032	98.9	100.0	0.0288	0.0441
200	199.9	200.0	0.0012	0.0016	199.4	200.0	0.0164	0.0227

Table 7.2—*Continued*

R_{RUP} (km)	**M** = 5.0				**M** = 7.0			
	R_{JB}	R_{SEIS}	PSA, 3.0s (*g*)		R_{JB}	R_{SEIS}	PSA, 3.0s (*g*)	
			CB-NGA	CB03			CB-NGA	CB03
1	—	—	—	—	0.0	3.4	0.1251	0.1669
3	—	—	—	—	0.0	3.2	0.1070	0.1701
5	0.0	5.0	0.00542	0.00509	0.0	5.0	0.0876	0.1428
10	7.0	10.0	0.00298	0.00261	0.0	10.0	0.0575	0.0916
15	13.2	15.0	0.00196	0.00177	6.2	15.0	0.0401	0.0593
30	29.1	30.0	0.00091	0.00091	26.0	30.0	0.0218	0.0313
50	49.5	50.0	0.00051	0.00055	47.7	50.0	0.0143	0.0193
100	99.7	100.0	0.00023	0.00028	98.9	100.0	0.0081	0.0099
200	199.9	200.0	0.00010	0.00015	199.4	200.0	0.0046	0.0051
R_{RUP} (km)	R_{JB}	R_{SEIS}	PGV (cm/s)		R_{JB}	R_{SEIS}	PGV (cm/s)	
			CB-NGA	C97			CB-NGA	C97
1	—	—	—	—	0.0	3.4	63.275	41.685
3	—	—	—	—	0.0	3.2	53.958	42.560
5	0.0	5.0	8.336	12.830	0.0	5.0	43.987	36.031
10	7.0	10.0	4.546	4.850	0.0	10.0	28.628	24.800
15	13.2	15.0	2.968	2.653	6.2	15.0	18.255	17.801
30	29.1	30.0	1.363	0.958	26.0	30.0	8.941	8.110
50	49.5	50.0	0.756	0.459	47.7	50.0	5.709	4.011
100	99.7	100.0	0.338	0.166	98.9	100.0	3.187	1.380
200	199.9	200.0	0.151	0.054	199.4	200.0	1.793	0.397

Table 7.3 Parameter values used for strike-slip faulting scenario given in Table 7.1.

CB-NGA		Campbell-Bozorgnia (2003)		Campbell (1997)	
Parameter	Value	Parameter	Value	Parameter	Value
F_{NM}	0.0	F_{RV}	0.0	F	0.0
F_{RV}	0.0	F_{TH}	0.0	S_{SR}	1.0
δ	90.0	δ	90.0	S_{HR}	0.0
Z_{TOR} ($\mathbf{M} = 7.0$)	0.0	S_{VFS}	0.0	S_{BC} (PSA at 1s)[1]	1.0
Z_{TOR} ($\mathbf{M} = 5.0$)	5.0	S_{SR}	0.5	D	1.0
V_{S30}	760.0	S_{FR}	0.5	Site location	—
$Z_{2.5}$	2.0	S_{BC}	1.0		
Site location	—	Site location	—		

[1] NEHRP BC adjustment factor for 1.0-second PSA from Campbell and Bozorgnia (2003a, 2003b, 2003c, 2004).

Table 7.4 Parameter values used for reverse-faulting scenario given in Table 7.2.

CB-NGA		Campbell-Bozorgnia (2003)		Campbell (1997)	
Parameter	Value	Parameter	Value	Parameter	Value
F_{NM}	0.0	F_{RV}	0.0	F	1.0
F_{RV}	1.0	F_{TH}	1.0	S_{SR}	1.0
δ	45.0	δ	45.0	S_{HR}	0.0
Z_{TOR} ($\mathbf{M} = 7.0$)	0.0	S_{VFS}	0.0	S_{BC} (PSA at 1s)[1]	1.0
Z_{TOR} ($\mathbf{M} = 5.0$)	5.0	S_{SR}	0.5	D	1.0
V_{S30}	760.0	S_{FR}	0.5	Site location	—
$Z_{2.5}$	2.0	S_{BC}	1.0		
Site location	HW	Site location	HW		

[1] NEHRP BC adjustment factor for 1.0-second PSA from Campbell and Bozorgnia (2003a, 2003b, 2003c, 2004).

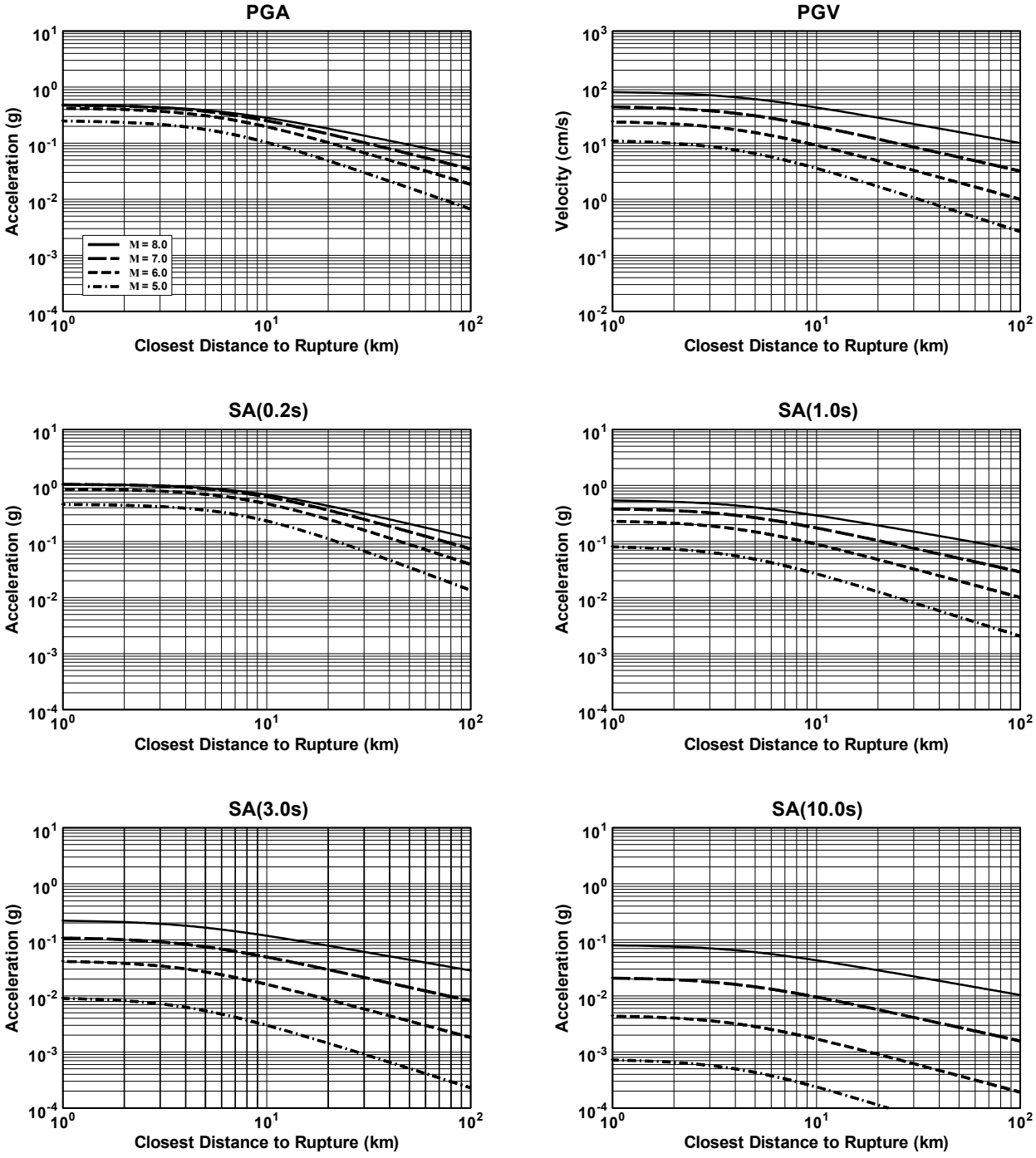

Fig. 7.1 Ground motion scaling with rupture distance.

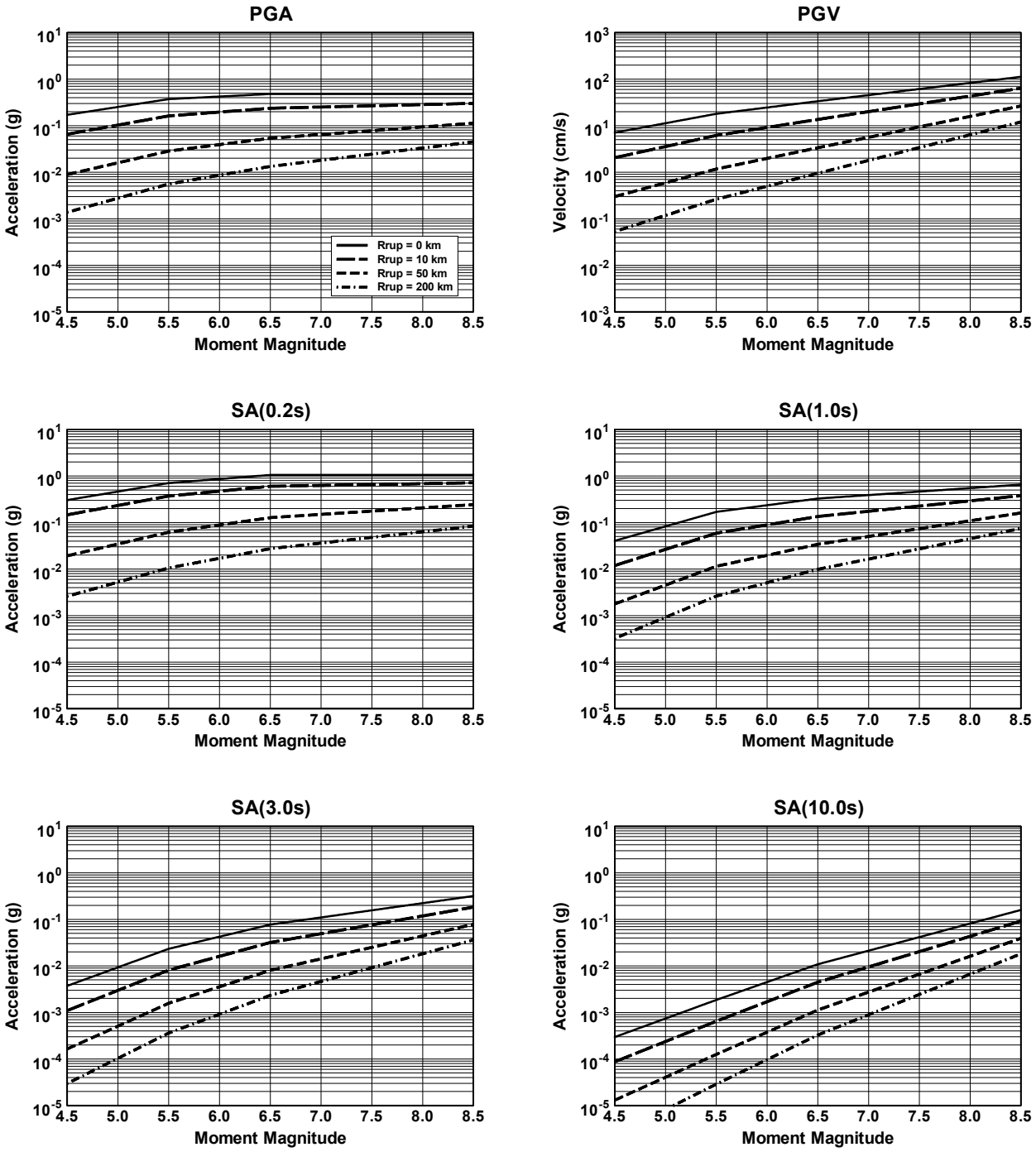

Fig. 7.2 Ground motion scaling with earthquake magnitude.

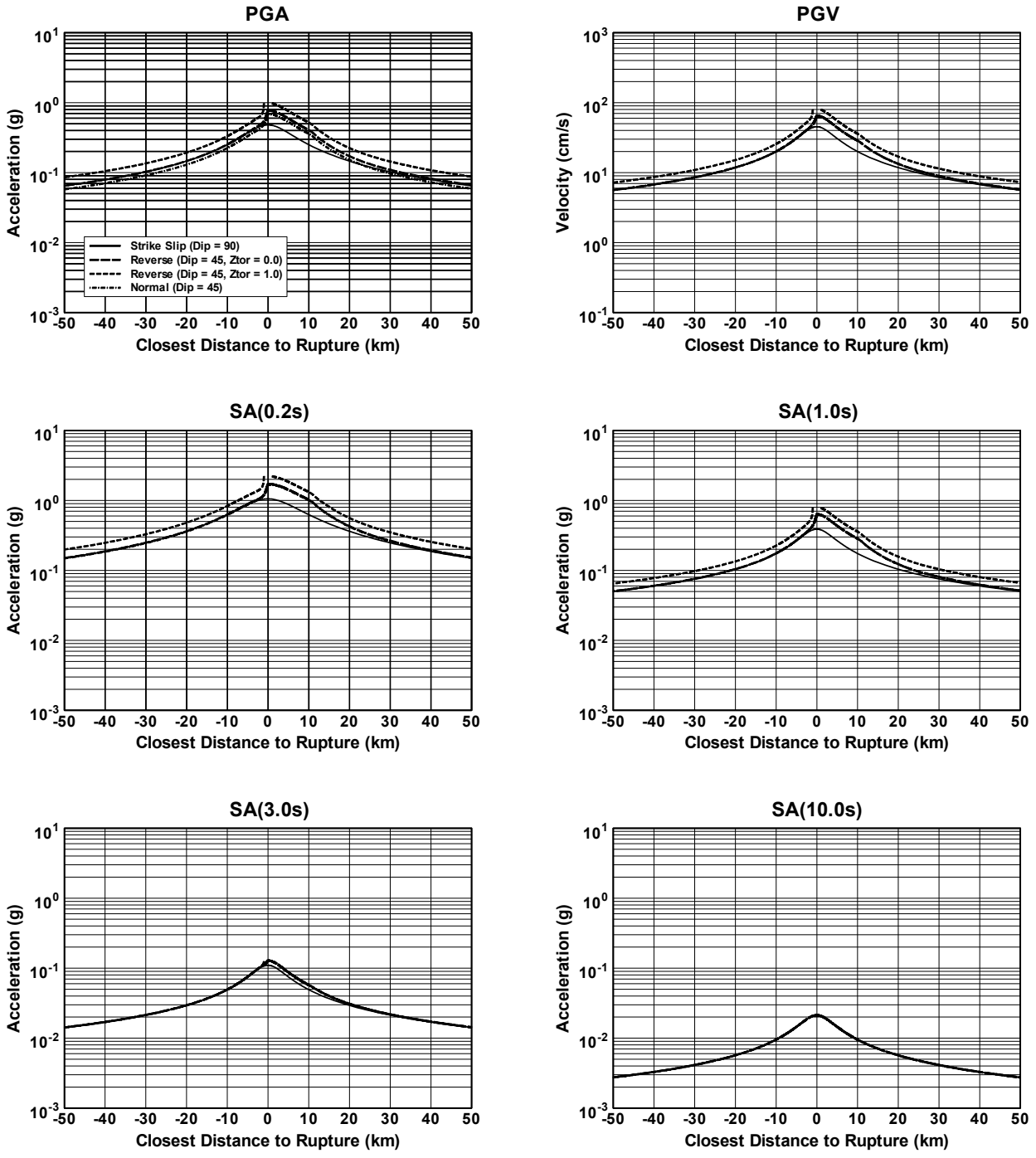

Fig. 7.3 Ground motion scaling with style of faulting and hanging-wall/footwall site locations for M = 7.0. Positive distances denote site locations on hanging-wall, and negative distances denote site locations on footwall.

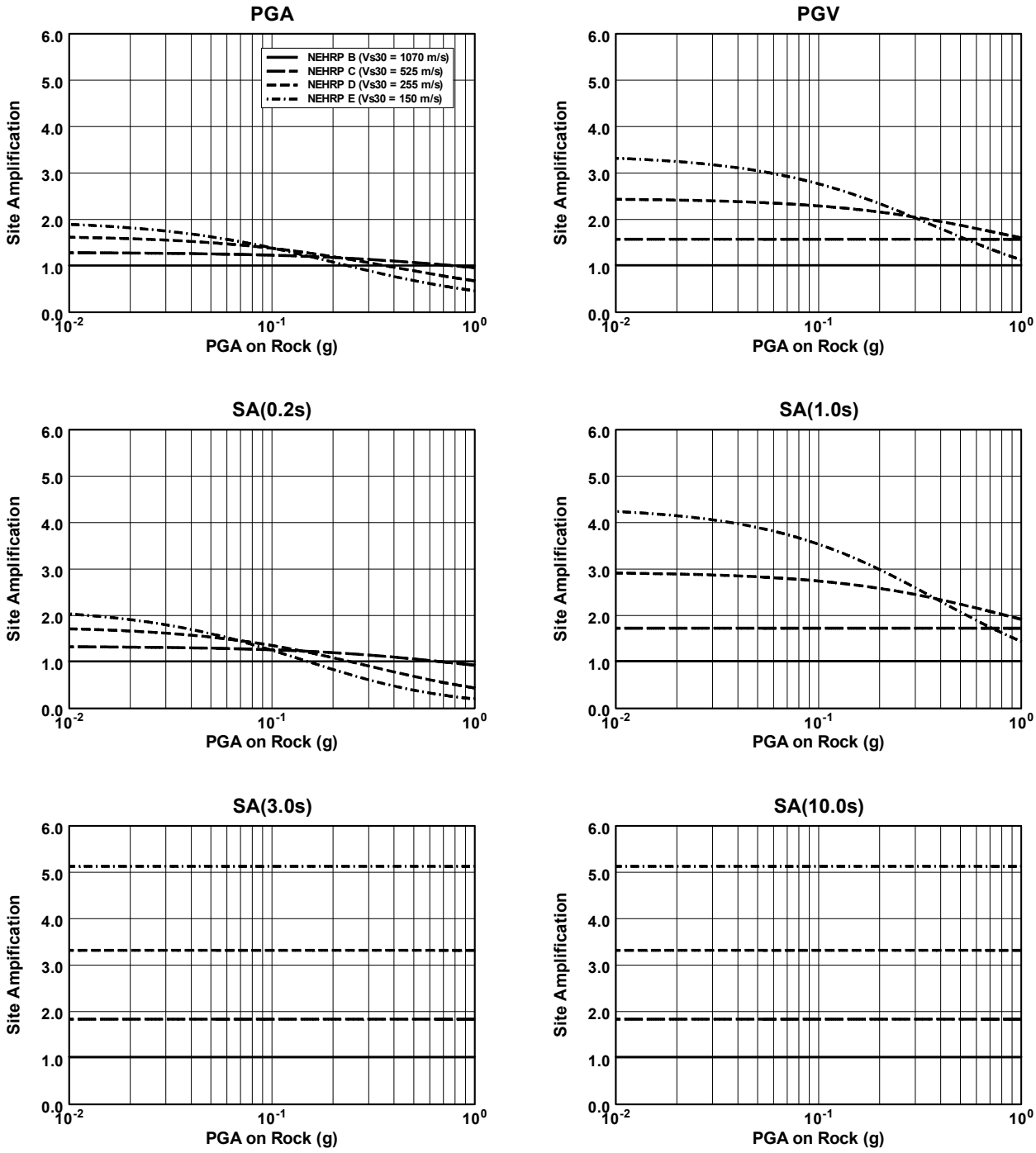

Fig. 7.4 Shallow site amplification scaling with rock PGA.

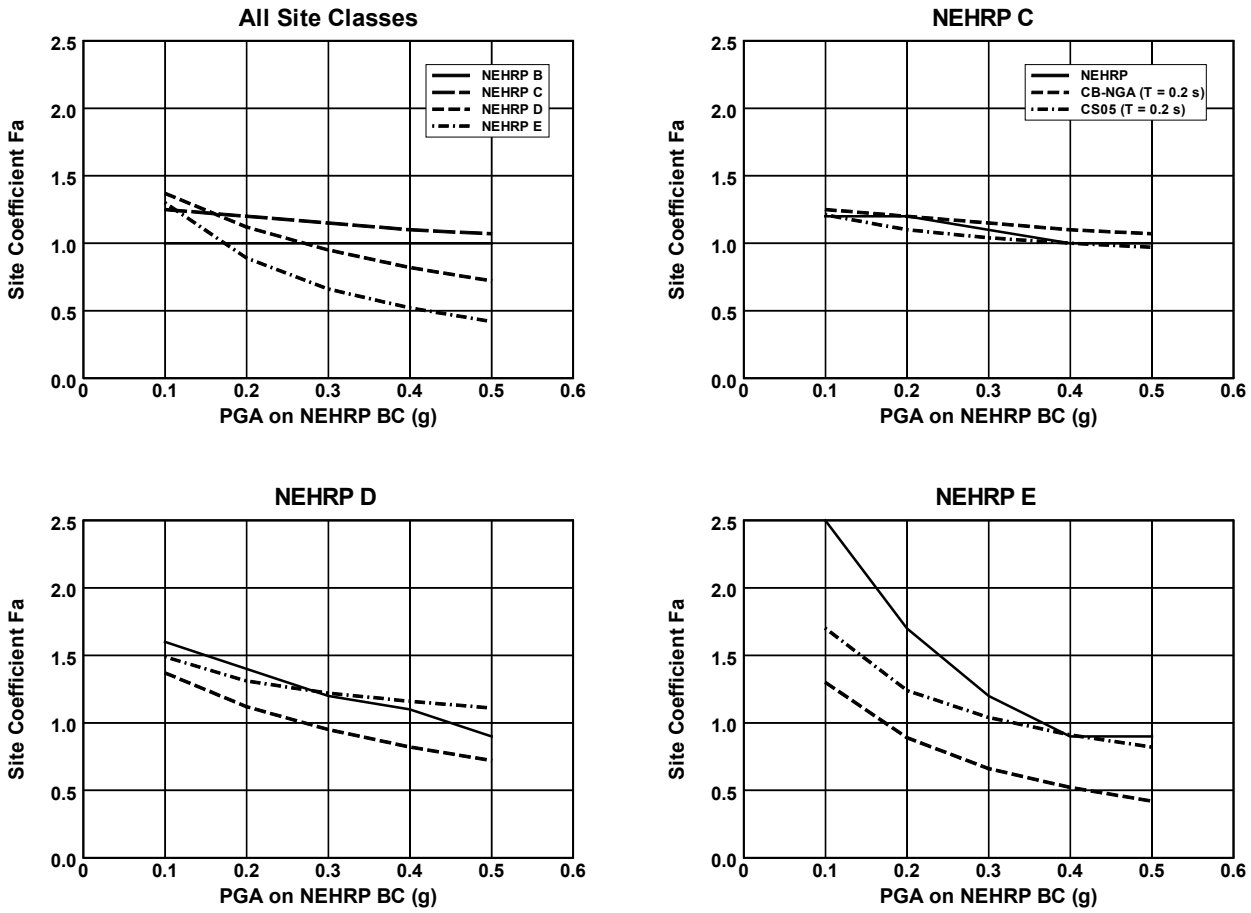

Fig. 7.5 NEHRP site coefficient F_a scaling with PGA on NEHRP BC site conditions.

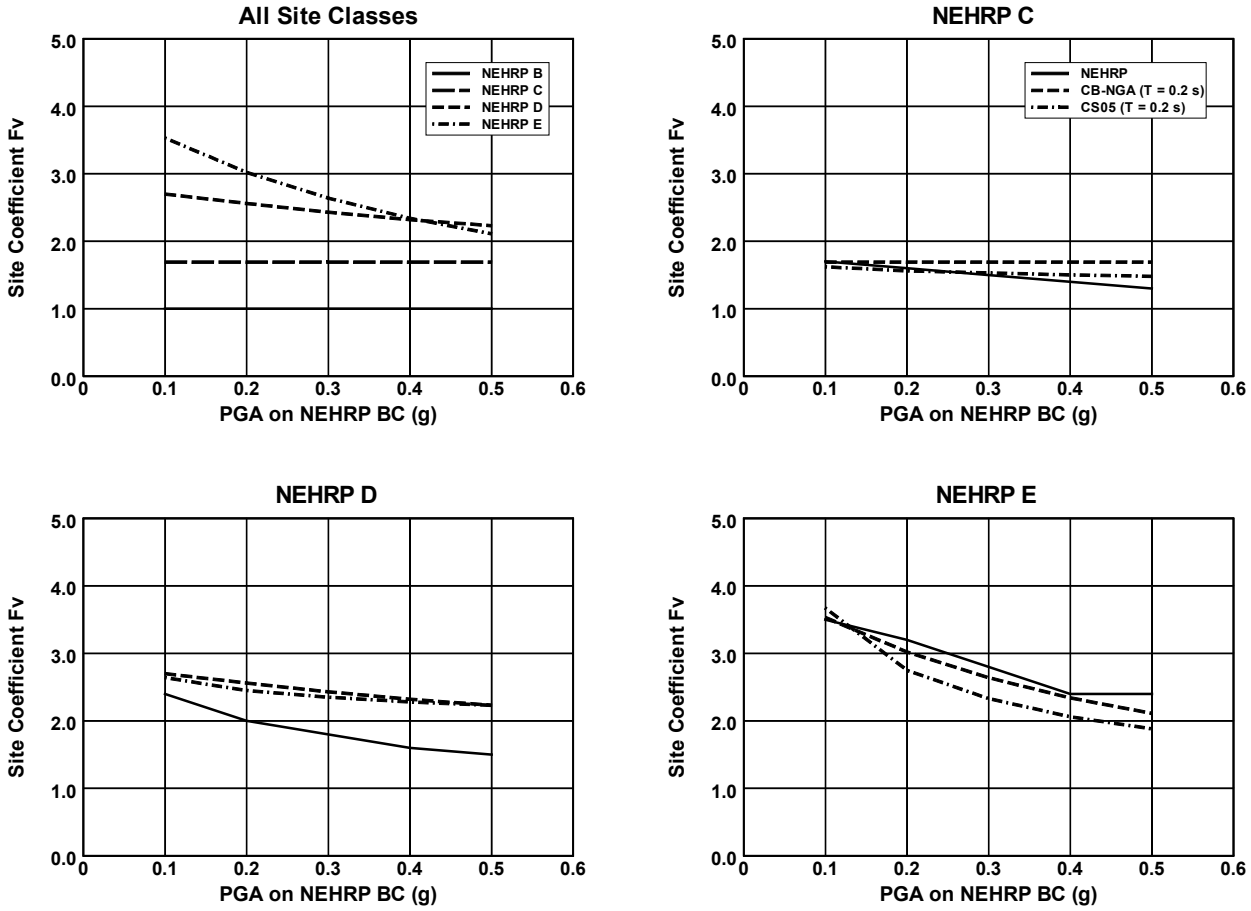

Fig. 7.6 NEHRP site coefficient F_v scaling with PGA on NEHRP BC site conditions.

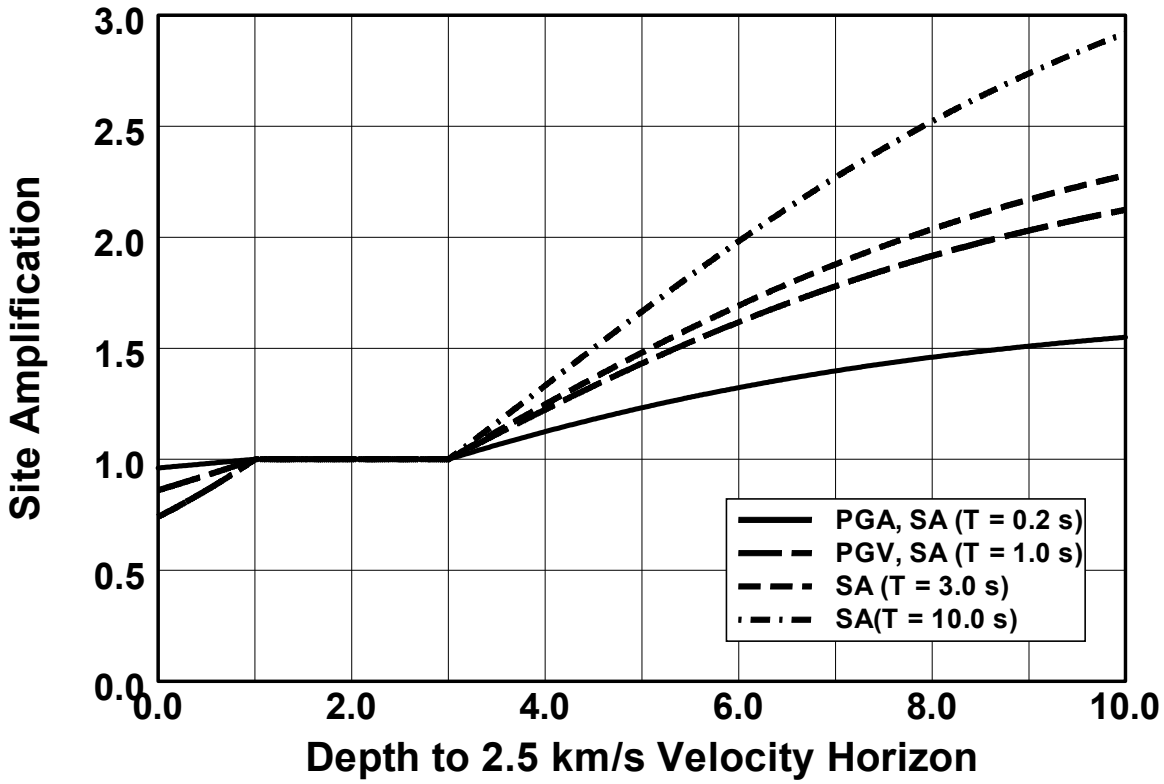

Fig. 7.7 Deep site amplification scaling with depth to 2.5 km velocity horizon.

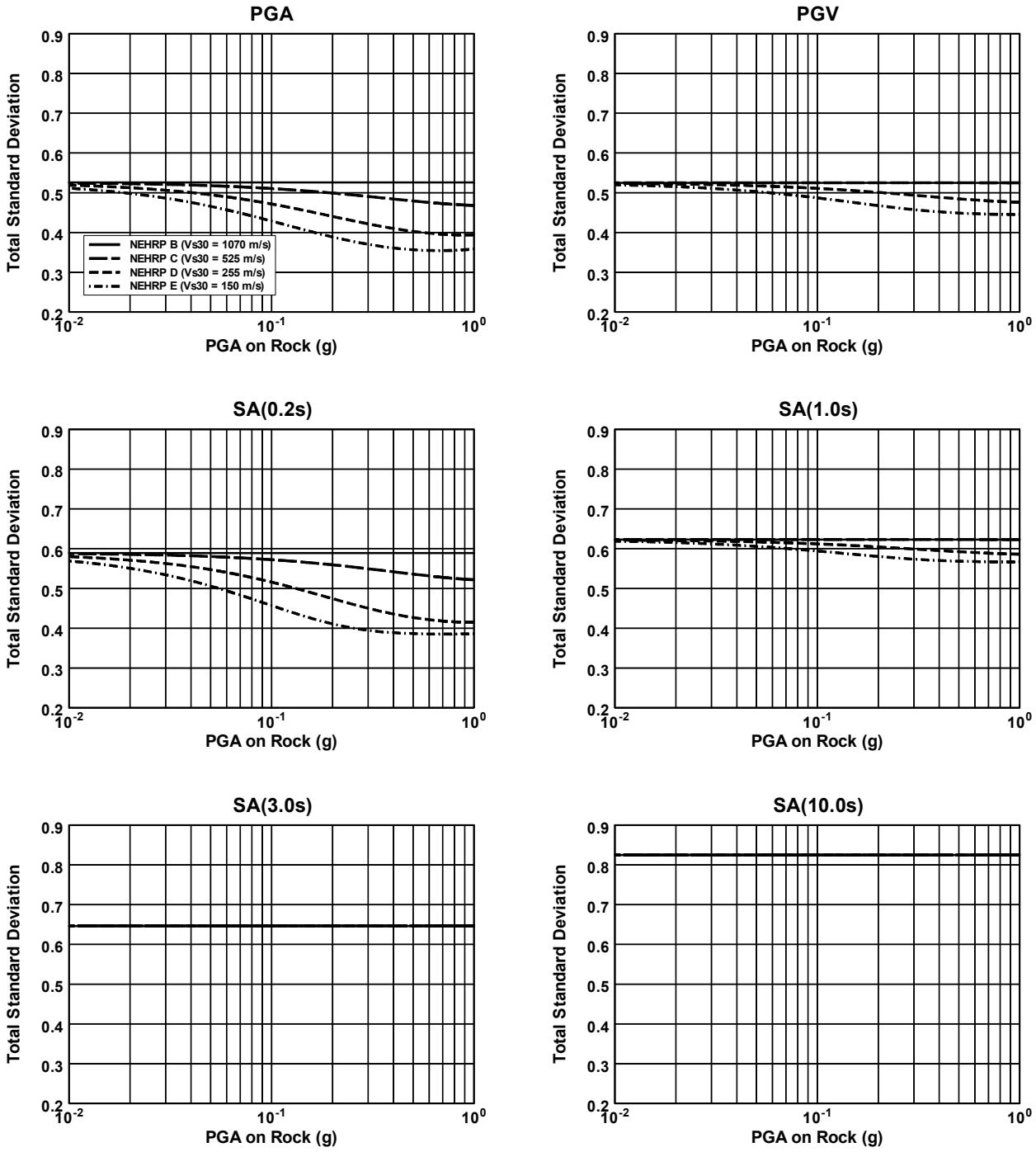

Fig. 7.8 Total standard deviation scaling with rock PGA.

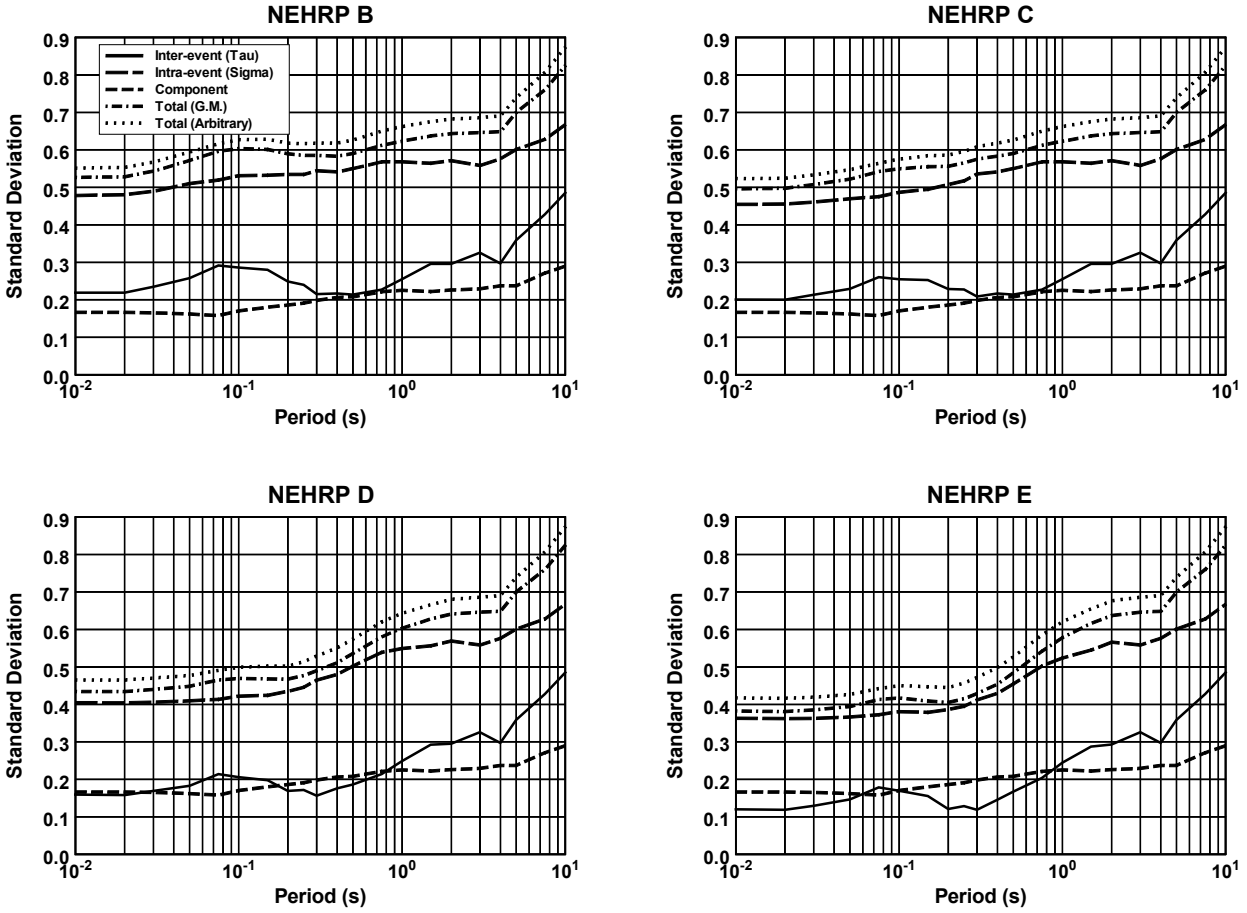

Fig. 7.9 Standard deviation scaling with oscillator period for $\mathbf{M = 7.0}$ and $R_{RUP} = 10$ km.

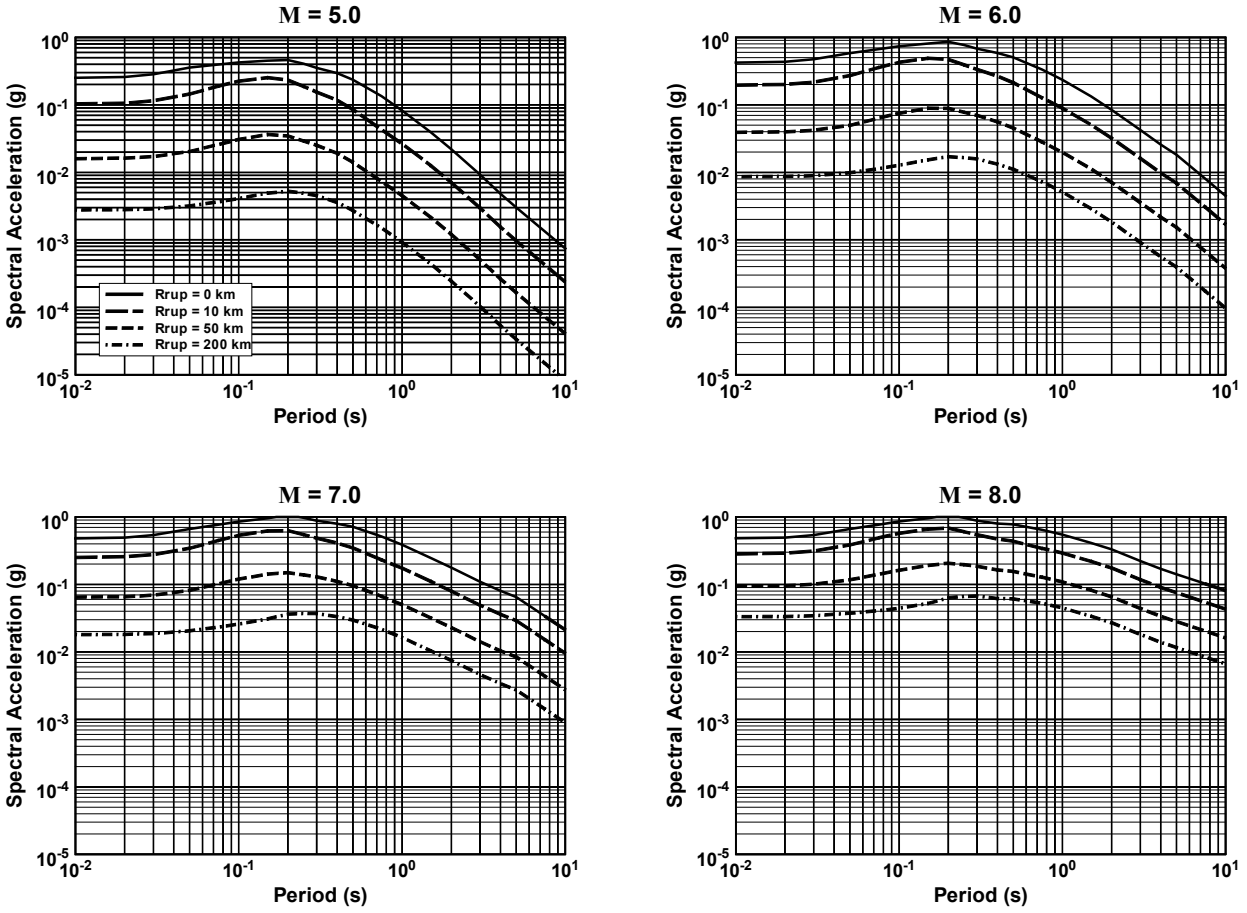

Fig. 7.10 Spectral acceleration scaling with rupture distance.

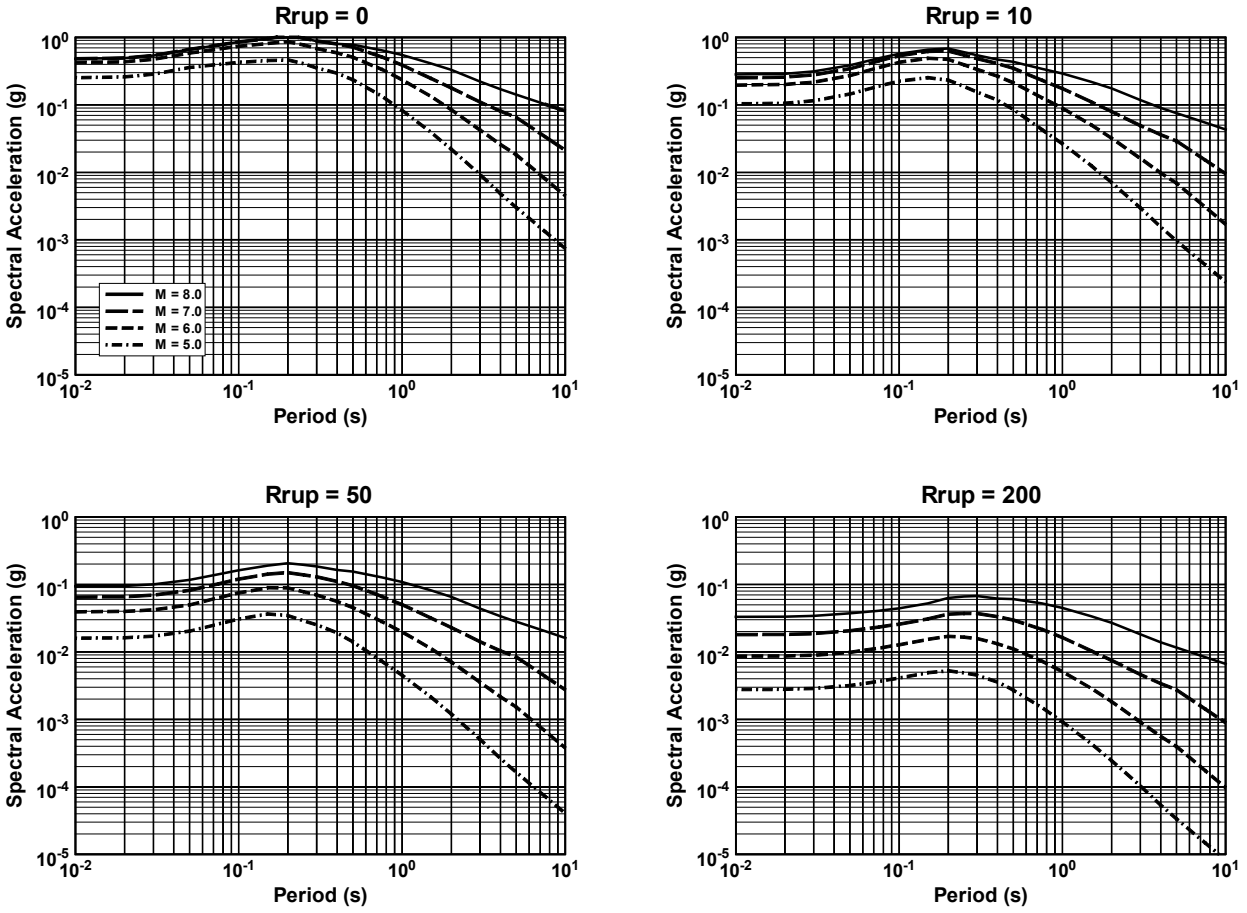

Fig. 7.11 Spectral acceleration scaling with earthquake magnitude.

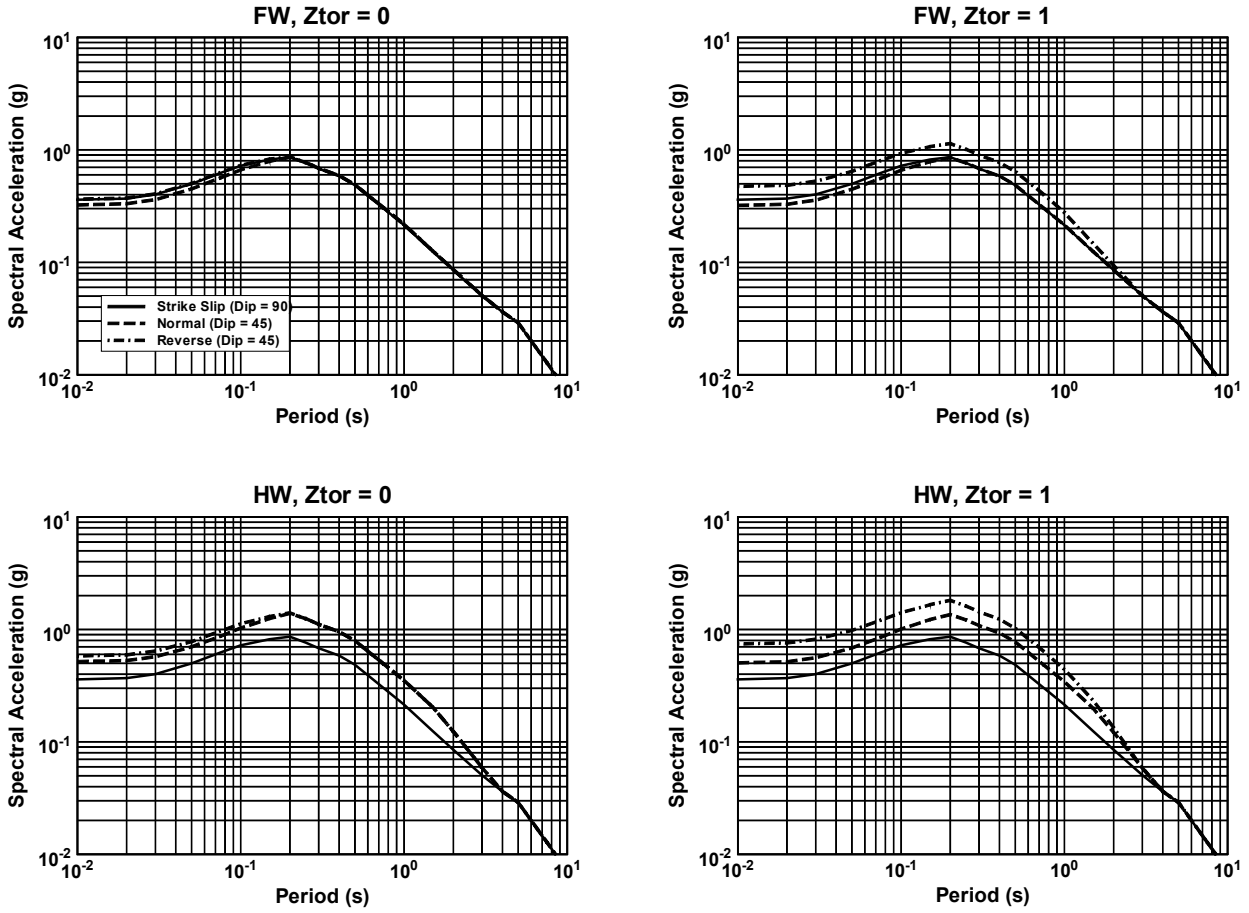

Fig. 7.12 Spectral acceleration scaling with style of faulting, hanging-wall/footwall site locations, and rupture depth for $M = 6.5$ and $R_{RUP} = 5$ km.

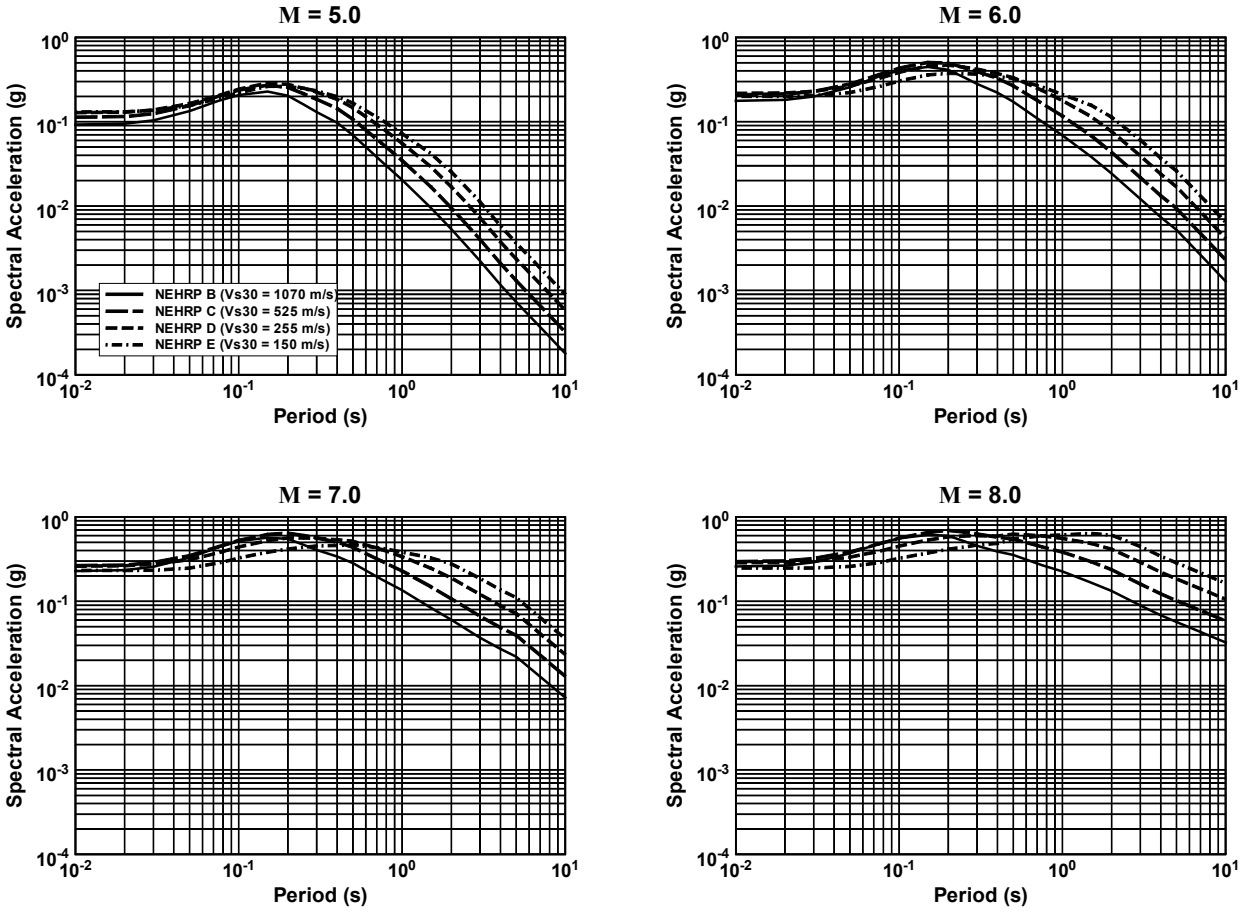

Fig. 7.13 Spectral acceleration scaling with shallow site conditions for $R_{RUP} = 10$ km.

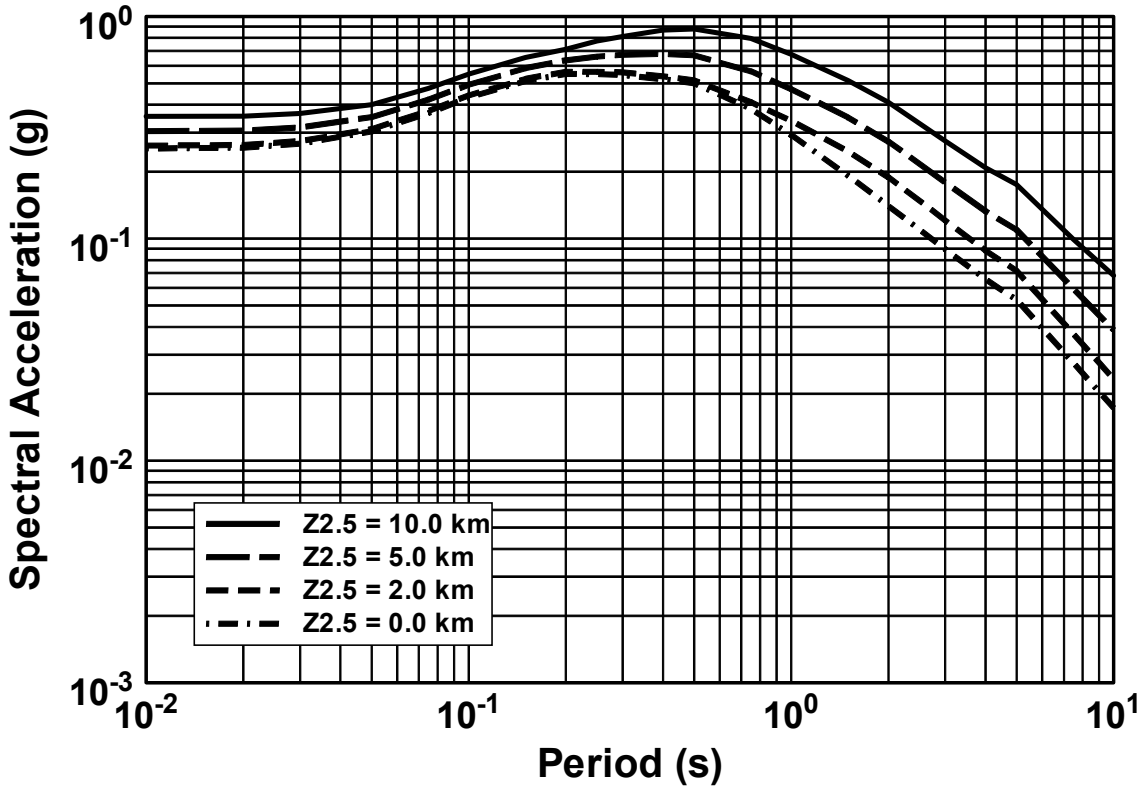

Fig. 7.14 Spectral acceleration scaling with sediment depth for $M = 7.0$, $R_{RUP} = 10$ km, and NEHRP D site conditions.

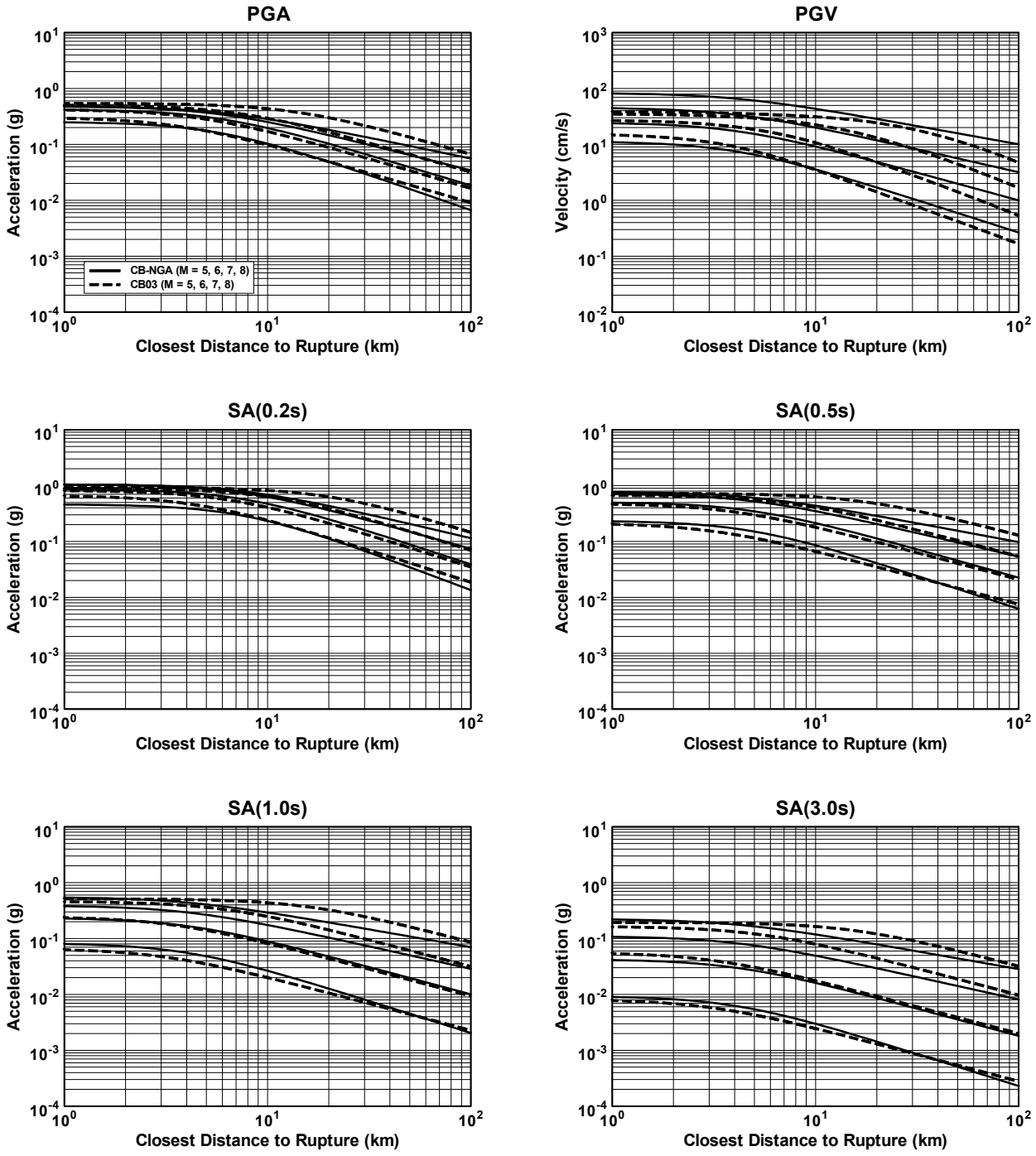

Fig. 7.15 Comparison of ground motion scaling with rupture distance between CB-NGA and CB03 and C97 (PGV) ground motion models for NEHRP BC site conditions.

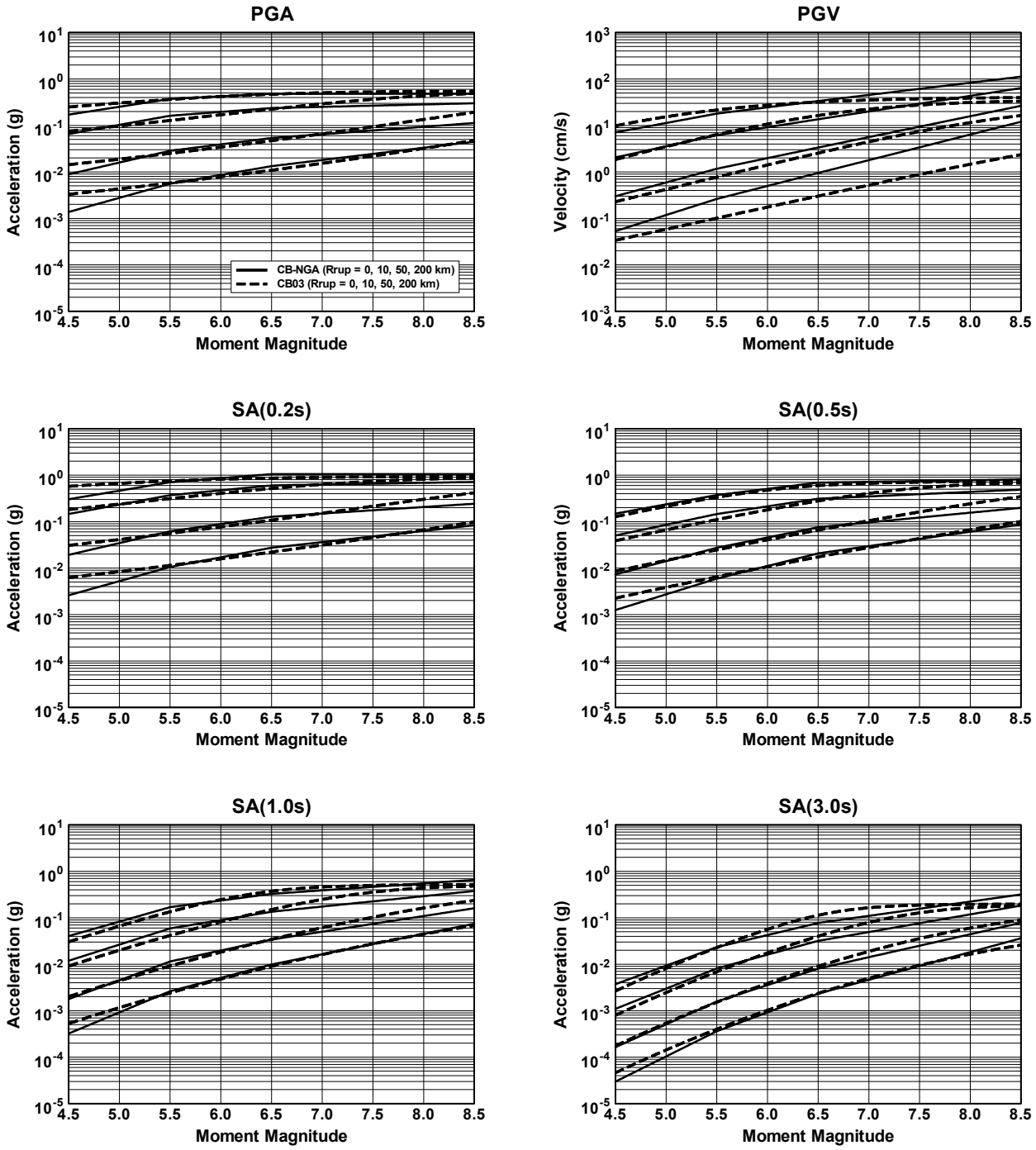

Fig. 7.16 Comparison of ground motion scaling with earthquake magnitude between CB-NGA and CB03 and C97 (PGV) ground motion models for NEHRP BC site conditions.

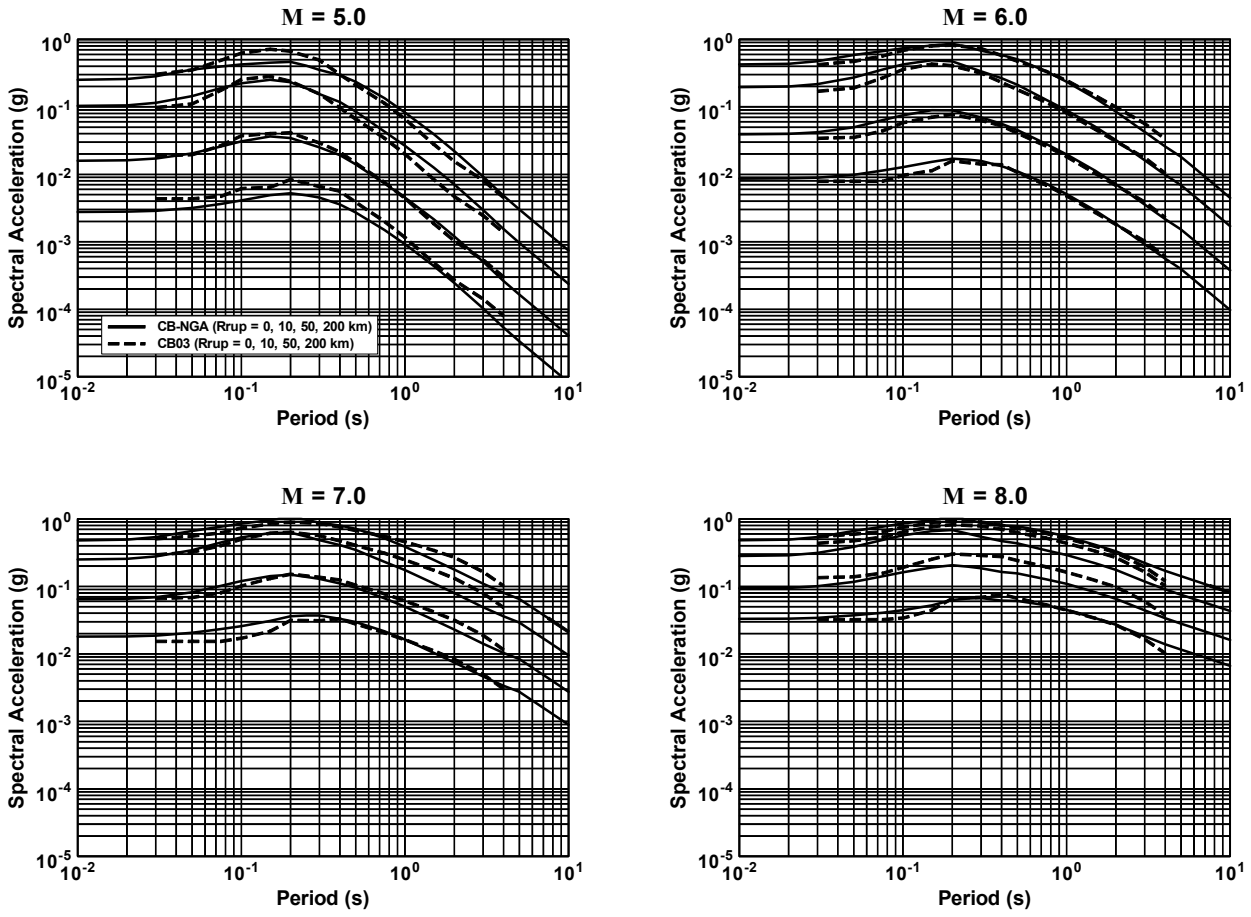

Fig. 7.17 Comparison of spectral acceleration scaling with rupture distance between CB-NGA and CB03 ground motion models for NEHRP BC site conditions.

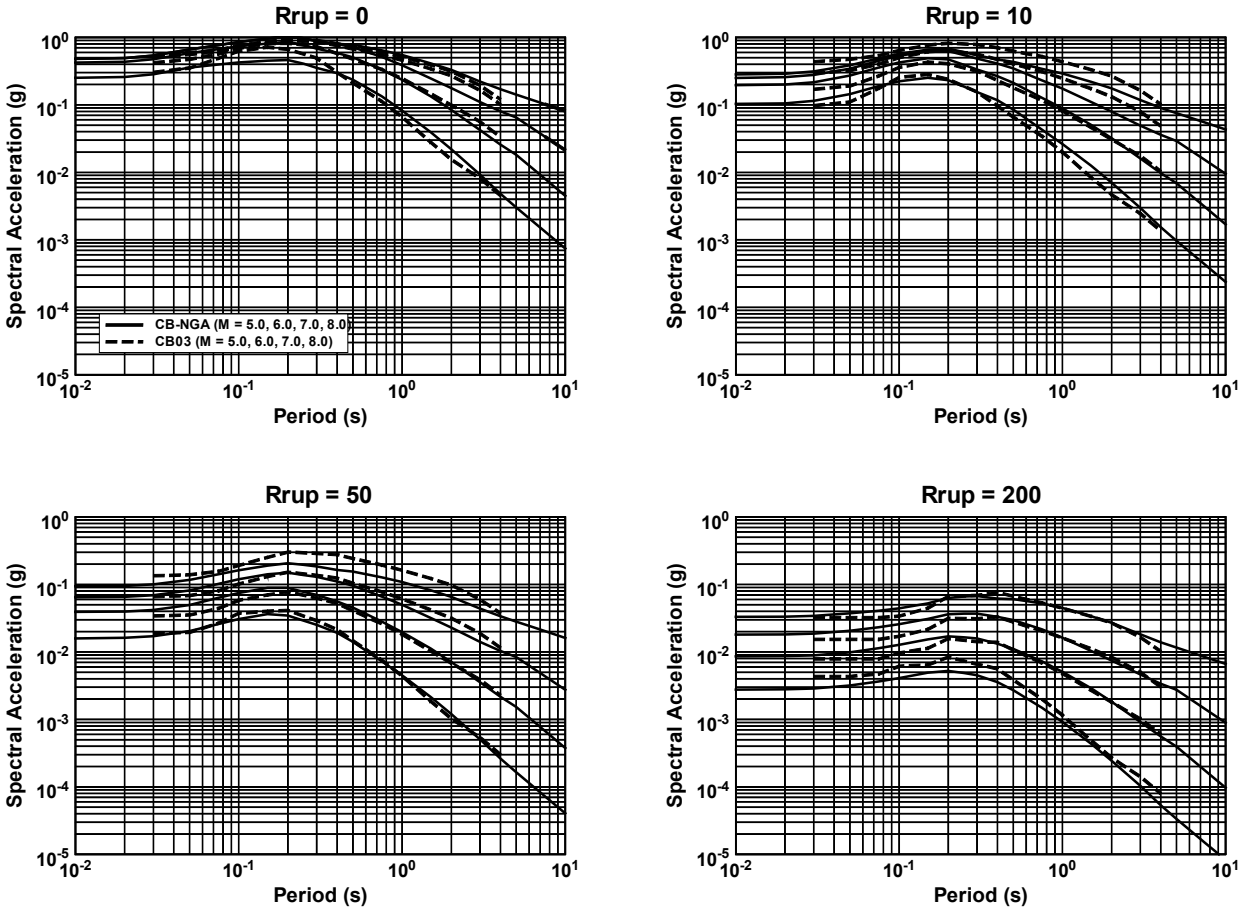

Fig. 7.18 Comparison of spectral acceleration scaling with earthquake magnitude between CB-NGA and CB03 ground motion models for NEHRP BC site conditions.

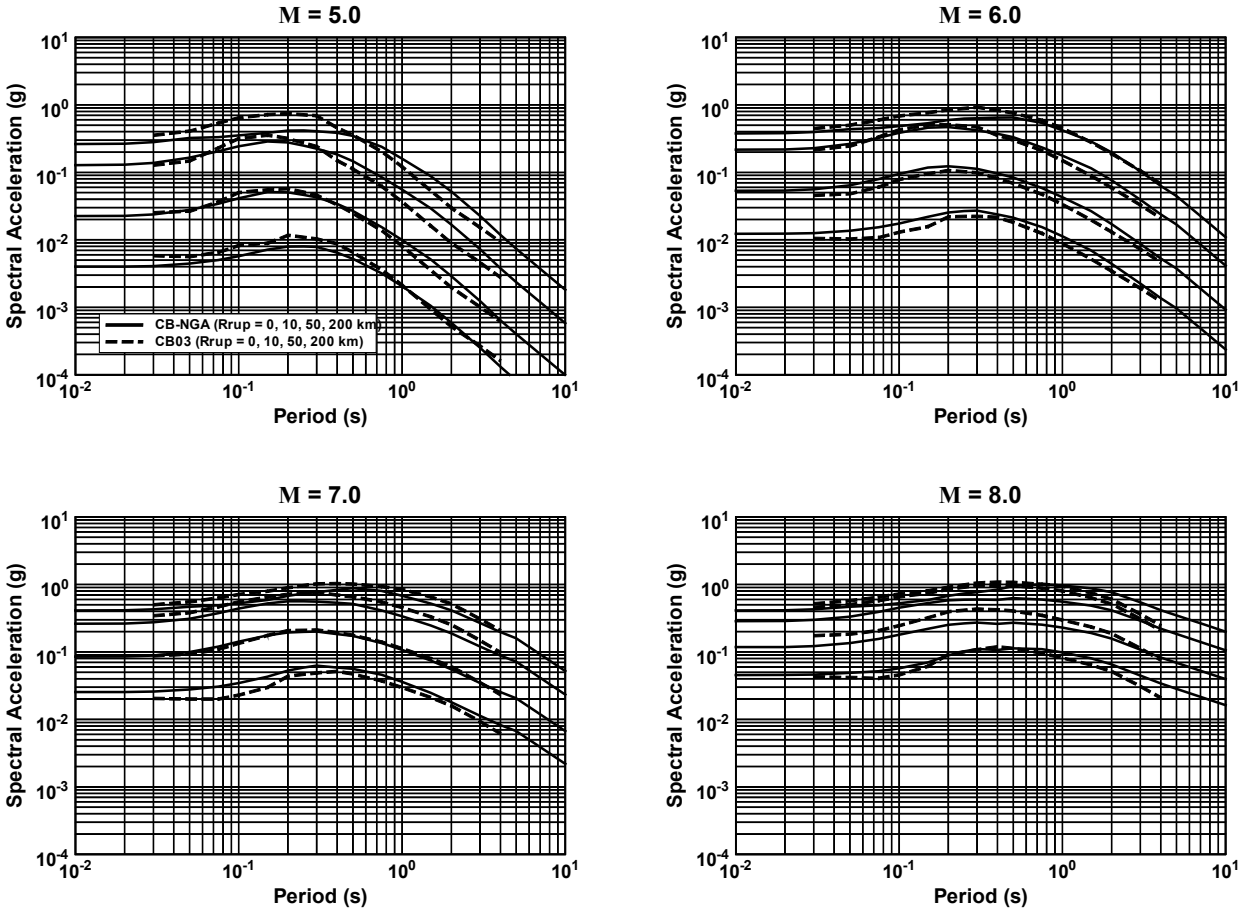

Fig. 7.19 Comparison of spectral acceleration scaling with rupture distance between CB-NGA and CB03 ground motion models for NEHRP D site conditions.

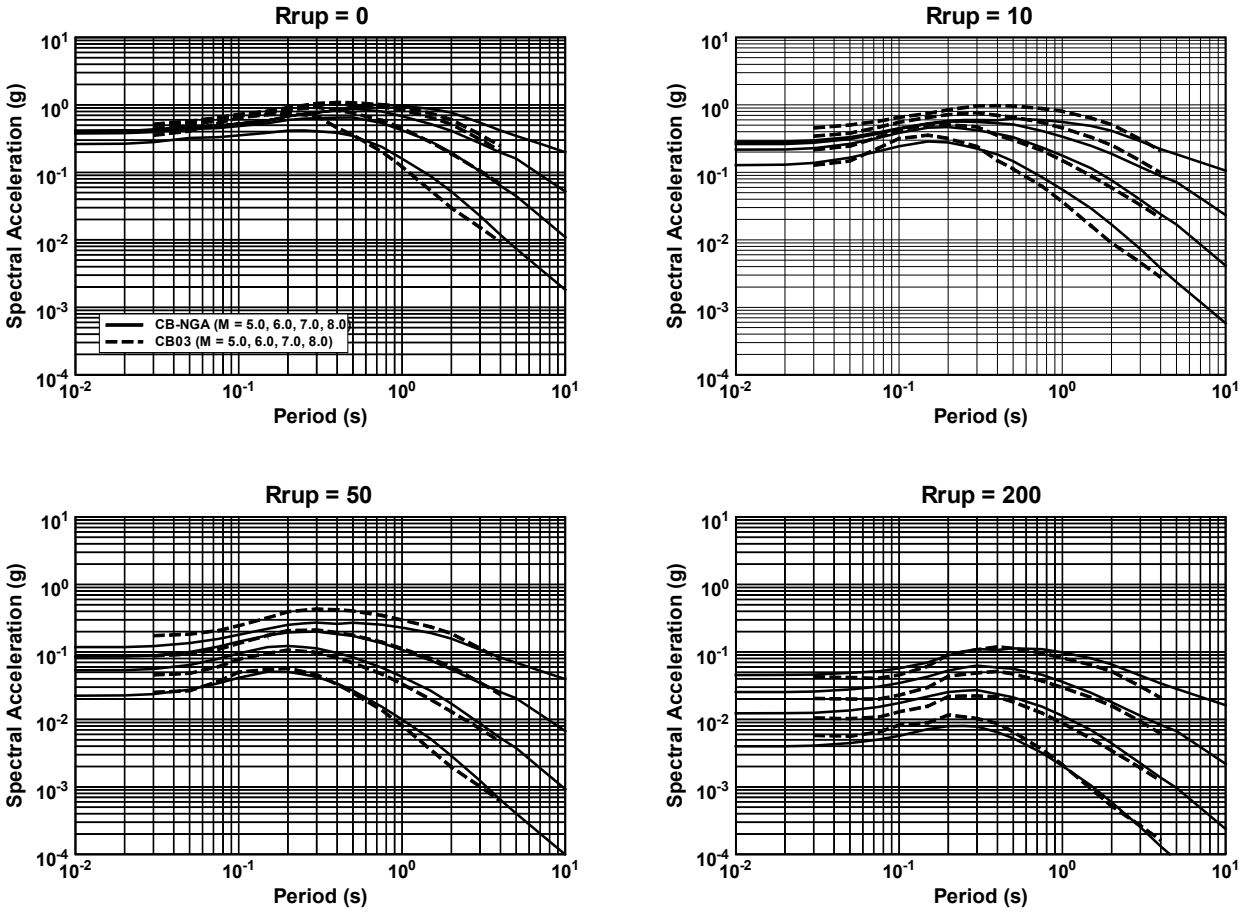

Fig. 7.20 Comparison of spectral acceleration scaling with earthquake magnitude between CB-NGA and CB03 ground motion models for NEHRP D site conditions.

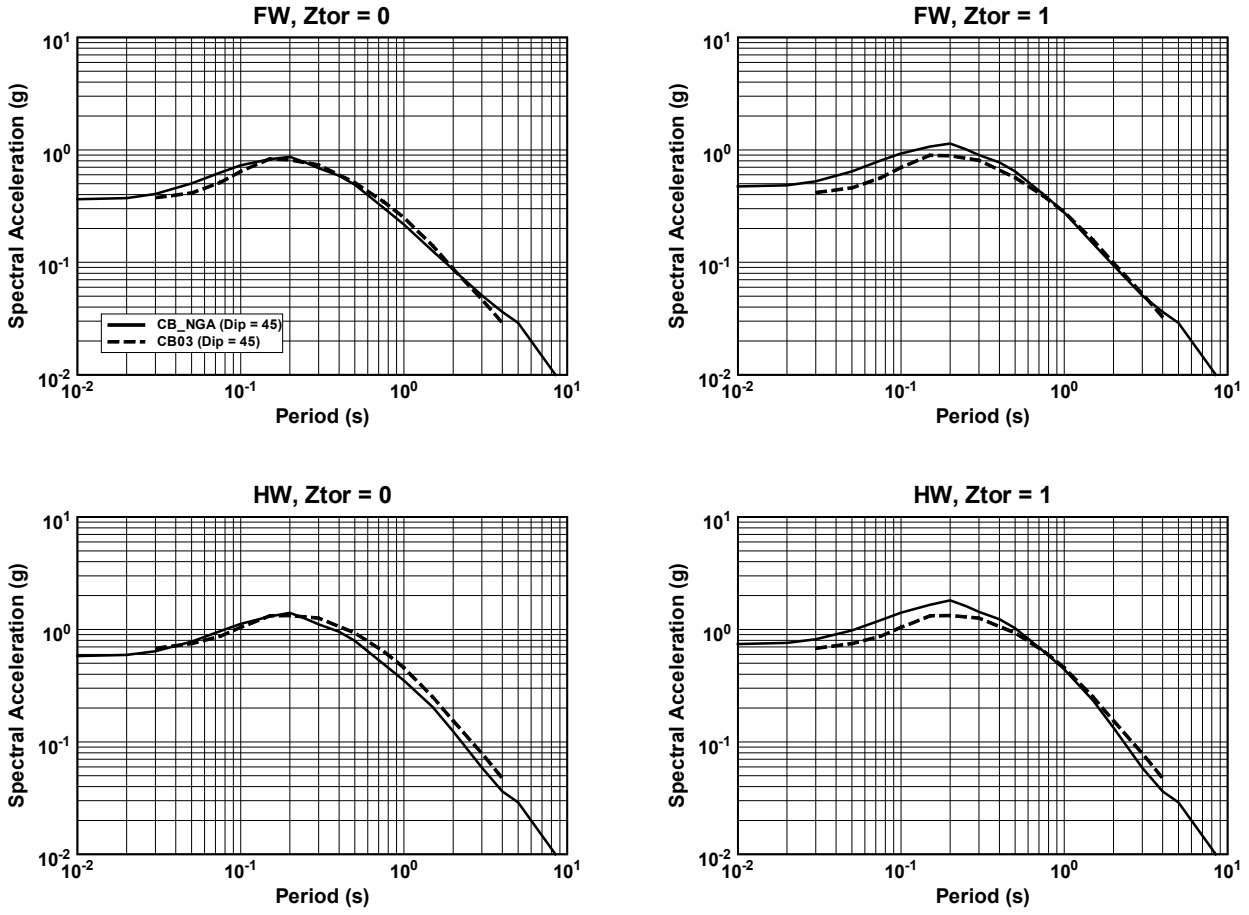

Fig. 7.21 Comparison of spectral acceleration scaling with style of faulting, hanging-wall/footwall site locations, and rupture depth between CB-NGA and CB03 ground motion models for reverse faults, $M = 6.5$, $R_{RUP} = 5$ km, and $\delta = 45°$.

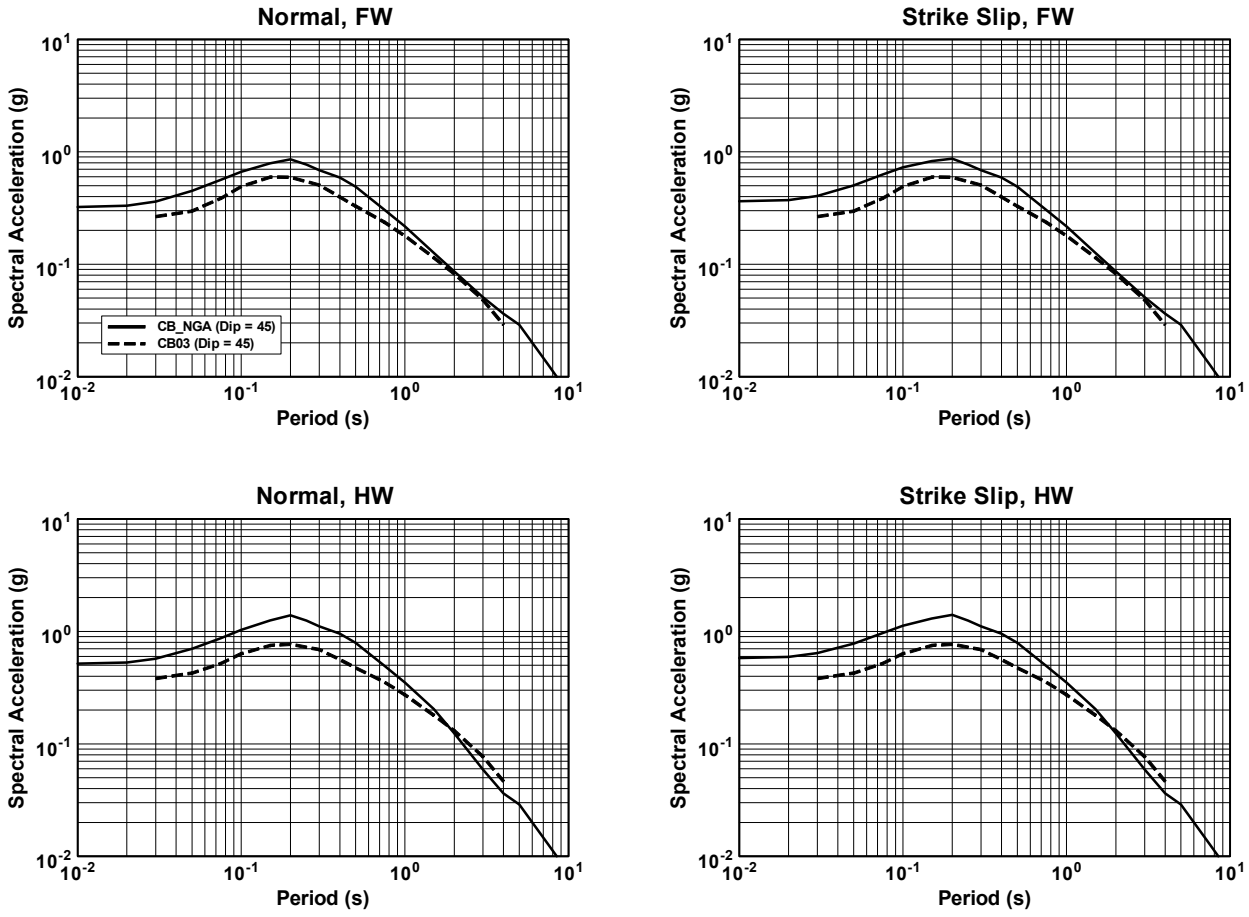

Fig. 7.22 Comparison of spectral acceleration scaling with style of faulting and hanging-wall/footwall site locations between CB-NGA and CB03 ground motion models for normal and strike-slip faults, $M = 6.5$, $R_{RUP} = 5$ km, and $\delta = 45°$.

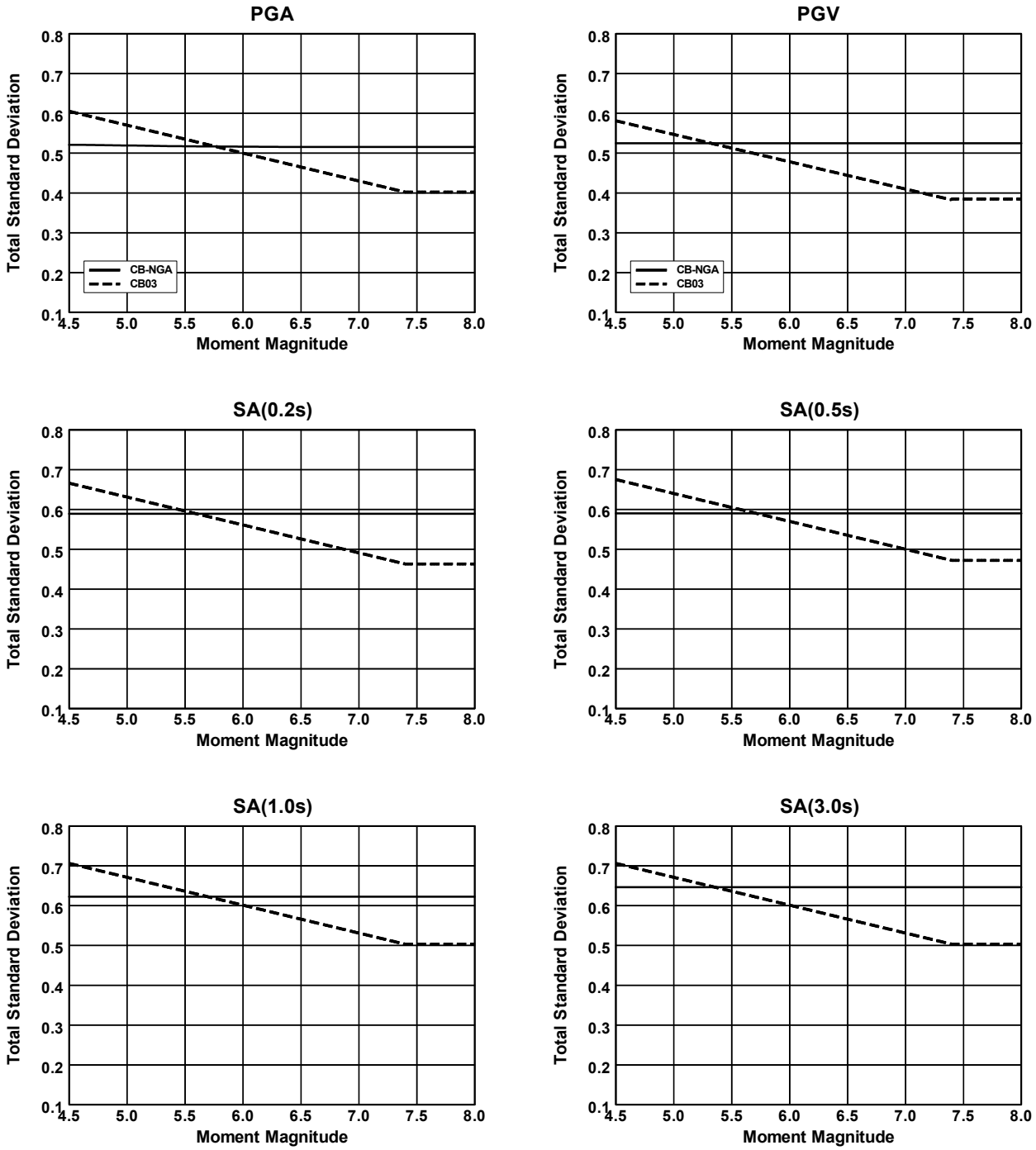

Fig. 7.23 Comparison of total standard deviations between CB-NGA and CB03 and C97 (PGV) ground motion models for NEHRP BC site conditions and $R_{RUP} = 0$.

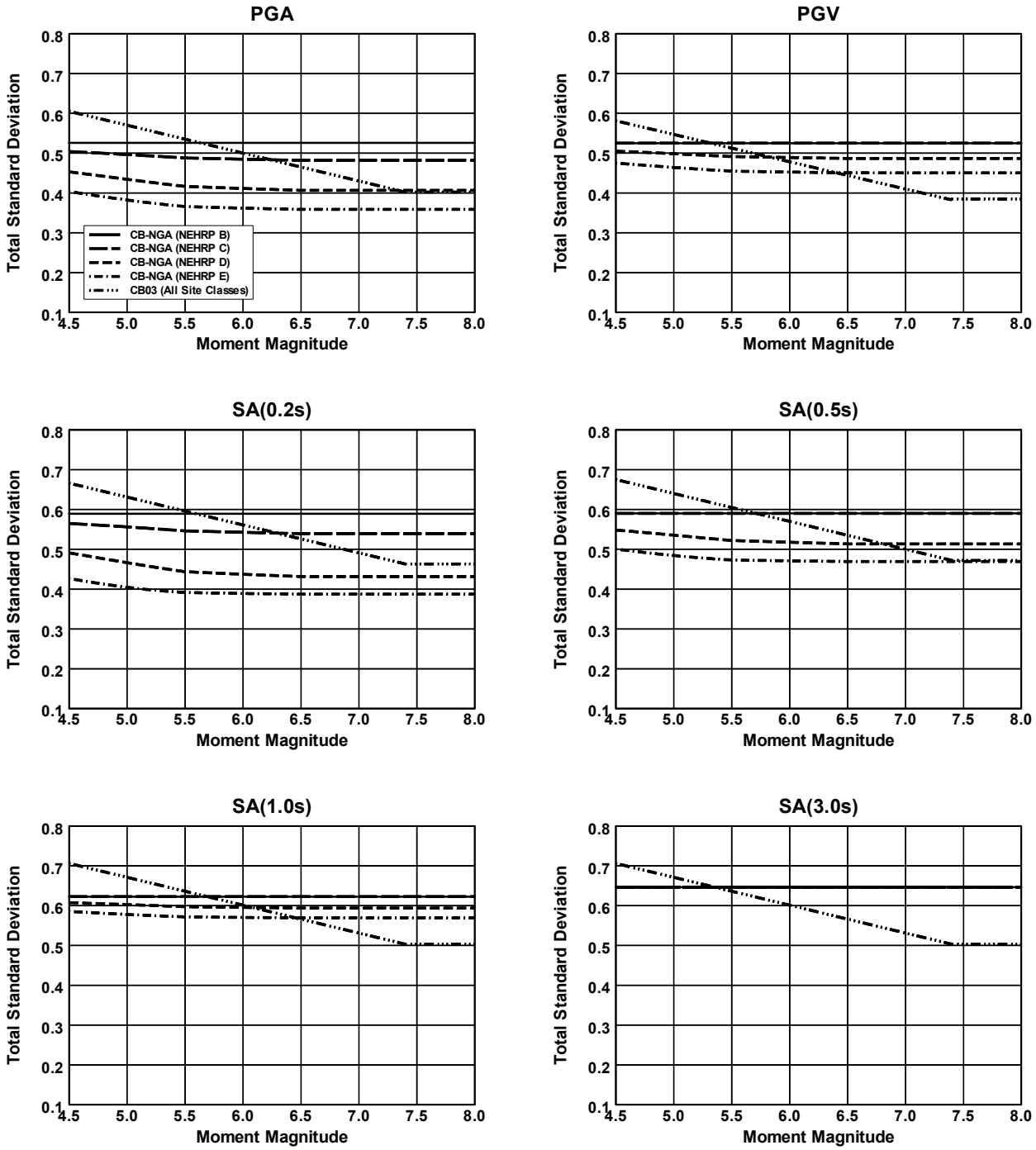

Fig. 7.24 Comparison of total standard deviations between CB-NGA and CB03 and C97 (PGV) ground motion models for NEHRP B, C, D, and E site conditions and $R_{RUP} = 0$.

REFERENCES

Abrahamson, N. A., and W. J. Silva (2007). *Abrahamson-Silva NGA ground motion relations for the geometric mean horizontal component of peak and spectral ground motion parameters.* PEER Report 2007/03 (forthcoming). Berkeley, Calif.: Pacific Earthquake Engineering Research Center, University of California.

Abrahamson, N. A., W. J. Silva. (1997). Empirical response spectral attenuation relations for shallow crustal earthquakes. *Seism. Res. Lett.* 68**:** 94–127.

Abrahamson, N. A., and R. R. Youngs. (1992). A stable algorithm for regression analyses using the random effects model. *Bull. Seism. Soc. Am.* 82**:** 505–10.

Atkinson, G. M., and W. Silva. (2000). Stochastic modeling of California ground motions. *Bull. Seism. Soc. Am.* 90: 255–74.

Atkinson, G. M., and W. Silva. (1997). An empirical study of earthquake source spectra for California earthquakes. *Bull. Seism. Soc. Am.* 87**:** 97–113.

Baker, J. W., and C. A. Cornell. (2006). Which spectral acceleration are you using? *Earthquake Spectra* 22**:** 293–312.

Beyer, K., and J. J. Bommer. (2006). Relationships between median values and between aleatory variabilities for different definitions of the horizontal component of motion. *Bull. Seism. Soc. Am.* 96**:** 1512–22.

Bommer, J., F. Scherbaum, H. Bungum, F. Cotton., F. Sabetta., and N. Abrahamson. (2005). On the use of logic trees for ground-motion prediction equations in seismic-hazard analysis. *Bull. Seism. Soc. Am.* 95**:** 377–89.

Boore, D. M., and G. M. Atkinson. (2007). *Boore-Atkinson NGA ground motion relations for the geometric mean horizontal component of peak and spectral ground motion parameters.* PEER Report 2007/01. Berkeley, Calif.: Pacific Earthquake Engineering Research Center, University of California.

Boore, D. M. (2005). Erratum: Equations for estimating horizontal response spectra and peak acceleration from western North American earthquakes: a summary of recent work. *Seism. Res. Lett.* 76**:** 368–69.

Boore, D. M. (2003). Prediction of ground motion using the stochastic method. *Pure Appl. Geophys.* 160**:** 635–76.

Boore, D. M., J. B. Joyner, and T. E. Fumal (1997). Equations for estimating horizontal response spectra and peak acceleration from western North American earthquakes: a summary of recent work. *Seism. Res. Lett.* 68**:** 128–53.

Boore, D. M., W. B. Joyner., and T. E. Fumal. (1994). *Estimation of response spectra and peak accelerations from western North American earthquakes*: *an interim report, part 2.* U.S. Geological Survey., Open-File Report 94-127.

Boore, D. M., W. B. Joyner., and T. E. Fumal. (1993). *Estimation of response spectra and peak accelerations from western North American earthquakes: an interim report.* U.S. Geological Survey Open-File Report. 93-509.

Boore, D. M., J. Watson-Lamprey, and N. Abrahamson. (2006). Orientation-independent measures of ground motion. *Bull. Seism. Soc. Am.* 96**:** 1502–11.

Borcherdt, R. D. (1994). Estimates of site-dependent response spectra for design (methodology and justification). *Earthquake Spectra* 10**:** 617–53.

Bouchon, M., D. Hatzfeld, J. A. Jackson., and E. Haghsenas. (2006). Some insight on why Bam (Iran) was destroyed by an earthquake of relatively moderate size. *Geophys. Res. Letts.* 33**:** Paper L09309, doi:10.1029/2006GL025906.

Bozorgnia, Y., and K. W. Campbell. (2004). Engineering characterization of ground motion. In *Earthquake Engineering: From Engineering Seismology to Performance-Based Engineering.* Bozorgnia, Y., and V. V. Bertero (eds.), 5-1–5-74. Boca Raton, Florida: CRC Press.

Bozorgnia, Y., M. M. Hachem, and K. W. Campbell. (2006). Attenuation of inelastic and damage spectra. In *Proceedings, Eighth National Conference on Earthquake Engineering.* Proceedings CD-ROM, Paper No. 1127. Oakland, Calif.: Earthquake Engineering Research Institute.

Brune, J. (1971). Correction: Tectonic stress and the spectra of seismic shear waves. *J. Geophys. Res.* 76**:** 5002.

Brune, J. (1970). Tectonic stress and the spectra of seismic shear waves. *J. Geophys. Res.* 75, 4997–5009.

BSSC (2004). *NEHRP (National Earthquake Hazard Reduction Program) recommended provisions for new buildings and other structures (FEMA 450), 2003 Edition*. Report prepared for the Federal Emergency Management Agency (FEMA). Washington, D.C.: Building Seismic Safety Council, National Institute of Building Sciences.

Budnitz, R. J., G. Apostolakis., D. M. Boore, L. S. Cluff, K. J. Coppersmith., C. A. Cornell, and P. A. Morris. (1997). *Recommendations for probabilistic seismic hazard analysis: guidance on uncertainty and use of experts.* Report prepared for the U.S. Nuclear Regulatory Commission, the U.S. Department of Energy, and the Electric Power Research Institute by the Senior Seismic Hazard Analysis Committee (SSHAC). Report NUREG/CR-6372. Washington, D.C.: U.S. Nuclear Regulatory Commission.

Campbell, K. W. (2004). Engineering models of strong ground motion. In *Earthquake Engineering Handbook,* Chen, W.F., and C. Scawthorn (eds.), 5-1–5-76. Boca Raton, Florida: CRC Press.

Campbell, K. W. (2003). Prediction of strong ground motion using the hybrid empirical method and its use in the development of ground-motion (attenuation) relations in eastern North America. *Bull. Seism. Soc. Am.* 93**:** 1012–33.

Campbell, K. W. (2001). Erratum: Empirical near-source attenuation relationships for horizontal and vertical components of peak ground acceleration, peak ground velocity, and pseudo-absolute acceleration response spectra. *Seism. Res. Lett.* 72**:** 474.

Campbell, K. W. (2000). Erratum: Empirical near-source attenuation relationships for horizontal and vertical components of peak ground acceleration, peak ground velocity, and pseudo-absolute acceleration response spectra. *Seism. Res. Lett.* 71**:** 352–54.

Campbell, K. W. (1997). Empirical near-source attenuation relationships for horizontal and vertical components of peak ground acceleration, peak ground velocity, and pseudo-absolute acceleration response spectra. *Seism. Res. Lett.* 68**:** 154–79.

Campbell, K. W. (1981). Near-source attenuation of peak horizontal acceleration. *Bull. Seism. Soc. Am.* 71**:** 2039–70.

Campbell, K. W., and Y. Bozorgnia. (2004). Erratum: Updated near-source ground motion (attenuation) relations for the horizontal and vertical components of peak ground acceleration and acceleration response spectra. *Bull. Seism. Soc. Am.* 94**:** 2417.

Campbell, K. W., and Y. Bozorgnia. (2003a). Updated near-source ground motion (attenuation) relations for the horizontal and vertical components of peak ground acceleration and acceleration response spectra. *Bull. Seism. Soc. Am.* 93**:** 314–31.

Campbell, K. W., and Y. Bozorgnia. (2003b). Erratum: Updated near-source ground motion (attenuation) relations for the horizontal and vertical components of peak ground acceleration and acceleration response spectra. *Bull. Seism. Soc. Am.* 93**:** 1413.

Campbell, K. W., and Y. Bozorgnia. (2003c). Erratum: Updated near-source ground motion (attenuation) relations for the horizontal and vertical components of peak ground acceleration and acceleration response spectra. *Bull. Seism. Soc. Am.* 93**:** 1872.

Campbell, K. W., and Y. Bozorgnia. (1994). Near-source attenuation of peak horizontal acceleration from worldwide accelerograms recorded from 1957 to 1933. In *Proceedings, Fifth U.S. National Conference on Earthquake Engineering,* Vol. III, 283–92. Oakland, Calif.: Earthquake Engineering Research Institute.

Cao, T., W. A. Bryant., B. Rowshandel., D. Branum., and C. J. Wills. (2003). *The revised 2002 California probabilistic seismic hazard maps*. Online at http://www.consrv.ca.gov/CGS/rghm/psha/index.htm. Sacramento, Calif.: California Geological Survey.

Chiou, B. S.-J., R. R. Youngs. (2007). *Chiou-Youngs NGA ground motion relations for the geometric mean horizontal component of peak and spectral ground motion parameters.* (forthcoming) PEER Report. Berkeley, Calif.: Pacific Earthquake Engineering Research Center, University of California.

Choi, Y., and J. P. Stewart. (2005). Nonlinear site amplification as function of 30 m shear wave velocity. *Earthquake Spectra* 21**:** 1–30.

Collins, N., R. Graves., G. Ichinose, and P. Somerville. (2006). *Ground motion attenuation relations for the Intermountain West.* Final report prepared for the U.S. Geological Survey, Award No. 05HQGR0031. Pasadena, Calif.: URS Corporation.

Day, S. M., J. Bielak, D. Dreger., R. Graves, S. Larsen, K. Olsen., A. Pitarka, and L. Ramirez-Guzman. (2006). Numerical simulation of basin effects on long-period ground motion. In *Proceedings, Eighth National Conference on Earthquake Engineering.* Proceedings CD-ROM, Paper No. 1857. Oakland, Calif.: Earthquake Engineering Research Institute.

Di Toro, G., T. Hirose, S. Nielsen, G. Pennacchioni., and T. Shimamoto. (2006). Natural and experimental evidence of melt lubrication of faults during earthquakes. *Science* 311**:** 647–49.

Douglas, J. (2002). Note on scaling of peak ground acceleration and peak ground velocity with magnitude. *Geophys. J. Int.* 148: 336–39.

EPRI (1993). *Methods and guidelines for estimating earthquake ground motion in eastern North America: guidelines for determining design basis ground motions.* Report. EPRI TR-102293, Vol. 1. Palo Alto, Calif.: Electric Power Research Institute.

Faccioli, E., R. Paolucci, and J. Rey. (2004). Displacement spectra at long periods. *Earthquake Spectra* 20**:** 347–76.

Field, E. H. (2000). A modified ground-motion attenuation relationship for southern California that accounts for detailed site classification and a basin-depth effect. *Bull. Seism. Soc. Am.* 90**:** S209–S221.

Frankel, A. D. (2007). Do the next generation attenuation relations make physical sense? Abstract. *Seism. Res. Lett.* 78**:** 287.

Frankel, A. D., M. D. Petersen, C. S. Mueller, K. M. Haller, R. L. Wheeler., E. V. Leyendecker, R. L. Wesson, S. C. Harmsen, C. H. Cramer, D. M. Perkins, and K. S. Rukstales. (2002). *Documentation for the 2002 update of the national seismic hazard maps*. U.S. Geological Survey, Open-File Report 02-420.

Halldorsson, B., and A. S. Papgeorgiou. (2005). Calibration of the specific barrier model to earthquakes of different tectonic regions. *Bull. Seism. Soc. Am.* 95**:** 1276–1300.

Hanks, T. C., and W. H. Bakun. (2002). A bilinear source-scaling model for **M**–log *A* observations of continental earthquakes. *Bull. Seism. Soc. Am.* 92**:** 1841–46.

Howard, J. K., C. A. Tracy, and R. G. Burns. (2005). Comparing observed and predicted directivity in near-source ground motion. *Earthquake Spectra* 21**:** 1063–92.

Hudson, D. E. (1979). *Reading and interpreting strong motion accelerograms*. Berkeley, Calif.: Earthquake Engineering Research Institute.

Idriss, I. M. (2007). *Empirical model for estimating the average horizontal values of pseudo-absolute spectral accelerations generated by crustal earthquakes, Volume 1, Sites with V_{s30} = 450 to 900 m/s.* Interim project report. Berkeley, Calif.: Pacific Earthquake Engineering Research Center, University of California.

Idriss, I. M. (1991). *Selection of earthquake ground motions at rock sites.* Report prepared for the Structures Division, Building and Fire Research Laboratory, National Institute of Standards and Technology. Davis, Calif.: Department of Civil Engineering, University of California.

Johnston, A. C. (1996). Seismic moment assessment of earthquakes in stable continental regions—I. Instrumental seismicity. *Geophys. J. Int.* 124**:** 381–414.

Joyner, W. B., and D. M. Boore. (1993). Methods for regression analysis of strong-motion data. *Bull. Seism. Soc. Am.* 83**:** 469–87.

Kwok, A. O., and J. P. Stewart. (2006). Evaluation of the effectiveness of theoretical 1D amplification factors for earthquake ground-motion prediction. *Bull. Seism. Soc. Am.* 96**:** 1422–36.

Lay, T., and T. C. Wallace. (1995). *Modern Global Seismology*. San Diego: Academic Press.

Lee, W. H. K., T. C. Shin, K. W. Kuo., K. C. Chen., and C. F. Wu. (2001). Data files from "CWB free-field strong-motion data from the 21 September Chi-Chi, Taiwan, Earthquake." *Bull. Seism. Soc. Am.* 91**:** 1390.

NGA (2005). Metadata used in the PEER Lifelines Next Generation Attenuation project for the development of the NGA flatfile, http://peer.berkeley.edu/products/nga_project.html.

NSHMP (2007). *Preliminary documentation for the 2007 update of the United States national seismic hazard maps*. Draft Open-File Report prepared by the National Seismic Hazard Mapping Project.

Pitarka, A., N. Collins, T. K. Thio, R. Graves, and P. Somerville. (2006). Implication of rupture process and site effects in the spatial distribution and amplitude of the near-fault ground motion from the 2004 Parkfield earthquake. In *Proceedings, SMIP06 Seminar on Utilization of Strong motion Data*, 19–40. Sacramento, Calif.: California Strong Motion Instrumentation Program, California Geological Survey.

Power, M., R. Borcherdt, and J. Stewart. (2004). *Site amplification factors from empirical studies*. Report of NGA Working Group #5. Berkeley, Calif.: Pacific Earthquake Engineering Research Center, University of California.

Power, M., B. Chiou, N. Abrahamson, and C. Roblee. (2006). The next generation of ground motion attenuation models (NGA) project: an overview. In *Proceedings, Eighth National Conference on Earthquake Engineering*, Proceedings CD-ROM, Paper No. 2022. Oakland, Calif.: Earthquake Engineering Research Institute.

Rowe, C., D. Christensen, and G. Carver (eds.). (2004). The 2002 Denali fault earthquake sequence. *Bull. Seism. Soc. Am.* 94**:** Part B, Supplement.

Rowshandel, B. (2006). Incorporating source rupture characteristics into ground-motion hazard analysis models. *Seism. Res. Lett.* 77**:** 708–22.

Sadigh, K., C. Y. Chang, N. A. Abrahamson, S.-J. Chiou, and M. S. Power. (1993). Specification of long-period ground motions: updated attenuation relationships for rock site conditions and adjustment factors for near-fault effects. In *Proceedings, ATC-17-1 Seminar on Seismic Isolation, Passive Energy, and Active Control*, 59–70. Palo Alto, Calif.: Applied Technology Council.

Sadigh, K., C. Y. Chang, J. A. Egan, F. Makdisi, and R. R. Youngs. (1997). Attenuation relationships for shallow crustal earthquakes based on California strong motion data. *Seism. Res. Lett.* 68**:** 180–89.

Scherbaum, F., J. Schmedes, and F. Cotton. (2004). On the conversion of source-to-site distance measures for extended earthquake source models. *Bull. Seism. Soc. Am.* 94**:** 1053–69.

Scholz, C. H. (1982). Scaling laws for large earthquakes: consequences for physical models. *Bull. Seism. Soc. Am.* 72**:** 1–14.

Schmedes, J., and R. J. Archuleta. (2007). Oversaturation of peak ground velocity along strike slip faults. Abstract. *Seism. Res. Lett.* 78**:** 272.

Shakal, A., H. Haddadi, V. Graizer, K. Lin, and M. Huang. (2006). Some key features of the strong-motion data from the **M** 6.0 Parkfield, California, earthquake of 28 September 2004. *Bull. Seism. Soc. Am.* 96**:** S90–S118.

Silva, W. J. (2005). *Site response simulations for the NGA project*. Report prepared for the Pacific Earthquake Engineering Research Center, University of California, Berkeley. El Cerrito, Calif.: Pacific Engineering and Analysis..

Silva, W. J., L. Sylvia, B. R. Darragh, and N. Gregor. (1999). *Surface geology based strong motion amplification factors for the San Francisco Bay and Los Angeles Areas.* Report prepared for the Pacific Earthquake Engineering Research Center, University of California, Berkeley, Task 5B. El Cerrito, Calif.: Pacific Engineering and Analysis.

Somerville, P. G. (2003). Magnitude scaling of the near fault rupture directivity pulse. *Physics of the Earth and Planetary Interiors* 137**:** 201–12.

Somerville, P., and A. Pitarka. (2006). Differences in earthquake source and ground motion characteristics between surface and buried earthquakes. In *Proceedings, Eighth National Conference on Earthquake Engineering,* Proceedings CD-ROM, Paper No. 977. Oakland, Calif.: Earthquake Engineering Research Institute.

Somerville, P. G., N. F. Smith, R. W. Graves., and N. A. Abrahamson. (1997). Modification of empirical strong ground motion attenuation relations to include the amplitude and duration effects of rupture directivity. *Seism. Res. Lett.* 68**:** 199–222.

Spudich, P., and B. J.-S. Chiou. (2006). *Directivity in preliminary NGA residuals.* Final project report to Pacific Earthquake Engineering Research Center, University of California, Berkeley, Task 1M01, Subagreement SA5146-15811. Menlo Park, Calif.: U.S. Geological Survey.

Spudich, P., B. J.-S. Chiou, R. Graves, N. Collins, and P. Somerville. (2004). *A formulation of directivity for earthquake sources using isochrone theory*. U.S. Geological Survey, Open-File Report 2004-1268.

Walling, M., and N. Abrahamson. (2006). Non-linear soil response model. In *Proceedings, Eighth National Conference on Earthquake Engineering*, Proceedings CD-ROM, Paper No. 1030. Oakland, Calif.: Earthquake Engineering Research Institute.

Wells, D. L., and K. J. Coppersmith. (1994). New empirical relationships among magnitude, rupture length, rupture width, rupture area, and surface displacement. *Bull. Seism. Soc. Am.* 84**:** 974–1002.

Wells, D. L., and K. J. Coppersmith. (1993). Likelihood of surface rupture as a function of magnitude. Abstract. *Seism. Res. Lett.* 64**:** 54.

Wills, C. J., and K. B. Clahan. (2005). *NGA: Site conditions metadata from geology*. Report prepared for Pacific Earthquake Engineering Research Center, University of California, Berkeley, Project 1L05. Sacramento, Calif.: California Geological Survey.

Wills, C. J., and W. Silva. (1998). Shear-wave velocity characteristics of geologic units in California. *Earthquake Spectra* 14**:** 533–56.

Wills, C. J., M. Petersen, W. A. Bryant, M. Reichle, G. J. Saucedo, S. Tan., G. Taylor, and J. Treiman. (2000). A site-conditions map for California based on geology and shear-wave velocity. *Bull. Seism. Soc. Am.* 90**:** S187–S208.

WGCEP (2003). *Earthquake probabilities in the San Francisco Bay region: 2002–2031*. Report prepared by Working Group on California Earthquake Probabilities. U.S. Geological Survey, Open-File Rept. 03-214.

Youngs, R. R., et al. (2003). A methodology for probabilistic fault displacement hazard analysis (PFSHA). *Earthquake Spectra* 19**:** 191–219.

Zoback, M. L. (1992). First and second-order patterns of stress in the lithosphere: the world stress map project. *J. Geophys. Res.* 97**:** 11703–11728.

Appendix A: Summary of Strong Motion Database Used in the Analysis

Table A.1 Summary of strong motion database used in the analysis.

Record No	Event No.	Event Name	**M**	Station Code	Station Name
12	12	Kern County	7.36	24303	LA - Hollywood Stor FF
28	25	Parkfield	6.19	1016	Cholame - Shandon Array #12
30	25	Parkfield	6.19	1014	Cholame - Shandon Array #5
31	25	Parkfield	6.19	1015	Cholame - Shandon Array #8
33	25	Parkfield	6.19	1438	Temblor pre-1969
41	29	Lytle Creek	5.33	24278	Castaic - Old Ridge Route
42	29	Lytle Creek	5.33	112	Cedar Springs Pumphouse
43	29	Lytle Creek	5.33	111	Cedar Springs, Allen Ranch
44	29	Lytle Creek	5.33	113	Colton - So Cal Edison
45	29	Lytle Creek	5.33	620	Devil's Canyon
46	29	Lytle Creek	5.33	24303	LA - Hollywood Stor FF
47	29	Lytle Creek	5.33	24271	Lake Hughes #1
48	29	Lytle Creek	5.33	278	Puddingstone Dam (Abutment)
49	29	Lytle Creek	5.33	104	Santa Anita Dam
50	29	Lytle Creek	5.33	290	Wrightwood - 6074 Park Dr
51	30	San Fernando	6.61	411	2516 Via Tejon PV
52	30	San Fernando	6.61	103	Anza Post Office
55	30	San Fernando	6.61	1	Buena Vista - Taft
56	30	San Fernando	6.61	108	Carbon Canyon Dam
57	30	San Fernando	6.61	24278	Castaic - Old Ridge Route
58	30	San Fernando	6.61	112	Cedar Springs Pumphouse
59	30	San Fernando	6.61	111	Cedar Springs, Allen Ranch
62	30	San Fernando	6.61	113	Colton - So Cal Edison
63	30	San Fernando	6.61	121	Fairmont Dam
64	30	San Fernando	6.61	998	Fort Tejon
65	30	San Fernando	6.61	994	Gormon - Oso Pump Plant
66	30	San Fernando	6.61	12331	Hemet Fire Station
67	30	San Fernando	6.61	1035	Isabella Dam (Aux Abut)
68	30	San Fernando	6.61	24303	LA - Hollywood Stor FF
70	30	San Fernando	6.61	24271	Lake Hughes #1
71	30	San Fernando	6.61	128	Lake Hughes #12
72	30	San Fernando	6.61	126	Lake Hughes #4
73	30	San Fernando	6.61	127	Lake Hughes #9
74	30	San Fernando	6.61	1041	Maricopa Array #1
75	30	San Fernando	6.61	1042	Maricopa Array #2
76	30	San Fernando	6.61	1043	Maricopa Array #3
78	30	San Fernando	6.61	262	Palmdale Fire Station
81	30	San Fernando	6.61	269	Pearblossom Pump
82	30	San Fernando	6.61	272	Port Hueneme
83	30	San Fernando	6.61	278	Puddingstone Dam (Abutment)
85	30	San Fernando	6.61	465	San Juan Capistrano
86	30	San Fernando	6.61	280	San Onofre - So Cal Edison
87	30	San Fernando	6.61	104	Santa Anita Dam
89	30	San Fernando	6.61	1027	Tehachapi Pump
91	30	San Fernando	6.61	287	Upland - San Antonio Dam
92	30	San Fernando	6.61	1102	Wheeler Ridge - Ground
93	30	San Fernando	6.61	289	Whittier Narrows Dam
94	30	San Fernando	6.61	290	Wrightwood - 6074 Park Dr
95	31	Managua, Nicaragua-01	6.24	3501	Managua, ESSO
121	40	Friuli, Italy-01	6.50	8002	Barcis
122	40	Friuli, Italy-01	6.50	8004	Codroipo
123	40	Friuli, Italy-01	6.50	8005	Conegliano
124	40	Friuli, Italy-01	6.50	8007	Feltre
125	40	Friuli, Italy-01	6.50	8012	Tolmezzo
126	41	Gazli, USSR	6.80	9201	Karakyr
137	46	Tabas, Iran	7.35	69	Bajestan
138	46	Tabas, Iran	7.35	70	Boshrooyeh
139	46	Tabas, Iran	7.35	9102	Dayhook
140	46	Tabas, Iran	7.35	71	Ferdows

141	46	Tabas, Iran	7.35	72	Kashmar
142	46	Tabas, Iran	7.35	73	Sedeh
143	46	Tabas, Iran	7.35	9101	Tabas
145	48	Coyote Lake	5.74	57217	Coyote Lake Dam (SW Abut)
146	48	Coyote Lake	5.74	47379	Gilroy Array #1
147	48	Coyote Lake	5.74	47380	Gilroy Array #2
148	48	Coyote Lake	5.74	47381	Gilroy Array #3
149	48	Coyote Lake	5.74	57382	Gilroy Array #4
150	48	Coyote Lake	5.74	57383	Gilroy Array #6
151	48	Coyote Lake	5.74	57191	Halls Valley
152	48	Coyote Lake	5.74	47315	SJB Overpass, Bent 3 g.l.
153	48	Coyote Lake	5.74	47315	SJB Overpass, Bent 5 g.l.
154	48	Coyote Lake	5.74	47126	San Juan Bautista, 24 Polk St
155	49	Norcia, Italy	5.90	99999	Bevagna
156	49	Norcia, Italy	5.90	99999	Cascia
157	49	Norcia, Italy	5.90	99999	Spoleto
158	50	Imperial Valley-06	6.53	6616	Aeropuerto Mexicali
159	50	Imperial Valley-06	6.53	6618	Agrarias
160	50	Imperial Valley-06	6.53	5054	Bonds Corner
161	50	Imperial Valley-06	6.53	5060	Brawley Airport
162	50	Imperial Valley-06	6.53	5053	Calexico Fire Station
163	50	Imperial Valley-06	6.53	5061	Calipatria Fire Station
164	50	Imperial Valley-06	6.53	6604	Cerro Prieto
165	50	Imperial Valley-06	6.53	6621	Chihuahua
166	50	Imperial Valley-06	6.53	5066	Coachella Canal #4
167	50	Imperial Valley-06	6.53	6622	Compuertas
169	50	Imperial Valley-06	6.53	6605	Delta
170	50	Imperial Valley-06	6.53	1136	EC County Center FF
171	50	Imperial Valley-06	6.53	1336	EC Meloland Overpass FF
172	50	Imperial Valley-06	6.53	5056	El Centro Array #1
173	50	Imperial Valley-06	6.53	412	El Centro Array #10
174	50	Imperial Valley-06	6.53	5058	El Centro Array #11
175	50	Imperial Valley-06	6.53	931	El Centro Array #12
176	50	Imperial Valley-06	6.53	5059	El Centro Array #13
178	50	Imperial Valley-06	6.53	5057	El Centro Array #3
179	50	Imperial Valley-06	6.53	955	El Centro Array #4
180	50	Imperial Valley-06	6.53	952	El Centro Array #5
181	50	Imperial Valley-06	6.53	5158	El Centro Array #6
182	50	Imperial Valley-06	6.53	5028	El Centro Array #7
183	50	Imperial Valley-06	6.53	958	El Centro Array #8
184	50	Imperial Valley-06	6.53	5165	El Centro Differential Array
185	50	Imperial Valley-06	6.53	5055	Holtville Post Office
186	50	Imperial Valley-06	6.53	11023	Niland Fire Station
187	50	Imperial Valley-06	6.53	5051	Parachute Test Site
188	50	Imperial Valley-06	6.53	5052	Plaster City
189	50	Imperial Valley-06	6.53	6619	SAHOP Casa Flores
190	50	Imperial Valley-06	6.53	286	Superstition Mtn Camera
191	50	Imperial Valley-06	6.53	6610	Victoria
192	50	Imperial Valley-06	6.53	11369	Westmorland Fire Sta
210	53	Livermore-01	5.80	58219	APEEL 3E Hayward CSUH
213	53	Livermore-01	5.80	57064	Fremont - Mission San Jose
214	53	Livermore-01	5.80	57187	San Ramon - Eastman Kodak
215	53	Livermore-01	5.80	57134	San Ramon Fire Station
216	53	Livermore-01	5.80	57063	Tracy - Sewage Treatm Plant
225	55	Anza (Horse Canyon)-01	5.19	5044	Anza - Pinyon Flat
226	55	Anza (Horse Canyon)-01	5.19	5045	Anza - Terwilliger Valley
227	55	Anza (Horse Canyon)-01	5.19	5160	Anza Fire Station
228	55	Anza (Horse Canyon)-01	5.19	5049	Borrego Air Ranch
229	55	Anza (Horse Canyon)-01	5.19	5047	Rancho De Anza
230	56	Mammoth Lakes-01	6.06	54099	Convict Creek
231	56	Mammoth Lakes-01	6.06	54214	Long Valley Dam (Upr L Abut)
232	56	Mammoth Lakes-01	6.06	54301	Mammoth Lakes H. S.
265	64	Victoria, Mexico	6.33	6604	Cerro Prieto

266	64	Victoria, Mexico	6.33	6621	Chihuahua
268	64	Victoria, Mexico	6.33	6619	SAHOP Casa Flores
269	64	Victoria, Mexico	6.33	6624	Victoria Hospital Sotano
283	68	Irpinia, Italy-01	6.90	99999	Arienzo
284	68	Irpinia, Italy-01	6.90	99999	Auletta
285	68	Irpinia, Italy-01	6.90	99999	Bagnoli Irpinio
286	68	Irpinia, Italy-01	6.90	99999	Bisaccia
287	68	Irpinia, Italy-01	6.90	99999	Bovino
288	68	Irpinia, Italy-01	6.90	99999	Brienza
289	68	Irpinia, Italy-01	6.90	99999	Calitri
290	68	Irpinia, Italy-01	6.90	99999	Mercato San Severino
291	68	Irpinia, Italy-01	6.90	99999	Rionero In Vulture
292	68	Irpinia, Italy-01	6.90	99999	Sturno
293	68	Irpinia, Italy-01	6.90	99999	Torre Del Greco
294	68	Irpinia, Italy-01	6.90	99999	Tricarico
313	72	Corinth, Greece	6.60	99999	Corinth
314	73	Westmorland	5.90	5060	Brawley Airport
315	73	Westmorland	5.90	11023	Niland Fire Station
316	73	Westmorland	5.90	5051	Parachute Test Site
317	73	Westmorland	5.90	5062	Salton Sea Wildlife Refuge
318	73	Westmorland	5.90	286	Superstition Mtn Camera
319	73	Westmorland	5.90	11369	Westmorland Fire Sta
322	76	Coalinga-01	6.36	46314	Cantua Creek School
323	76	Coalinga-01	6.36	36229	Parkfield - Cholame 12W
324	76	Coalinga-01	6.36	36452	Parkfield - Cholame 1E
325	76	Coalinga-01	6.36	36230	Parkfield - Cholame 2E
326	76	Coalinga-01	6.36	36228	Parkfield - Cholame 2WA
327	76	Coalinga-01	6.36	36450	Parkfield - Cholame 3E
328	76	Coalinga-01	6.36	36410	Parkfield - Cholame 3W
329	76	Coalinga-01	6.36	36412	Parkfield - Cholame 4AW
330	76	Coalinga-01	6.36	36411	Parkfield - Cholame 4W
331	76	Coalinga-01	6.36	36227	Parkfield - Cholame 5W
332	76	Coalinga-01	6.36	36451	Parkfield - Cholame 6W
333	76	Coalinga-01	6.36	36226	Parkfield - Cholame 8W
334	76	Coalinga-01	6.36	36407	Parkfield - Fault Zone 1
335	76	Coalinga-01	6.36	36444	Parkfield - Fault Zone 10
336	76	Coalinga-01	6.36	36453	Parkfield - Fault Zone 11
337	76	Coalinga-01	6.36	36138	Parkfield - Fault Zone 12
338	76	Coalinga-01	6.36	36456	Parkfield - Fault Zone 14
339	76	Coalinga-01	6.36	36445	Parkfield - Fault Zone 15
340	76	Coalinga-01	6.36	36457	Parkfield - Fault Zone 16
341	76	Coalinga-01	6.36	36413	Parkfield - Fault Zone 2
342	76	Coalinga-01	6.36	36408	Parkfield - Fault Zone 3
343	76	Coalinga-01	6.36	36414	Parkfield - Fault Zone 4
344	76	Coalinga-01	6.36	36454	Parkfield - Fault Zone 6
345	76	Coalinga-01	6.36	36431	Parkfield - Fault Zone 7
346	76	Coalinga-01	6.36	36449	Parkfield - Fault Zone 8
347	76	Coalinga-01	6.36	36443	Parkfield - Fault Zone 9
348	76	Coalinga-01	6.36	36415	Parkfield - Gold Hill 1W
349	76	Coalinga-01	6.36	36421	Parkfield - Gold Hill 2E
350	76	Coalinga-01	6.36	36416	Parkfield - Gold Hill 2W
351	76	Coalinga-01	6.36	36439	Parkfield - Gold Hill 3E
352	76	Coalinga-01	6.36	36420	Parkfield - Gold Hill 3W
353	76	Coalinga-01	6.36	36433	Parkfield - Gold Hill 4W
354	76	Coalinga-01	6.36	36434	Parkfield - Gold Hill 5W
355	76	Coalinga-01	6.36	36432	Parkfield - Gold Hill 6W
356	76	Coalinga-01	6.36	36422	Parkfield - Stone Corral 2E
357	76	Coalinga-01	6.36	36437	Parkfield - Stone Corral 3E
358	76	Coalinga-01	6.36	36438	Parkfield - Stone Corral 4E
359	76	Coalinga-01	6.36	36455	Parkfield - Vineyard Cany 1E
360	76	Coalinga-01	6.36	36448	Parkfield - Vineyard Cany 1W
362	76	Coalinga-01	6.36	36447	Parkfield - Vineyard Cany 2W
363	76	Coalinga-01	6.36	36176	Parkfield - Vineyard Cany 3W

364	76	Coalinga-01	6.36	36446	Parkfield - Vineyard Cany 4W
366	76	Coalinga-01	6.36	36441	Parkfield - Vineyard Cany 6W
368	76	Coalinga-01	6.36	1162	Pleasant Valley P.P. - yard
369	76	Coalinga-01	6.36	46175	Slack Canyon
437	87	Borah Peak, ID-01	6.88	99999	CPP-610
439	87	Borah Peak, ID-01	6.88	99999	TAN-719
446	90	Morgan Hill	6.19	58376	APEEL 1E - Hayward
447	90	Morgan Hill	6.19	57066	Agnews State Hospital
448	90	Morgan Hill	6.19	1652	Anderson Dam (Downstream)
449	90	Morgan Hill	6.19	47125	Capitola
450	90	Morgan Hill	6.19	57007	Corralitos
451	90	Morgan Hill	6.19	57217	Coyote Lake Dam (SW Abut)
452	90	Morgan Hill	6.19	58375	Foster City - APEEL 1
453	90	Morgan Hill	6.19	57064	Fremont - Mission San Jose
454	90	Morgan Hill	6.19	47006	Gilroy - Gavilan Coll.
455	90	Morgan Hill	6.19	47379	Gilroy Array #1
456	90	Morgan Hill	6.19	47380	Gilroy Array #2
457	90	Morgan Hill	6.19	47381	Gilroy Array #3
458	90	Morgan Hill	6.19	57382	Gilroy Array #4
459	90	Morgan Hill	6.19	57383	Gilroy Array #6
460	90	Morgan Hill	6.19	57425	Gilroy Array #7
461	90	Morgan Hill	6.19	57191	Halls Valley
463	90	Morgan Hill	6.19	1656	Hollister Diff Array #1
464	90	Morgan Hill	6.19	1656	Hollister Diff Array #3
465	90	Morgan Hill	6.19	1656	Hollister Diff Array #4
466	90	Morgan Hill	6.19	1656	Hollister Diff Array #5
467	90	Morgan Hill	6.19	1656	Hollister Diff. Array
468	90	Morgan Hill	6.19	56012	Los Banos
469	90	Morgan Hill	6.19	58223	SF Intern. Airport
470	90	Morgan Hill	6.19	47126	San Juan Bautista, 24 Polk St
471	90	Morgan Hill	6.19	1655	San Justo Dam (L Abut)
472	90	Morgan Hill	6.19	1655	San Justo Dam (R Abut)
476	90	Morgan Hill	6.19	58135	UCSC Lick Observatory
477	91	Lazio-Abruzzo, Italy	5.80	99999	Atina
478	91	Lazio-Abruzzo, Italy	5.80	99999	Garigliano-Centrale Nucleare
479	91	Lazio-Abruzzo, Italy	5.80	99999	Isernia-Sant'Agapito
480	91	Lazio-Abruzzo, Italy	5.80	99999	Pontecorvo
481	91	Lazio-Abruzzo, Italy	5.80	99999	Roccamonfina
495	97	Nahanni, Canada	6.76	6097	Site 1
496	97	Nahanni, Canada	6.76	6098	Site 2
497	97	Nahanni, Canada	6.76	6099	Site 3
498	98	Hollister-04	5.45	1656	Hollister Diff Array #1
499	98	Hollister-04	5.45	1656	Hollister Diff Array #3
501	98	Hollister-04	5.45	47189	SAGO South - Surface
511	101	N. Palm Springs	6.06	5224	Anza - Red Mountain
512	101	N. Palm Springs	6.06	5231	Anza - Tule Canyon
513	101	N. Palm Springs	6.06	5160	Anza Fire Station
514	101	N. Palm Springs	6.06	5073	Cabazon
515	101	N. Palm Springs	6.06	754	Colton Interchange - Vault
516	101	N. Palm Springs	6.06	5157	Cranston Forest Station
517	101	N. Palm Springs	6.06	12149	Desert Hot Springs
518	101	N. Palm Springs	6.06	5069	Fun Valley
519	101	N. Palm Springs	6.06	12331	Hemet Fire Station
520	101	N. Palm Springs	6.06	23321	Hesperia
521	101	N. Palm Springs	6.06	5043	Hurkey Creek Park
522	101	N. Palm Springs	6.06	5067	Indio
523	101	N. Palm Springs	6.06	12026	Indio - Coachella Canal
524	101	N. Palm Springs	6.06	22170	Joshua Tree
526	101	N. Palm Springs	6.06	22T13	Landers Fire Station
527	101	N. Palm Springs	6.06	5071	Morongo Valley
528	101	N. Palm Springs	6.06	13198	Murrieta Hot Springs
529	101	N. Palm Springs	6.06	5070	North Palm Springs
530	101	N. Palm Springs	6.06	12025	Palm Springs Airport

531	101	N. Palm Springs	6.06	12168	Puerta La Cruz
532	101	N. Palm Springs	6.06	23497	Rancho Cucamonga - FF
533	101	N. Palm Springs	6.06	13123	Riverside Airport
534	101	N. Palm Springs	6.06	12204	San Jacinto - Soboba
535	101	N. Palm Springs	6.06	12202	San Jacinto - Valley Cemetary
536	101	N. Palm Springs	6.06	5230	Santa Rosa Mountain
537	101	N. Palm Springs	6.06	12206	Silent Valley - Poppet Flat
538	101	N. Palm Springs	6.06	5038	Sunnymead
539	101	N. Palm Springs	6.06	13172	Temecula - 6th & Mercedes
540	101	N. Palm Springs	6.06	5072	Whitewater Trout Farm
541	101	N. Palm Springs	6.06	13199	Winchester Bergman Ran
542	101	N. Palm Springs	6.06	13201	Winchester Page Bros R
543	102	Chalfant Valley-01	5.77	54100	Benton
544	102	Chalfant Valley-01	5.77	54171	Bishop - LADWP South St
545	102	Chalfant Valley-01	5.77	54424	Bishop - Paradise Lodge
546	102	Chalfant Valley-01	5.77	54T03	Lake Crowley - Shehorn Res.
547	102	Chalfant Valley-01	5.77	54428	Zack Brothers Ranch
548	103	Chalfant Valley-02	6.19	54100	Benton
549	103	Chalfant Valley-02	6.19	54171	Bishop - LADWP South St
550	103	Chalfant Valley-02	6.19	54424	Bishop - Paradise Lodge
551	103	Chalfant Valley-02	6.19	54099	Convict Creek
552	103	Chalfant Valley-02	6.19	54T03	Lake Crowley - Shehorn Res.
553	103	Chalfant Valley-02	6.19	54214	Long Valley Dam (Downst)
554	103	Chalfant Valley-02	6.19	54214	Long Valley Dam (L Abut)
555	103	Chalfant Valley-02	6.19	54T04	Mammoth Lakes Sheriff Subst.
556	103	Chalfant Valley-02	6.19	1661	McGee Creek - Surface
557	103	Chalfant Valley-02	6.19	54101	Tinemaha Res. Free Field
558	103	Chalfant Valley-02	6.19	54428	Zack Brothers Ranch
586	111	New Zealand-02	6.60	113A	Maraenui Primary School
587	111	New Zealand-02	6.60	99999	Matahina Dam
589	113	Whittier Narrows-01	5.99	24461	Alhambra - Fremont School
590	113	Whittier Narrows-01	5.99	24402	Altadena - Eaton Canyon
591	113	Whittier Narrows-01	5.99	90088	Anaheim - W Ball Rd
592	113	Whittier Narrows-01	5.99	90093	Arcadia - Campus Dr
593	113	Whittier Narrows-01	5.99	24087	Arleta - Nordhoff Fire Sta
594	113	Whittier Narrows-01	5.99	90069	Baldwin Park - N Holly
595	113	Whittier Narrows-01	5.99	90094	Bell Gardens - Jaboneria
596	113	Whittier Narrows-01	5.99	90014	Beverly Hills - 12520 Mulhol
597	113	Whittier Narrows-01	5.99	90013	Beverly Hills - 14145 Mulhol
598	113	Whittier Narrows-01	5.99	90061	Big Tujunga, Angeles Nat F
600	113	Whittier Narrows-01	5.99	951	Brea Dam (Downstream)
601	113	Whittier Narrows-01	5.99	951	Brea Dam (L Abut)
602	113	Whittier Narrows-01	5.99	90012	Burbank - N Buena Vista
603	113	Whittier Narrows-01	5.99	90052	Calabasas - N Las Virg
604	113	Whittier Narrows-01	5.99	90053	Canoga Park - Topanga Can
605	113	Whittier Narrows-01	5.99	90057	Canyon Country - W Lost Cany
606	113	Whittier Narrows-01	5.99	108	Carbon Canyon Dam
607	113	Whittier Narrows-01	5.99	90040	Carson - Catskill Ave
608	113	Whittier Narrows-01	5.99	90081	Carson - Water St
609	113	Whittier Narrows-01	5.99	24277	Castaic - Hasley Canyon
610	113	Whittier Narrows-01	5.99	24278	Castaic - Old Ridge Route
611	113	Whittier Narrows-01	5.99	90078	Compton - Castlegate St
612	113	Whittier Narrows-01	5.99	90068	Covina - S Grand Ave
613	113	Whittier Narrows-01	5.99	90070	Covina - W Badillo
614	113	Whittier Narrows-01	5.99	90079	Downey - Birchdale
615	113	Whittier Narrows-01	5.99	14368	Downey - Co Maint Bldg
616	113	Whittier Narrows-01	5.99	90066	El Monte - Fairview Av
617	113	Whittier Narrows-01	5.99	13122	Featherly Park - Maint
618	113	Whittier Narrows-01	5.99	90002	Fountain Valley - Euclid
619	113	Whittier Narrows-01	5.99	709	Garvey Res. - Control Bldg
620	113	Whittier Narrows-01	5.99	90063	Glendale - Las Palmas
621	113	Whittier Narrows-01	5.99	90065	Glendora - N Oakbank
622	113	Whittier Narrows-01	5.99	90073	Hacienda Heights - Colima

623	113	Whittier Narrows-01	5.99	12331	Hemet Fire Station
624	113	Whittier Narrows-01	5.99	13197	Huntington Beach - Lake St
625	113	Whittier Narrows-01	5.99	14196	Inglewood - Union Oil
626	113	Whittier Narrows-01	5.99	14403	LA - 116th St School
627	113	Whittier Narrows-01	5.99	24157	LA - Baldwin Hills
628	113	Whittier Narrows-01	5.99	90054	LA - Centinela St
629	113	Whittier Narrows-01	5.99	24389	LA - Century City CC North
630	113	Whittier Narrows-01	5.99	24390	LA - Century City CC South
631	113	Whittier Narrows-01	5.99	90015	LA - Chalon Rd
632	113	Whittier Narrows-01	5.99	90033	LA - Cypress Ave
634	113	Whittier Narrows-01	5.99	90034	LA - Fletcher Dr
635	113	Whittier Narrows-01	5.99	24303	LA - Hollywood Stor FF
636	113	Whittier Narrows-01	5.99	90016	LA - N Faring Rd
637	113	Whittier Narrows-01	5.99	90032	LA - N Figueroa St
638	113	Whittier Narrows-01	5.99	90021	LA - N Westmoreland
639	113	Whittier Narrows-01	5.99	24400	LA - Obregon Park
640	113	Whittier Narrows-01	5.99	90022	LA - S Grand Ave
641	113	Whittier Narrows-01	5.99	90091	LA - Saturn St
642	113	Whittier Narrows-01	5.99	90023	LA - W 70th St
643	113	Whittier Narrows-01	5.99	90017	LA - Wonderland Ave
644	113	Whittier Narrows-01	5.99	14395	LB - Harbor Admin FF
645	113	Whittier Narrows-01	5.99	90080	LB - Orange Ave
646	113	Whittier Narrows-01	5.99	14242	LB - Rancho Los Cerritos
647	113	Whittier Narrows-01	5.99	14241	LB - Recreation Park
648	113	Whittier Narrows-01	5.99	90060	La Crescenta - New York
649	113	Whittier Narrows-01	5.99	90074	La Habra - Briarcliff
650	113	Whittier Narrows-01	5.99	90072	La Puente - Rimgrove Av
651	113	Whittier Narrows-01	5.99	24271	Lake Hughes #1
652	113	Whittier Narrows-01	5.99	90084	Lakewood - Del Amo Blvd
653	113	Whittier Narrows-01	5.99	24526	Lancaster - Med Off FF
654	113	Whittier Narrows-01	5.99	90045	Lawndale - Osage Ave
655	113	Whittier Narrows-01	5.99	24055	Leona Valley #5 - Ritter
656	113	Whittier Narrows-01	5.99	24309	Leona Valley #6
657	113	Whittier Narrows-01	5.99	90050	Malibu - Las Flores Canyon
658	113	Whittier Narrows-01	5.99	24396	Malibu - Point Dume Sch
659	113	Whittier Narrows-01	5.99	90051	Malibu - W Pacific Cst Hwy
661	113	Whittier Narrows-01	5.99	90062	Mill Creek, Angeles Nat For
662	113	Whittier Narrows-01	5.99	24283	Moorpark - Fire Sta
663	113	Whittier Narrows-01	5.99	24399	Mt Wilson - CIT Seis Sta
664	113	Whittier Narrows-01	5.99	90009	N Hollywood - Coldwater Can
665	113	Whittier Narrows-01	5.99	24279	Newhall - Fire Sta
666	113	Whittier Narrows-01	5.99	90056	Newhall - W Pico Canyon Rd.
667	113	Whittier Narrows-01	5.99	90003	Northridge - 17645 Saticoy St
668	113	Whittier Narrows-01	5.99	634	Norwalk - Imp Hwy, S Grnd
669	113	Whittier Narrows-01	5.99	697	Orange Co. Reservoir
670	113	Whittier Narrows-01	5.99	90049	Pacific Palisades - Sunset
671	113	Whittier Narrows-01	5.99	24088	Pacoima Kagel Canyon
672	113	Whittier Narrows-01	5.99	90005	Pacoima Kagel Canyon USC
673	113	Whittier Narrows-01	5.99	90007	Panorama City - Roscoe
674	113	Whittier Narrows-01	5.99	80046	Pasadena - Brown Gym
677	113	Whittier Narrows-01	5.99	80047	Pasadena - CIT Calif Blvd
678	113	Whittier Narrows-01	5.99	80051	Pasadena - CIT Indust. Rel
681	113	Whittier Narrows-01	5.99	80048	Pasadena - CIT Lura St
683	113	Whittier Narrows-01	5.99	90095	Pasadena - Old House Rd
684	113	Whittier Narrows-01	5.99	90047	Playa Del Rey - Saran
685	113	Whittier Narrows-01	5.99	23525	Pomona - 4th & Locust FF
686	113	Whittier Narrows-01	5.99	23497	Rancho Cucamonga - FF
687	113	Whittier Narrows-01	5.99	90044	Rancho Palos Verdes - Luconia
688	113	Whittier Narrows-01	5.99	13123	Riverside Airport
689	113	Whittier Narrows-01	5.99	24274	Rosamond - Goode Ranch
690	113	Whittier Narrows-01	5.99	90019	San Gabriel - E Grand Ave
691	113	Whittier Narrows-01	5.99	24401	San Marino - SW Academy
692	113	Whittier Narrows-01	5.99	90077	Santa Fe Springs - E.Joslin

693	113	Whittier Narrows-01	5.99	90048	Santa Monica - Second St
694	113	Whittier Narrows-01	5.99	90010	Studio City - Coldwater Can
695	113	Whittier Narrows-01	5.99	90006	Sun Valley - Roscoe Blvd
696	113	Whittier Narrows-01	5.99	90008	Sun Valley - Sunland
697	113	Whittier Narrows-01	5.99	90058	Sunland - Mt Gleason Ave
698	113	Whittier Narrows-01	5.99	24514	Sylmar - Olive View Med FF
699	113	Whittier Narrows-01	5.99	90001	Sylmar - Sayre St
701	113	Whittier Narrows-01	5.99	90082	Terminal Island - S Seaside
702	113	Whittier Narrows-01	5.99	90038	Torrance - W 226th St
703	113	Whittier Narrows-01	5.99	24047	Vasquez Rocks Park
704	113	Whittier Narrows-01	5.99	90090	Villa Park - Serrano Ave
705	113	Whittier Narrows-01	5.99	90071	West Covina - S Orange Ave
706	113	Whittier Narrows-01	5.99	289	Whittier Narrows Dam upstream
707	114	Whittier Narrows-02	5.27	24461	Alhambra - Fremont School
708	114	Whittier Narrows-02	5.27	24402	Altadena - Eaton Canyon
709	114	Whittier Narrows-02	5.27	14368	Downey - Co Maint Bldg
710	114	Whittier Narrows-02	5.27	14196	Inglewood - Union Oil
711	114	Whittier Narrows-02	5.27	14403	LA - 116th St School
712	114	Whittier Narrows-02	5.27	24157	LA - Baldwin Hills
713	114	Whittier Narrows-02	5.27	24303	LA - Hollywood Stor FF
714	114	Whittier Narrows-02	5.27	24400	LA - Obregon Park
715	114	Whittier Narrows-02	5.27	24399	Mt Wilson - CIT Seis Sta
716	114	Whittier Narrows-02	5.27	24401	San Marino - SW Academy
718	115	Superstition Hills-01	6.22	5210	Wildlife Liquef. Array
719	116	Superstition Hills-02	6.54	5060	Brawley Airport
720	116	Superstition Hills-02	6.54	5061	Calipatria Fire Station
721	116	Superstition Hills-02	6.54	1335	El Centro Imp. Co. Cent
722	116	Superstition Hills-02	6.54	9401	Kornbloom Road (temp)
723	116	Superstition Hills-02	6.54	5051	Parachute Test Site
724	116	Superstition Hills-02	6.54	5052	Plaster City
725	116	Superstition Hills-02	6.54	9400	Poe Road (temp)
726	116	Superstition Hills-02	6.54	5062	Salton Sea Wildlife Refuge
727	116	Superstition Hills-02	6.54	286	Superstition Mtn Camera
728	116	Superstition Hills-02	6.54	11369	Westmorland Fire Sta
729	116	Superstition Hills-02	6.54	5210	Wildlife Liquef. Array
731	118	Loma Prieta	6.93	58373	APEEL 10 - Skyline
732	118	Loma Prieta	6.93	1002	APEEL 2 - Redwood City
733	118	Loma Prieta	6.93	58393	APEEL 2E Hayward Muir Sch
734	118	Loma Prieta	6.93	58219	APEEL 3E Hayward CSUH
735	118	Loma Prieta	6.93	58378	APEEL 7 - Pulgas
736	118	Loma Prieta	6.93	1161	APEEL 9 - Crystal Springs Res
737	118	Loma Prieta	6.93	57066	Agnews State Hospital
738	118	Loma Prieta	6.93	99999	Alameda Naval Air Stn Hanger
739	118	Loma Prieta	6.93	1652	Anderson Dam (Downstream)
740	118	Loma Prieta	6.93	1652	Anderson Dam (L Abut)
741	118	Loma Prieta	6.93	13	BRAN
742	118	Loma Prieta	6.93	1210	Bear Valley #1, Fire Station
743	118	Loma Prieta	6.93	1479	Bear Valley #10, Webb Residence
744	118	Loma Prieta	6.93	1481	Bear Valley #12, Williams Ranch
745	118	Loma Prieta	6.93	1483	Bear Valley #14, Upper Butts Rn
746	118	Loma Prieta	6.93	1474	Bear Valley #5, Callens Ranch
747	118	Loma Prieta	6.93	1476	Bear Valley #7, Pinnacles
749	118	Loma Prieta	6.93	1005	Berkeley - Strawberry Canyon
750	118	Loma Prieta	6.93	58471	Berkeley LBL
751	118	Loma Prieta	6.93	1687	Calaveras Reservoir
752	118	Loma Prieta	6.93	47125	Capitola
753	118	Loma Prieta	6.93	57007	Corralitos
754	118	Loma Prieta	6.93	57504	Coyote Lake Dam (Downst)
755	118	Loma Prieta	6.93	57217	Coyote Lake Dam (SW Abut)
756	118	Loma Prieta	6.93	1689	Dublin - Fire Station
757	118	Loma Prieta	6.93	58664	Dumbarton Bridge West End FF
758	118	Loma Prieta	6.93	1662	Emeryville - 6363 Christie
759	118	Loma Prieta	6.93	58375	Foster City - APEEL 1

760	118	Loma Prieta	6.93	1515	Foster City - Menhaden Court
761	118	Loma Prieta	6.93	1686	Fremont - Emerson Court
762	118	Loma Prieta	6.93	57064	Fremont - Mission San Jose
763	118	Loma Prieta	6.93	47006	Gilroy - Gavilan Coll.
764	118	Loma Prieta	6.93	57476	Gilroy - Historic Bldg.
765	118	Loma Prieta	6.93	47379	Gilroy Array #1
766	118	Loma Prieta	6.93	47380	Gilroy Array #2
767	118	Loma Prieta	6.93	47381	Gilroy Array #3
768	118	Loma Prieta	6.93	57382	Gilroy Array #4
769	118	Loma Prieta	6.93	57383	Gilroy Array #6
770	118	Loma Prieta	6.93	57425	Gilroy Array #7
771	118	Loma Prieta	6.93	1678	Golden Gate Bridge
772	118	Loma Prieta	6.93	57191	Halls Valley
773	118	Loma Prieta	6.93	58498	Hayward - BART Sta
776	118	Loma Prieta	6.93	47524	Hollister - South & Pine
778	118	Loma Prieta	6.93	1656	Hollister Diff. Array
779	118	Loma Prieta	6.93	16	LGPC
780	118	Loma Prieta	6.93	1590	Larkspur Ferry Terminal (FF)
781	118	Loma Prieta	6.93	58233	Lower Crystal Springs Dam dwnst
782	118	Loma Prieta	6.93	47377	Monterey City Hall
783	118	Loma Prieta	6.93	58472	Oakland - Outer Harbor Wharf
784	118	Loma Prieta	6.93	58224	Oakland - Title & Trust
785	118	Loma Prieta	6.93	68003	Olema - Point Reyes Station
786	118	Loma Prieta	6.93	58264	Palo Alto - 1900 Embarc.
787	118	Loma Prieta	6.93	1601	Palo Alto - SLAC Lab
788	118	Loma Prieta	6.93	58338	Piedmont Jr High
789	118	Loma Prieta	6.93	58043	Point Bonita
790	118	Loma Prieta	6.93	58505	Richmond City Hall
791	118	Loma Prieta	6.93	47189	SAGO South - Surface
792	118	Loma Prieta	6.93	1675	SF - 1295 Shafter
794	118	Loma Prieta	6.93	58130	SF - Diamond Heights
795	118	Loma Prieta	6.93	58131	SF - Pacific Heights
796	118	Loma Prieta	6.93	58222	SF - Presidio
797	118	Loma Prieta	6.93	58151	SF - Rincon Hill
799	118	Loma Prieta	6.93	58223	SF Intern. Airport
800	118	Loma Prieta	6.93	47179	Salinas - John & Work
801	118	Loma Prieta	6.93	57563	San Jose - Santa Teresa Hills
802	118	Loma Prieta	6.93	58065	Saratoga - Aloha Ave
803	118	Loma Prieta	6.93	58235	Saratoga - W Valley Coll.
804	118	Loma Prieta	6.93	58539	So. San Francisco, Sierra Pt.
806	118	Loma Prieta	6.93	1695	Sunnyvale - Colton Ave.
807	118	Loma Prieta	6.93	1688	Sunol - Forest Fire Station
808	118	Loma Prieta	6.93	58117	Treasure Island
809	118	Loma Prieta	6.93	15	UCSC
810	118	Loma Prieta	6.93	58135	UCSC Lick Observatory
811	118	Loma Prieta	6.93	14	WAHO
812	118	Loma Prieta	6.93	58127	Woodside
813	118	Loma Prieta	6.93	58163	Yerba Buena Island
3548	118	Loma Prieta	6.93	57180	Los Gatos - Lexington Dam
815	119	Griva, Greece	6.10	99999	Kilkis
821	121	Erzican, Turkey	6.69	95	Erzincan
825	123	Cape Mendocino	7.01	89005	Cape Mendocino
826	123	Cape Mendocino	7.01	89509	Eureka - Myrtle & West
827	123	Cape Mendocino	7.01	89486	Fortuna - Fortuna Blvd
828	123	Cape Mendocino	7.01	89156	Petrolia
829	123	Cape Mendocino	7.01	89324	Rio Dell Overpass - FF
830	123	Cape Mendocino	7.01	89530	Shelter Cove Airport
832	125	Landers	7.28	21081	Amboy
833	125	Landers	7.28	90088	Anaheim - W Ball Rd
834	125	Landers	7.28	90099	Arcadia - Arcadia Av
835	125	Landers	7.28	90093	Arcadia - Campus Dr
836	125	Landers	7.28	32075	Baker Fire Station
837	125	Landers	7.28	90069	Baldwin Park - N Holly

838	125	Landers	7.28	23559	Barstow
839	125	Landers	7.28	90094	Bell Gardens - Jaboneria
840	125	Landers	7.28	90061	Big Tujunga, Angeles Nat F
841	125	Landers	7.28	33083	Boron Fire Station
842	125	Landers	7.28	90087	Brea - S Flower Av
843	125	Landers	7.28	90086	Buena Park - La Palma
844	125	Landers	7.28	90012	Burbank - N Buena Vista
845	125	Landers	7.28	90052	Calabasas - N Las Virg
846	125	Landers	7.28	90004	Chatsworth - Devonshire
847	125	Landers	7.28	90078	Compton - Castlegate St
848	125	Landers	7.28	23	Coolwater
849	125	Landers	7.28	90070	Covina - W Badillo
850	125	Landers	7.28	12149	Desert Hot Springs
851	125	Landers	7.28	14368	Downey - Co Maint Bldg
852	125	Landers	7.28	90067	Duarte - Mel Canyon Rd.
853	125	Landers	7.28	90066	El Monte - Fairview Av
854	125	Landers	7.28	13122	Featherly Park - Maint
855	125	Landers	7.28	24577	Fort Irwin
856	125	Landers	7.28	90002	Fountain Valley - Euclid
857	125	Landers	7.28	90063	Glendale - Las Palmas
858	125	Landers	7.28	90065	Glendora - N Oakbank
859	125	Landers	7.28	90073	Hacienda Heights - Colima
860	125	Landers	7.28	12331	Hemet Fire Station
861	125	Landers	7.28	90083	Huntington Bch - Waikiki
862	125	Landers	7.28	12026	Indio - Coachella Canal
863	125	Landers	7.28	14196	Inglewood - Union Oil
864	125	Landers	7.28	22170	Joshua Tree
865	125	Landers	7.28	14403	LA - 116th St School
867	125	Landers	7.28	90034	LA - Fletcher Dr
868	125	Landers	7.28	90032	LA - N Figueroa St
869	125	Landers	7.28	90021	LA - N Westmoreland
870	125	Landers	7.28	24400	LA - Obregon Park
871	125	Landers	7.28	90022	LA - S Grand Ave
872	125	Landers	7.28	90020	LA - W 15th St
873	125	Landers	7.28	90023	LA - W 70th St
874	125	Landers	7.28	90080	LB - Orange Ave
875	125	Landers	7.28	90060	La Crescenta - New York
876	125	Landers	7.28	90074	La Habra - Briarcliff
877	125	Landers	7.28	90072	La Puente - Rimgrove Av
878	125	Landers	7.28	90084	Lakewood - Del Amo Blvd
879	125	Landers	7.28	24	Lucerne
880	125	Landers	7.28	100	Mission Creek Fault
881	125	Landers	7.28	5071	Morongo Valley
882	125	Landers	7.28	5070	North Palm Springs
883	125	Landers	7.28	90003	Northridge - 17645 Saticoy St
884	125	Landers	7.28	12025	Palm Springs Airport
885	125	Landers	7.28	23525	Pomona - 4th & Locust FF
886	125	Landers	7.28	12168	Puerta La Cruz
887	125	Landers	7.28	13123	Riverside Airport
888	125	Landers	7.28	23542	San Bernardino - E & Hospitality
889	125	Landers	7.28	90019	San Gabriel - E Grand Ave
890	125	Landers	7.28	90077	Santa Fe Springs - E.Joslin
891	125	Landers	7.28	12206	Silent Valley - Poppet Flat
892	125	Landers	7.28	90006	Sun Valley - Roscoe Blvd
893	125	Landers	7.28	90008	Sun Valley - Sunland
894	125	Landers	7.28	90058	Sunland - Mt Gleason Ave
896	125	Landers	7.28	90089	Tustin - E Sycamore
897	125	Landers	7.28	22161	Twentynine Palms
898	125	Landers	7.28	90090	Villa Park - Serrano Ave
899	125	Landers	7.28	90071	West Covina - S Orange Ave
900	125	Landers	7.28	22074	Yermo Fire Station
901	126	Big Bear-01	6.46	22561	Big Bear Lake - Civic Center
902	126	Big Bear-01	6.46	12149	Desert Hot Springs

903	126	Big Bear-01	6.46	12626	Desert Shores
904	126	Big Bear-01	6.46	24575	Elizabeth Lake
905	126	Big Bear-01	6.46	13122	Featherly Park - Maint
906	126	Big Bear-01	6.46	12331	Hemet Fire Station
907	126	Big Bear-01	6.46	23583	Hesperia - 4th & Palm
908	126	Big Bear-01	6.46	12026	Indio - Coachella Canal
909	126	Big Bear-01	6.46	12543	Indio - Riverside Co Fair Grnds
910	126	Big Bear-01	6.46	22170	Joshua Tree
912	126	Big Bear-01	6.46	24592	LA - City Terrace
913	126	Big Bear-01	6.46	24611	LA - Temple & Hope
914	126	Big Bear-01	6.46	24605	LA - Univ. Hospital
915	126	Big Bear-01	6.46	12624	Lake Cachulla
916	126	Big Bear-01	6.46	11625	Mecca - CVWD Yard
917	126	Big Bear-01	6.46	23572	Mt Baldy - Elementary Sch
918	126	Big Bear-01	6.46	13160	Newport Bch - Irvine Ave. F.S
919	126	Big Bear-01	6.46	11591	North Shore - Durmid
920	126	Big Bear-01	6.46	11613	North Shore - Salton Sea Pk HQ
921	126	Big Bear-01	6.46	12025	Palm Springs Airport
922	126	Big Bear-01	6.46	23584	Pear Blossom - Pallet Creek
923	126	Big Bear-01	6.46	23597	Phelan - Wilson Ranch
924	126	Big Bear-01	6.46	12168	Puerta La Cruz
925	126	Big Bear-01	6.46	23598	Rancho Cucamonga - Deer Can
926	126	Big Bear-01	6.46	23497	Rancho Cucamonga - FF
927	126	Big Bear-01	6.46	13123	Riverside Airport
928	126	Big Bear-01	6.46	12636	Sage - Fire Station
929	126	Big Bear-01	6.46	11628	Salton City
931	126	Big Bear-01	6.46	23542	San Bernardino - E & Hospitality
932	126	Big Bear-01	6.46	12202	San Jacinto - Valley Cemetary
933	126	Big Bear-01	6.46	14578	Seal Beach - Office Bldg
934	126	Big Bear-01	6.46	12206	Silent Valley - Poppet Flat
935	126	Big Bear-01	6.46	12630	Snow Creek
937	126	Big Bear-01	6.46	13172	Temecula - 6th & Mercedes
938	126	Big Bear-01	6.46	13199	Winchester Bergman Ran
939	126	Big Bear-01	6.46	23573	Wrightwood - Nielson Ranch
940	126	Big Bear-01	6.46	23574	Wrightwood - Swarthout
941	126	Big Bear-01	6.46	22074	Yermo Fire Station
942	127	Northridge-01	6.69	24461	Alhambra - Fremont School
943	127	Northridge-01	6.69	25169	Anacapa Island
944	127	Northridge-01	6.69	90088	Anaheim - W Ball Rd
945	127	Northridge-01	6.69	24576	Anaverde Valley - City R
946	127	Northridge-01	6.69	24310	Antelope Buttes
947	127	Northridge-01	6.69	90099	Arcadia - Arcadia Av
948	127	Northridge-01	6.69	90093	Arcadia - Campus Dr
949	127	Northridge-01	6.69	24087	Arleta - Nordhoff Fire Sta
950	127	Northridge-01	6.69	90069	Baldwin Park - N Holly
951	127	Northridge-01	6.69	90094	Bell Gardens - Jaboneria
952	127	Northridge-01	6.69	90014	Beverly Hills - 12520 Mulhol
953	127	Northridge-01	6.69	90013	Beverly Hills - 14145 Mulhol
954	127	Northridge-01	6.69	90061	Big Tujunga, Angeles Nat F
955	127	Northridge-01	6.69	90087	Brea - S Flower Av
956	127	Northridge-01	6.69	90086	Buena Park - La Palma
957	127	Northridge-01	6.69	90059	Burbank - Howard Rd.
958	127	Northridge-01	6.69	25282	Camarillo
959	127	Northridge-01	6.69	90053	Canoga Park - Topanga Can
960	127	Northridge-01	6.69	90057	Canyon Country - W Lost Cany
961	127	Northridge-01	6.69	90040	Carson - Catskill Ave
962	127	Northridge-01	6.69	90081	Carson - Water St
963	127	Northridge-01	6.69	24278	Castaic - Old Ridge Route
964	127	Northridge-01	6.69	90078	Compton - Castlegate St
965	127	Northridge-01	6.69	90068	Covina - S Grand Ave
966	127	Northridge-01	6.69	90070	Covina - W Badillo
967	127	Northridge-01	6.69	90079	Downey - Birchdale
968	127	Northridge-01	6.69	14368	Downey - Co Maint Bldg

969	127	Northridge-01	6.69	90067	Duarte - Mel Canyon Rd.
970	127	Northridge-01	6.69	90066	El Monte - Fairview Av
971	127	Northridge-01	6.69	24575	Elizabeth Lake
972	127	Northridge-01	6.69	13122	Featherly Park - Maint
973	127	Northridge-01	6.69	90085	Garden Grove - Santa Rita
974	127	Northridge-01	6.69	90063	Glendale - Las Palmas
975	127	Northridge-01	6.69	90065	Glendora - N Oakbank
976	127	Northridge-01	6.69	90073	Hacienda Heights - Colima
977	127	Northridge-01	6.69	13660	Hemet - Ryan Airfield
978	127	Northridge-01	6.69	90018	Hollywood - Willoughby Ave
979	127	Northridge-01	6.69	90083	Huntington Bch - Waikiki
980	127	Northridge-01	6.69	13197	Huntington Beach - Lake St
981	127	Northridge-01	6.69	14196	Inglewood - Union Oil
983	127	Northridge-01	6.69	655	Jensen Filter Plant Generator
984	127	Northridge-01	6.69	14403	LA - 116th St School
985	127	Northridge-01	6.69	24157	LA - Baldwin Hills
986	127	Northridge-01	6.69	638	LA - Brentwood VA Hospital
987	127	Northridge-01	6.69	90054	LA - Centinela St
988	127	Northridge-01	6.69	24389	LA - Century City CC North
989	127	Northridge-01	6.69	90015	LA - Chalon Rd
990	127	Northridge-01	6.69	24592	LA - City Terrace
991	127	Northridge-01	6.69	90033	LA - Cypress Ave
993	127	Northridge-01	6.69	90034	LA - Fletcher Dr
994	127	Northridge-01	6.69	141	LA - Griffith Park Observatory
995	127	Northridge-01	6.69	24303	LA - Hollywood Stor FF
996	127	Northridge-01	6.69	90016	LA - N Faring Rd
997	127	Northridge-01	6.69	90032	LA - N Figueroa St
998	127	Northridge-01	6.69	90021	LA - N Westmoreland
999	127	Northridge-01	6.69	24400	LA - Obregon Park
1000	127	Northridge-01	6.69	24612	LA - Pico & Sentous
1001	127	Northridge-01	6.69	90022	LA - S Grand Ave
1003	127	Northridge-01	6.69	90091	LA - Saturn St
1004	127	Northridge-01	6.69	637	LA - Sepulveda VA Hospital
1005	127	Northridge-01	6.69	24611	LA - Temple & Hope
1006	127	Northridge-01	6.69	24688	LA - UCLA Grounds
1007	127	Northridge-01	6.69	24605	LA - Univ. Hospital
1008	127	Northridge-01	6.69	90020	LA - W 15th St
1011	127	Northridge-01	6.69	90017	LA - Wonderland Ave
1012	127	Northridge-01	6.69	99999	LA 00
1013	127	Northridge-01	6.69	0	LA Dam
1014	127	Northridge-01	6.69	14560	LB - City Hall
1015	127	Northridge-01	6.69	14242	LB - Rancho Los Cerritos
1016	127	Northridge-01	6.69	90060	La Crescenta - New York
1017	127	Northridge-01	6.69	90074	La Habra - Briarcliff
1018	127	Northridge-01	6.69	90072	La Puente - Rimgrove Av
1019	127	Northridge-01	6.69	24271	Lake Hughes #1
1020	127	Northridge-01	6.69	24607	Lake Hughes #12A
1021	127	Northridge-01	6.69	24469	Lake Hughes #4 - Camp Mend
1022	127	Northridge-01	6.69	24523	Lake Hughes #4B - Camp Mend
1023	127	Northridge-01	6.69	127	Lake Hughes #9
1024	127	Northridge-01	6.69	90084	Lakewood - Del Amo Blvd
1025	127	Northridge-01	6.69	24475	Lancaster - Fox Airfield Grnd
1026	127	Northridge-01	6.69	90045	Lawndale - Osage Ave
1027	127	Northridge-01	6.69	24305	Leona Valley #1
1028	127	Northridge-01	6.69	24306	Leona Valley #2
1029	127	Northridge-01	6.69	24307	Leona Valley #3
1030	127	Northridge-01	6.69	24308	Leona Valley #4
1031	127	Northridge-01	6.69	24055	Leona Valley #5 - Ritter
1032	127	Northridge-01	6.69	24309	Leona Valley #6
1033	127	Northridge-01	6.69	23595	Littlerock - Brainard Can
1034	127	Northridge-01	6.69	24396	Malibu - Point Dume Sch
1035	127	Northridge-01	6.69	90046	Manhattan Beach - Manhattan
1036	127	Northridge-01	6.69	34093	Mojave - Hwys 14 & 58

1037	127	Northridge-01	6.69	34237	Mojave - Oak Creek Canyon
1038	127	Northridge-01	6.69	90011	Montebello - Bluff Rd.
1039	127	Northridge-01	6.69	24283	Moorpark - Fire Sta
1040	127	Northridge-01	6.69	23572	Mt Baldy - Elementary Sch
1041	127	Northridge-01	6.69	24399	Mt Wilson - CIT Seis Sta
1042	127	Northridge-01	6.69	90009	N Hollywood - Coldwater Can
1043	127	Northridge-01	6.69	24586	Neenach - Sacatara Ck
1044	127	Northridge-01	6.69	24279	Newhall - Fire Sta
1045	127	Northridge-01	6.69	90056	Newhall - W Pico Canyon Rd.
1046	127	Northridge-01	6.69	13160	Newport Bch - Irvine Ave. F.S
1047	127	Northridge-01	6.69	13610	Newport Bch - Newp & Coast
1048	127	Northridge-01	6.69	90003	Northridge - 17645 Saticoy St
1049	127	Northridge-01	6.69	90049	Pacific Palisades - Sunset
1050	127	Northridge-01	6.69	24207	Pacoima Dam (downstr)
1052	127	Northridge-01	6.69	24088	Pacoima Kagel Canyon
1053	127	Northridge-01	6.69	24521	Palmdale - Hwy 14 & Palmdale
1054	127	Northridge-01	6.69	99999	Pardee - SCE
1055	127	Northridge-01	6.69	90095	Pasadena - N Sierra Madre
1056	127	Northridge-01	6.69	23597	Phelan - Wilson Ranch
1057	127	Northridge-01	6.69	90047	Playa Del Rey - Saran
1058	127	Northridge-01	6.69	25148	Point Mugu - Laguna Peak
1059	127	Northridge-01	6.69	25281	Port Hueneme - Naval Lab.
1060	127	Northridge-01	6.69	23598	Rancho Cucamonga - Deer Can
1061	127	Northridge-01	6.69	14404	Rancho Palos Verdes - Hawth
1062	127	Northridge-01	6.69	90044	Rancho Palos Verdes - Luconia
1063	127	Northridge-01	6.69	77	Rinaldi Receiving Sta
1064	127	Northridge-01	6.69	13123	Riverside Airport
1065	127	Northridge-01	6.69	14405	Rolling Hills Est-Rancho Vista
1066	127	Northridge-01	6.69	24092	Rosamond - Airport
1067	127	Northridge-01	6.69	23672	San Bernardino - CSUSB Gr
1068	127	Northridge-01	6.69	5245	San Bernardino - Co Service Bldg - Freefield
1069	127	Northridge-01	6.69	23542	San Bernardino - E & Hospitality
1070	127	Northridge-01	6.69	90019	San Gabriel - E Grand Ave
1071	127	Northridge-01	6.69	12673	San Jacinto - CDF Fire Sta
1072	127	Northridge-01	6.69	24401	San Marino - SW Academy
1073	127	Northridge-01	6.69	14159	San Pedro - Palos Verdes
1074	127	Northridge-01	6.69	24644	Sandberg - Bald Mtn
1075	127	Northridge-01	6.69	25091	Santa Barbara - UCSB Goleta
1076	127	Northridge-01	6.69	90077	Santa Fe Springs - E.Joslin
1077	127	Northridge-01	6.69	24538	Santa Monica City Hall
1078	127	Northridge-01	6.69	5108	Santa Susana Ground
1079	127	Northridge-01	6.69	14578	Seal Beach - Office Bldg
1080	127	Northridge-01	6.69	90055	Simi Valley - Katherine Rd
1082	127	Northridge-01	6.69	90006	Sun Valley - Roscoe Blvd
1083	127	Northridge-01	6.69	90058	Sunland - Mt Gleason Ave
1084	127	Northridge-01	6.69	74	Sylmar - Converter Sta
1085	127	Northridge-01	6.69	75	Sylmar - Converter Sta East
1086	127	Northridge-01	6.69	24514	Sylmar - Olive View Med FF
1088	127	Northridge-01	6.69	90082	Terminal Island - S Seaside
1089	127	Northridge-01	6.69	5081	Topanga - Fire Sta
1090	127	Northridge-01	6.69	90089	Tustin - E Sycamore
1091	127	Northridge-01	6.69	24047	Vasquez Rocks Park
1092	127	Northridge-01	6.69	25340	Ventura - Harbor & California
1093	127	Northridge-01	6.69	90090	Villa Park - Serrano Ave
1094	127	Northridge-01	6.69	90071	West Covina - S Orange Ave
1095	127	Northridge-01	6.69	90075	Whittier - S. Alta Dr
1096	127	Northridge-01	6.69	23590	Wrightwood - Jackson Flat
1097	127	Northridge-01	6.69	23573	Wrightwood - Nielson Ranch
1098	127	Northridge-01	6.69	23574	Wrightwood - Swarthout
1100	129	Kobe, Japan	6.90	99999	Abeno
1101	129	Kobe, Japan	6.90	99999	Amagasaki
1102	129	Kobe, Japan	6.90	99999	Chihaya
1103	129	Kobe, Japan	6.90	99999	FUK

1104	129	Kobe, Japan	6.90	99999	Fukushima
1105	129	Kobe, Japan	6.90	99999	HIK
1106	129	Kobe, Japan	6.90	99999	KJMA
1107	129	Kobe, Japan	6.90	99999	Kakogawa
1108	129	Kobe, Japan	6.90	99999	Kobe University
1109	129	Kobe, Japan	6.90	99999	MZH
1110	129	Kobe, Japan	6.90	99999	Morigawachi
1111	129	Kobe, Japan	6.90	99999	Nishi-Akashi
1112	129	Kobe, Japan	6.90	99999	OKA
1113	129	Kobe, Japan	6.90	99999	OSAJ
1114	129	Kobe, Japan	6.90	99999	Port Island (0 m)
1115	129	Kobe, Japan	6.90	99999	Sakai
1116	129	Kobe, Japan	6.90	99999	Shin-Osaka
1117	129	Kobe, Japan	6.90	99999	TOT
1118	129	Kobe, Japan	6.90	99999	Tadoka
1119	129	Kobe, Japan	6.90	99999	Takarazuka
1120	129	Kobe, Japan	6.90	99999	Takatori
1121	129	Kobe, Japan	6.90	99999	Yae
1123	130	Kozani, Greece-01	6.40	99999	Florina
1124	130	Kozani, Greece-01	6.40	99999	Kardista
1126	130	Kozani, Greece-01	6.40	99999	Kozani
1139	134	Dinar, Turkey	6.40	99999	Cardak
1141	134	Dinar, Turkey	6.40	99999	Dinar
1147	136	Kocaeli, Turkey	7.51	99999	Ambarli
1148	136	Kocaeli, Turkey	7.51	99999	Arcelik
1149	136	Kocaeli, Turkey	7.51	99999	Atakoy
1151	136	Kocaeli, Turkey	7.51	99999	Balikesir
1153	136	Kocaeli, Turkey	7.51	99999	Botas
1154	136	Kocaeli, Turkey	7.51	99999	Bursa Sivil
1155	136	Kocaeli, Turkey	7.51	99999	Bursa Tofas
1157	136	Kocaeli, Turkey	7.51	99999	Cekmece
1158	136	Kocaeli, Turkey	7.51	99999	Duzce
1159	136	Kocaeli, Turkey	7.51	99999	Eregli
1160	136	Kocaeli, Turkey	7.51	99999	Fatih
1162	136	Kocaeli, Turkey	7.51	99999	Goynuk
1163	136	Kocaeli, Turkey	7.51	99999	Hava Alani
1164	136	Kocaeli, Turkey	7.51	99999	Istanbul
1165	136	Kocaeli, Turkey	7.51	99999	Izmit
1166	136	Kocaeli, Turkey	7.51	99999	Iznik
1167	136	Kocaeli, Turkey	7.51	99999	Kutahya
1169	136	Kocaeli, Turkey	7.51	99999	Maslak
1170	136	Kocaeli, Turkey	7.51	99999	Mecidiyekoy
1172	136	Kocaeli, Turkey	7.51	99999	Tekirdag
1176	136	Kocaeli, Turkey	7.51	99999	Yarimca
1177	136	Kocaeli, Turkey	7.51	99999	Zeytinburnu
1180	137	Chi-Chi, Taiwan	7.62	99999	CHY002
1181	137	Chi-Chi, Taiwan	7.62	99999	CHY004
1182	137	Chi-Chi, Taiwan	7.62	99999	CHY006
1183	137	Chi-Chi, Taiwan	7.62	99999	CHY008
1184	137	Chi-Chi, Taiwan	7.62	99999	CHY010
1185	137	Chi-Chi, Taiwan	7.62	99999	CHY012
1186	137	Chi-Chi, Taiwan	7.62	99999	CHY014
1187	137	Chi-Chi, Taiwan	7.62	99999	CHY015
1188	137	Chi-Chi, Taiwan	7.62	99999	CHY016
1189	137	Chi-Chi, Taiwan	7.62	99999	CHY017
1190	137	Chi-Chi, Taiwan	7.62	99999	CHY019
1191	137	Chi-Chi, Taiwan	7.62	99999	CHY022
1192	137	Chi-Chi, Taiwan	7.62	99999	CHY023
1193	137	Chi-Chi, Taiwan	7.62	99999	CHY024
1194	137	Chi-Chi, Taiwan	7.62	99999	CHY025
1195	137	Chi-Chi, Taiwan	7.62	99999	CHY026
1196	137	Chi-Chi, Taiwan	7.62	99999	CHY027
1197	137	Chi-Chi, Taiwan	7.62	99999	CHY028

1198	137	Chi-Chi, Taiwan	7.62	99999	CHY029
1199	137	Chi-Chi, Taiwan	7.62	99999	CHY032
1200	137	Chi-Chi, Taiwan	7.62	99999	CHY033
1201	137	Chi-Chi, Taiwan	7.62	99999	CHY034
1202	137	Chi-Chi, Taiwan	7.62	99999	CHY035
1203	137	Chi-Chi, Taiwan	7.62	99999	CHY036
1204	137	Chi-Chi, Taiwan	7.62	99999	CHY039
1205	137	Chi-Chi, Taiwan	7.62	99999	CHY041
1206	137	Chi-Chi, Taiwan	7.62	99999	CHY042
1207	137	Chi-Chi, Taiwan	7.62	99999	CHY044
1208	137	Chi-Chi, Taiwan	7.62	99999	CHY046
1209	137	Chi-Chi, Taiwan	7.62	99999	CHY047
1210	137	Chi-Chi, Taiwan	7.62	99999	CHY050
1211	137	Chi-Chi, Taiwan	7.62	99999	CHY052
1212	137	Chi-Chi, Taiwan	7.62	99999	CHY054
1213	137	Chi-Chi, Taiwan	7.62	99999	CHY055
1214	137	Chi-Chi, Taiwan	7.62	99999	CHY057
1215	137	Chi-Chi, Taiwan	7.62	99999	CHY058
1216	137	Chi-Chi, Taiwan	7.62	99999	CHY059
1217	137	Chi-Chi, Taiwan	7.62	99999	CHY060
1218	137	Chi-Chi, Taiwan	7.62	99999	CHY061
1220	137	Chi-Chi, Taiwan	7.62	99999	CHY063
1221	137	Chi-Chi, Taiwan	7.62	99999	CHY065
1222	137	Chi-Chi, Taiwan	7.62	99999	CHY066
1223	137	Chi-Chi, Taiwan	7.62	99999	CHY067
1224	137	Chi-Chi, Taiwan	7.62	99999	CHY069
1225	137	Chi-Chi, Taiwan	7.62	99999	CHY070
1226	137	Chi-Chi, Taiwan	7.62	99999	CHY071
1227	137	Chi-Chi, Taiwan	7.62	99999	CHY074
1228	137	Chi-Chi, Taiwan	7.62	99999	CHY076
1229	137	Chi-Chi, Taiwan	7.62	99999	CHY078
1230	137	Chi-Chi, Taiwan	7.62	99999	CHY079
1231	137	Chi-Chi, Taiwan	7.62	99999	CHY080
1232	137	Chi-Chi, Taiwan	7.62	99999	CHY081
1233	137	Chi-Chi, Taiwan	7.62	99999	CHY082
1234	137	Chi-Chi, Taiwan	7.62	99999	CHY086
1235	137	Chi-Chi, Taiwan	7.62	99999	CHY087
1236	137	Chi-Chi, Taiwan	7.62	99999	CHY088
1237	137	Chi-Chi, Taiwan	7.62	99999	CHY090
1238	137	Chi-Chi, Taiwan	7.62	99999	CHY092
1239	137	Chi-Chi, Taiwan	7.62	99999	CHY093
1240	137	Chi-Chi, Taiwan	7.62	99999	CHY094
1241	137	Chi-Chi, Taiwan	7.62	99999	CHY096
1242	137	Chi-Chi, Taiwan	7.62	99999	CHY099
1243	137	Chi-Chi, Taiwan	7.62	99999	CHY100
1244	137	Chi-Chi, Taiwan	7.62	99999	CHY101
1245	137	Chi-Chi, Taiwan	7.62	99999	CHY102
1246	137	Chi-Chi, Taiwan	7.62	99999	CHY104
1247	137	Chi-Chi, Taiwan	7.62	99999	CHY107
1248	137	Chi-Chi, Taiwan	7.62	9999917	CHY109
1250	137	Chi-Chi, Taiwan	7.62	99999	CHY116
1256	137	Chi-Chi, Taiwan	7.62	99999	HWA002
1257	137	Chi-Chi, Taiwan	7.62	99999	HWA003
1258	137	Chi-Chi, Taiwan	7.62	99999	HWA005
1259	137	Chi-Chi, Taiwan	7.62	99999	HWA006
1260	137	Chi-Chi, Taiwan	7.62	99999	HWA007
1261	137	Chi-Chi, Taiwan	7.62	99999	HWA009
1262	137	Chi-Chi, Taiwan	7.62	99999	HWA011
1263	137	Chi-Chi, Taiwan	7.62	99999	HWA012
1264	137	Chi-Chi, Taiwan	7.62	99999	HWA013
1265	137	Chi-Chi, Taiwan	7.62	99999	HWA014
1266	137	Chi-Chi, Taiwan	7.62	99999	HWA015
1267	137	Chi-Chi, Taiwan	7.62	99999	HWA016

1268	137	Chi-Chi, Taiwan	7.62	99999	HWA017
1269	137	Chi-Chi, Taiwan	7.62	99999	HWA019
1270	137	Chi-Chi, Taiwan	7.62	99999	HWA020
1271	137	Chi-Chi, Taiwan	7.62	99999	HWA022
1272	137	Chi-Chi, Taiwan	7.62	99999	HWA023
1273	137	Chi-Chi, Taiwan	7.62	99999	HWA024
1274	137	Chi-Chi, Taiwan	7.62	99999	HWA025
1275	137	Chi-Chi, Taiwan	7.62	99999	HWA026
1276	137	Chi-Chi, Taiwan	7.62	99999	HWA027
1277	137	Chi-Chi, Taiwan	7.62	99999	HWA028
1278	137	Chi-Chi, Taiwan	7.62	99999	HWA029
1279	137	Chi-Chi, Taiwan	7.62	99999	HWA030
1280	137	Chi-Chi, Taiwan	7.62	99999	HWA031
1281	137	Chi-Chi, Taiwan	7.62	99999	HWA032
1282	137	Chi-Chi, Taiwan	7.62	99999	HWA033
1283	137	Chi-Chi, Taiwan	7.62	99999	HWA034
1284	137	Chi-Chi, Taiwan	7.62	99999	HWA035
1285	137	Chi-Chi, Taiwan	7.62	99999	HWA036
1286	137	Chi-Chi, Taiwan	7.62	99999	HWA037
1287	137	Chi-Chi, Taiwan	7.62	99999	HWA038
1288	137	Chi-Chi, Taiwan	7.62	99999	HWA039
1289	137	Chi-Chi, Taiwan	7.62	99999	HWA041
1290	137	Chi-Chi, Taiwan	7.62	99999	HWA043
1291	137	Chi-Chi, Taiwan	7.62	99999	HWA044
1292	137	Chi-Chi, Taiwan	7.62	99999	HWA045
1293	137	Chi-Chi, Taiwan	7.62	99999	HWA046
1294	137	Chi-Chi, Taiwan	7.62	99999	HWA048
1295	137	Chi-Chi, Taiwan	7.62	99999	HWA049
1296	137	Chi-Chi, Taiwan	7.62	99999	HWA050
1297	137	Chi-Chi, Taiwan	7.62	99999	HWA051
1300	137	Chi-Chi, Taiwan	7.62	99999	HWA055
1301	137	Chi-Chi, Taiwan	7.62	99999	HWA056
1302	137	Chi-Chi, Taiwan	7.62	99999	HWA057
1303	137	Chi-Chi, Taiwan	7.62	99999	HWA058
1304	137	Chi-Chi, Taiwan	7.62	99999	HWA059
1305	137	Chi-Chi, Taiwan	7.62	99999	HWA060
1306	137	Chi-Chi, Taiwan	7.62	99999	HWA2
1307	137	Chi-Chi, Taiwan	7.62	99999	ILA001
1308	137	Chi-Chi, Taiwan	7.62	99999	ILA002
1309	137	Chi-Chi, Taiwan	7.62	99999	ILA003
1310	137	Chi-Chi, Taiwan	7.62	99999	ILA004
1311	137	Chi-Chi, Taiwan	7.62	99999	ILA005
1312	137	Chi-Chi, Taiwan	7.62	99999	ILA006
1313	137	Chi-Chi, Taiwan	7.62	99999	ILA007
1314	137	Chi-Chi, Taiwan	7.62	99999	ILA008
1315	137	Chi-Chi, Taiwan	7.62	99999	ILA010
1316	137	Chi-Chi, Taiwan	7.62	99999	ILA012
1317	137	Chi-Chi, Taiwan	7.62	99999	ILA013
1318	137	Chi-Chi, Taiwan	7.62	99999	ILA014
1319	137	Chi-Chi, Taiwan	7.62	99999	ILA015
1320	137	Chi-Chi, Taiwan	7.62	99999	ILA016
1321	137	Chi-Chi, Taiwan	7.62	99999	ILA021
1322	137	Chi-Chi, Taiwan	7.62	99999	ILA024
1323	137	Chi-Chi, Taiwan	7.62	9999917	ILA027
1324	137	Chi-Chi, Taiwan	7.62	99999	ILA030
1325	137	Chi-Chi, Taiwan	7.62	99999	ILA031
1326	137	Chi-Chi, Taiwan	7.62	9999917	ILA032
1327	137	Chi-Chi, Taiwan	7.62	9999917	ILA035
1328	137	Chi-Chi, Taiwan	7.62	99999	ILA036
1329	137	Chi-Chi, Taiwan	7.62	99999	ILA037
1330	137	Chi-Chi, Taiwan	7.62	9999917	ILA039
1331	137	Chi-Chi, Taiwan	7.62	99999	ILA041
1332	137	Chi-Chi, Taiwan	7.62	99999	ILA042

1333	137	Chi-Chi, Taiwan	7.62	9999917	ILA043
1334	137	Chi-Chi, Taiwan	7.62	99999	ILA044
1335	137	Chi-Chi, Taiwan	7.62	99999	ILA046
1336	137	Chi-Chi, Taiwan	7.62	99999	ILA048
1337	137	Chi-Chi, Taiwan	7.62	99999	ILA049
1338	137	Chi-Chi, Taiwan	7.62	99999	ILA050
1339	137	Chi-Chi, Taiwan	7.62	99999	ILA051
1340	137	Chi-Chi, Taiwan	7.62	99999	ILA052
1341	137	Chi-Chi, Taiwan	7.62	99999	ILA054
1342	137	Chi-Chi, Taiwan	7.62	99999	ILA055
1343	137	Chi-Chi, Taiwan	7.62	99999	ILA056
1344	137	Chi-Chi, Taiwan	7.62	99999	ILA059
1345	137	Chi-Chi, Taiwan	7.62	99999	ILA061
1346	137	Chi-Chi, Taiwan	7.62	99999	ILA062
1347	137	Chi-Chi, Taiwan	7.62	99999	ILA063
1348	137	Chi-Chi, Taiwan	7.62	99999	ILA064
1349	137	Chi-Chi, Taiwan	7.62	99999	ILA066
1350	137	Chi-Chi, Taiwan	7.62	99999	ILA067
1351	137	Chi-Chi, Taiwan	7.62	99999	KAU001
1352	137	Chi-Chi, Taiwan	7.62	99999	KAU003
1353	137	Chi-Chi, Taiwan	7.62	99999	KAU006
1354	137	Chi-Chi, Taiwan	7.62	99999	KAU007
1355	137	Chi-Chi, Taiwan	7.62	99999	KAU008
1356	137	Chi-Chi, Taiwan	7.62	99999	KAU010
1357	137	Chi-Chi, Taiwan	7.62	99999	KAU011
1358	137	Chi-Chi, Taiwan	7.62	99999	KAU012
1359	137	Chi-Chi, Taiwan	7.62	99999	KAU015
1360	137	Chi-Chi, Taiwan	7.62	99999	KAU018
1361	137	Chi-Chi, Taiwan	7.62	99999	KAU020
1362	137	Chi-Chi, Taiwan	7.62	99999	KAU022
1363	137	Chi-Chi, Taiwan	7.62	99999	KAU030
1364	137	Chi-Chi, Taiwan	7.62	99999	KAU032
1365	137	Chi-Chi, Taiwan	7.62	99999	KAU033
1367	137	Chi-Chi, Taiwan	7.62	99999	KAU037
1368	137	Chi-Chi, Taiwan	7.62	99999	KAU038
1373	137	Chi-Chi, Taiwan	7.62	99999	KAU044
1374	137	Chi-Chi, Taiwan	7.62	99999	KAU046
1375	137	Chi-Chi, Taiwan	7.62	99999	KAU047
1376	137	Chi-Chi, Taiwan	7.62	99999	KAU048
1377	137	Chi-Chi, Taiwan	7.62	99999	KAU050
1380	137	Chi-Chi, Taiwan	7.62	99999	KAU054
1381	137	Chi-Chi, Taiwan	7.62	99999	KAU057
1382	137	Chi-Chi, Taiwan	7.62	99999	KAU058
1383	137	Chi-Chi, Taiwan	7.62	99999	KAU062
1384	137	Chi-Chi, Taiwan	7.62	99999	KAU063
1385	137	Chi-Chi, Taiwan	7.62	99999	KAU064
1386	137	Chi-Chi, Taiwan	7.62	99999	KAU066
1387	137	Chi-Chi, Taiwan	7.62	99999	KAU069
1388	137	Chi-Chi, Taiwan	7.62	99999	KAU073
1389	137	Chi-Chi, Taiwan	7.62	99999	KAU074
1390	137	Chi-Chi, Taiwan	7.62	99999	KAU075
1391	137	Chi-Chi, Taiwan	7.62	99999	KAU077
1392	137	Chi-Chi, Taiwan	7.62	99999	KAU078
1393	137	Chi-Chi, Taiwan	7.62	99999	KAU081
1394	137	Chi-Chi, Taiwan	7.62	99999	KAU082
1395	137	Chi-Chi, Taiwan	7.62	99999	KAU083
1396	137	Chi-Chi, Taiwan	7.62	99999	KAU085
1397	137	Chi-Chi, Taiwan	7.62	99999	KAU086
1398	137	Chi-Chi, Taiwan	7.62	99999	KAU087
1399	137	Chi-Chi, Taiwan	7.62	99999	KAU088
1402	137	Chi-Chi, Taiwan	7.62	9999917	NST
1409	137	Chi-Chi, Taiwan	7.62	9999917	TAP
1410	137	Chi-Chi, Taiwan	7.62	99999	TAP003

1411	137	Chi-Chi, Taiwan	7.62	99999	TAP005
1412	137	Chi-Chi, Taiwan	7.62	99999	TAP006
1413	137	Chi-Chi, Taiwan	7.62	99999	TAP007
1414	137	Chi-Chi, Taiwan	7.62	99999	TAP008
1415	137	Chi-Chi, Taiwan	7.62	99999	TAP010
1416	137	Chi-Chi, Taiwan	7.62	99999	TAP012
1417	137	Chi-Chi, Taiwan	7.62	99999	TAP013
1418	137	Chi-Chi, Taiwan	7.62	99999	TAP014
1419	137	Chi-Chi, Taiwan	7.62	99999	TAP017
1420	137	Chi-Chi, Taiwan	7.62	99999	TAP020
1421	137	Chi-Chi, Taiwan	7.62	99999	TAP021
1422	137	Chi-Chi, Taiwan	7.62	99999	TAP024
1423	137	Chi-Chi, Taiwan	7.62	99999	TAP026
1424	137	Chi-Chi, Taiwan	7.62	99999	TAP028
1425	137	Chi-Chi, Taiwan	7.62	99999	TAP032
1426	137	Chi-Chi, Taiwan	7.62	99999	TAP034
1427	137	Chi-Chi, Taiwan	7.62	99999	TAP035
1428	137	Chi-Chi, Taiwan	7.62	99999	TAP036
1429	137	Chi-Chi, Taiwan	7.62	99999	TAP041
1430	137	Chi-Chi, Taiwan	7.62	99999	TAP042
1431	137	Chi-Chi, Taiwan	7.62	99999	TAP043
1432	137	Chi-Chi, Taiwan	7.62	99999	TAP046
1433	137	Chi-Chi, Taiwan	7.62	99999	TAP047
1434	137	Chi-Chi, Taiwan	7.62	99999	TAP049
1435	137	Chi-Chi, Taiwan	7.62	99999	TAP051
1436	137	Chi-Chi, Taiwan	7.62	99999	TAP052
1437	137	Chi-Chi, Taiwan	7.62	99999	TAP053
1438	137	Chi-Chi, Taiwan	7.62	99999	TAP059
1439	137	Chi-Chi, Taiwan	7.62	99999	TAP060
1440	137	Chi-Chi, Taiwan	7.62	99999	TAP065
1442	137	Chi-Chi, Taiwan	7.62	99999	TAP067
1443	137	Chi-Chi, Taiwan	7.62	99999	TAP069
1444	137	Chi-Chi, Taiwan	7.62	99999	TAP072
1445	137	Chi-Chi, Taiwan	7.62	99999	TAP075
1446	137	Chi-Chi, Taiwan	7.62	99999	TAP077
1447	137	Chi-Chi, Taiwan	7.62	99999	TAP078
1448	137	Chi-Chi, Taiwan	7.62	99999	TAP079
1449	137	Chi-Chi, Taiwan	7.62	99999	TAP081
1450	137	Chi-Chi, Taiwan	7.62	99999	TAP083
1451	137	Chi-Chi, Taiwan	7.62	99999	TAP084
1452	137	Chi-Chi, Taiwan	7.62	99999	TAP086
1453	137	Chi-Chi, Taiwan	7.62	99999	TAP087
1454	137	Chi-Chi, Taiwan	7.62	99999	TAP090
1455	137	Chi-Chi, Taiwan	7.62	99999	TAP094
1456	137	Chi-Chi, Taiwan	7.62	99999	TAP095
1457	137	Chi-Chi, Taiwan	7.62	99999	TAP097
1458	137	Chi-Chi, Taiwan	7.62	99999	TAP098
1459	137	Chi-Chi, Taiwan	7.62	99999	TAP100
1463	137	Chi-Chi, Taiwan	7.62	99999	TCU003
1464	137	Chi-Chi, Taiwan	7.62	99999	TCU006
1465	137	Chi-Chi, Taiwan	7.62	99999	TCU007
1466	137	Chi-Chi, Taiwan	7.62	99999	TCU008
1468	137	Chi-Chi, Taiwan	7.62	99999	TCU010
1470	137	Chi-Chi, Taiwan	7.62	99999	TCU014
1471	137	Chi-Chi, Taiwan	7.62	99999	TCU015
1472	137	Chi-Chi, Taiwan	7.62	99999	TCU017
1473	137	Chi-Chi, Taiwan	7.62	99999	TCU018
1475	137	Chi-Chi, Taiwan	7.62	99999	TCU026
1476	137	Chi-Chi, Taiwan	7.62	99999	TCU029
1477	137	Chi-Chi, Taiwan	7.62	99999	TCU031
1478	137	Chi-Chi, Taiwan	7.62	99999	TCU033
1479	137	Chi-Chi, Taiwan	7.62	99999	TCU034
1480	137	Chi-Chi, Taiwan	7.62	99999	TCU036

1481	137	Chi-Chi, Taiwan	7.62	99999	TCU038
1482	137	Chi-Chi, Taiwan	7.62	99999	TCU039
1483	137	Chi-Chi, Taiwan	7.62	99999	TCU040
1484	137	Chi-Chi, Taiwan	7.62	99999	TCU042
1485	137	Chi-Chi, Taiwan	7.62	99999	TCU045
1486	137	Chi-Chi, Taiwan	7.62	99999	TCU046
1487	137	Chi-Chi, Taiwan	7.62	99999	TCU047
1488	137	Chi-Chi, Taiwan	7.62	99999	TCU048
1489	137	Chi-Chi, Taiwan	7.62	99999	TCU049
1490	137	Chi-Chi, Taiwan	7.62	99999	TCU050
1491	137	Chi-Chi, Taiwan	7.62	99999	TCU051
1492	137	Chi-Chi, Taiwan	7.62	99999	TCU052
1493	137	Chi-Chi, Taiwan	7.62	99999	TCU053
1494	137	Chi-Chi, Taiwan	7.62	99999	TCU054
1495	137	Chi-Chi, Taiwan	7.62	99999	TCU055
1496	137	Chi-Chi, Taiwan	7.62	99999	TCU056
1497	137	Chi-Chi, Taiwan	7.62	99999	TCU057
1498	137	Chi-Chi, Taiwan	7.62	99999	TCU059
1499	137	Chi-Chi, Taiwan	7.62	99999	TCU060
1500	137	Chi-Chi, Taiwan	7.62	99999	TCU061
1501	137	Chi-Chi, Taiwan	7.62	99999	TCU063
1502	137	Chi-Chi, Taiwan	7.62	99999	TCU064
1503	137	Chi-Chi, Taiwan	7.62	99999	TCU065
1504	137	Chi-Chi, Taiwan	7.62	99999	TCU067
1505	137	Chi-Chi, Taiwan	7.62	99999	TCU068
1506	137	Chi-Chi, Taiwan	7.62	99999	TCU070
1507	137	Chi-Chi, Taiwan	7.62	99999	TCU071
1508	137	Chi-Chi, Taiwan	7.62	99999	TCU072
1509	137	Chi-Chi, Taiwan	7.62	99999	TCU074
1510	137	Chi-Chi, Taiwan	7.62	99999	TCU075
1511	137	Chi-Chi, Taiwan	7.62	99999	TCU076
1512	137	Chi-Chi, Taiwan	7.62	99999	TCU078
1513	137	Chi-Chi, Taiwan	7.62	99999	TCU079
1515	137	Chi-Chi, Taiwan	7.62	99999	TCU082
1516	137	Chi-Chi, Taiwan	7.62	99999	TCU083
1517	137	Chi-Chi, Taiwan	7.62	99999	TCU084
1518	137	Chi-Chi, Taiwan	7.62	99999	TCU085
1519	137	Chi-Chi, Taiwan	7.62	99999	TCU087
1520	137	Chi-Chi, Taiwan	7.62	99999	TCU088
1521	137	Chi-Chi, Taiwan	7.62	99999	TCU089
1522	137	Chi-Chi, Taiwan	7.62	99999	TCU092
1523	137	Chi-Chi, Taiwan	7.62	99999	TCU094
1524	137	Chi-Chi, Taiwan	7.62	99999	TCU095
1525	137	Chi-Chi, Taiwan	7.62	99999	TCU096
1526	137	Chi-Chi, Taiwan	7.62	99999	TCU098
1527	137	Chi-Chi, Taiwan	7.62	99999	TCU100
1528	137	Chi-Chi, Taiwan	7.62	99999	TCU101
1529	137	Chi-Chi, Taiwan	7.62	99999	TCU102
1530	137	Chi-Chi, Taiwan	7.62	99999	TCU103
1531	137	Chi-Chi, Taiwan	7.62	99999	TCU104
1532	137	Chi-Chi, Taiwan	7.62	99999	TCU105
1533	137	Chi-Chi, Taiwan	7.62	99999	TCU106
1534	137	Chi-Chi, Taiwan	7.62	99999	TCU107
1535	137	Chi-Chi, Taiwan	7.62	99999	TCU109
1536	137	Chi-Chi, Taiwan	7.62	99999	TCU110
1537	137	Chi-Chi, Taiwan	7.62	99999	TCU111
1538	137	Chi-Chi, Taiwan	7.62	99999	TCU112
1539	137	Chi-Chi, Taiwan	7.62	99999	TCU113
1540	137	Chi-Chi, Taiwan	7.62	99999	TCU115
1541	137	Chi-Chi, Taiwan	7.62	99999	TCU116
1542	137	Chi-Chi, Taiwan	7.62	99999	TCU117
1543	137	Chi-Chi, Taiwan	7.62	99999	TCU118
1544	137	Chi-Chi, Taiwan	7.62	99999	TCU119

1545	137	Chi-Chi, Taiwan	7.62	99999	TCU120
1546	137	Chi-Chi, Taiwan	7.62	99999	TCU122
1547	137	Chi-Chi, Taiwan	7.62	99999	TCU123
1548	137	Chi-Chi, Taiwan	7.62	99999	TCU128
1549	137	Chi-Chi, Taiwan	7.62	9999936	TCU129
1550	137	Chi-Chi, Taiwan	7.62	99999	TCU136
1551	137	Chi-Chi, Taiwan	7.62	99999	TCU138
1552	137	Chi-Chi, Taiwan	7.62	99999	TCU140
1553	137	Chi-Chi, Taiwan	7.62	99999	TCU141
1554	137	Chi-Chi, Taiwan	7.62	99999	TCU145
1555	137	Chi-Chi, Taiwan	7.62	99999	TCU147
1557	137	Chi-Chi, Taiwan	7.62	99999	TTN001
1558	137	Chi-Chi, Taiwan	7.62	99999	TTN002
1559	137	Chi-Chi, Taiwan	7.62	99999	TTN003
1560	137	Chi-Chi, Taiwan	7.62	99999	TTN004
1561	137	Chi-Chi, Taiwan	7.62	99999	TTN005
1562	137	Chi-Chi, Taiwan	7.62	99999	TTN006
1563	137	Chi-Chi, Taiwan	7.62	99999	TTN007
1564	137	Chi-Chi, Taiwan	7.62	99999	TTN008
1565	137	Chi-Chi, Taiwan	7.62	99999	TTN009
1566	137	Chi-Chi, Taiwan	7.62	99999	TTN010
1567	137	Chi-Chi, Taiwan	7.62	99999	TTN012
1568	137	Chi-Chi, Taiwan	7.62	99999	TTN013
1569	137	Chi-Chi, Taiwan	7.62	99999	TTN014
1570	137	Chi-Chi, Taiwan	7.62	99999	TTN015
1572	137	Chi-Chi, Taiwan	7.62	99999	TTN018
1573	137	Chi-Chi, Taiwan	7.62	99999	TTN020
1574	137	Chi-Chi, Taiwan	7.62	99999	TTN022
1575	137	Chi-Chi, Taiwan	7.62	99999	TTN023
1576	137	Chi-Chi, Taiwan	7.62	99999	TTN024
1577	137	Chi-Chi, Taiwan	7.62	99999	TTN025
1578	137	Chi-Chi, Taiwan	7.62	99999	TTN026
1579	137	Chi-Chi, Taiwan	7.62	99999	TTN027
1580	137	Chi-Chi, Taiwan	7.62	99999	TTN028
1581	137	Chi-Chi, Taiwan	7.62	99999	TTN031
1582	137	Chi-Chi, Taiwan	7.62	99999	TTN032
1583	137	Chi-Chi, Taiwan	7.62	99999	TTN033
1584	137	Chi-Chi, Taiwan	7.62	99999	TTN036
1585	137	Chi-Chi, Taiwan	7.62	99999	TTN040
1586	137	Chi-Chi, Taiwan	7.62	99999	TTN041
1587	137	Chi-Chi, Taiwan	7.62	99999	TTN042
1588	137	Chi-Chi, Taiwan	7.62	99999	TTN044
1589	137	Chi-Chi, Taiwan	7.62	99999	TTN045
1590	137	Chi-Chi, Taiwan	7.62	99999	TTN046
1592	137	Chi-Chi, Taiwan	7.62	99999	TTN048
1593	137	Chi-Chi, Taiwan	7.62	99999	TTN050
1594	137	Chi-Chi, Taiwan	7.62	99999	TTN051
1598	137	Chi-Chi, Taiwan	7.62	9999917	WTC
1599	138	Duzce, Turkey	7.14	99999	Ambarli
1600	138	Duzce, Turkey	7.14	99999	Arcelik
1601	138	Duzce, Turkey	7.14	99999	Aslan R.
1602	138	Duzce, Turkey	7.14	99999	Bolu
1603	138	Duzce, Turkey	7.14	99999	Bursa Tofas
1604	138	Duzce, Turkey	7.14	99999	Cekmece
1605	138	Duzce, Turkey	7.14	99999	Duzce
1606	138	Duzce, Turkey	7.14	99999	Fatih
1608	138	Duzce, Turkey	7.14	99999	Hava Alani
1609	138	Duzce, Turkey	7.14	99999	Kocamustafapaba Tomb
1610	138	Duzce, Turkey	7.14	99999	Kutahya
1619	138	Duzce, Turkey	7.14	99999	Mudurnu
1620	138	Duzce, Turkey	7.14	99999	Sakarya
1621	138	Duzce, Turkey	7.14	99999	Yarimca
1626	140	Sitka, Alaska	7.68	2714	Sitka Observatory

1627	141	Caldiran, Turkey	7.21	37	Maku
1628	142	St Elias, Alaska	7.54	2734	Icy Bay
1629	142	St Elias, Alaska	7.54	2728	Yakutat
1630	143	Upland	5.63	99999	Ocean Floor SEMS III
1631	143	Upland	5.63	23525	Pomona - 4th & Locust FF
1632	143	Upland	5.63	23497	Rancho Cucamonga - FF
1633	144	Manjil, Iran	7.37	99999	Abbar
1634	144	Manjil, Iran	7.37	99999	Abhar
1636	144	Manjil, Iran	7.37	99999	Qazvin
1637	144	Manjil, Iran	7.37	99999	Rudsar
1638	144	Manjil, Iran	7.37	99999	Tehran - Building & Housing
1639	144	Manjil, Iran	7.37	99999	Tehran - Sarif University
1640	144	Manjil, Iran	7.37	99999	Tonekabun
1641	145	Sierra Madre	5.61	24402	Altadena - Eaton Canyon
1642	145	Sierra Madre	5.61	23210	Cogswell Dam - Right Abutment
1643	145	Sierra Madre	5.61	24592	LA - City Terrace
1644	145	Sierra Madre	5.61	24400	LA - Obregon Park
1645	145	Sierra Madre	5.61	24399	Mt Wilson - CIT Seis Sta
1646	145	Sierra Madre	5.61	5296	Pasadena - USGS/NSMP Office
1647	145	Sierra Madre	5.61	24401	San Marino - SW Academy
1649	145	Sierra Madre	5.61	24047	Vasquez Rocks Park
1740	152	Little Skull Mtn,NV	5.65	99999	Station #1-Lathrop Wells
1741	152	Little Skull Mtn,NV	5.65	99999	Station #2-NTS Control Pt. 1
1742	152	Little Skull Mtn,NV	5.65	99999	Station #3-Beaty
1743	152	Little Skull Mtn,NV	5.65	99999	Station #4-Pahrump 2
1744	152	Little Skull Mtn,NV	5.65	99999	Station #5-Pahrump 1
1745	152	Little Skull Mtn,NV	5.65	99999	Station #6-Las Vegas Calico Basin
1746	152	Little Skull Mtn,NV	5.65	99999	Station #7-Las Vegas Ann Road
1747	152	Little Skull Mtn,NV	5.65	99999	Station #8-Death Valley Scotties Castle
1759	158	Hector Mine	7.13	5239	12440 Imperial Hwy, North Grn
1761	158	Hector Mine	7.13	24402	Altadena - Eaton Canyon
1762	158	Hector Mine	7.13	21081	Amboy
1763	158	Hector Mine	7.13	5044	Anza - Pinyon Flat
1764	158	Hector Mine	7.13	5222	Anza - Tripp Flats Training
1765	158	Hector Mine	7.13	24087	Arleta - Nordhoff Fire Sta
1766	158	Hector Mine	7.13	32075	Baker Fire Station
1767	158	Hector Mine	7.13	12674	Banning - Twin Pines Road
1768	158	Hector Mine	7.13	23559	Barstow
1769	158	Hector Mine	7.13	5402	Beverly Hills Pac Bell Bsmt
1770	158	Hector Mine	7.13	22791	Big Bear Lake - Fire Station
1771	158	Hector Mine	7.13	5271	Bombay Beach Fire Station
1772	158	Hector Mine	7.13	5398	Burbank Airport
1773	158	Hector Mine	7.13	5073	Cabazon
1776	158	Hector Mine	7.13	12149	Desert Hot Springs
1777	158	Hector Mine	7.13	5265	Devore - Devore Water Company
1778	158	Hector Mine	7.13	14368	Downey - Co Maint Bldg
1779	158	Hector Mine	7.13	412	El Centro Array #10
1780	158	Hector Mine	7.13	13122	Featherly Park - Maint
1782	158	Hector Mine	7.13	5075	Forest Falls Post Office
1783	158	Hector Mine	7.13	24577	Fort Irwin
1784	158	Hector Mine	7.13	11684	Frink
1785	158	Hector Mine	7.13	5069	Fun Valley
1786	158	Hector Mine	7.13	22T04	Heart Bar State Park
1787	158	Hector Mine	7.13	99999	Hector
1788	158	Hector Mine	7.13	12331	Hemet Fire Station
1789	158	Hector Mine	7.13	23583	Hesperia - 4th & Palm
1790	158	Hector Mine	7.13	13197	Huntington Beach - Lake St
1791	158	Hector Mine	7.13	12026	Indio - Coachella Canal
1792	158	Hector Mine	7.13	12543	Indio - Riverside Co Fair Grnds
1794	158	Hector Mine	7.13	22170	Joshua Tree
1795	158	Hector Mine	7.13	12647	Joshua Tree N.M. - Keys View
1796	158	Hector Mine	7.13	14403	LA - 116th St School
1797	158	Hector Mine	7.13	24592	LA - City Terrace

1798	158	Hector Mine	7.13	14787	LA - MLK Hospital Grounds
1799	158	Hector Mine	7.13	24400	LA - Obregon Park
1800	158	Hector Mine	7.13	24612	LA - Pico & Sentous
1801	158	Hector Mine	7.13	24611	LA - Temple & Hope
1803	158	Hector Mine	7.13	14560	LB - City Hall
1804	158	Hector Mine	7.13	5408	La Canada - Wald Residence
1805	158	Hector Mine	7.13	24271	Lake Hughes #1
1806	158	Hector Mine	7.13	5029	Leona Valley - Fire Station #1
1807	158	Hector Mine	7.13	5030	Little Rock Post Office
1808	158	Hector Mine	7.13	5396	Los Angeles - Acosta Residence
1809	158	Hector Mine	7.13	5409	Lytle Creek Fire Station
1810	158	Hector Mine	7.13	11625	Mecca - CVWD Yard
1811	158	Hector Mine	7.13	5162	Mentone Fire Station #9
1812	158	Hector Mine	7.13	5076	Mill Creek Ranger Station
1813	158	Hector Mine	7.13	5071	Morongo Valley
1814	158	Hector Mine	7.13	24279	Newhall - Fire Sta
1815	158	Hector Mine	7.13	13160	Newport Bch - Irvine Ave. F.S
1816	158	Hector Mine	7.13	5295	North Palm Springs Fire Sta #36
1817	158	Hector Mine	7.13	11591	North Shore - Durmid
1818	158	Hector Mine	7.13	24088	Pacoima Kagel Canyon
1819	158	Hector Mine	7.13	262	Palmdale Fire Station
1820	158	Hector Mine	7.13	24691	Pasadena - Fair Oaks & Walnut
1821	158	Hector Mine	7.13	23525	Pomona - 4th & Locust FF
1822	158	Hector Mine	7.13	13123	Riverside Airport
1823	158	Hector Mine	7.13	11628	Salton City
1824	158	Hector Mine	7.13	5331	San Bernardino - Del Rosa Wk Sta
1825	158	Hector Mine	7.13	23542	San Bernardino - E & Hospitality
1826	158	Hector Mine	7.13	5339	San Bernardino - Fire Sta. #10
1827	158	Hector Mine	7.13	5337	San Bernardino - Fire Sta. #4
1828	158	Hector Mine	7.13	5330	San Bernardino - Fire Sta. #9
1829	158	Hector Mine	7.13	5328	San Bernardino - Mont. Mem Pk
1830	158	Hector Mine	7.13	5371	San Bernardino - N Verdemont Sch
1831	158	Hector Mine	7.13	12204	San Jacinto - Soboba
1832	158	Hector Mine	7.13	5300	Seven Oaks Dam Project Office
1833	158	Hector Mine	7.13	12630	Snow Creek
1834	158	Hector Mine	7.13	24763	Sylmar - County Hospital Grounds
1835	158	Hector Mine	7.13	13172	Temecula - 6th & Mercedes
1836	158	Hector Mine	7.13	22161	Twentynine Palms
1837	158	Hector Mine	7.13	5031	Valyermo Forest Fire Station
1838	158	Hector Mine	7.13	5072	Whitewater Trout Farm
1839	158	Hector Mine	7.13	14840	Whittier - Scott & Whittier
1840	158	Hector Mine	7.13	289	Whittier Narrows Dam downstream
1841	158	Hector Mine	7.13	23573	Wrightwood - Nielson Ranch
1842	158	Hector Mine	7.13	5282	Wrightwood Post Office
1843	160	Yountville	5.00	1002	APEEL 2 - Redwood City
1844	160	Yountville	5.00	1756	Alameda - Oakland Airport FS #4
1845	160	Yountville	5.00	1755	Alameda Fire Station #1
1846	160	Yountville	5.00	1760	Benicia Fire Station #1
1847	160	Yountville	5.00	1690	Danville Fire Station
1848	160	Yountville	5.00	1689	Dublin - Fire Station
1849	160	Yountville	5.00	1737	El Cerrito - Mira Vista Country
1850	160	Yountville	5.00	1753	Foster City - Bowditch School
1851	160	Yountville	5.00	1678	Golden Gate Bridge
1852	160	Yountville	5.00	1590	Larkspur Ferry Terminal (FF)
1853	160	Yountville	5.00	1765	Napa Fire Station #3
1854	160	Yountville	5.00	1762	Novato Fire Station #1
1855	160	Yountville	5.00	1751	Novato Fire Station #4
1856	160	Yountville	5.00	1743	Petaluma Fire Station
1857	160	Yountville	5.00	1768	Petaluma Fire Station #1
1858	160	Yountville	5.00	1691	Pleasant Hill Fire Station #2
1859	160	Yountville	5.00	1785	Pleasanton Fire Station #1
1860	160	Yountville	5.00	1749	Richmond - Point Molate
1861	160	Yountville	5.00	1722	Richmond Rod & Gun Club

1862	160	Yountville	5.00	1735	San Francisco - 9th Circuit Crt
1863	160	Yountville	5.00	1774	San Francisco - Fire Station #2
1865	160	Yountville	5.00	1767	Santa Rosa Fire Station #1
1866	160	Yountville	5.00	1761	Sonoma Fire Station #1
1867	160	Yountville	5.00	1759	Vallejo Fire Station #1
1868	161	Big Bear-02	4.53	23788	Colton - Hospital Complex FF
1869	161	Big Bear-02	4.53	5341	Colton - Kaiser Medical Clinic
1870	161	Big Bear-02	4.53	5265	Devore - Devore Water Company
1871	161	Big Bear-02	4.53	5075	Forest Falls Post Office
1872	161	Big Bear-02	4.53	23957	Helendale - Helendale & Vista
1873	161	Big Bear-02	4.53	12331	Hemet Fire Station
1874	161	Big Bear-02	4.53	23583	Hesperia - 4th & Palm
1875	161	Big Bear-02	4.53	5161	Highland Fire Station
1876	161	Big Bear-02	4.53	13924	Homeland - Hwy 74 & Sultanas
1877	161	Big Bear-02	4.53	5294	Indio - Jackson Road
1878	161	Big Bear-02	4.53	12904	Indio - Monroe & Carreon
1879	161	Big Bear-02	4.53	22959	Landers - Hwy 247 & Jesse
1880	161	Big Bear-02	4.53	129	Loma Linda Univ Medical Center
1881	161	Big Bear-02	4.53	5409	Lytle Creek Fire Station
1882	161	Big Bear-02	4.53	5162	Mentone Fire Station #9
1883	161	Big Bear-02	4.53	5076	Mill Creek Ranger Station
1884	161	Big Bear-02	4.53	13927	Moreno Valley - Alessandro&More
1885	161	Big Bear-02	4.53	13925	Moreno Valley - Indian & Kennedy
1886	161	Big Bear-02	4.53	5071	Morongo Valley
1887	161	Big Bear-02	4.53	5295	North Palm Springs Fire Sta #36
1888	161	Big Bear-02	4.53	23958	Pinon Hills - Hwy 138 & Mtn Road
1889	161	Big Bear-02	4.53	5037	Reche Canyon - Olive Dell Ranch
1890	161	Big Bear-02	4.53	13915	Riverside - I215 & 3rd
1891	161	Big Bear-02	4.53	5331	San Bernardino - Del Rosa Wk Sta
1892	161	Big Bear-02	4.53	23542	San Bernardino - E & Hospitality
1893	161	Big Bear-02	4.53	5339	San Bernardino - Fire Sta. #10
1894	161	Big Bear-02	4.53	5329	San Bernardino - Fire Sta. #11
1895	161	Big Bear-02	4.53	5337	San Bernardino - Fire Sta. #4
1896	161	Big Bear-02	4.53	5327	San Bernardino - Fire Sta. #7
1897	161	Big Bear-02	4.53	5330	San Bernardino - Fire Sta. #9
1898	161	Big Bear-02	4.53	5373	San Bernardino - Lincoln School
1899	161	Big Bear-02	4.53	23898	San Bernardino - Medical Center
1900	161	Big Bear-02	4.53	5328	San Bernardino - Mont. Mem Pk
1901	161	Big Bear-02	4.53	23780	San Bernardino - Mtn Vw & Clstr
1902	161	Big Bear-02	4.53	5336	San Bernardino - Serrano School
1903	161	Big Bear-02	4.53	5300	Seven Oaks Dam Downstream Surf.
1904	161	Big Bear-02	4.53	5300	Seven Oaks Dam Right Abt.
1905	161	Big Bear-02	4.53	13930	Sun City - I215 & McCall Blvd
1906	161	Big Bear-02	4.53	5031	Valyermo Forest Fire Station
1907	161	Big Bear-02	4.53	5072	Whitewater Trout Farm
1908	161	Big Bear-02	4.53	5282	Wrightwood Post Office
1909	161	Big Bear-02	4.53	22074	Yermo Fire Station
1910	161	Big Bear-02	4.53	23920	Yucaipa Valley - Calimesa & Cnty
1911	162	Mohawk Val, Portola	5.17	2019	Carson City - Nevada Com College
1912	162	Mohawk Val, Portola	5.17	1133	Martis Creek Dam (Dwn Stream)
1913	162	Mohawk Val, Portola	5.17	1133	Martis Creek Dam (Left Abtmnt)
1914	162	Mohawk Val, Portola	5.17	1133	Martis Creek Dam (Right Abtmnt)
1915	162	Mohawk Val, Portola	5.17	2023	Reno - Sierra Pacific Power Co
1916	162	Mohawk Val, Portola	5.17	2018	Silver Springs Fire Station
1917	163	Anza-02	4.92	2467	Alpine Fire Station
1918	163	Anza-02	4.92	5044	Anza - Pinyon Flat
1919	163	Anza-02	4.92	5222	Anza - Tripp Flats Training
1920	163	Anza-02	4.92	5160	Anza Fire Station
1921	163	Anza-02	4.92	12919	Beaumont - 6th & Maple
1922	163	Anza-02	4.92	22791	Big Bear Lake - Fire Station
1923	163	Anza-02	4.92	5220	Borrego Springs - Scripps Clinic
1924	163	Anza-02	4.92	5073	Cabazon
1925	163	Anza-02	4.92	5053	Calexico Fire Station

1926	163	Anza-02	4.92	13096	Canyon Lake Vacation Dr&San Joaq
1927	163	Anza-02	4.92	12076	Coachella - 6th & Palm
1928	163	Anza-02	4.92	13099	Corona - 6th & Smith
1929	163	Anza-02	4.92	13098	Corona - Hwy 91 & McKinley
1930	163	Anza-02	4.92	464	El Centro - Meadows Union School
1931	163	Anza-02	4.92	412	El Centro Array #10
1932	163	Anza-02	4.92	5058	El Centro Array #11
1933	163	Anza-02	4.92	5028	El Centro Array #7
1934	163	Anza-02	4.92	5069	Fun Valley
1935	163	Anza-02	4.92	12923	Hemet - Acacia & Stanford
1936	163	Anza-02	4.92	13093	Hemet - Cawston & Devonshire
1937	163	Anza-02	4.92	12331	Hemet Fire Station
1938	163	Anza-02	4.92	5161	Highland Fire Station
1940	163	Anza-02	4.92	13924	Homeland - Hwy 74 & Sultanas
1941	163	Anza-02	4.92	5043	Hurkey Creek Park
1942	163	Anza-02	4.92	12116	Idyllwild - Hwy 243 & Pine Crest
1943	163	Anza-02	4.92	5232	Idyllwild - Keenwild Fire Sta.
1944	163	Anza-02	4.92	5372	Idyllwild - Kenworthy Fire Sta.
1945	163	Anza-02	4.92	12966	Indian Wells - Hwy111 & El Dorad
1946	163	Anza-02	4.92	5294	Indio - Jackson Road
1947	163	Anza-02	4.92	22170	Joshua Tree
1948	163	Anza-02	4.92	12951	La Quinta - Bermudas & Durango
1949	163	Anza-02	4.92	13922	Lake Elsinore - Graham & Poe
1950	163	Anza-02	4.92	5270	Mecca Fire Station
1951	163	Anza-02	4.92	13929	Menifee Valley - Murrieta&Scott
1952	163	Anza-02	4.92	5076	Mill Creek Ranger Station
1953	163	Anza-02	4.92	23091	Mira Loma - Mission&San Sevaine
1954	163	Anza-02	4.92	13927	Moreno Valley - Alessandro&More
1955	163	Anza-02	4.92	13925	Moreno Valley - Indian & Kennedy
1956	163	Anza-02	4.92	13080	Moreno Valley - Sunny Mead & Vil
1957	163	Anza-02	4.92	5071	Morongo Valley
1958	163	Anza-02	4.92	5223	Mountain Center - Pine Mtn Rnch
1959	163	Anza-02	4.92	11023	Niland Fire Station
1960	163	Anza-02	4.92	5295	North Palm Springs Fire Sta #36
1961	163	Anza-02	4.92	13095	Nuevo - 11th & McKinley
1962	163	Anza-02	4.92	5375	Ocotillo Wells - Veh. Rec. Area
1963	163	Anza-02	4.92	12952	Palm Desert - Country Club & Por
1964	163	Anza-02	4.92	13928	Perris - San Jacinto & C Street
1965	163	Anza-02	4.92	3449	Poway - City Hall Grounds
1966	163	Anza-02	4.92	12092	Radec - Sage & Cottonwood School
1967	163	Anza-02	4.92	12953	Rancho Mirage - G Ford & B Hope
1968	163	Anza-02	4.92	5037	Reche Canyon - Olive Dell Ranch
1969	163	Anza-02	4.92	13913	Riverside - Hole & La Sierra
1970	163	Anza-02	4.92	13079	Riverside - Hwy 91 & Van Buren
1971	163	Anza-02	4.92	13921	Riverside - Limonite & Downey
1972	163	Anza-02	4.92	13916	Riverside - Van Buren&Trautwein
1973	163	Anza-02	4.92	13123	Riverside Airport
1974	163	Anza-02	4.92	12636	Sage - Fire Station
1975	163	Anza-02	4.92	5331	San Bernardino - Del Rosa Wk Sta
1976	163	Anza-02	4.92	5339	San Bernardino - Fire Sta. #10
1977	163	Anza-02	4.92	5329	San Bernardino - Fire Sta. #11
1978	163	Anza-02	4.92	5337	San Bernardino - Fire Sta. #4
1979	163	Anza-02	4.92	5327	San Bernardino - Fire Sta. #7
1980	163	Anza-02	4.92	5373	San Bernardino - Lincoln School
1981	163	Anza-02	4.92	5328	San Bernardino - Mont. Mem Pk
1982	163	Anza-02	4.92	5336	San Bernardino - Serrano School
1983	163	Anza-02	4.92	5289	San Jacinto - MWD West Portal
1984	163	Anza-02	4.92	12102	San Jacinto CDF Fire Station 25
1985	163	Anza-02	4.92	5300	Seven Oaks Dam Downstream Surf.
1986	163	Anza-02	4.92	13930	Sun City - I215 & McCall Blvd
1987	163	Anza-02	4.92	13172	Temecula - 6th & Mercedes
1988	163	Anza-02	4.92	22954	Twentynine Palms - Two Miles&Alp
1989	163	Anza-02	4.92	5072	Whitewater Trout Farm

1990	164	Gulf of California	5.70	5054	Bonds Corner
1991	164	Gulf of California	5.70	5053	Calexico Fire Station
1992	164	Gulf of California	5.70	5061	Calipatria Fire Station
1993	164	Gulf of California	5.70	464	El Centro - Meadows Union School
1994	164	Gulf of California	5.70	412	El Centro Array #10
1995	164	Gulf of California	5.70	5058	El Centro Array #11
1996	164	Gulf of California	5.70	5028	El Centro Array #7
1998	164	Gulf of California	5.70	5055	Holtville Post Office
1999	164	Gulf of California	5.70	5272	Imperial Valley - Midway Well
2000	164	Gulf of California	5.70	5052	Plaster City
2001	164	Gulf of California	5.70	5273	Seeley School
2002	165	CA/Baja Border Area	5.31	5060	Brawley Airport
2003	165	CA/Baja Border Area	5.31	5053	Calexico Fire Station
2004	165	CA/Baja Border Area	5.31	5061	Calipatria Fire Station
2005	165	CA/Baja Border Area	5.31	464	El Centro - Meadows Union School
2006	165	CA/Baja Border Area	5.31	412	El Centro Array #10
2007	165	CA/Baja Border Area	5.31	5058	El Centro Array #11
2008	165	CA/Baja Border Area	5.31	5028	El Centro Array #7
2009	165	CA/Baja Border Area	5.31	5055	Holtville Post Office
2010	165	CA/Baja Border Area	5.31	5062	Salton Sea Wildlife Refuge
2011	166	Gilroy	4.90	1756	Alameda - Oakland Airport FS #4
2012	166	Gilroy	4.90	1755	Alameda Fire Station #1
2013	166	Gilroy	4.90	47729	Big Sur - Hwy 1 & Pfeiffer Cyn
2014	166	Gilroy	4.90	1720	Cupertino - Sunnyvale Rod & Gun
2015	166	Gilroy	4.90	1689	Dublin - Fire Station
2016	166	Gilroy	4.90	1753	Foster City - Bowditch School
2017	166	Gilroy	4.90	1750	Fremont - Coyote Hills Park
2018	166	Gilroy	4.90	57064	Fremont - Mission San Jose
2019	166	Gilroy	4.90	47006	Gilroy - Gavilan Coll.
2020	166	Gilroy	4.90	47381	Gilroy Array #3
2021	166	Gilroy	4.90	57383	Gilroy Array #6
2022	166	Gilroy	4.90	1678	Golden Gate Bridge
2023	166	Gilroy	4.90	1754	Hayward Fire - Station #1
2024	166	Gilroy	4.90	1797	Hollister - Airport Bldg #3
2026	166	Gilroy	4.90	47524	Hollister - South & Pine
2027	166	Gilroy	4.90	1697	Los Gatos - Los Altos Rod & Gun
2028	166	Gilroy	4.90	1784	Menlo Park - USGS Bldg #11 Shop
2029	166	Gilroy	4.90	1745	Menlo Park - USGS Bldg #15 FF
2030	166	Gilroy	4.90	1758	Morgan Hill - El Toro Fire Sta
2031	166	Gilroy	4.90	1787	Palo Alto - Fire Station #7 SLAC
2032	166	Gilroy	4.90	1749	Richmond - Point Molate
2033	166	Gilroy	4.90	47762	Salinas - County Hospital Gnds
2034	166	Gilroy	4.90	1675	San Francisco - Fire Station #17
2036	166	Gilroy	4.90	57600	San Jose - Emory & Bellrose
2037	166	Gilroy	4.90	57604	San Jose - S Clara Co Bldg Grnd
2038	166	Gilroy	4.90	1742	San Jose - Weather Station
2039	166	Gilroy	4.90	47126	San Juan Bautista, 24 Polk St
2040	166	Gilroy	4.90	57748	Santa Clara - Hwy 237/Alviso OVP
2041	166	Gilroy	4.90	48906	Santa Cruz - Co Office Bldg Gnds
2042	166	Gilroy	4.90	1695	Sunnyvale - Colton Ave.
2043	166	Gilroy	4.90	1688	Sunol - Forest Fire Station
2044	166	Gilroy	4.90	1684	Sunol - Ohlone Wilderness Reg Pk
2045	166	Gilroy	4.90	1739	Union City - Masonic Home
2046	166	Gilroy	4.90	1752	Woodside - Filoli Visitor Center
2047	167	Yorba Linda	4.27	13066	Anaheim - Brookhurst & Crescent
2048	167	Yorba Linda	4.27	13068	Anaheim - Hwy 91 & Weir Cyn Rd
2049	167	Yorba Linda	4.27	13849	Anaheim - Lakeview & Riverdale
2050	167	Yorba Linda	4.27	13873	Brea - Central Ave Caltrans Yard
2051	167	Yorba Linda	4.27	24941	City of Commerce - Whittier &
2052	167	Yorba Linda	4.27	13099	Corona - 6th & Smith
2053	167	Yorba Linda	4.27	13100	Corona - Green River & Cyn Crest
2054	167	Yorba Linda	4.27	13878	Fullerton - CSU Fullerton Grnds
2055	167	Yorba Linda	4.27	13880	Fullerton - Hermosa & Harbor

2056	167	Yorba Linda	4.27	13879	Fullerton - Valencia&Brookhurst
2057	167	Yorba Linda	4.27	13881	La Habra - La Habra&Monte Vista
2058	167	Yorba Linda	4.27	13079	Riverside - Hwy 91 & Van Buren
2089	168	Nenana Mountain, Alaska	6.70	FA02	Fairbanks - Ester Fire Station
2090	168	Nenana Mountain, Alaska	6.70	2797	Fairbanks - Geophysic. Obs, CIGO
2091	168	Nenana Mountain, Alaska	6.70	ps07	TAPS Pump Station #07
2092	168	Nenana Mountain, Alaska	6.70	ps08	TAPS Pump Station #08
2093	168	Nenana Mountain, Alaska	6.70	ps09	TAPS Pump Station #09
2107	169	Denali, Alaska	7.90	Carl	Carlo (temp)
2109	169	Denali, Alaska	7.90	FA02	Fairbanks - Ester Fire Station
2110	169	Denali, Alaska	7.90	2797	Fairbanks - Geophysic. Obs, CIGO
2111	169	Denali, Alaska	7.90	R109	R109 (temp)
2112	169	Denali, Alaska	7.90	ps08	TAPS Pump Station #08
2113	169	Denali, Alaska	7.90	ps09	TAPS Pump Station #09
2114	169	Denali, Alaska	7.90	ps10	TAPS Pump Station #10
2115	169	Denali, Alaska	7.90	ps11	TAPS Pump Station #11
2116	169	Denali, Alaska	7.90	ps12	TAPS Pump Station #12
2119	170	Big Bear City	4.92	5222	Anza - Tripp Flats Training
2120	170	Big Bear City	4.92	5073	Cabazon
2121	170	Big Bear City	4.92	5341	Colton - Kaiser Medical Clinic
2122	170	Big Bear City	4.92	5265	Devore - Devore Water Company
2123	170	Big Bear City	4.92	5075	Forest Falls Post Office
2124	170	Big Bear City	4.92	5161	Highland Fire Station
2125	170	Big Bear City	4.92	5294	Indio - Jackson Road
2126	170	Big Bear City	4.92	5029	Leona Valley - Fire Station #1
2127	170	Big Bear City	4.92	129	Loma Linda Univ Medical Center
2128	170	Big Bear City	4.92	5396	Los Angeles - Acosta Residence
2129	170	Big Bear City	4.92	5162	Mentone Fire Station #9
2130	170	Big Bear City	4.92	5076	Mill Creek Ranger Station
2131	170	Big Bear City	4.92	5071	Morongo Valley
2132	170	Big Bear City	4.92	5295	North Palm Springs Fire Sta #36
2133	170	Big Bear City	4.92	262	Palmdale Fire Station
2134	170	Big Bear City	4.92	5032	Paradise Springs - Camp Office
2135	170	Big Bear City	4.92	5296	Pasadena - USGS/NSMP Office
2137	170	Big Bear City	4.92	5245	San Bernardino - Co Service Bldg - Freefield
2138	170	Big Bear City	4.92	5331	San Bernardino - Del Rosa Wk Sta
2139	170	Big Bear City	4.92	5339	San Bernardino - Fire Sta. #10
2140	170	Big Bear City	4.92	5329	San Bernardino - Fire Sta. #11
2141	170	Big Bear City	4.92	5337	San Bernardino - Fire Sta. #4
2142	170	Big Bear City	4.92	5327	San Bernardino - Fire Sta. #7
2143	170	Big Bear City	4.92	5330	San Bernardino - Fire Sta. #9
2144	170	Big Bear City	4.92	5373	San Bernardino - Lincoln School
2145	170	Big Bear City	4.92	5328	San Bernardino - Mont. Mem Pk
2146	170	Big Bear City	4.92	5371	San Bernardino - N Verdemont Sch
2147	170	Big Bear City	4.92	5336	San Bernardino - Serrano School
2148	170	Big Bear City	4.92	5036	San Bernardino - Sycamore FS
2149	170	Big Bear City	4.92	5300	Seven Oaks Dam Downstream Surf.
2150	170	Big Bear City	4.92	5300	Seven Oaks Dam Right Abt.
2151	170	Big Bear City	4.92	5435	Sky Valley - Fire Station #56
2152	170	Big Bear City	4.92	5423	Sylmar - Fire Station #91
2153	170	Big Bear City	4.92	5031	Valyermo Forest Fire Station
2154	170	Big Bear City	4.92	5072	Whitewater Trout Farm
2155	170	Big Bear City	4.92	5282	Wrightwood Post Office

Appendix B: Response to Questions by the U.S. Geological Survey (USGS) and California Geological Survey (CGS)

This appendix presents our response to USGS and CGS questions that were submitted to the NGA model developers in advance of the September 25, 2006, USGS independent expert panel review workshop. Only those questions and responses that pertain either specifically or generically to the CB-NGA model are presented. While most of the responses listed in this appendix were written by the authors, the responses to Questions B.12, B.13 and B.14 were taken in whole or in part from written responses by Norm Abrahamson (written communication, 2006).

B.1 USGS QUESTION #1

Do you consider your ground motion prediction equations appropriate for seismic hazard assessments of California and throughout the western U.S.? Please explain. If you had left out international data and only used California data would you get a significantly different answer? Please explain.

There are really two issues to address regarding this question. The first issue is the potential difference between extensional and non-extensional tectonic regimes and the second issue is the potential difference between different geographic regions. The first issue regarding different tectonic regimes is important since much of California is in a non-extensional tectonic regime whereas most of the remainder of the western U.S. (WUS) is in an extensional tectonic regime. This issue is addressed by showing plots of inter-event residuals versus magnitude segregated by tectonic regime. The second issue is addressed by showing plots of inter-event residuals versus magnitude and intra-event residuals versus distance (R_{RUP}) and 30m shear-wave velocity (V_{S30}), all segregated by geographic region.

B.1.1 Regional Distribution of Database

Before responding to the question, we would first like to summarize the geographical distribution of our database. The distribution of the database by magnitude, distance and geographic region is given in Figure B.1. The regions identified in this figure are California, the WUS outside of California, Alaska and Taiwan. All other regions are combined into a single category called Other. Figure B.1 clearly shows that the database for $\mathbf{M} < 7.3$ events is dominated by strong motion recordings from California. The limited amount of WUS data fall within the data cloud for California. At larger magnitudes, the data from Taiwan, Alaska, and the Other regions predominate. The extent to which the different geographic regions might have influenced our model is discussed below.

B.1.2 Distribution of Inter-Event Residuals by Geographic Region

The distribution of the inter-event residuals (source terms) by geographic region plotted against magnitude is shown in Figures B.2–B.5 for PGA and PSA at periods of 0.2, 1.0 and 3.0s,

respectively. One might argue that the residuals show a slight bias towards underpredicting ground motions for California earthquakes. But the average residuals for California indicate that there is only a +5% bias in the predicted ground motions at short periods and a +9% bias in the predicted ground motions at long periods. The biggest biases are for Alaska, where ground motions are overpredicted at all periods, and the WUS, where ground motions are grossly overpredicted at long periods. The Taiwan (i.e., 1999 Chi-Chi) earthquake (**M** 7.6) is overpredicted at short periods but is well-predicted at long periods. Of course, these biases are based on the assumption that the magnitude scaling predicted by the model is correct.

A second concern is whether the magnitude scaling at large magnitudes is biased. It appears that the California bias might be larger for events with $\mathbf{M} > 6.7$. If this is true, the magnitude scaling would need to be adjusted. However, there are only five California earthquakes between $\mathbf{M} = 6.7$ and 7.4, which are not enough to constrain magnitude scaling at large magnitudes. It is primarily the Alaska earthquakes that are responsible for offsetting the California events. We see no reason why these Alaska events are not a suitable analogue for California. In fact, many seismologists have used the 2002 Denali (**M** 7.9) earthquake as a prototype for a large earthquake on the San Andreas Fault. One of the more spectacular results is the very low residuals (near –1.0) at periods of 1.0 and 3.0s for two WUS earthquakes. A potential reason for this bias is discussed in the next section.

B.1.3 Distribution of Inter-Event Residuals by Tectonic Regime

The distribution of the inter-event residuals (source terms) by tectonic regime plotted against magnitude is shown in Figures B.6–B.9 for PGA and PSA at periods of 0.2, 1.0 and 3.0s, respectively. It should be noted that the classification of a region as extensional or non-extensional was taken directly from the PEER database. In this database, the 1999 Kocaeli (**M** 7.5) and 1999 Duzce (**M** 7.1) earthquakes, both from western Turkey, and the 1992 Landers (**M** 7.3) and the 1999 Hector Mine (**M** 7.1) earthquakes, both from the Mojave Desert in California, are classified as coming from a non-extensional regime. Art Frankel of the USGS and John Anderson of the University of Nevada (Reno) have suggested that both of these regions might be extensional rather than non-extensional.[1]

The figures show that there does not appear to be a significant bias between extensional and non-extensional regimes at short periods. Nor does there appear to be a bias associated with the four earthquakes of questionable tectonic regime classification. One of the more spectacular results is the very low residuals (near –1.0) at 1.0 and 3.0s periods for two WUS earthquakes: 1983 Borah Peak (**M** 6.9) and 1992 Little Skull Mtn. (**M** 5.7). Both events occurred in the extensional tectonic regime of the Basin and Range Province and have residuals at short periods that are not out of line with the other earthquakes. Both of these earthquakes occurred in a region dominated by volcanic rock, possibly at or very near the surface, which is likely to have a very shallow sediment depth (i.e., a small value of $Z_{2.5}$). However, our database does not

[1] After this response was written, Paul Spudich and Dave Boore of the USGS investigated the four earthquakes in question and determined that they occurred within a non-extensional regime.

contain estimates of sediment depth for the sites that recorded these earthquakes. Our model predicts very low long-period ground motions for sites with $Z_{2.5} < 1$ km, which might explain the observed biases. Because of this, we did not allow these events to bias the normal-faulting factor at long periods in our model. See the discussion of this issue in the main text of the report.

B.1.4 Distribution of Intra-Event Residuals by Distance and 30m Shear-Wave Velocity

The distribution of the intra-event residuals by geographic region plotted against distance (R_{RUP}) is shown in Figures B.10–B.13 for PGA and PSA at periods of 0.2, 1.0 and 3.0s, respectively. The plots are shown in terms of log distance to be consistent with how the parameter is used in the regression and to emphasize those recordings at short distances that are of greater engineering interest. These figures indicate that there does not appear to be a regional bias in any of the residuals.

The distribution of the intra-event residuals by geographic region plotted against 30m shear-wave velocity (V_{S30}) is shown in Figures B.14–B.17. Similar to the plots with distance, these figures indicate that there does not appear to be a regional bias in any of the residuals, except for a tendency to underpredict 3.0s spectral accelerations at $V_{S30} > 1000$ m/s in both California and Taiwan. The reason for this underprediction is unknown at the present time. It is interesting to note that in general the model seems valid for predicting ground motions for NEHRP E sites, even though we have recommended in our report that the user exercise caution when predicting ground motions for such low-velocity sites. We made this recommendation to bring attention to the fact that the shaking response of some NEHRP E sites is problematic at high values of ground motion and are best addressed using site-specific response analyses.

B.1.5 Conclusion

Based on the results and discussion presented above, we believe that our empirical ground motion model is appropriate for predicting ground motions in California for purposes of seismic hazard assessment. Its validity in the WUS is more problematic, because there are only three earthquakes in our database that are outside of California and all three come from the extensional Basin and Range Province. Two of these events have long-period ground motions that are grossly overpredicted at long periods, which we attribute to shallow sediments of unknown depth. Aside from these two earthquakes, we believe that our residuals show that our ground-motion predictions do not appear to have a significant regional bias and that earthquakes from regions outside of California and the WUS are appropriate for estimating ground motions in these regions.[2]

The question of whether our results would have been significantly different had we used only California data is difficult to answer without the painstaking task of re-running our analysis and re-interpreting the results. This question gets at the appropriateness of our predicted magnitude scaling at $\mathbf{M} > 6.7$, which is based on only five California earthquakes, the largest being 7.4. We believe that the five California earthquakes in our database within this magnitude range are insufficient to constrain magnitude scaling at large magnitudes, so we would not recommend re-running our analysis with only California earthquakes. Assuming the same magnitude scaling predicted by our model, we find a bias of only 5–9%, depending on period, in the predicted California ground motions, which we do not find to be significant. We do

[2] The USGS Tiger Team came to the same conclusion.

acknowledge that the magnitude scaling at large magnitudes is less certain that that at smaller magnitudes, which is appropriately addressed by increasing the epistemic uncertainty at these magnitudes. In our opinion, restricting the database to the few California earthquakes at $\mathbf{M} > 6.7$ would more likely significantly bias the magnitude scaling and, therefore, the median predictions of ground motion at large magnitudes at the expense of reducing both the aleatory and epistemic uncertainty.

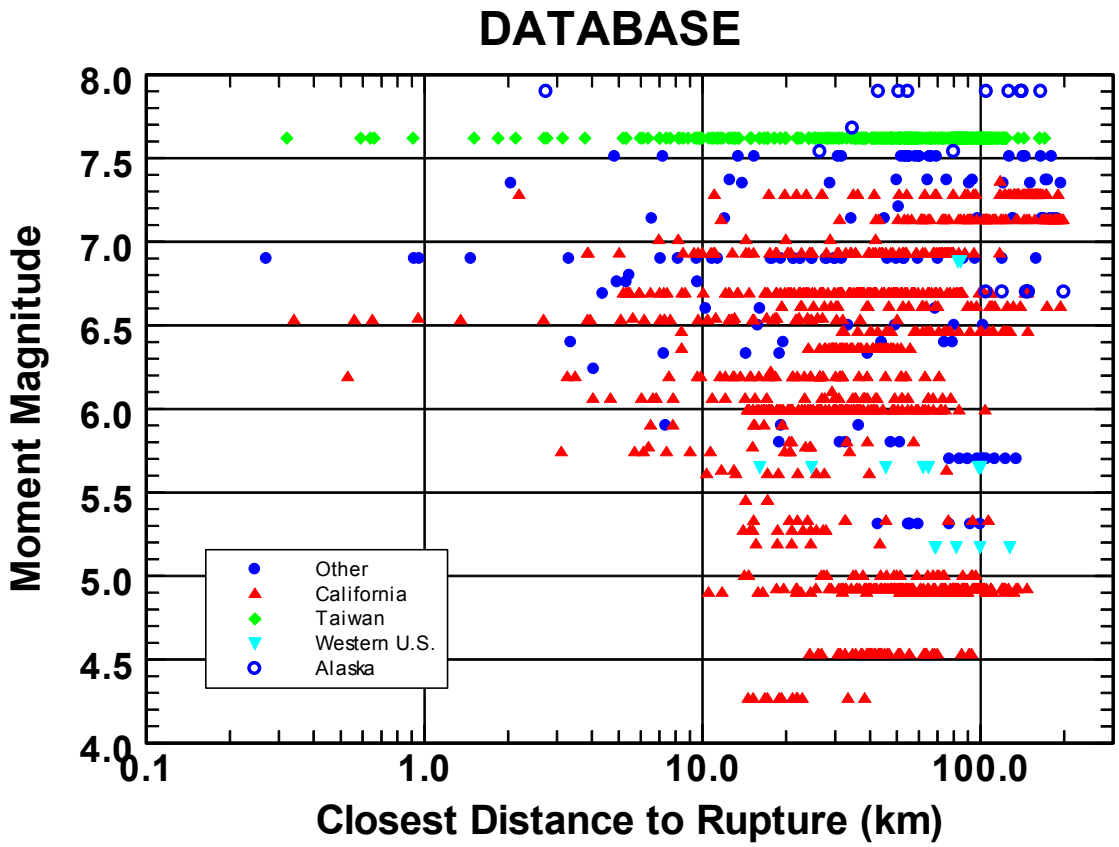

Fig. B.1 Plot of the distribution of recordings with respect to magnitude, distance and geographic region for the Campbell-Bozorgnia (CB06) NGA database. The regions identified in the legend include: California, the western United States outside of California, Alaska, Taiwan, and all other regions.

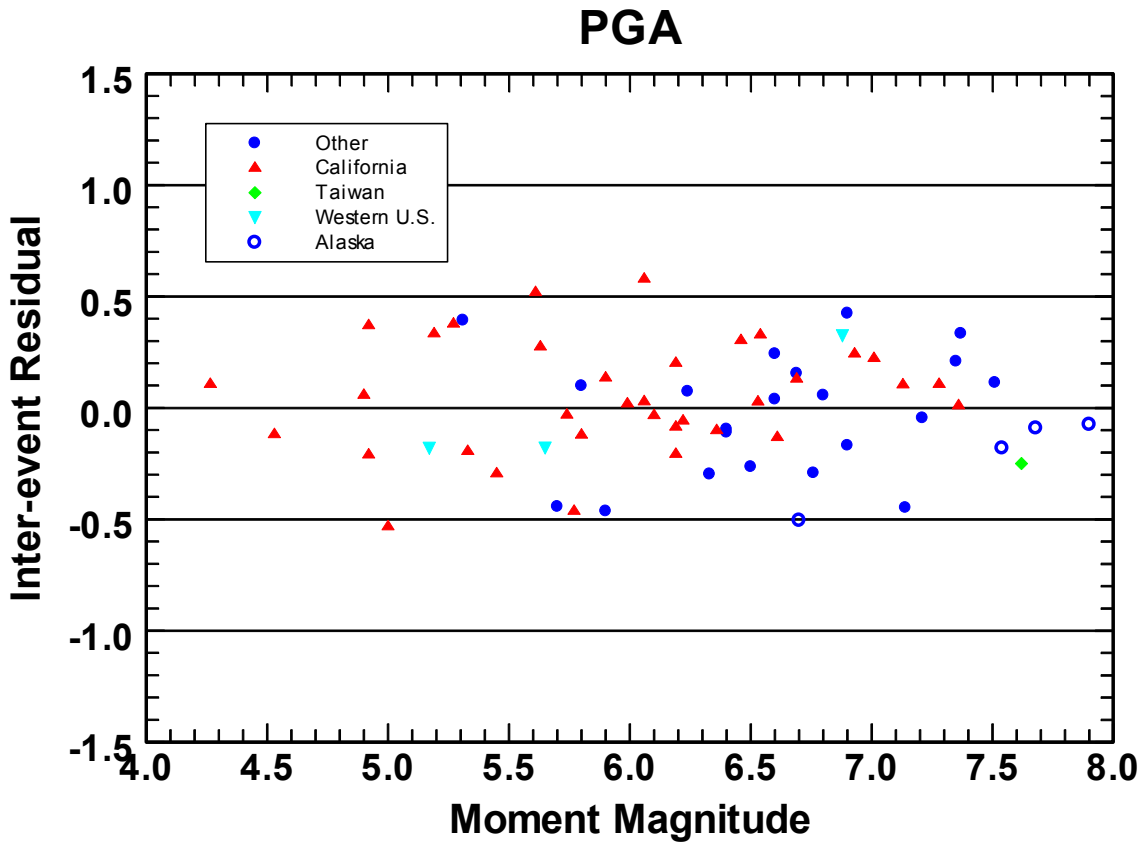

Fig. B.2 Plot of inter-event residuals for PGA for the Campbell and Bozorgnia (CB06) NGA model showing their distribution with respect to geographic region.

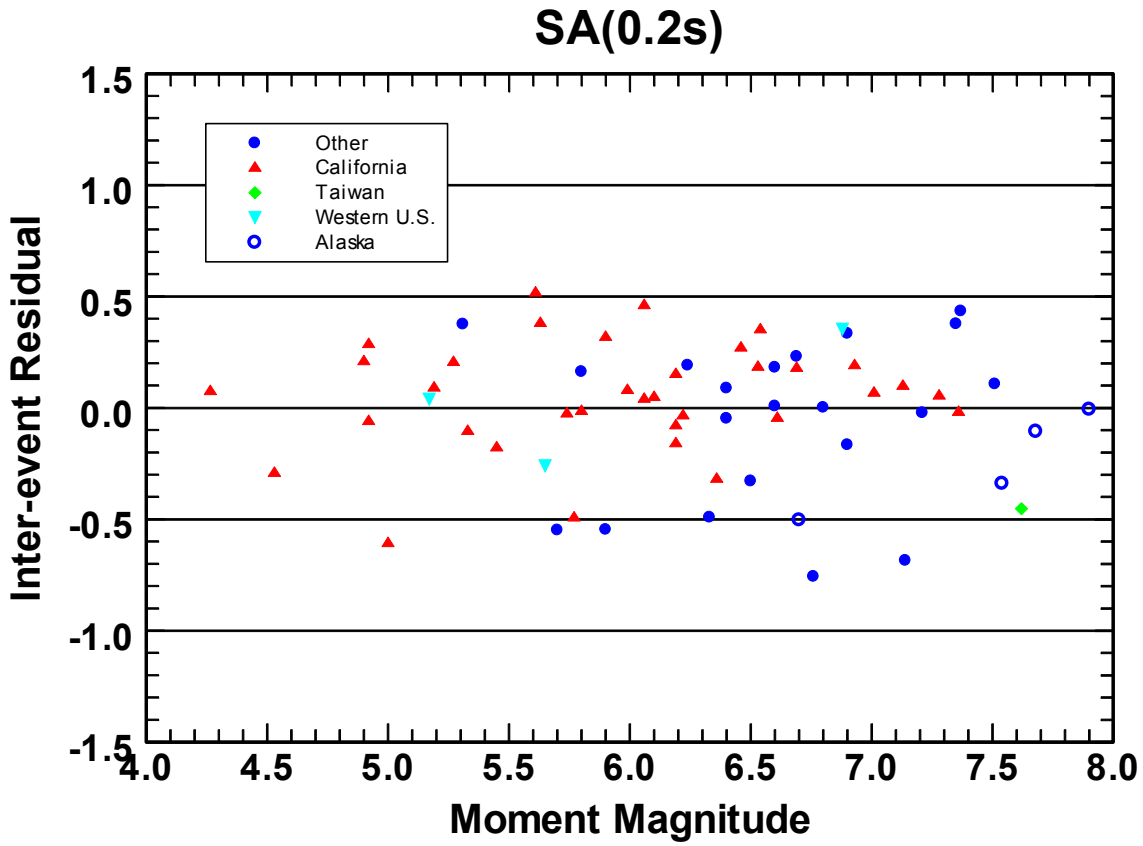

Fig. B.3 **Plot of inter-event residuals for 0.2s spectral acceleration for the Campbell and Bozorgnia (CB06) NGA model showing their distribution with respect to geographic region.**

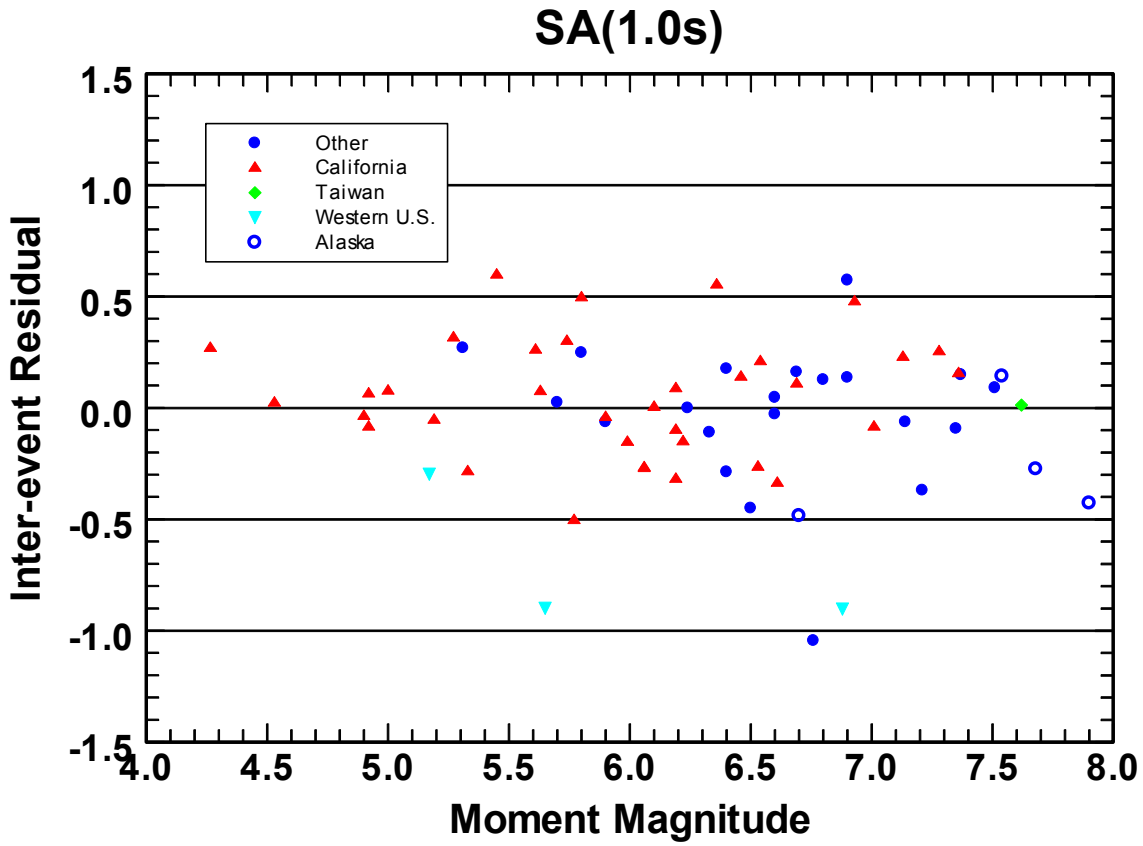

Fig. B.4 **Plot of inter-event residuals for 1.0s spectral acceleration for the Campbell and Bozorgnia (CB06) NGA model showing their distribution with respect to geographic region.**

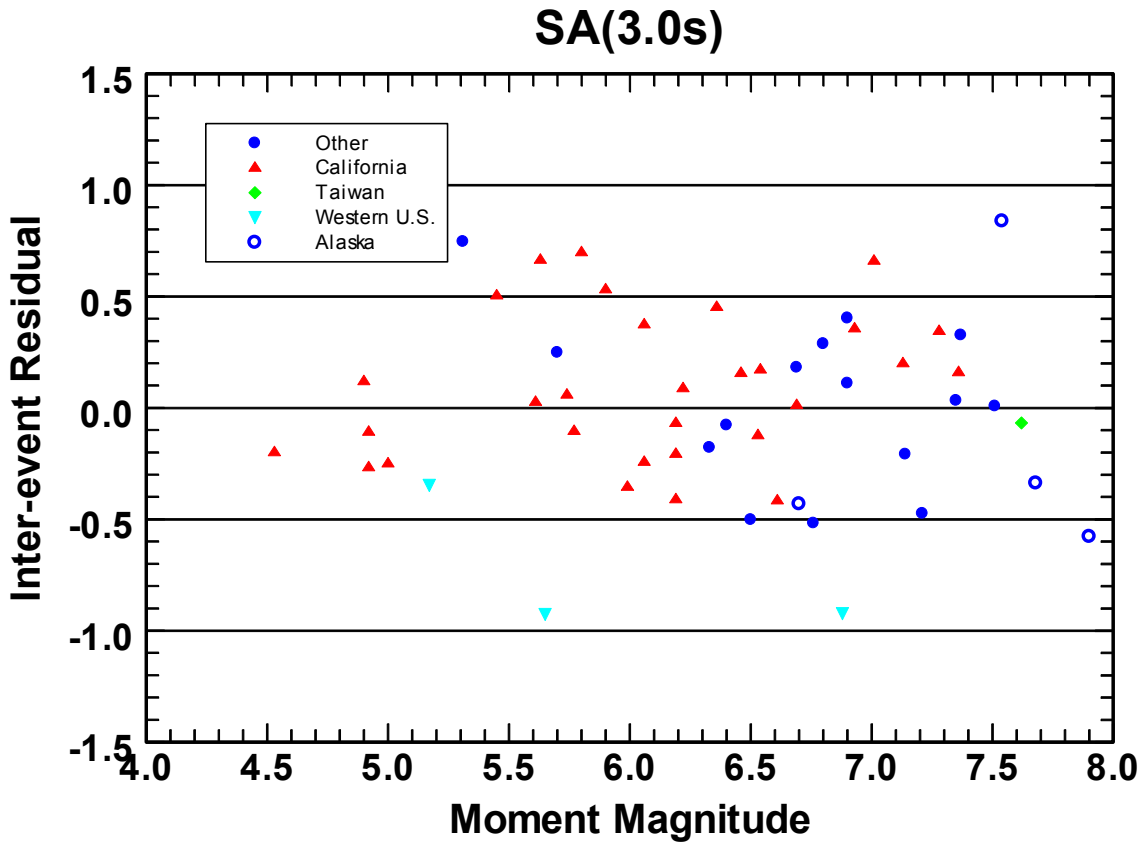

Fig. B.5 **Plot of inter-event residuals for 3.0s spectral acceleration for the Campbell and Bozorgnia (CB06) NGA model showing their distribution with respect to geographic region.**

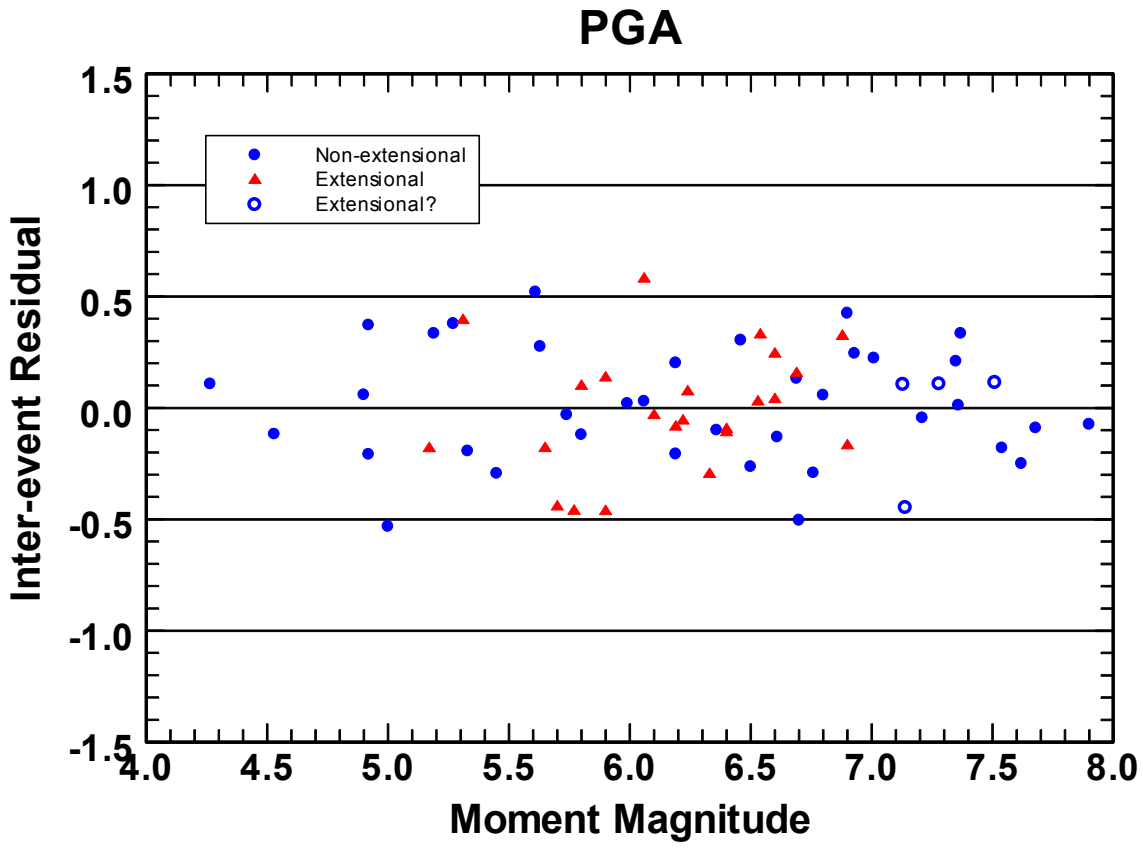

Fig. B.6 Plot of inter-event residuals for PGA for the Campbell and Bozorgnia (CB06) NGA model showing their distribution with respect to tectonic regime.

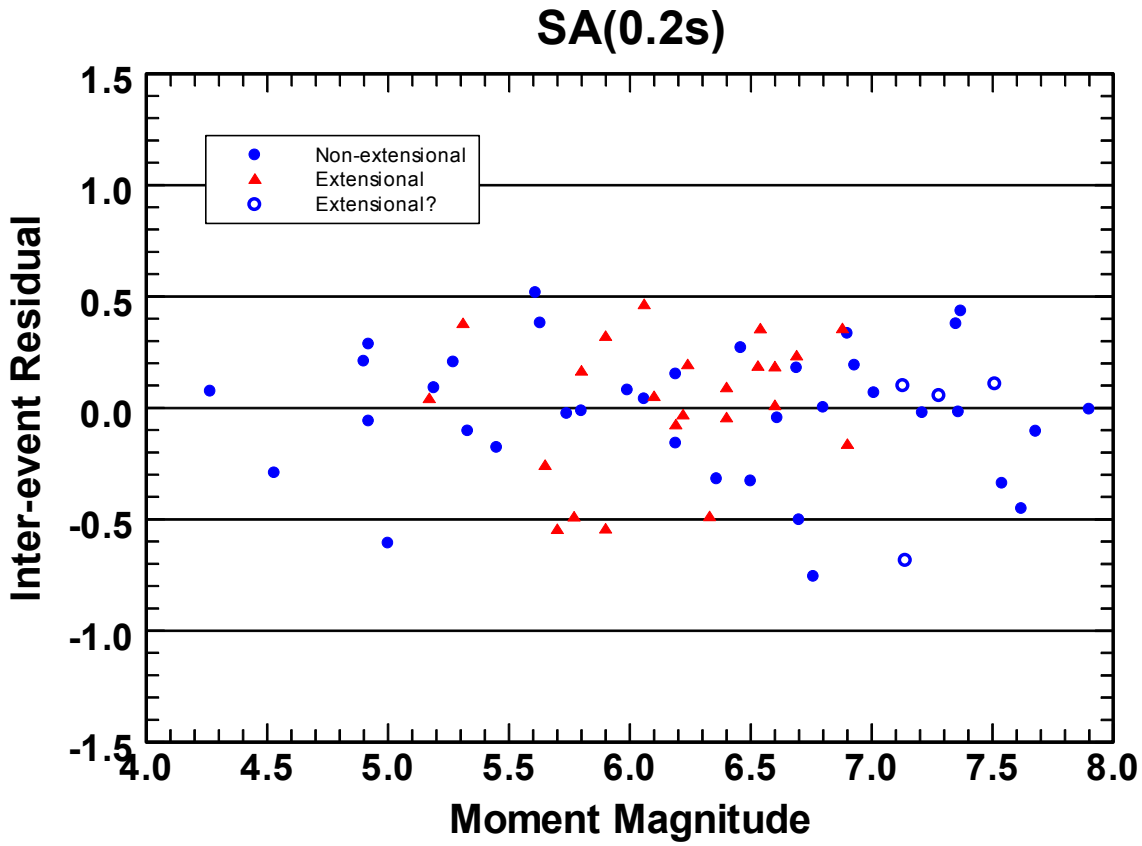

Fig. B.7 **Plot of inter-event residuals for 0.2s spectral acceleration for the Campbell and Bozorgnia (CB06) NGA model showing their distribution with respect to tectonic regime.**

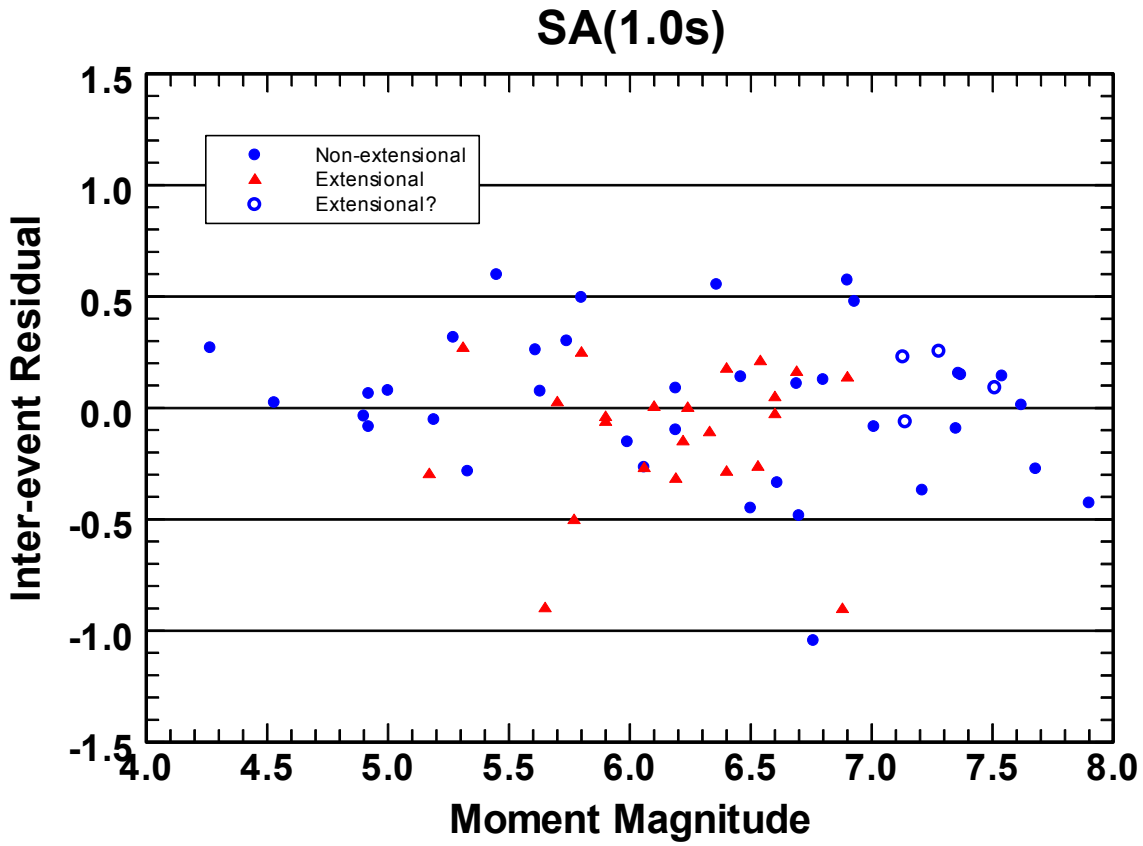

Fig. B.8 **Plot of inter-event residuals for 1.0s spectral acceleration for the Campbell and Bozorgnia (CB06) NGA model showing their distribution with respect to tectonic regime.**

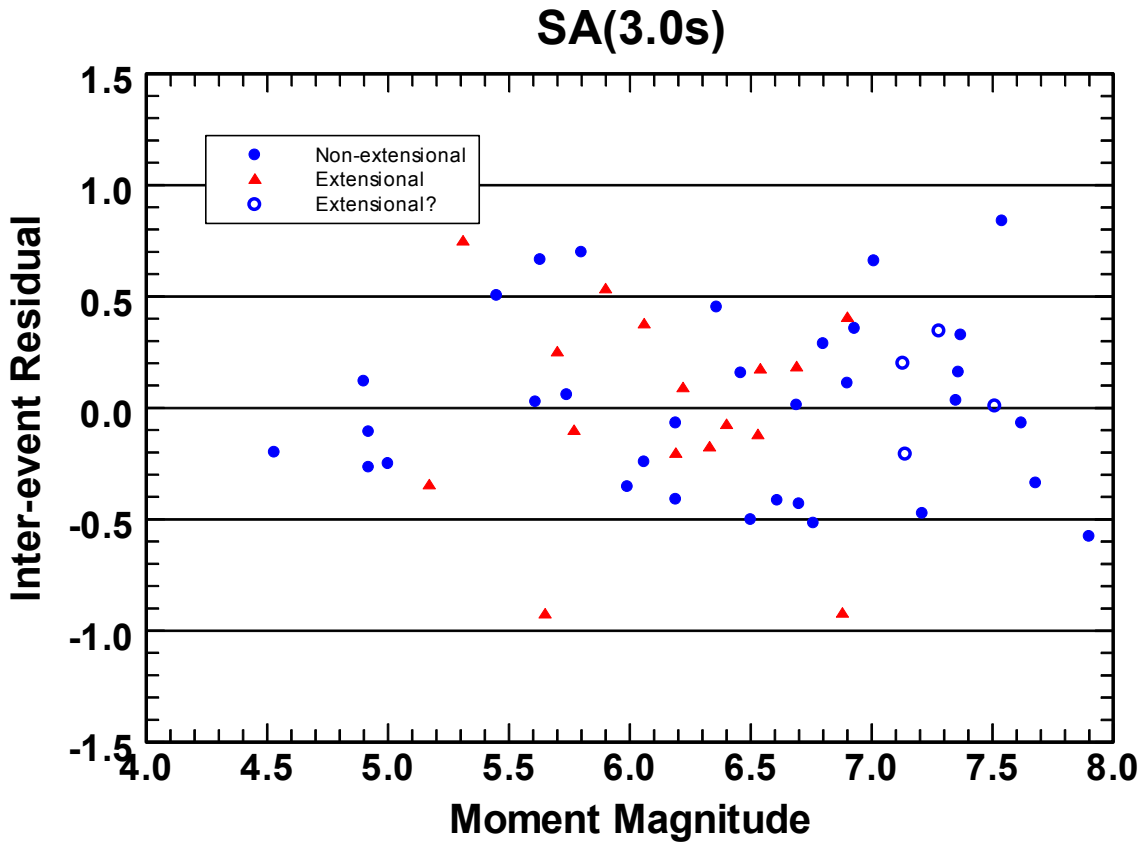

Fig. B.9. Plot of inter-event residuals for 3.0s spectral acceleration for the Campbell and Bozorgnia (CB06) NGA model showing their distribution with respect to tectonic regime.

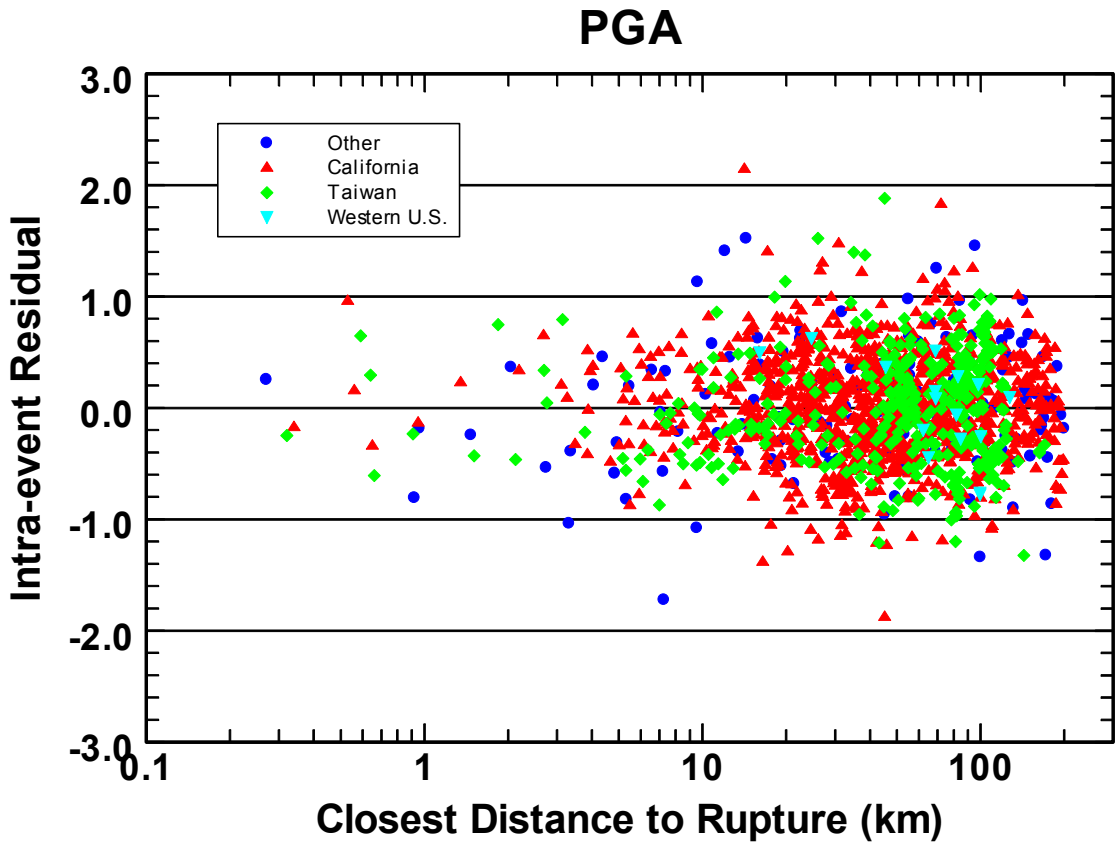

Fig. B.10 Plot of intra-event residuals for PGA for the Campbell and Bozorgnia (CB06) NGA model showing their distribution with respect to distance.

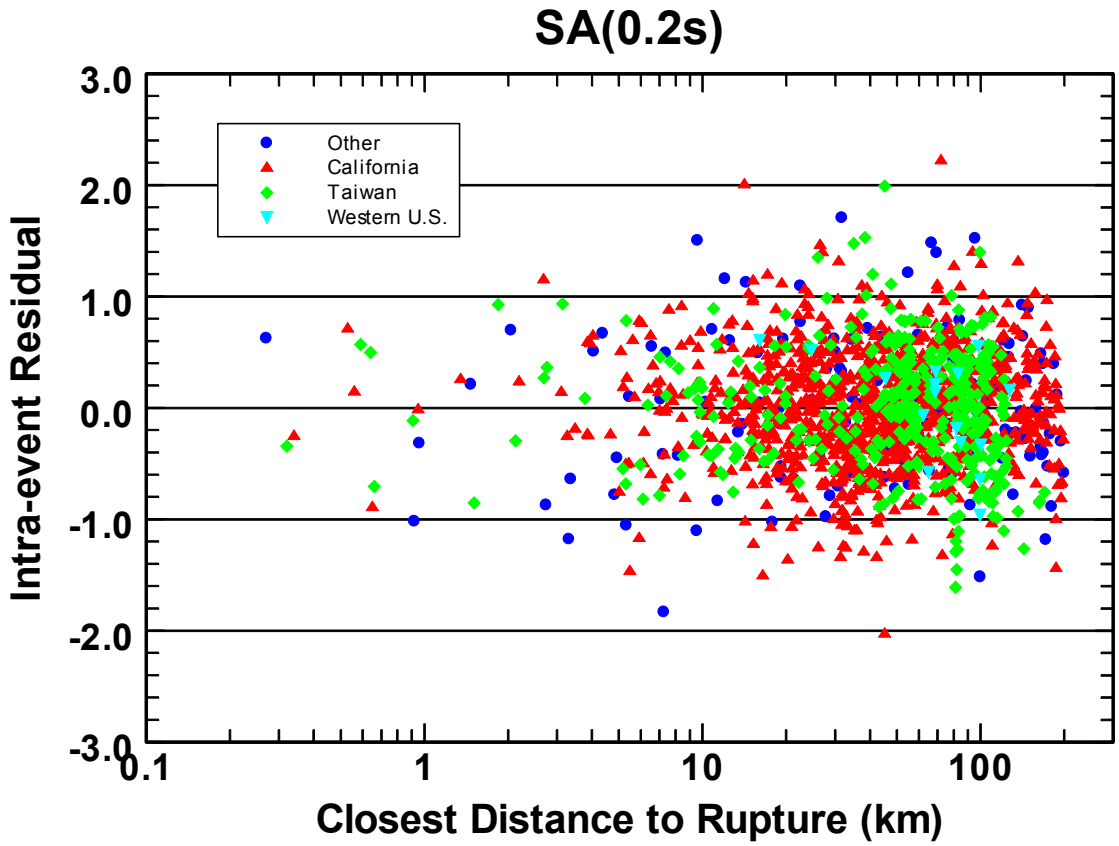

Fig. B.11 Plot of intra-event residuals for 0.2s spectral acceleration for the Campbell and Bozorgnia (CB06) NGA model showing their distribution with respect to distance.

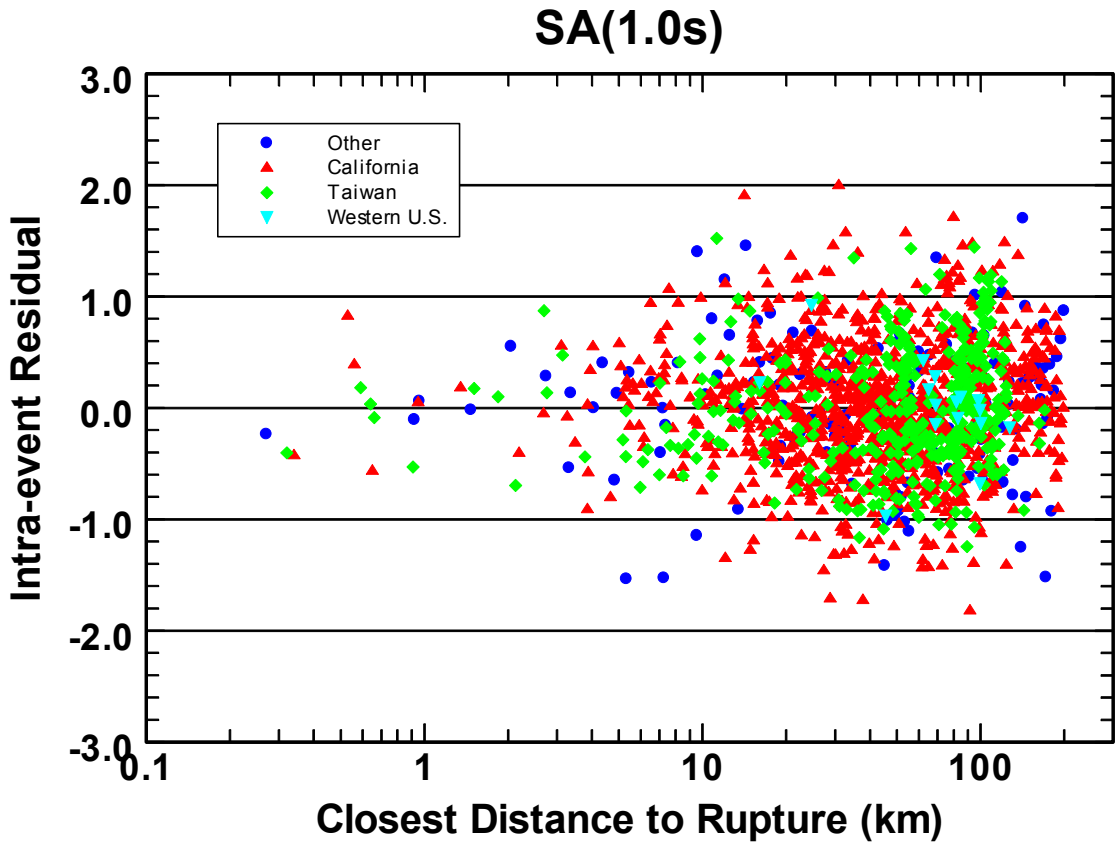

Fig. B.12 Plot of intra-event residuals for 1.0s spectral acceleration for the Campbell and Bozorgnia (CB06) NGA model showing their distribution with respect to distance.

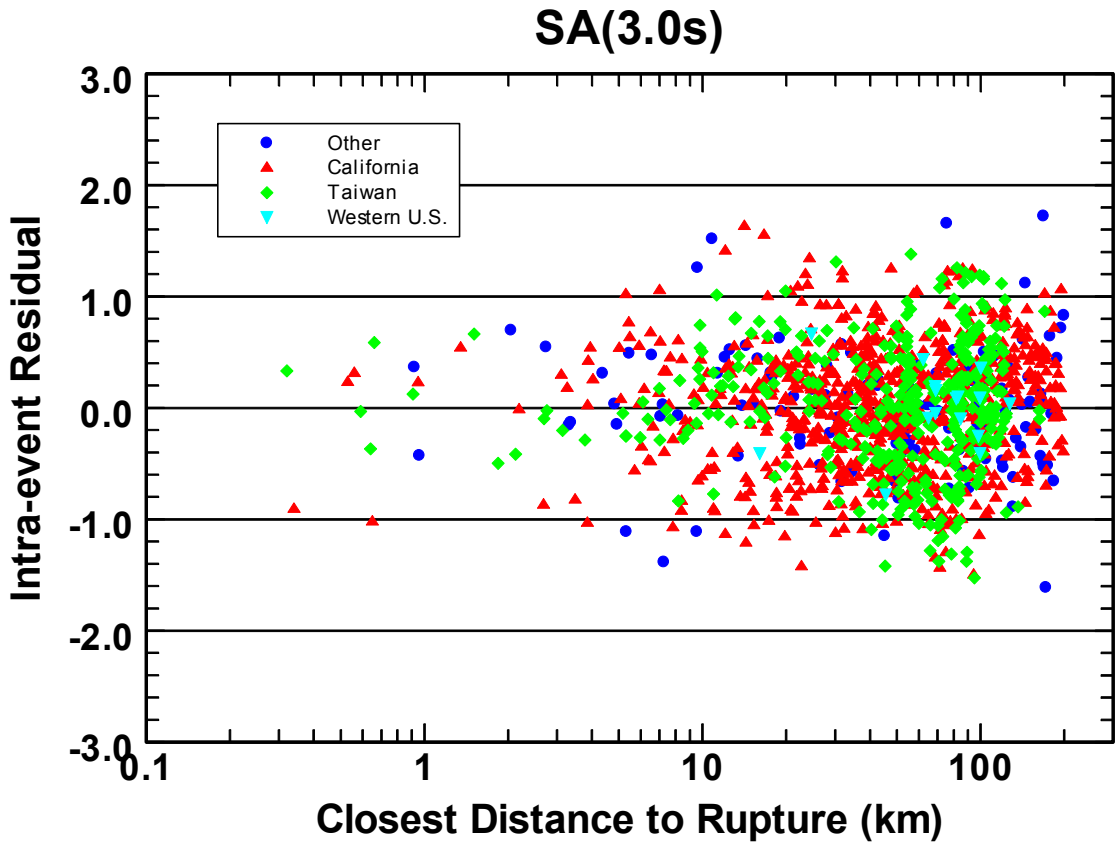

Fig. B.13 Plot of intra-event residuals for 3.0s spectral acceleration for the Campbell and Bozorgnia (CB06) NGA model showing their distribution with respect to distance.

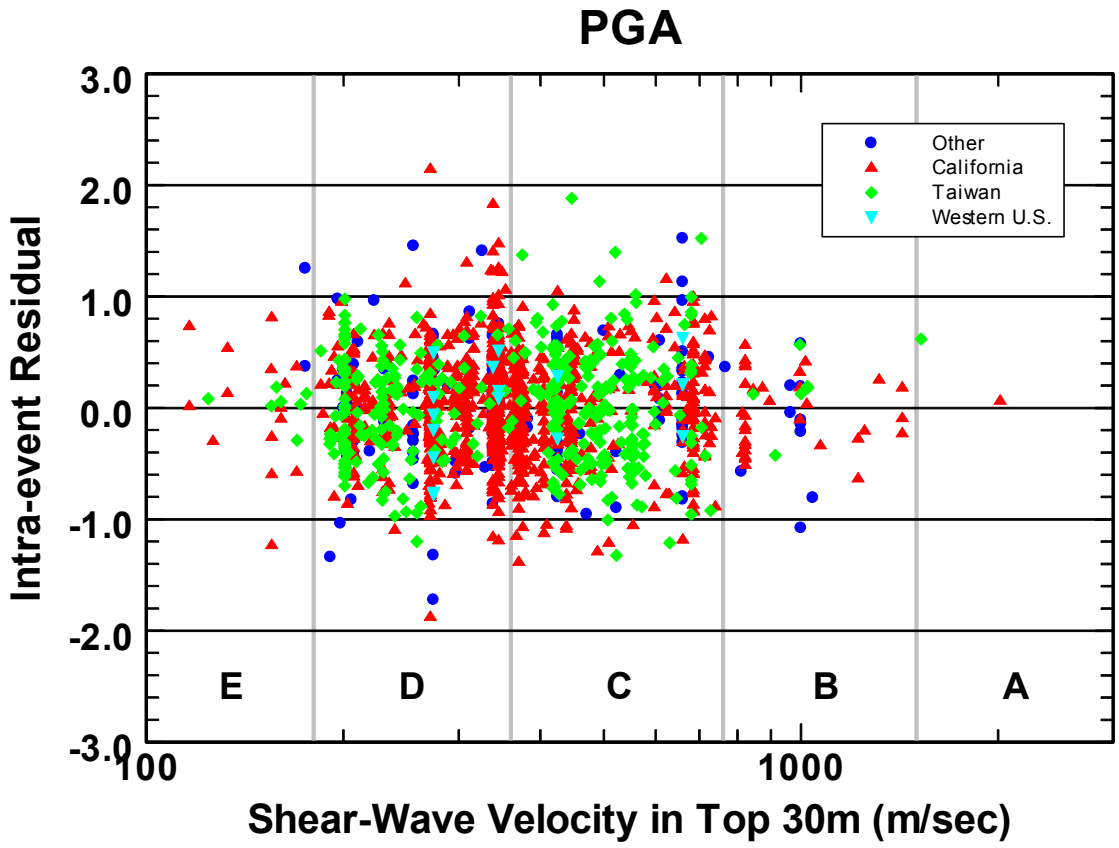

Fig. B.14 Plot of intra-event residuals for PGA for the Campbell and Bozorgnia (CB06) NGA model showing their distribution with respect to 30m shear-wave velocity. Also shown for reference are the ranges of V_{S30} corresponding to NEHRP site categories A–E.

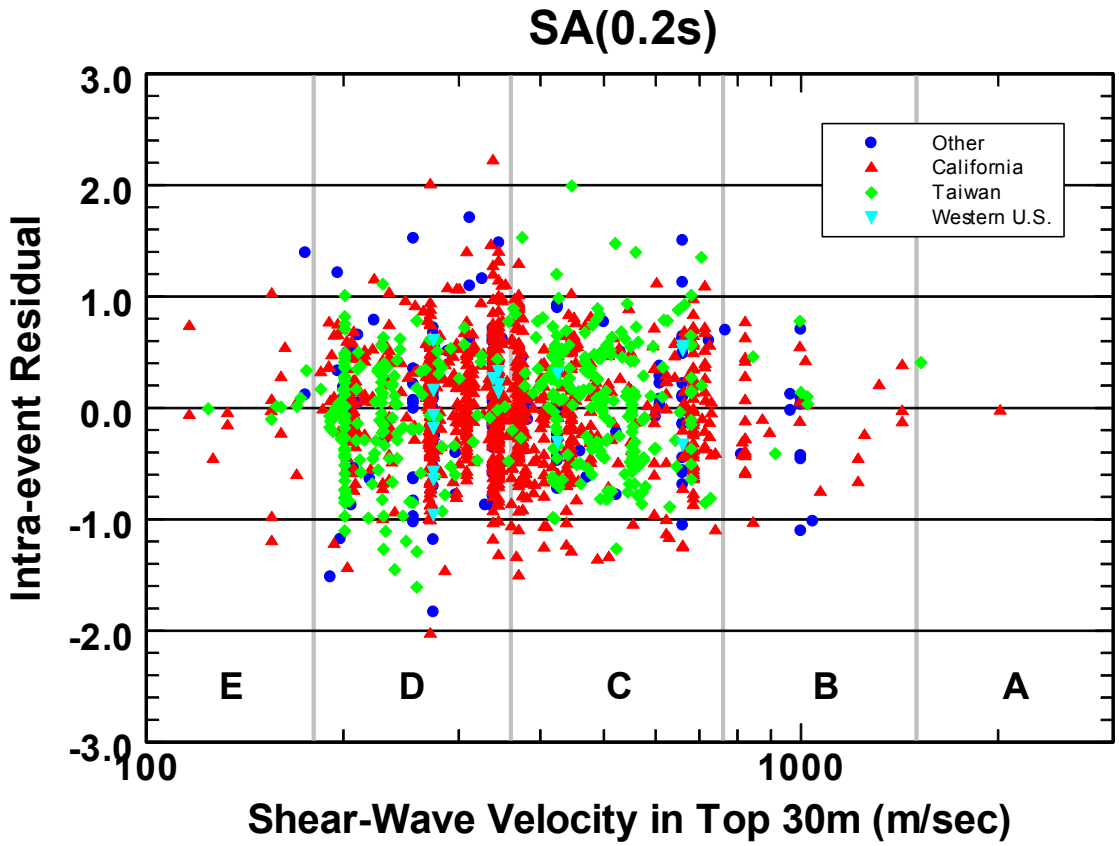

Fig. B.15 **Plot of intra-event residuals for 0.2s spectral acceleration for the Campbell and Bozorgnia (CB06) NGA model showing their distribution with respect to 30m shear-wave velocity. Also shown for reference are the ranges of V_{S30} corresponding to NEHRP site categories A–E.**

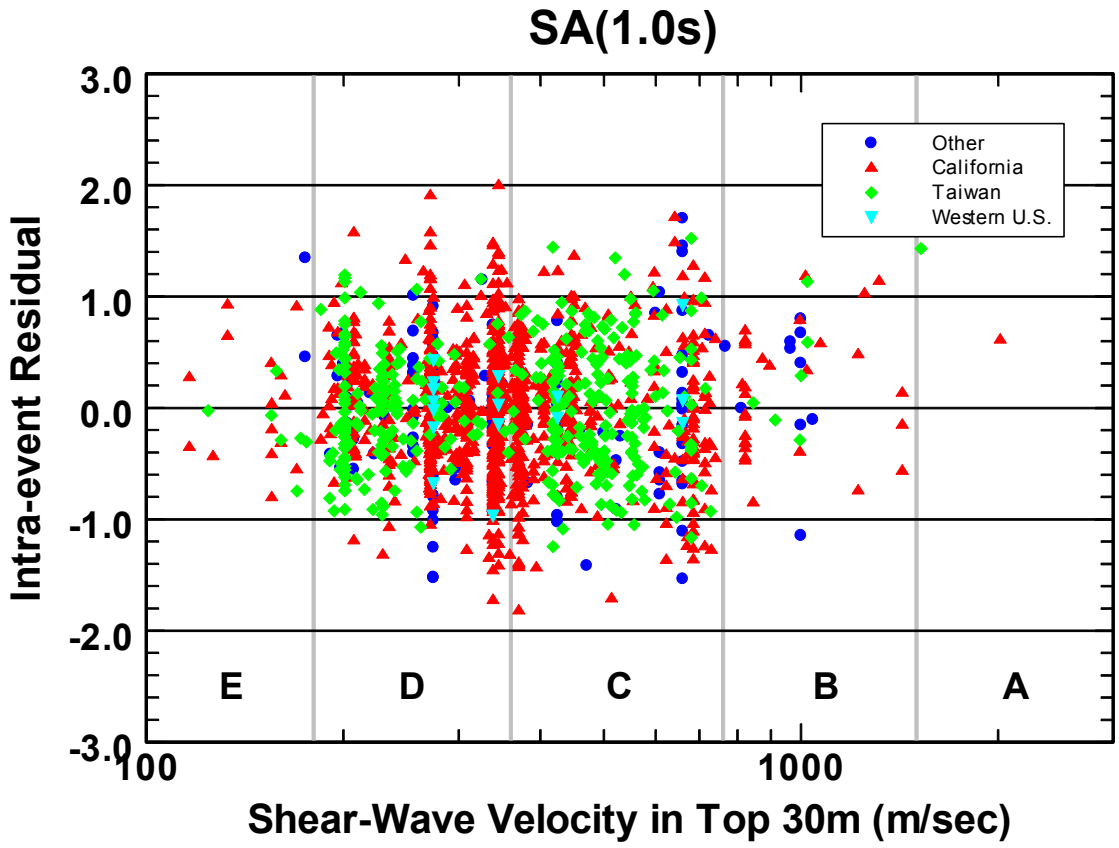

Fig. B.16 **Plot of intra-event residuals for 1.0s spectral acceleration for the Campbell and Bozorgnia (CB06) NGA model showing their distribution with respect to 30m shear-wave velocity. Also shown for reference are the ranges of V_{S30} corresponding to NEHRP site categories A–E.**

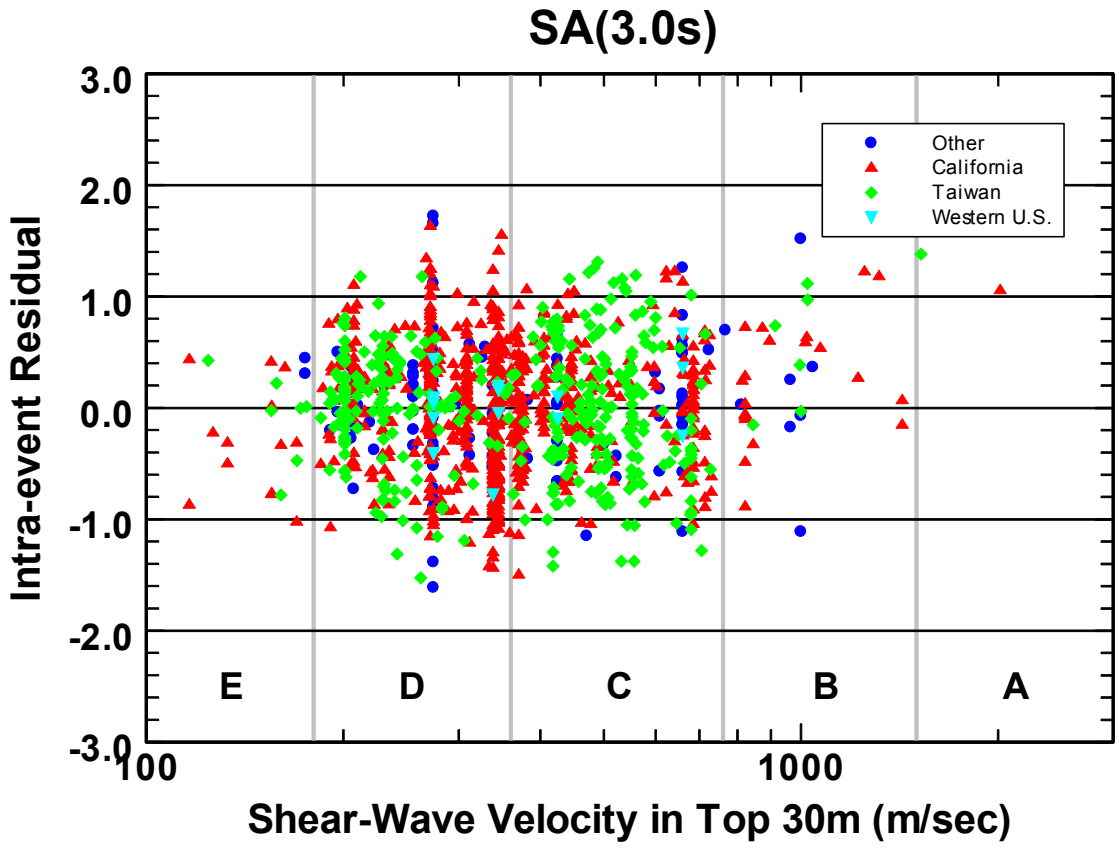

Fig. B.17 **Plot of intra-event residuals for 3.0s spectral acceleration for the Campbell and Bozorgnia (CB06) NGA model showing their distribution with respect to 30m shear-wave velocity. Also shown for reference are the ranges of V_{S30} corresponding to NEHRP site categories A–E.**

B.2 USGS QUESTION #2

Do you feel that your equations have adequately accounted for epistemic and aleatory uncertainties to be used for public policy? Please explain. How do you suggest that the USGS account for the epistemic uncertainties in the ground motion relations in the national maps?

Because of the increase in the number of earthquakes and recording sites in the PEER database, we were able to apply stricter criteria to the selection of the data we used in the development of our NGA empirical ground motion model (see our report for a description of these criteria). One of the consequences of the larger number of events and recordings was to get a better estimate of the inter-event and intra-event aleatory uncertainties at both small and large magnitudes. These refined estimates of uncertainty led us to propose inter-event and intra-event standard deviations that are independent of magnitude. The result was to increase uncertainty at large magnitudes and decrease uncertainty at small magnitudes compared to our previous model (Campbell and Bozorgnia, 2003a). The question, which we address below, is whether this change in aleatory uncertainty is warranted.

The PEER NGA Project also led to an increased degree of similarity in the new NGA models. This increased similarity is due mainly to the availability of a comprehensive database, supporting studies, and ample opportunity for Developer interaction. There is still epistemic uncertainty in the actual subset of data used, in the functional forms (especially magnitude scaling and nonlinear site response), and in the use of supporting data to constrain the models (see each Developer's NGA report). In particular, the data selection criteria were quite different amongst the various developers in terms of, for example, whether only near-source recordings should be used and whether aftershocks should be included. Nevertheless, this uncertainty has been reduced from that implied by the previous models. The question, which will be addressed below, is whether the NGA models as a whole sufficiently represent the epistemic uncertainty in the median ground motions.

B.2.1 Aleatory Uncertainty

We believe that the better constrained magnitude-independent aleatory uncertainty predicted by our NGA model is appropriate and well-constrained, even at close distances. This latter conclusion has come under question because of the apparent increased scatter in near-fault ground motions from the 2004 Parkfield (**M** 6.0) earthquake. The large number of near-source recordings from this earthquake appears to show that intra-event uncertainty might increase very near the fault (e.g., see Figure B.18). No other earthquake has provided such a large number of near-fault recordings with which to address this issue, except possibly the 1999 Chi-Chi (**M** 7.6) earthquake, which we address below. Scientifically, it makes sense that ground motions might become more variable as one approaches the causative fault due to such factors as rupture complexity (e.g., asperities), fault zone effects (e.g., wave guides and focusing), directivity effects, and more variable site response. However, the question is whether it is larger than that calculated for a large number of earthquakes and a large range of distances, as done for our NGA model.

There is very little data with which to address this issue in our database, but some does exist (Figure B.19). To estimate what the impacts of these effects might be on near-fault aleatory uncertainty, we first looked at the variability of the ground motions from the 2004 Parkfield earthquake for PGA and PSA at periods of 0.2, 1.0 and 3.0s. We found that variability in ground motions did seem to increase within about 10 km of the rupture (e.g., see Figure B.18), but only by a relatively modest amount (around 10%). However, our intra-event residuals within this same distance range (Figure B.19) for all earthquakes as a whole and for the Chi-Chi earthquake in particular do not show this same effect, as shown by our intra-event residuals plotted in terms of linear distance for $R_{RUP} < 50$ (Figures B.20–B.23). The intra-event residuals for the Taiwan region in these figures are from the Chi-Chi earthquake.

One possible explanation for the discrepancy between the near-fault variability in the Parkfield earthquake and that in the Chi-Chi earthquake and the database as a whole is the treatment of site effects. The Parkfield earthquake was evaluated without accounting for site effects, since site characteristics such as V_{S30} are not generally known, whereas site effects have been removed from the intra-event residuals of the Chi-Chi earthquake and the database as a whole. The complexity of the geological conditions in the vicinity of the Parkfield earthquake could easily explain the larger degree of variability that was observed. Until the cause of the increased near-fault variability in the 2004 Parkfield earthquake is better understood, we do not recommend altering our aleatory uncertainty model based on this one earthquake, when the Chi-Chi earthquake and our database as a whole do not show increased ground-motion variability near the fault.[3]

B.2.2 Epistemic Uncertainty

The intent of the PEER NGA Project was to obtain a better estimate of modeling uncertainty by providing all of the developers with a common comprehensive database. Although we believe that this goal was achieved, we also believe that the decreased variability in the median predictions from the NGA models that resulted from this process does not necessarily provide an appropriate characterization of the actual epistemic uncertainty in these models. As a result, we recommend that a separate epistemic uncertainty model should be developed and used in conjunction with our model. Norm Abrahamson has proposed a simplified statistical method for estimating such an epistemic model based on the number of earthquakes and recordings in a set of magnitude-distance bins; see Equation 2 of Chiou-Youngs response to this question. The following table shows the application of Equation 2 to the C-B data set. The Tau and Sigma used for this calculation are 0.219 and 0.478, respectively.

[3] Since this response was written there have been some studies that have indicated that some of the increase in the scatter at short periods is due to unusually low ground motions in the fault zone due to increased attenuation (see main text of the report).

Table B.1 Application of Equation (2) to the C-B data set.

M and R_{RUP} Range	Average **M**	Median R_{RUP}	n_{Eq}	n_{Sites}	$\sigma_{\overline{\ln[PGA(m,r)]}}$
M < 5 R_{RUP} < 10			0	0	
M < 5 10 ≤ R_{RUP} < 30	4.71	20.1	5	28	0.133
M < 5 R_{RUP} ≥ 30	4.71	61.2	5	169	0.105
5 ≤ **M** < 6 R_{RUP} < 10	5.83	6.4	4	9	0.193
5 ≤ **M** < 6 10 ≤ R_{RUP} < 30	5.60	20.0	15	110	0.073
5 ≤ **M** < 6 R_{RUP} ≥ 30	5.56	54.7	14	121	0.073
6 ≤ **M** < 7 R_{RUP} < 10	6.49	4.1	19	67	0.077
6 ≤ **M** < 7 10 ≤ R_{RUP} < 30	6.45	19.6	20	152	0.062
6 ≤ **M** < 7 R_{RUP} ≥ 30	6.54	55.5	18	309	0.058
M ≥ 7 R_{RUP} < 10	7.40	4.2	7	41	0.111
M ≥ 7 10 ≤ R_{RUP} < 30	7.33	18.0	9	70	0.093
M ≥ 7 R_{RUP} ≥ 30	7.39	83.7	13	485	0.065

Although this table provides a rough idea of what the epistemic uncertainty related to the selection of the data set is, it can't be evaluated when there are no data. Also, the degree of calculated uncertainty is strongly dependent on the bin sizes. We can probably use these results for something very simple, but the bootstrap and jackknife methods that Bob Youngs has proposed are the best means of assessing epistemic uncertainty.

B.1.3 Conclusion

Based on the above discussion, we conclude that our aleatory model is sufficient but that epistemic uncertainty as represented by the suite of NGA models is insufficient for determining ground motions to be used for engineering applications or for public policy (e.g., for developing national seismic hazard maps).

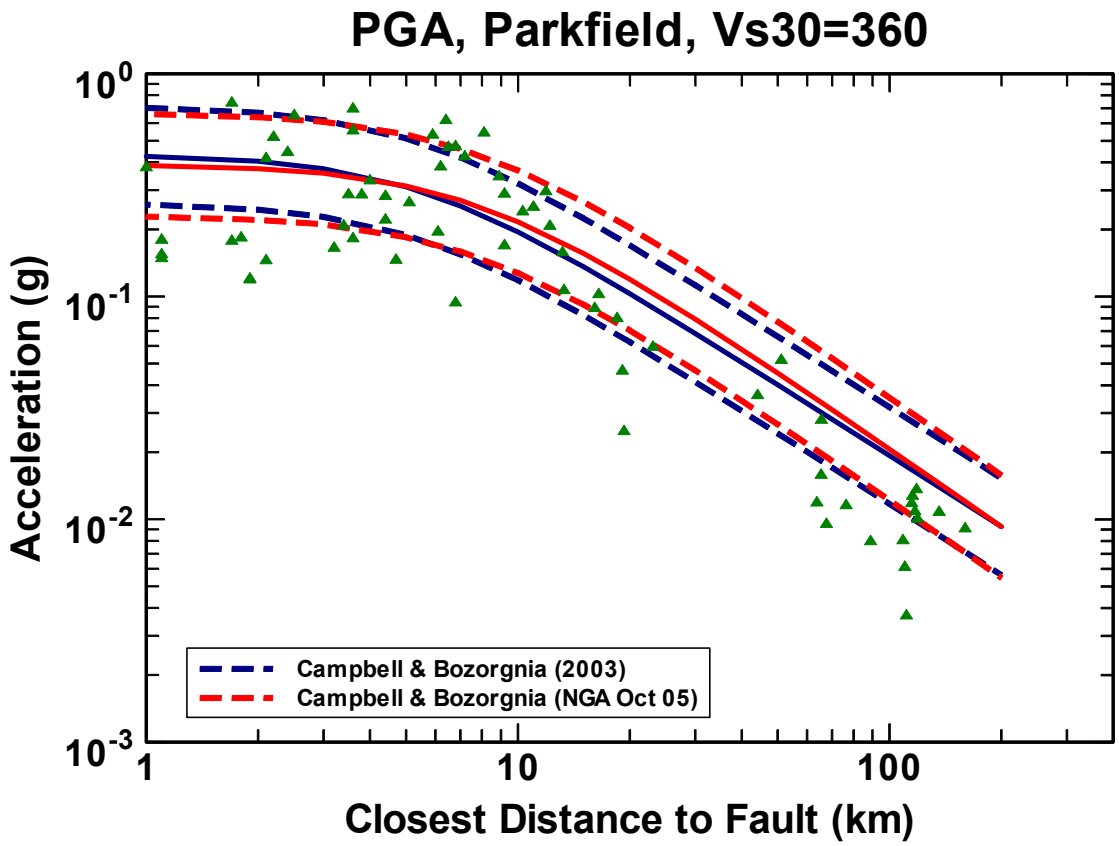

Fig. B.18 **Plot of PGA from the 2004 Parkfield earthquake (Dave Boore, written communication) compared to ground-motion predictions from the Campbell-Bozorgnia NGA (CB06) and 2003 (CB03) empirical ground motion models.**

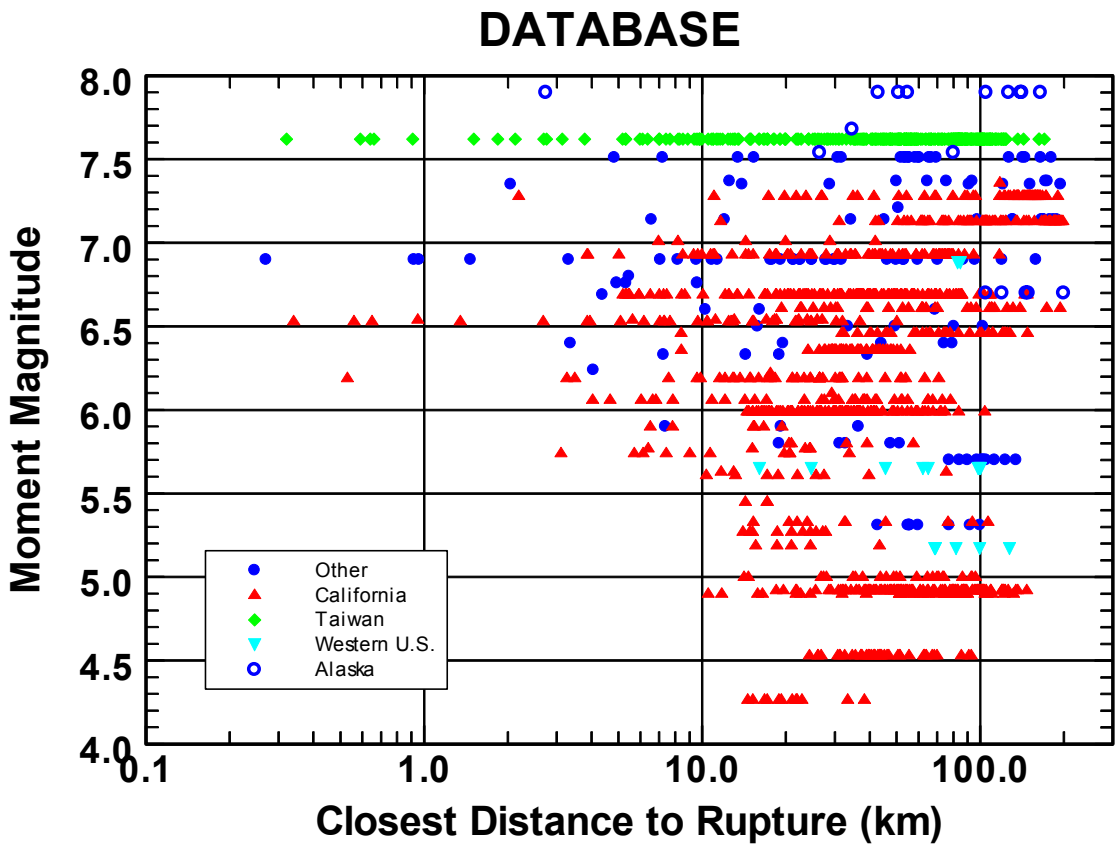

Fig. B.19 **Plot of the distribution of recordings with respect to magnitude, distance and geographic region for the Campbell-Bozorgnia (CB06) NGA database. The regions identified in the legend include: California, the western United States outside of California, Alaska, Taiwan, and all other regions.**

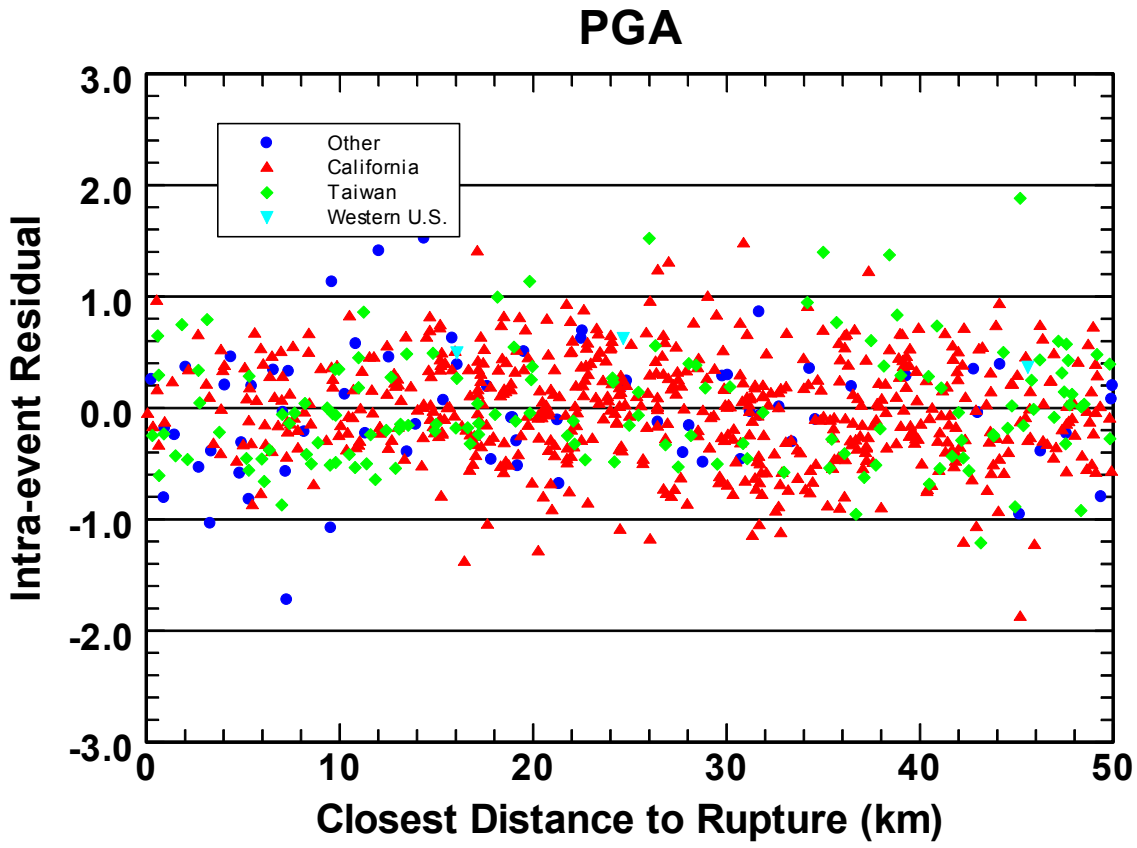

Fig. B.20 Plot of intra-event residuals for PGA for the Campbell and Bozorgnia (CB06) NGA model showing their distribution with respect to geographic region at near-fault distances.

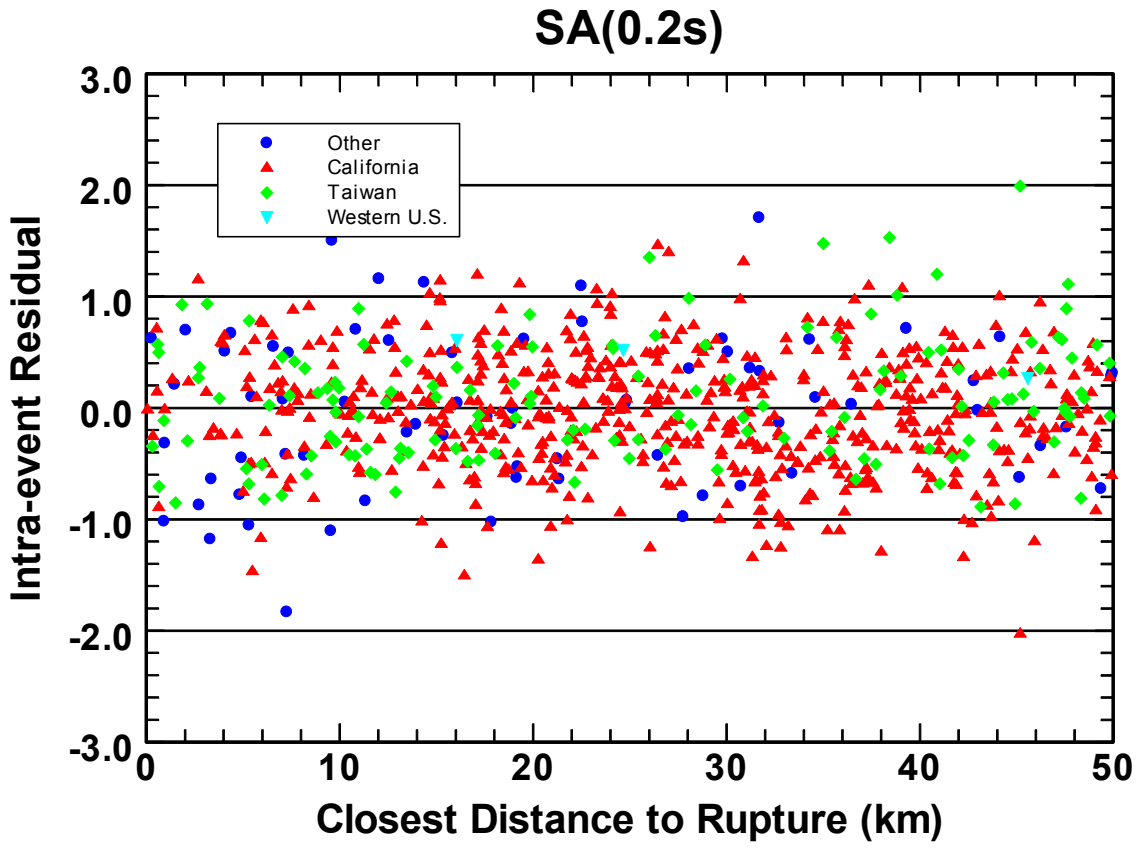

Fig. B.21 Plot of intra-event residuals for 0.2s spectral acceleration for the Campbell and Bozorgnia (CB06) NGA model showing their distribution with respect to geographic region at near-fault distances.

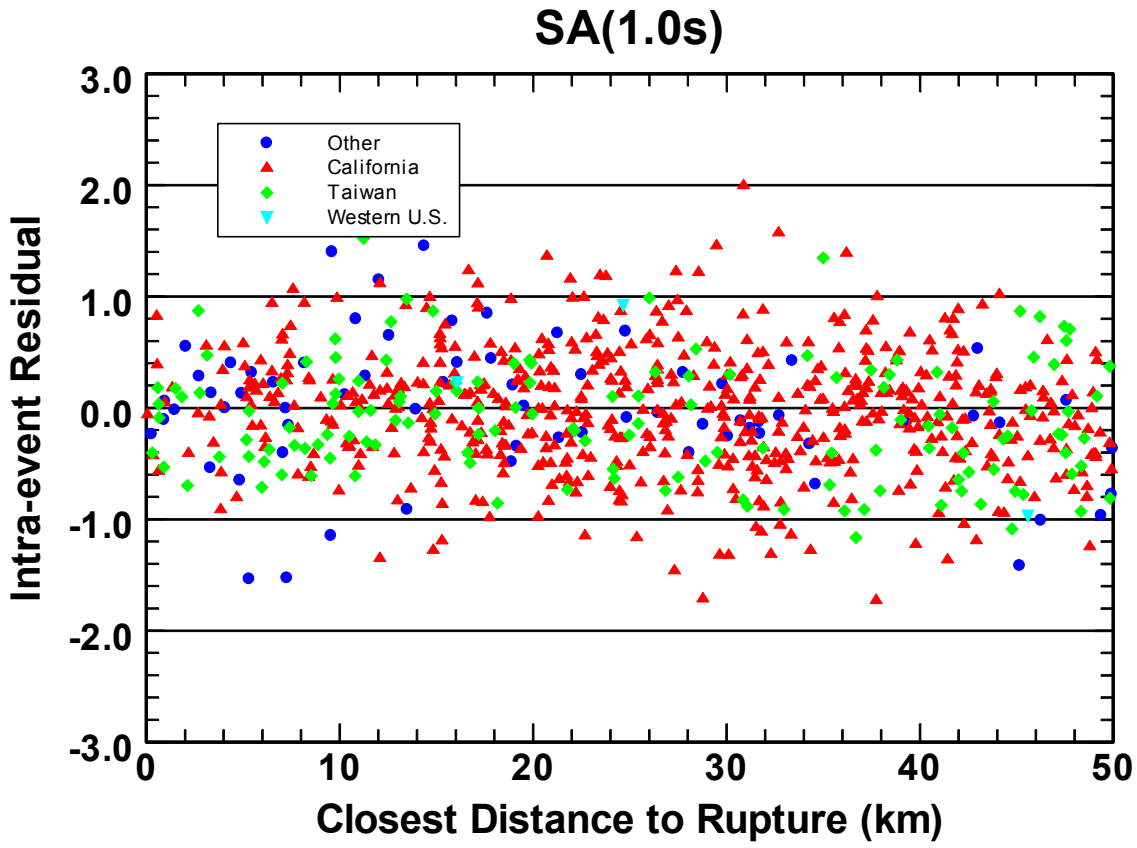

Fig. B.22 Plot of intra-event residuals for 1.0s spectral acceleration for the Campbell and Bozorgnia (CB06) NGA model showing their distribution with respect to geographic region at near-fault distances.

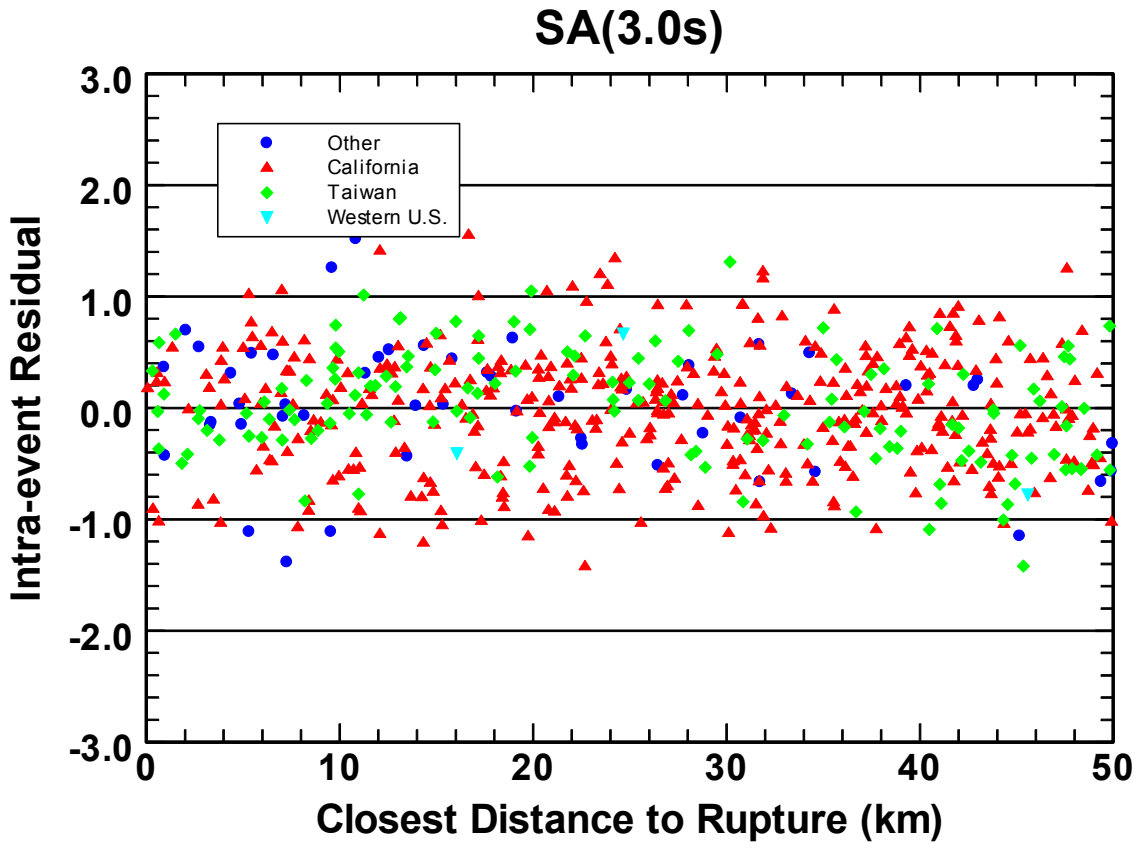

Fig. B.23 Plot of intra-event residuals for 3.0s spectral acceleration for the Campbell and Bozorgnia (CB06) NGA model showing their distribution with respect to geographic region at near-fault distances.

B.3 USGS QUESTION #3

When will you be able to provide the other spectral accelerations that were planned early in the process?

The current report addresses PGA, PGV, PGD and spectral accelerations for the full minimum set of periods for NGA models from zero to 10 seconds: 0.01, 0.02, 0.03, 0.05, 0.075, 0.1, 0.15, 0.2, 0.25, 0.3, 0.4, 0.5, 0.75, 1.0, 1.5, 2.0, 3.0, 4.0, 5.0, 7.5, and 10.0 seconds.

B.4 USGS QUESTION #4

Do you feel that the USGS could use your prediction equations with distance dependent uncertainties to account for directivity effects? Please explain. When will you provide these uncertainties?

As you know, the currently-developed NGA models do not incorporate directivity parameters. Studies in progress are evaluating effects of directivity on the average horizontal component and the fault-strike-normal and fault-strike-parallel components of spectral accelerations. Paul Spudich is working with the NGA developers using a directivity parameterization developed by Spudich et al. (2004) based on isochrone theory as well as the directivity parameterization developed by Somerville et al. (1997). Jennie Watson-Lamprey has begun a separate study to evaluate directivity effects on the average horizontal component in terms of a distance-dependent sigma using a hypocenter-independent directivity parameterization. The studies of directivity effects have had to receive a lower priority than completing the basic NGA models for the average horizontal component.

We recognize the need for a simple representation of directivity effects that can be applied in national ground motion mapping and hope that the studies in progress will result in or can be approximated by a simple representation for use in mapping. However, the studies to date have not established the magnitude of the directivity effects and we are not far enough long to estimate the future schedule. We hope to have a better indication of the magnitude of the effects and the schedule by the time of the September 25 review meeting and will be happy to provide a status report at the meeting.[4]

Spudich, P., Chiou, S.J., Graves, R., Collins, N., and Somerville, P. (2004). A formulation of directivity for earthquake sources using isochrone theory. *U.S. Geol. Surv., Open File Rept. 2004-1263.*

[4] The USGS Tiger Team concluded that directivity effects on the geometric mean horizontal ground motion was likely to be minimal and that, because of lack of any progress on this issue, directivity should not be included in the USGS national seismic hazard maps.

B.5 USGS QUESTION #5

Buried rupture versus surface rupture. Somerville and Pitarka (2006) find no significant difference in source terms, on average, between surface and buried ruptures for periods of 0.2 sec and shorter. Yet the NGA relations that do include terms for depth to top of rupture, predict significant differences between surface faulting and buried faulting at all periods. This discrepancy should be explained. It appears to me that the difference in surface and buried ruptures cited in Somerville and Pitarka (2006) may be at least partly due to the differences in the period of the forward directivity pulses. The buried ruptures used in their paper have magnitudes between 6.4 and 7.0, whereas the surface rupture events have magnitudes between 6.5 and 7.6 and produce forward directivity pulses with longer periods, on average.

In response to this question, we first summarize how each of the NGA models treats the depth to top of rupture (Z_{TOR}) parameter in their model. This is followed by some general comments regarding the Somerville and Pitarka (2006) paper.

B.5.1 Treatment of Buried Rupture in NGA Models

The Campbell and Bozorgnia (CB06) model uses Z_{TOR} to distinguish between buried and surface faulting for reverse-faulting events only, with buried faulting resulting in higher ground motions.[5] The effect is constant for source depths greater than 1 km and phases out for source depths less than 1 km and for mid-to-long periods. In essence, this term replaces the reverse and thrust faulting factor used in the Campbell and Bozorgnia (2003a) model, except that surface-faulting events are now excluded from this effect. This is tantamount to phasing out the source-depth effect for large magnitude earthquakes, which are more likely to have surface rupture.

B.5.2 Comments on Somerville and Pitarka (2006) Paper

Somerville and Pitarka (2006) provide both empirical and theoretical evidence to support their conclusion that ground motions from earthquakes that break the ground surface are weaker than ground motions from buried faulting events. Granted, the empirical evidence shown in their Figure 2 is weak at short periods, but as is pointed out, the comparison depends on only a few earthquakes with different magnitude ranges. The NGA results, for those models that include source depth as a parameter, are based on a larger number of earthquakes that include events with magnitudes less than those used by Somerville and Pitarka and, as a result, are statistically more robust.

The most compelling evidence of weaker ground motions from surface faulting events comes from their dynamic simulations and from similar modeling results by others. These simulations show that, if a weak zone exists at shallow depths, rupture of the shallow part of the fault will be controlled by velocity strengthening, with larger slip weakening distance, larger fracture energy, larger energy absorption from the crack tip, lower rupture velocity, and lower

[5] This response has been edited to restrict the discussion to the Campbell-Bozorgnia NGA model.

slip velocity than at greater depths on the fault. These properties lead to lower ground motions for surface faulting than for buried faulting events. If a weak shallow zone does not exist, then similar short-period ground motions would be expected for surface and buried faulting, as indicated in the top two panels of their Figure 6. The weaker the shallow zone, the greater the expected difference between surface and buried faulting. One possible reason for a shallow weak zone is the presence of thick fault gauge, which has been shown from rock mechanics experiments to cause velocity strengthening, similar to the ground motion simulations.

B.5.3 Conclusion

The issue of whether buried faulting events have stronger ground motions than surface faulting events is currently a topic of intense study by the scientific community and cannot be considered resolved at this time. However, considering the empirical, theoretical and laboratory results summarized by Somerville and Pitarka (2006), it is plausible that this effect exists, but that its effects are subject to large epistemic uncertainty. This uncertainty is reflected in the diverse treatment of this effect in the NGA models, which would appear to be consistent with the state of knowledge within the scientific community at this time.

We didn't find a strong relationship between ground motion and depth to top of rupture (Z_{TOR}) in the data that we used to develop our model, except for reverse-faulting events. In order to demonstrate this, we plot our inter-event residuals versus depth to top of rupture in Figures B.24–B.27 for PGA and spectral acceleration at periods of 0.2, 1.0 and 3.0s, respectively. This depth is taken to be hypocentral depth for earthquakes with magnitudes less than about 6.0, since no direct estimate of Z_{TOR} was available. There is some indication in Figures B.24 and B.25 that events with $Z_{TOR} > 10-12$ km are systematically underpredicted at short periods. The four deepest events that control this observation are the two Whittier Narrows earthquakes and two events from Anza. All four of these events use hypocentral depth as a proxy for depth to top of rupture. Actual values of Z_{TOR} would be smaller and might reduce the observed trend.

The possible bias seen in the inter-event residuals at short periods appears to phase out at long periods (Figures B.26 and B.27). So if the depth effect is real, it seems to be limited to short periods. Although it is tempting to add a factor to increase short-period ground motions for $Z_{TOR} > 10-12$ km, we believe that it is premature to include it at this time, at least based on our database, since the effect is controlled by only four earthquakes of $\mathbf{M} < 6.0$ from two specific regions in southern California for which we do not have a direct estimate of Z_{TOR}. That is not to say that we wouldn't expect higher ground motions at depth, only that its importance for moderate-to-large earthquakes is not sufficiently resolved at this time, except for reverse faults.

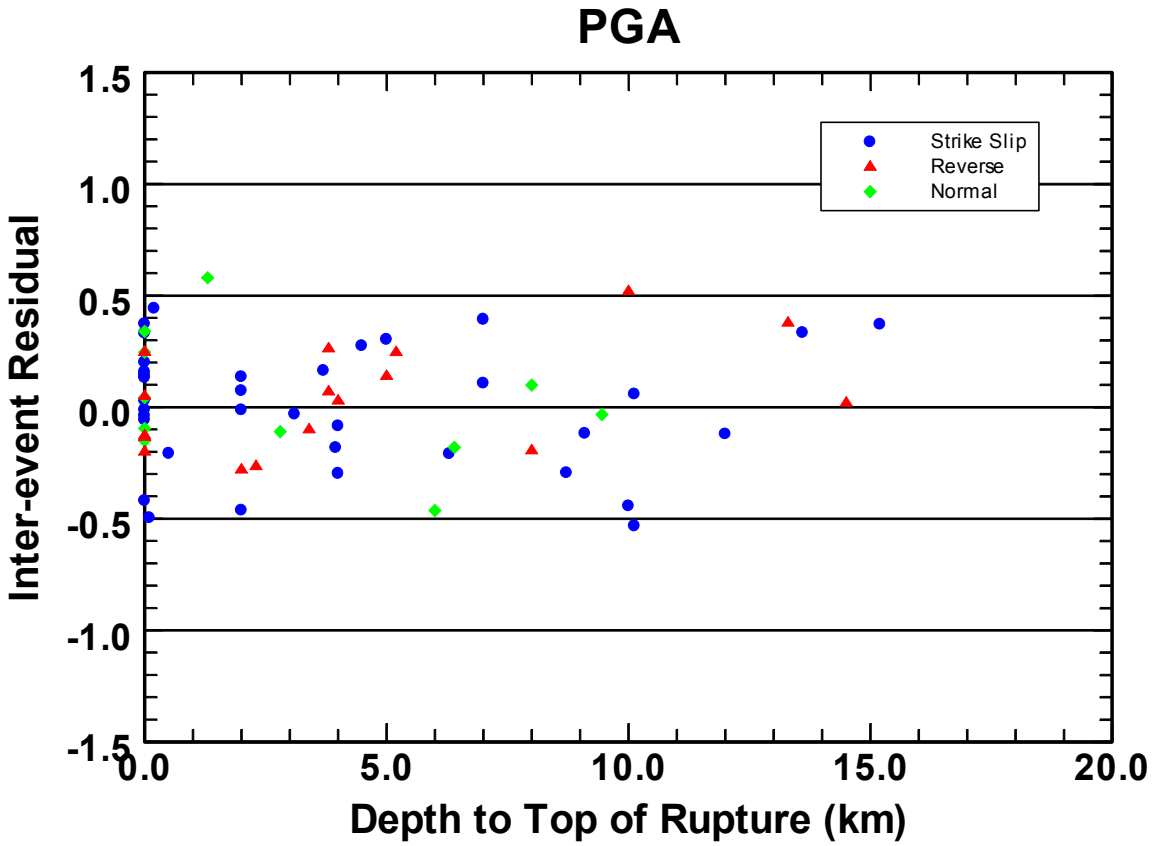

Fig. B.24 **Plot of inter-event residuals for PGA versus depth to top of rupture for the Campbell and Bozorgnia (CB06) NGA model. The symbols represent different styles of faulting as indicated in the legend.**

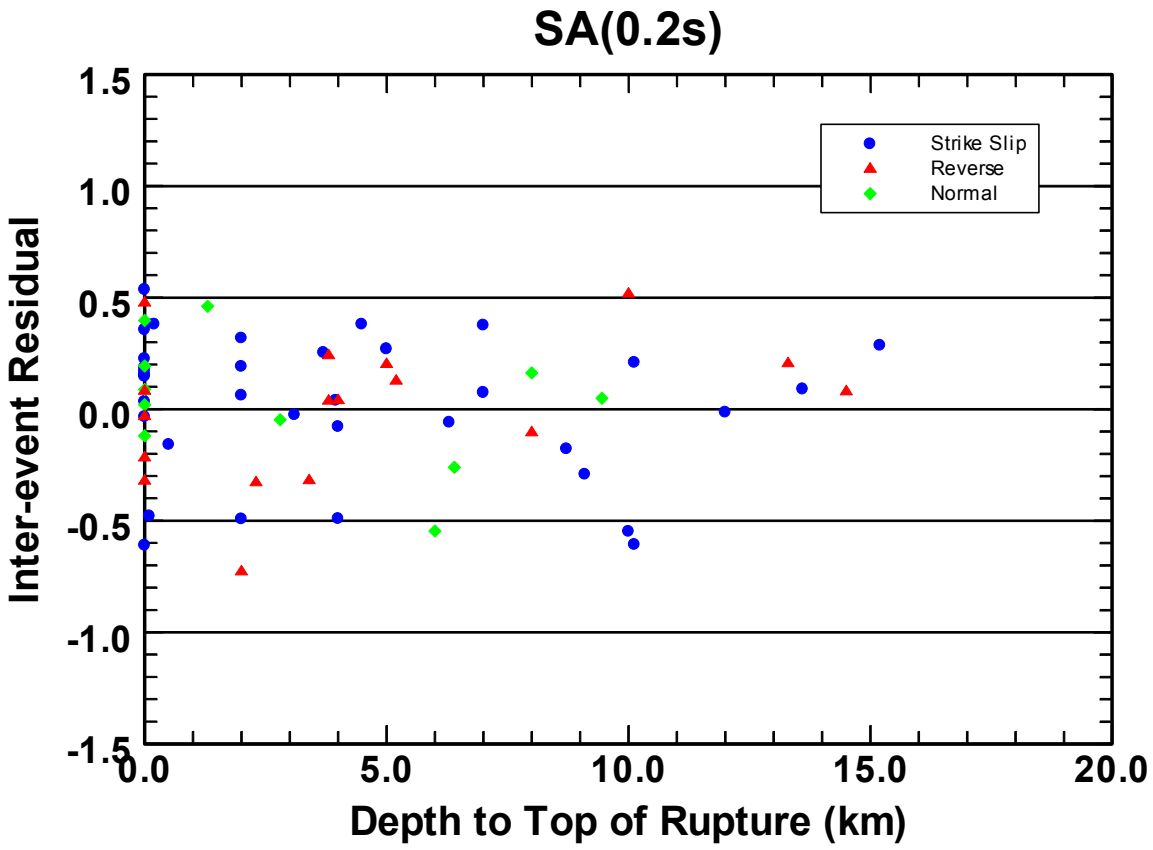

Fig. B.25 **Plot of inter-event residuals for 0.2s spectral acceleration versus depth to top of rupture for the Campbell and Bozorgnia (CB06) NGA model. The symbols represent different styles of faulting as indicated in the legend.**

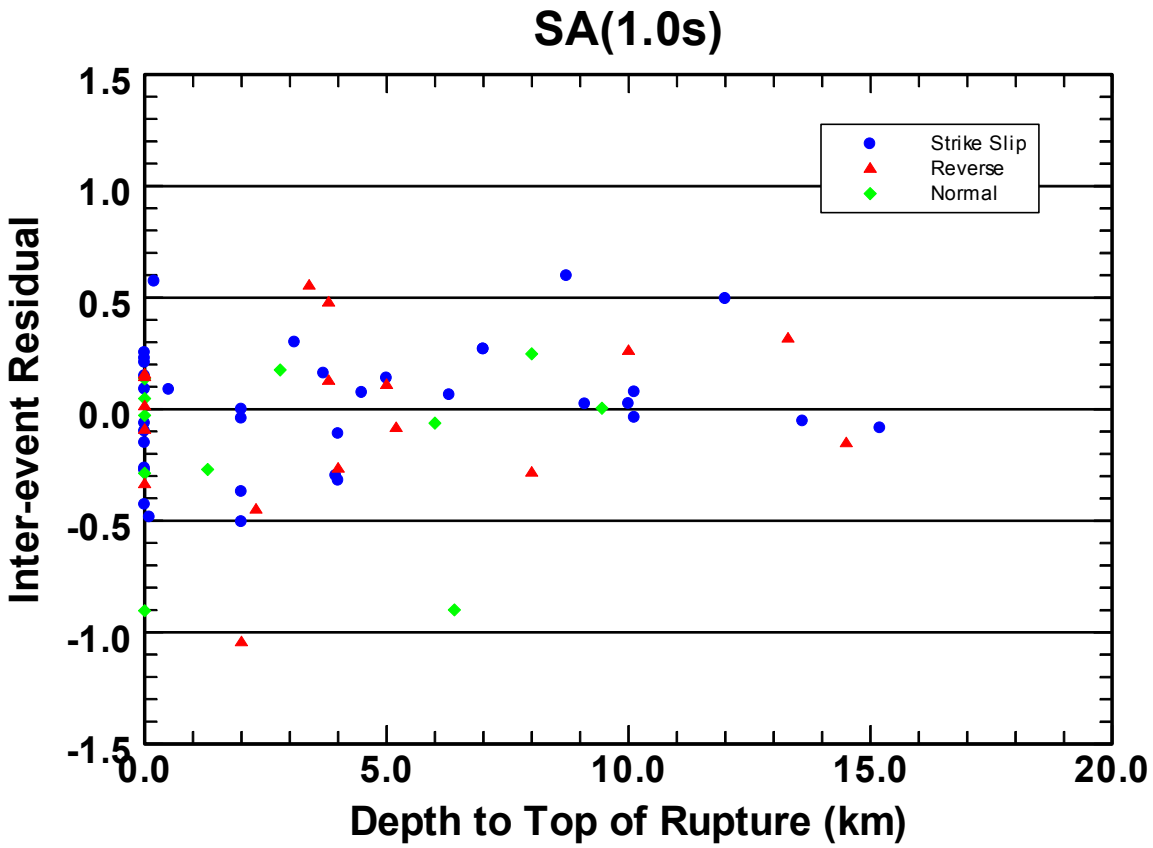

Fig. B.26 **Plot of inter-event residuals for 1.0s spectral acceleration versus depth to top of rupture for the Campbell and Bozorgnia (CB06) NGA model. The symbols represent different styles of faulting as indicated in the legend.**

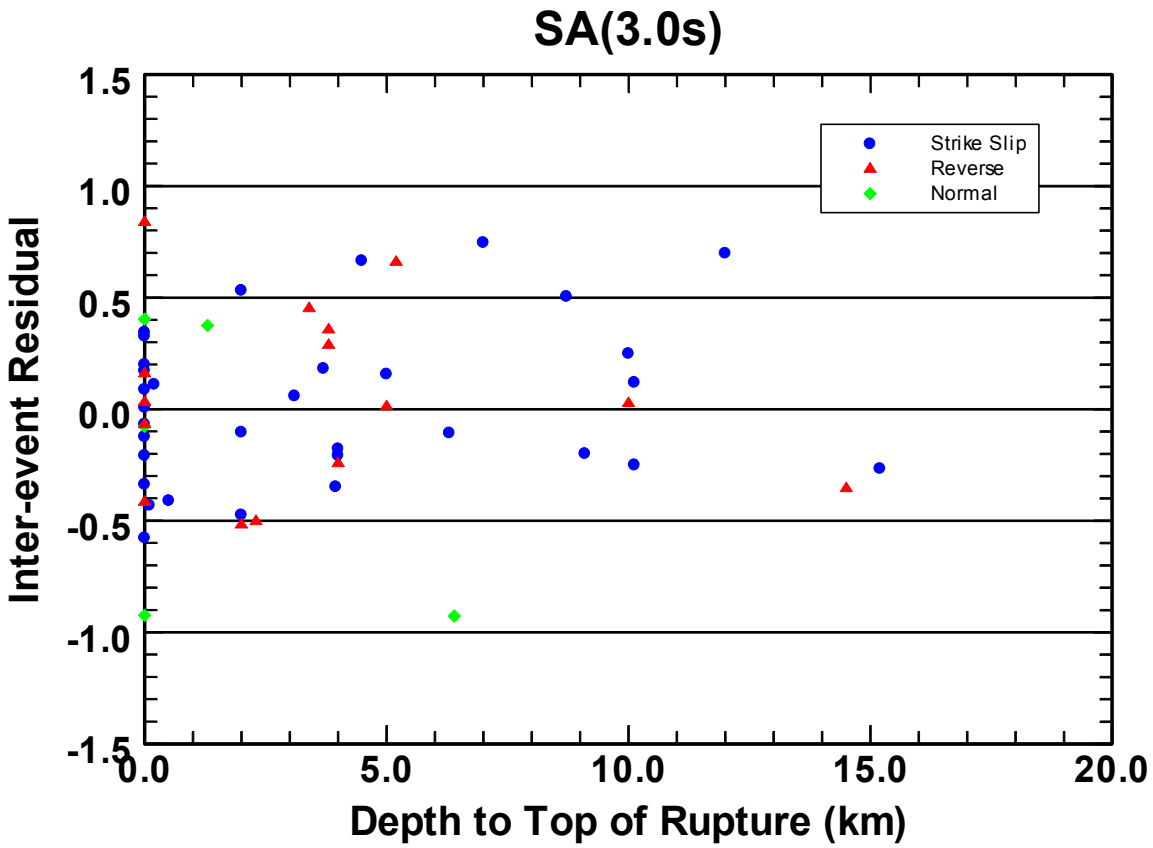

Fig. B.27 **Plot of inter-event residuals for 3.0s spectral acceleration versus depth to top of rupture for the Campbell and Bozorgnia (CB06) NGA model. The symbols represent different styles of faulting as indicated in the legend.**

B.6 USGS QUESTION #6

Too many predictive variables. The [previous question] points out the danger of using too many predictive variables. For example, magnitude-dependent effects may be confused with a depth to top of faulting effect. Larger events are more likely to rupture the surface. Also, rupture aspect ratio is correlated with magnitude, so it is not obvious these two effects can be separated using the available data.

B.6.1 Finding the Right Balance of Predictive Variables

There is a trade-off between using too few and too many predictive variables in an empirical ground motion model. Using too few predictive variables will lead to models that have higher aleatory uncertainty and that are less useful in many engineering applications. Using too many predictive variables can lead to models that also have higher aleatory uncertainty and that are less reliable (e.g., because of potential correlation between variables and poorly constrained coefficients). Both of these situations should be avoided and each NGA model did so in its own way. Our method for avoiding these two situations is described below.

We used a two-stage regression analysis to develop an appropriate functional form for the terms in our model before we applied the more comprehensive, but less transparent, random effects analysis to develop the final results (see the discussion in the main body of our report). This allowed us to evaluate the statistical significance of each term (a combination of coefficients, predictive variables, and functional forms) as we added it to the model as well as to evaluate its correlation with other terms in the model. We used an analysis of residuals to determine which terms should be included in the model in order not to exclude any important effects. Aside from a few exceptions, we only included coefficients that provided a reasonable degree of confidence (around 16% or better) and that were not strongly correlated with other coefficients in the model. Exceptions to this rule were made when a coefficient was statistically significant for some oscillator periods but not for others or when seismologists and engineers queried at USGS workshops and other scientific meetings over the course of the last few years believed that a modeled effect should be included even though there was insufficient data to constrain it. In the former case, the term was allowed to smoothly phase out with period, even though it was not statistically significant for many of the phase-out periods. In the second case, the coefficient was assigned a value based on an analogous parameter or on theoretical considerations.

Coefficients for those terms that were constrained in the model included: (1) hanging-wall effects for strike-slip and normal faults, (2) nonlinear soil effects, and (3) 3-D basin effects. For hanging-wall effects, the limited hanging-wall data from normal faults confirmed that these effects were similar on average to those empirically derived for reverse faults, as suggested by Jim Brune from foam rubber modeling. There was insufficient data to confirm these effects for dipping strike-slip faults, but Jim Brune could provide no seismological reason why such faults should not also be subject to hanging-wall effects. Nonlinear soil effects are well documented by observations and nonlinear site-response analyses and accepted by both seismologists and

geotechnical engineers. Model residuals, when plotted against PGA, definitely showed behavior consistent with nonlinear soil effects, but the data were insufficient to develop a functional form. Therefore, theoretical site-response analyses were used to constrain this term. 3-D basin effects were also visible in the data, but like the nonlinear soil effects, the data were insufficient to develop a functional form. Therefore, theoretical 3-D basin response analyses were used to constrain this term. More details and references regarding this topic can be found in the main body of our report.

Although we were reasonably successful at avoiding strong correlations between coefficients and predictor variables, there were two important variables for which this correlation could not be avoided, as discussed in the main body of our report. These two variables were sediment depth ($Z_{2.5}$) and 30m shear-wave velocity (V_{S30}). The two variables were found to be strongly correlated for $Z_{2.5} < 3$ km, which meant that only one of these parameters was needed to model local site conditions. Since we selected V_{S30} as the primary site-response variable (for consistency with engineering applications), we used it to model site-response and allowed $Z_{2.5}$ to enter the model for sediment depths greater than 3 km, where the model residuals indicated that this effect was significant at moderate-to-long periods. The residuals also indicated that an additional sediment-depth term was needed for $Z_{2.5} < 1$ km. Therefore, the sediment-depth terms were used only to provide an additional site effect when V_{S30} was found to be insufficient to model local soil conditions. More details and references regarding this topic can be found in the main body of our report.

B.6.2 Discussion of Specific Cited Examples

The question provides three examples where having too many predictive variables might make the model unreliable: (1) the potential correlation between magnitude scaling and the effects of depth to top of rupture, (2) the fact that larger earthquakes are more likely to rupture to the surface, and (3) the correlation between magnitude scaling and aspect ratio.

In our NGA model, the depth to top of rupture is used only to distinguish between reverse-faulting effects for earthquakes that rupture to the surface and those that do not. In essence, it allows large surface-rupturing reverse events to scale with magnitude similar to strike-slip and normal events. An analysis of residuals indicated that if this distinction was not made, either reverse-faulting effects would have been underestimated for the majority of the reverse earthquakes in the database or the magnitude-scaling for large strike-slip and normal events would have lead to an underestimation of ground motion for these events. Even at that, because of our decision to constrain the model to saturate when the analysis predicted oversaturation at large magnitudes and close distances, our model overestimates, on average, the short-period ground motions from the large surface-rupturing reverse earthquakes. Therefore, we believe that by allowing ground motions to be different between surface-rupturing and buried reverse earthquakes we have avoided biasing the reverse-faulting term and the magnitude-scaling effects for strike-slip and normal events.

We agree that larger earthquakes are more likely to rupture to the surface than smaller earthquakes, so there is indeed a correlation between magnitude scaling at large magnitudes and surface rupture. However, as noted above, we included a surface-faulting term only to determine when we applied an additional reverse-faulting factor to the predicted ground motions. We did not use it to change the magnitude-scaling term. As indicated above, our buried vs. surface-faulting term impacted the magnitude scaling for large earthquakes only to the extent that, had we not allowed this difference, the model would have predicted even a greater degree of oversaturation than it did. As it stands, the oversaturation predicted by the model (before constraining it to saturate) was reasonably small and not statistically significant, giving us a stronger justification for forcing saturation in our model.

As indicated in our report, we considered using aspect ratio in our model (in fact, we were the ones who first introduced it), but we decided not to when we discovered a discrepancy between the magnitude-dependence of the aspect ratios in the NGA database and those in the 2002 source model developed by the USGS and CGS. However, this is a separate issue than the one that you raised regarding the correlation between surface rupture and aspect ratio. Granted, surface-rupturing events are the ones with the largest aspect ratios. This simply means that one has to be careful not to adversely bias the magnitude-scaling term when aspect ratio is included in the model. We found that we could have just as easily accounted for the reduced magnitude-scaling at large magnitudes included in our model (for all styles of faulting) by not reducing the magnitude scaling at large magnitudes, but instead adding aspect ratio as a predictor variable. In other words, either one modeling approach or the other could be used. We chose to change the magnitude scaling rather than include aspect ratio as a predictor variable in our model for the reason specified above.

B.6.3 Conclusion

We believe that we avoided the pitfall of including too few or too many predictive variables in our NGA model by carefully reviewing each added term (coefficient) for its statistical significance and its lack of correlation with other terms (coefficients) in the model. We only included a predictor variable in the model when it was statistically significant or when it was supported by theoretical modeling or recommended by seismologists or engineers. Even in such cases, the model residuals were reviewed to see that they were consistent with the added term or, at least, did not violate it. Many predictor variables were reviewed through an analysis of residuals to ensure that no important variable was excluded. Therefore, we believe that we have not included too few or too many predictive variables in our NGA model.

B.7 USGS QUESTION #7

Foot wall term. Chang et al. (BSSA Dec. 2004) shows that there is a dip in residuals of the Chi-Chi footwall motions (at distances less than 15 km) when they are plotted as a function of nearest distance to rupture. This is caused by the fact that the distance to the center of the rupture is farther than the nearest distance for footwall sites. Is this relative dip of footwall ground motions accommodated in the functional forms used in NGA? If not, this could artificially lower ground motions in the distance ranges greater than 15 km. The dip in Chi Chi ground motions is also observed when using RJB. This dip does not appear to be present in the Northridge data. This calls into question the utility of the Chi Chi records for predicting ground motions for large events in other regions (see below).

B.7.1 Comments on Chang et al. (2004) Paper

Chang et al. (2004) developed an empirical ground motion model for the 1999 Chi-Chi earthquake using only hanging-wall and footwall stations in order to evaluate the impact of hanging-wall effects during this earthquake. They did this by fitting simultaneously a single relationship to both sets of data, then plotting the residuals from the relationship versus distance to look for hanging-wall effects. No adjustment for site effects was made. The bias in their residuals, suggesting overprediction of ground motions on the footwall at short distances, is visible in their Figures 4–6. We believe that this apparent bias does not necessarily represent a bias in the footwall ground motions for distances less than 15 km. Rather, it is likely caused by the requirement that the relationship must fit simultaneously the close-in hanging-wall and footwall recordings; thereby, overpredicting the footwall ground motions and underpredicting the hanging-wall ground motions. Had an appropriate hanging-wall term been included in the relationship, this apparent bias would have been reduced, if not completely eliminated. To demonstrate that this bias does not appear in our model, we show our residuals for the Chi-Chi earthquake below.

B.7.2 Residuals for Chi-Chi Earthquake

We plot the intra-event residuals from our NGA model for the Chi-Chi earthquake in Figures B.28–B.31 for PGA and PSA at periods of 0.2, 1.0 and 3.0s, respectively. The data are identified as being on the hanging-wall, the footwall, off the edge of the fault to the north in the direction of rupture, and off the edge of the fault to the south in the opposite direction of rupture. The horizontal dashed line shows the adjusted baseline after taking into account the inter-event (source) term and the overprediction resulting from constraining our model to saturate (as opposed to oversaturate) at short periods (see the main body of our report). A positive value for this adjusted baseline indicates an overprediction by the model (i.e., most of the points fall below this line). All of the figures show that overall the intra-event residuals are relatively unbiased with respect to distance, except for a few large-distant stations to the south. However, there is an interesting trend at large distances that will become evident below.

In order to understand how the residuals are impacted by azimuth, we plot only those residuals for stations located on the hanging-wall and the footwall in Figures B.32–B.35 for PGA and PSA at periods of 0.2, 1.0 and 3.0s, respectively. The distance range in these plots is more restricted than in the previous plots because of the limitation in the physical dimensions of Taiwan in the east-west direction. The bias noted by Chang et al. (2004) is not evident in these figures, although there is a tendency to overestimate the ground motion for footwall sites at distances greater than about 10–15 km, except for the 3.0s period, where the opposite trend is observed. This bias is particularly strong at short periods when the residuals are compared to the adjusted baseline. There is no noticeable bias in the hanging-wall sites except for a slight overprediction at short periods and at 3.0s with respect to the adjusted baseline.

Similar plots for stations located off the edge of the rupture to the north and to the south are shown in Figures B.36–B.39 for PGA and PSA at periods of 0.2, 1.0 and 3.0s, respectively. These figures indicate that the residuals are relatively unbiased out to distances of around 40–50 km, but display an interesting trend at larger distances. In particular, the residuals to the north (in the direction of rupture) beyond this distance show a decreased rate of attenuation and an underprediction of ground motion; whereas, the residuals to the south (in the opposite direction of rupture) show an increased rate of attenuation compared to the average trend. This could be caused by either anisotropic crustal properties or source directivity effects or both. We are not aware of any study that has addressed this issue. For PGA and the 0.2s spectral acceleration, the source term compensates completely for the underprediction of ground motions to the north at the expense of grossly overpredicting ground motions to the south. For the longer periods, the source term biases the predictions towards the northern stations, almost completely compensating for any potential underprediction to the north, at the expense of overpredicting ground motions to the south.

B.7.3 Conclusion

Our intra-event residual plots for the Chi-Chi earthquake do not show the biases in the footwall and hanging-wall residuals at short distances that were observed in the Chang et al. (2004) residual plots. As noted above, this bias was likely caused by these authors not including a hanging-wall term in their ground motion model. In fact, we find no bias with distance overall out to a distance of at least 100 km and no significant bias in the hanging-wall residuals out to the 60-km limit of the data, except at 3.0s period where the more distant hanging-wall ground motions are overpredicted. Footwall sites are overpredicted beyond a distance of 10–15 km, except at 3.0s period where they are underpredicted. We do find a bias in the rate of attenuation between stations located to the north and to the south for distances greater than about 40–50 km, which will need additional study to explain. Forcing saturation in our model generally causes it to overpredict ground motion at short periods, even for hanging wall sites. At longer periods, the predictions are biased towards the relatively higher ground motions to the north. In conclusion, we believe that our results confirm the utility in using the Chi-Chi recordings for predicting ground motion from large events in regions outside of Taiwan.

Chang, T.Y., Cotton, F., Tsai, Y.B., and Angelier, J. (2004). Quantification of hanging-wall effects on ground motion: some insights from the 1999 Chi-Chi earthquake. *Bull. Seism. Soc. Am.* **94**, 2186–2197.

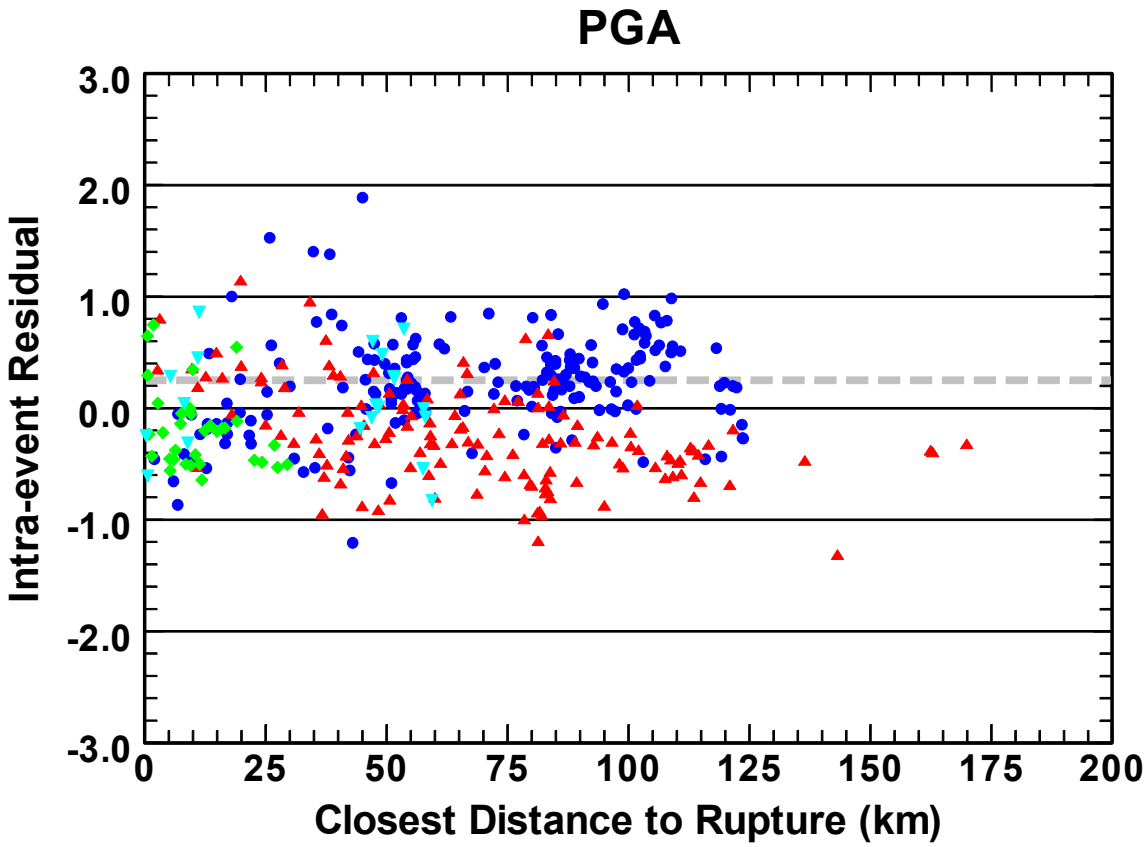

Fig. B.28 **Plot of the PGA intra-event residuals from the Campbell-Bozorgnia NGA model for the Chi-Chi mainshock. Recordings are identified as being on the hanging-wall (cyan inverted triangles), on the footwall (green diamonds), off the edge of the fault to the north in the direction of rupture (blue circles), and off the edge of the fault to the south in the opposite direction of rupture (red triangles). The horizontal dashed grey line represents the adjusted baseline after accounting for the source term and the additional bias caused by disallowing oversaturation, where a positive value represents an overprediction by the model (in this case a significant overprediction).**

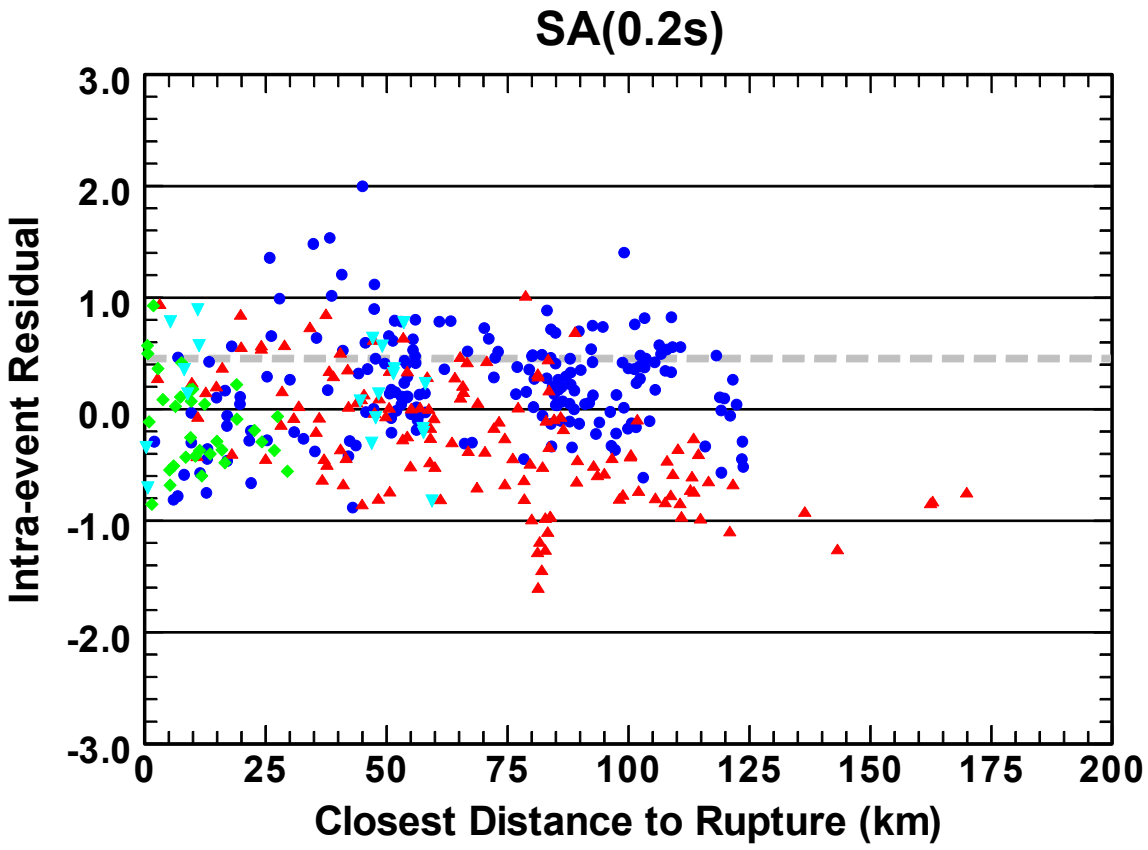

Fig. B.29 **Plot of the 0.2s spectral acceleration intra-event residuals from the Campbell-Bozorgnia NGA model for the Chi-Chi mainshock. The symbols and dashed grey line are the same as in Figure B.28.**

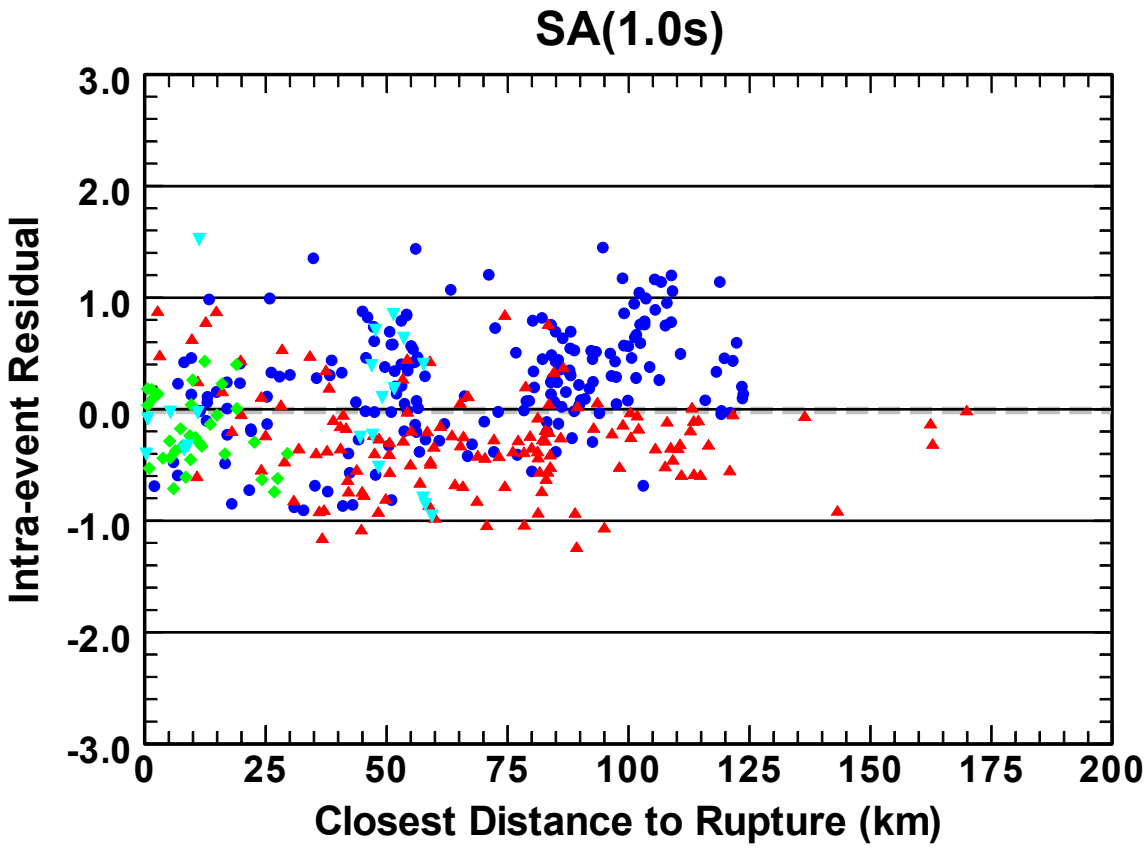

Fig. B.30 **Plot of the 1.0s spectral acceleration intra-event residuals from the Campbell-Bozorgnia NGA model for the Chi-Chi mainshock. The symbols and dashed grey line are the same as in Figure B.28.**

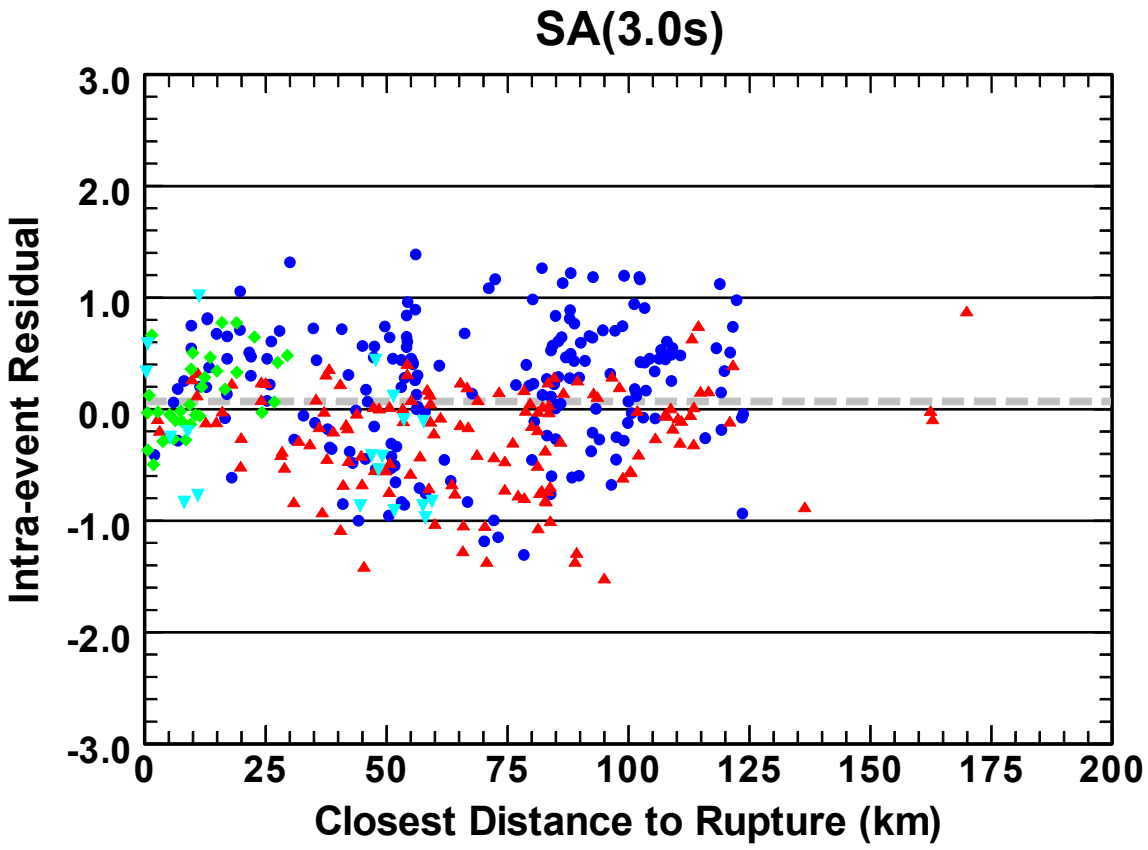

Fig. B.31 **Plot of the 3.0s spectral acceleration intra-event residuals from the Campbell-Bozorgnia NGA model for the Chi-Chi mainshock. The symbols and dashed grey line are the same as in Figure B.28.**

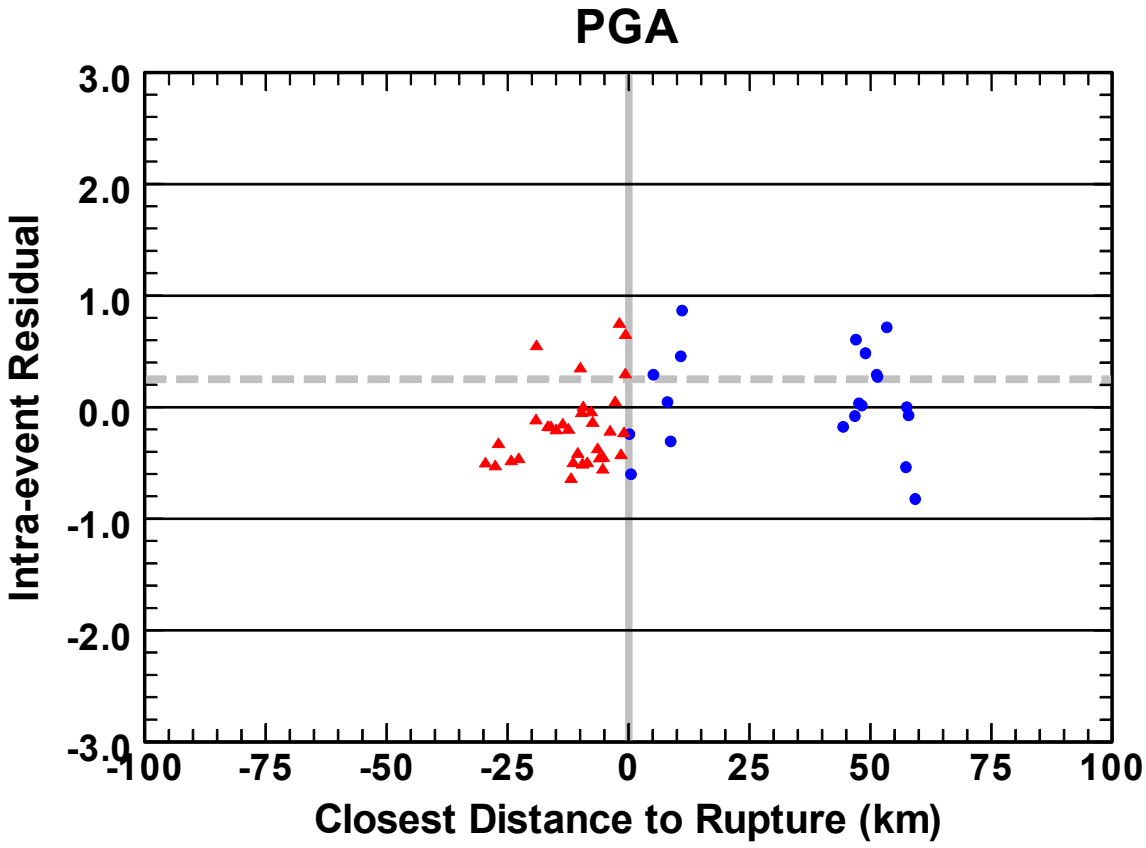

Fig. B.32 **Plot of the PGA intra-event residuals from the Campbell-Bozorgnia NGA model for the Chi-Chi mainshock. Recordings are identified as being on the hanging-wall (blue circles) or on the footwall (red triangles). Footwall distances are plotted as negative values for clarity. The vertical solid grey line demarks the transition from the hanging wall to the footwall. The horizontal dashed grey line represents the adjusted baseline after accounting for the source term and the additional bias caused by disallowing oversaturation, where a positive value represents an overprediction by the model (in this case a significant overprediction).**

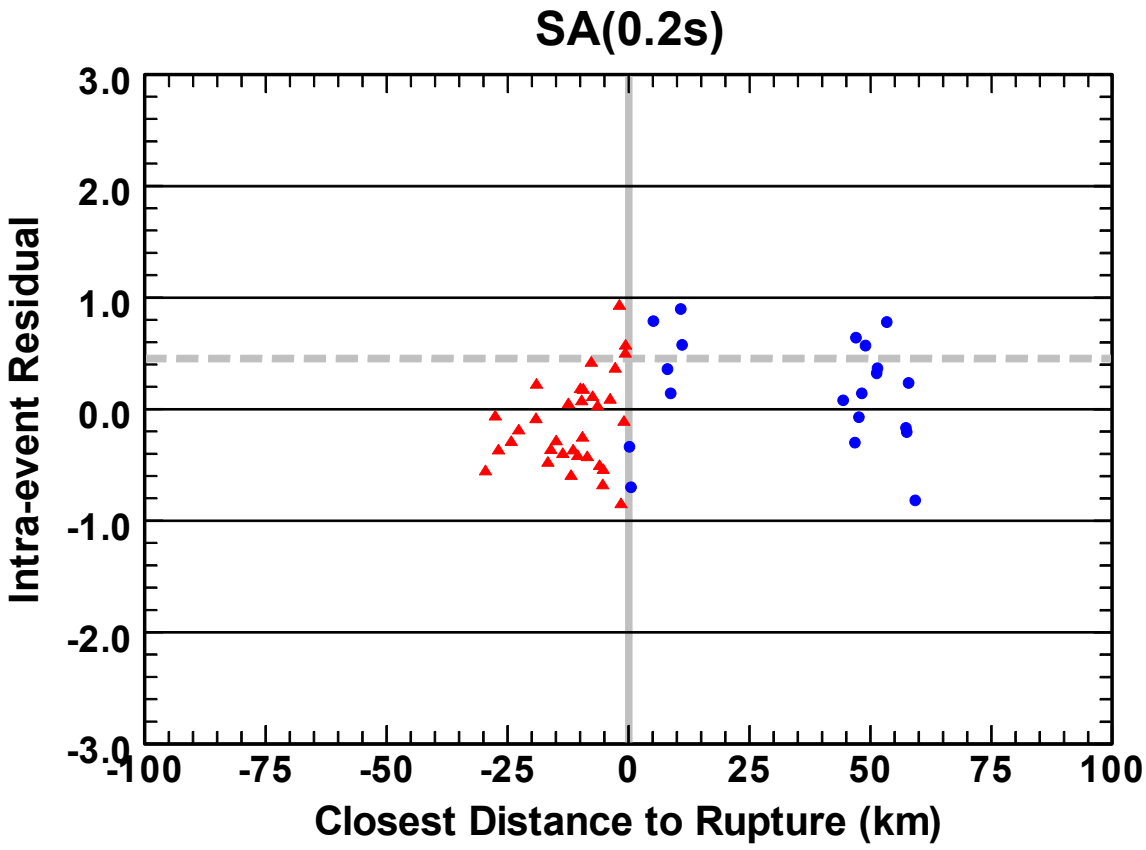

Fig. B.33 **Plot of the 0.2s spectral acceleration intra-event residuals from the Campbell-Bozorgnia NGA model for the Chi-Chi mainshock. Recordings are identified as being on the hanging-wall (blue circles) or on the footwall (red triangles). The symbols and solid and dashed grey lines are the same as in Figure B.32.**

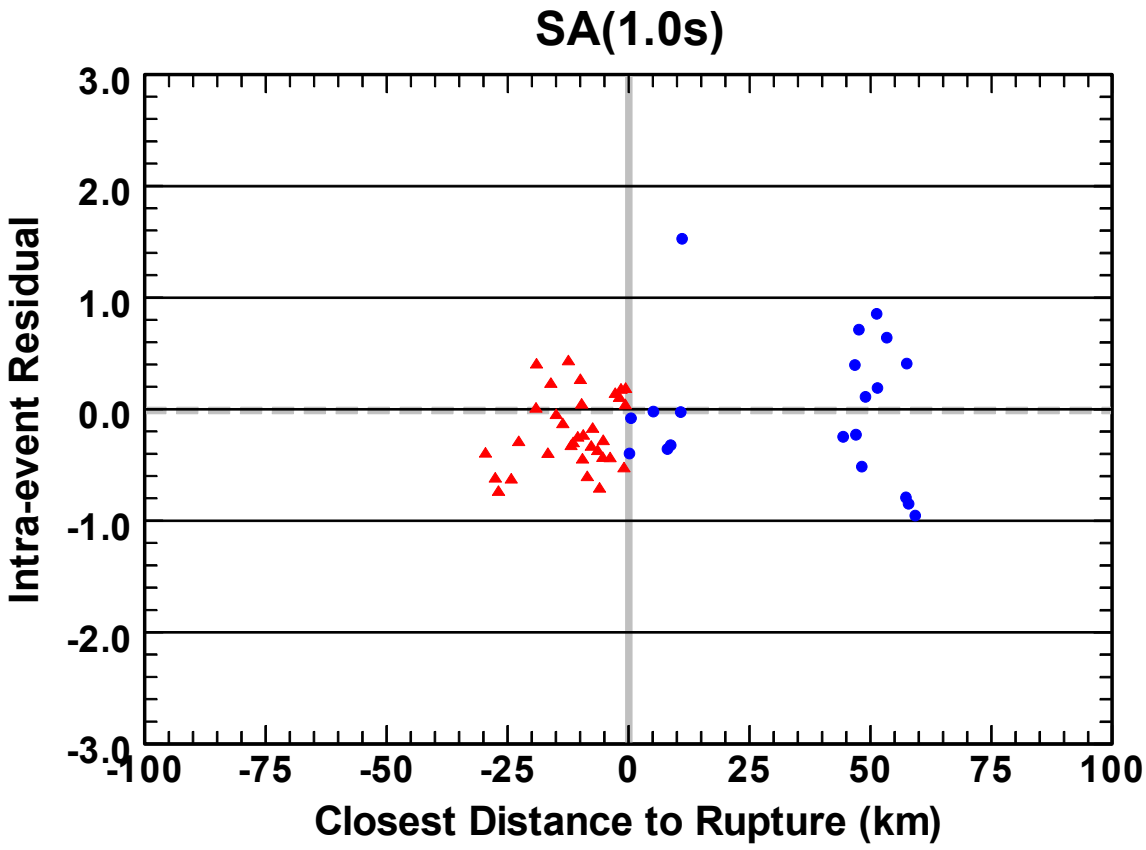

Fig. B.34 **Plot of the 1.0s spectral acceleration intra-event residuals from the Campbell-Bozorgnia NGA model for the Chi-Chi mainshock. Recordings are identified as being on the hanging-wall (blue circles) or on the footwall (red triangles). The symbols and solid and dashed grey lines are the same as in Figure B.32.**

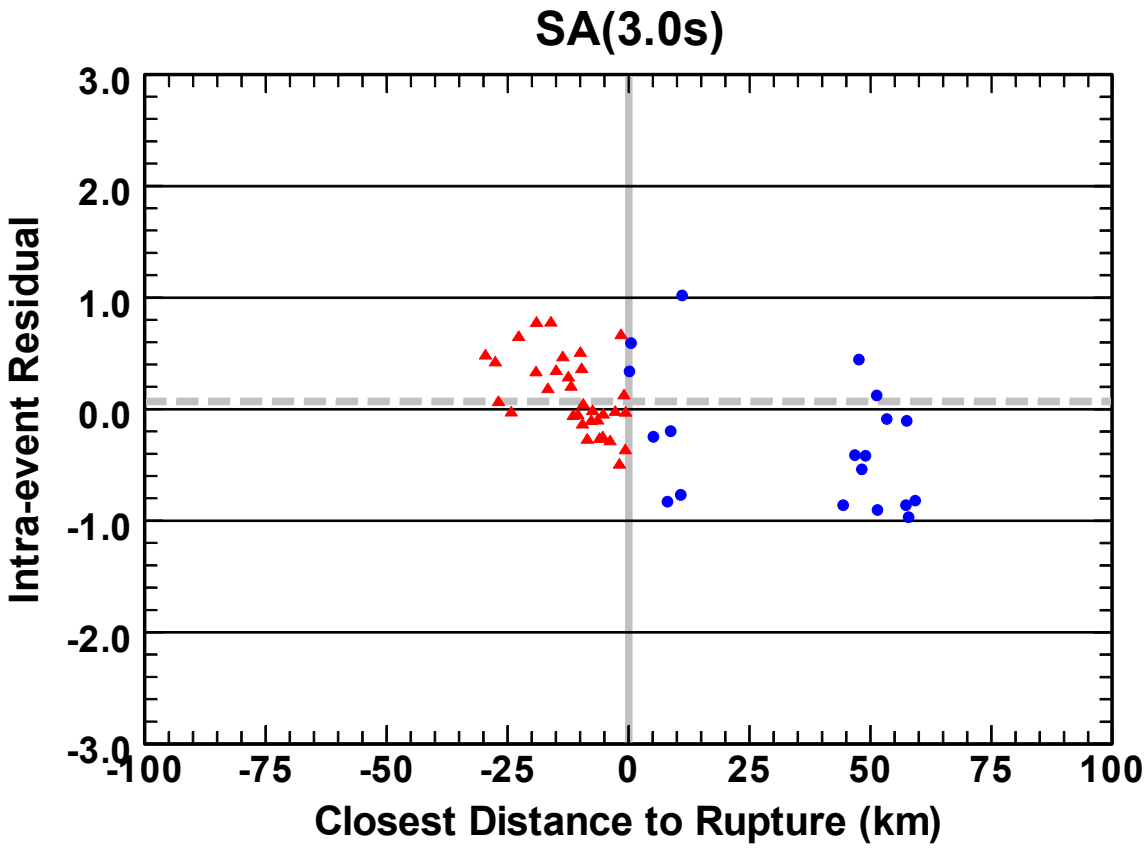

Fig. B.35 **Plot of the 3.0s spectral acceleration intra-event residuals from the Campbell-Bozorgnia NGA model for the Chi-Chi mainshock. Recordings are identified as being on the hanging-wall (blue circles) or on the footwall (red triangles). The symbols and solid and dashed grey lines are the same as in Figure B.32.**

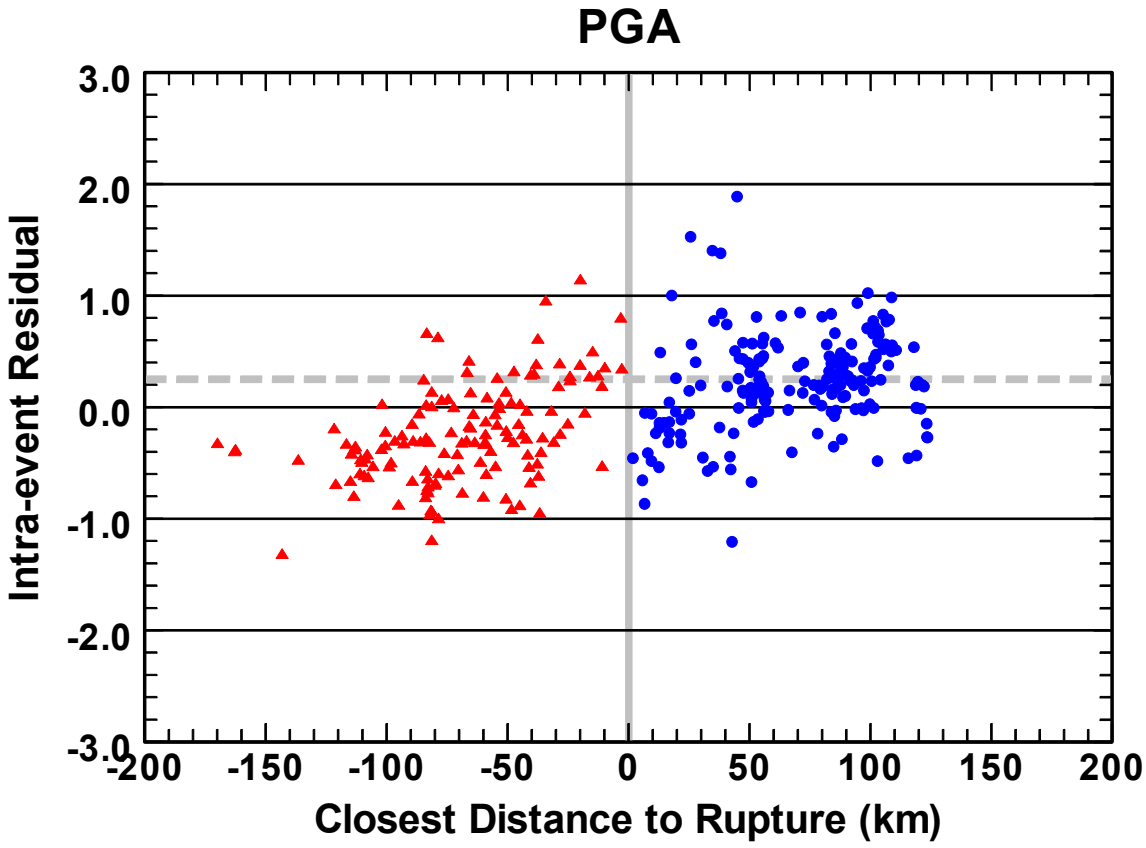

Fig. B.36 **Plot of the PGA intra-event residuals from the Campbell-Bozorgnia NGA model for the Chi-Chi mainshock. Recordings are identified as being off the edge of the fault to the north in the direction of rupture (blue circles) or off the edge of the fault to the south in the opposite direction of rupture (red triangles). Southern distances are plotted as negative values for clarity. The vertical solid grey line demarks the transition from the northern sites to the southern sites. The horizontal dashed grey line represents the adjusted baseline after accounting for the source term and the additional bias caused by disallowing oversaturation, where a positive value represents an overprediction by the model (in this case a significant overprediction).**

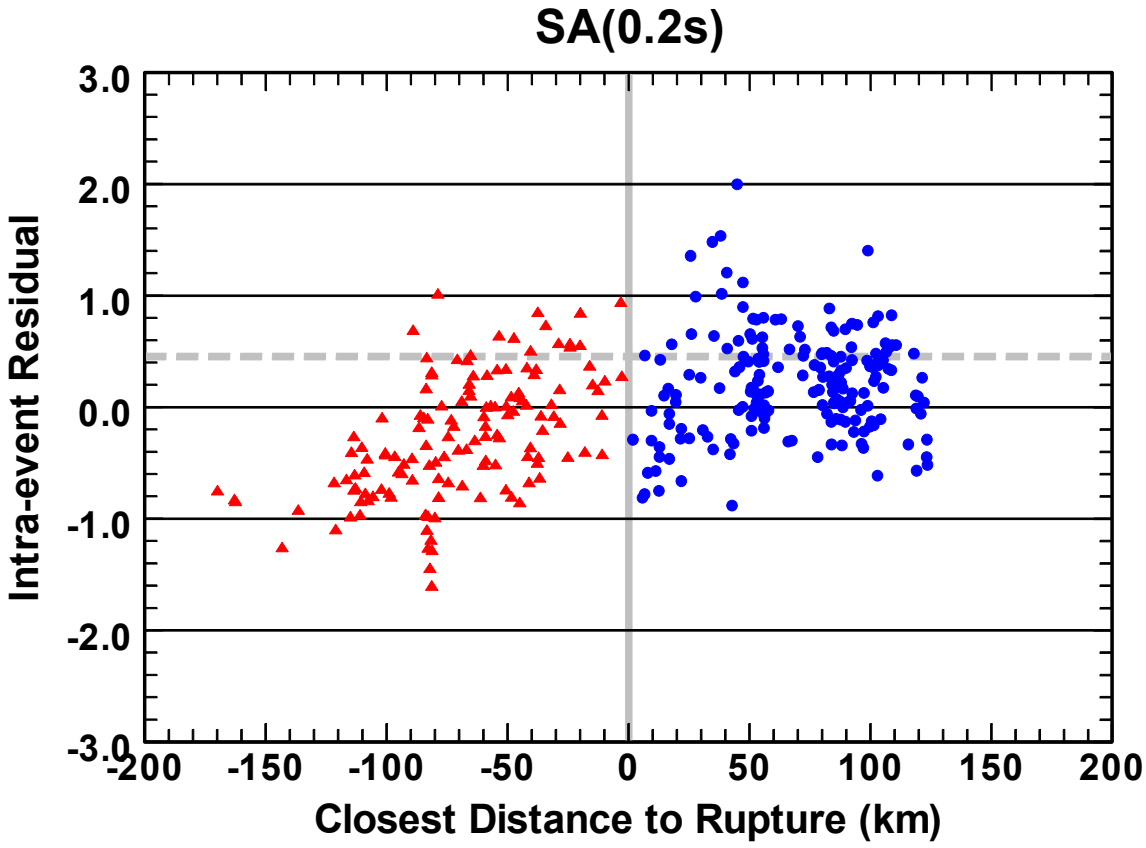

Fig. B.37 **Plot of the 0.2s spectral acceleration intra-event residuals from the Campbell-Bozorgnia NGA model for the Chi-Chi mainshock. The symbols and grey solid and dashed lines are the same as in Figure B.36.**

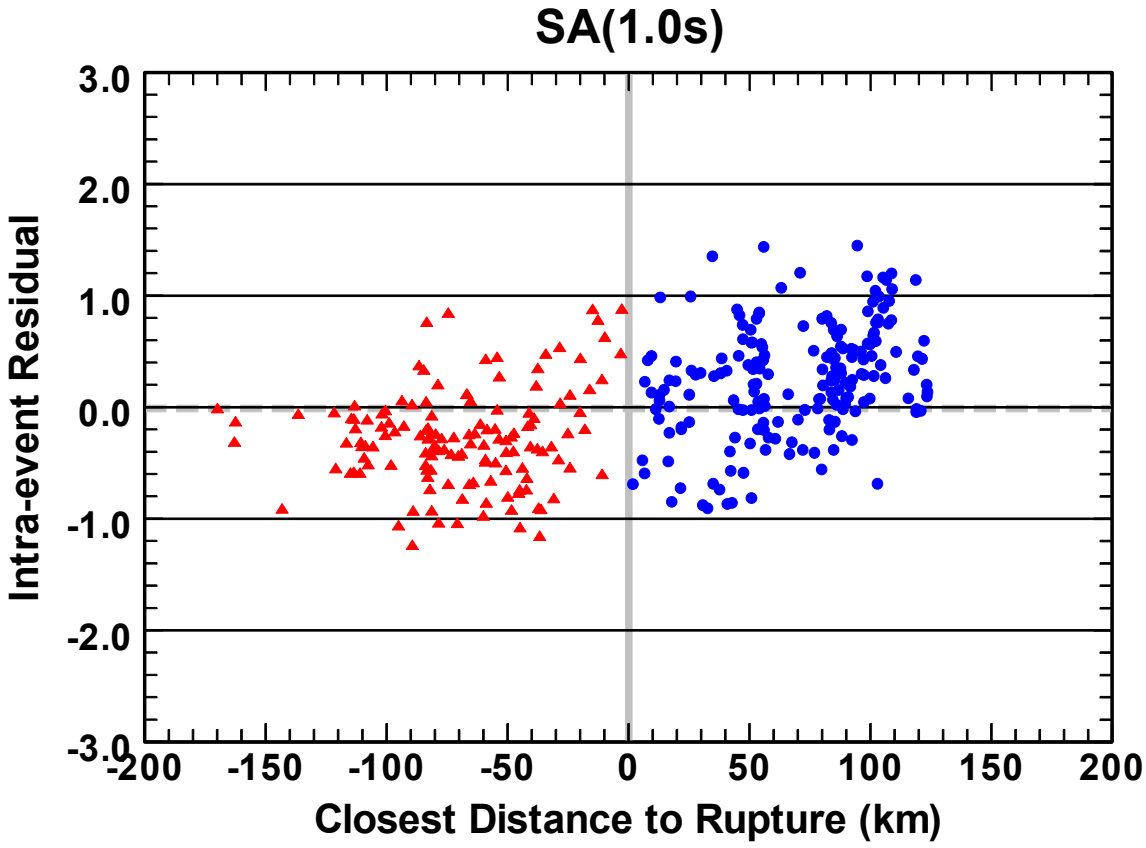

Fig. B.38 **Plot of the 1.0s spectral acceleration intra-event residuals from the Campbell-Bozorgnia NGA model for the Chi-Chi mainshock. The symbols and grey solid and dashed lines are the same as in Figure B.36.**

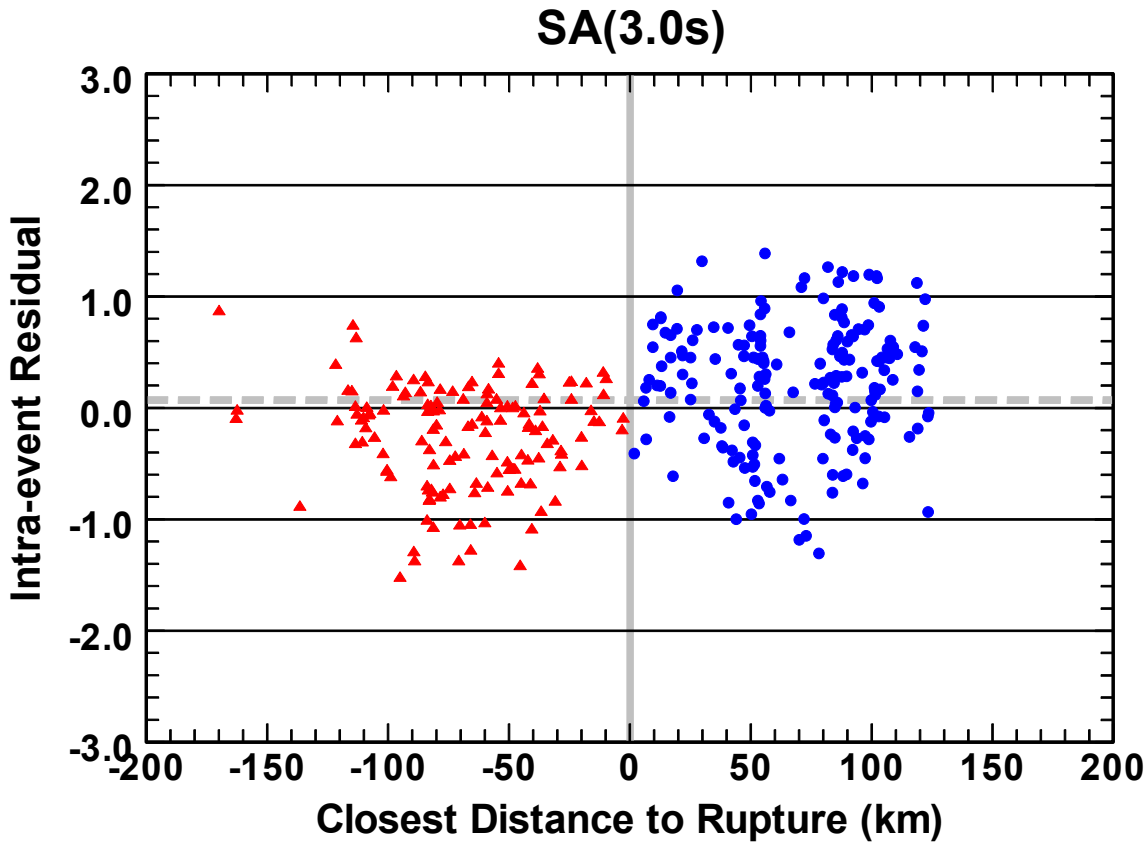

Fig. B.39 Plot of the 3.0s spectral acceleration intra-event residuals from the Campbell-Bozorgnia NGA model for the Chi-Chi mainshock. The symbols and grey solid and dashed lines are the same as in Figure B.36.

B.8 USGS QUESTION #8

Scaling with magnitude. For high frequencies (≥ 5hz), the spectral accelerations for close-in sites (< 10 km JB distance) are far higher for Superstition Hills, Landers, and Kobe earthquakes, than for the Kocaeli earthquake. Here [we] have chosen only strike slip earthquakes. This suggests there are regional differences in stress drop for strike slip earthquakes.

B.8.1 Comments on Regional Differences in Stress Drop

We acknowledge that there are likely to be regional differences in stress drop. The question is whether such differences lead to a bias in the predicted ground motions in regions where the empirical ground motion model will be applied. The earthquakes that you mention come from a variety of tectonic environments. The Kocaeli and Superstition Hills earthquakes occurred in a transtensional stress regime. The Landers earthquake also occurred in what is probably a transtensional stress regime (John Anderson, USGS Workshop, Reno, NV, 2006).[6] The Kobe earthquake occurred in a transpressional stress regime. Seismologists would likely expect the stress drops to be the largest in a transpressional stress regime and smallest in a transtensional stress regime. Of course, there is a large degree of variability in stress drops within a given tectonic environment, so a comparison of a few earthquakes is not really sufficient to derive general conclusions. Nonetheless, in the next section we look to see if there is a systematic bias in our NGA model predictions for these four earthquakes.

B.8.2 Comparison of Model Predictions

In the development of our model, we looked at possible differences in ground motion due to tectonic environment by comparing inter-event residuals (source terms) between extensional and non-extensional tectonic regimes after including coefficients for style of faulting. We didn't find any bias in the residuals of either group, which suggested that, at least for our dataset, there was no systematic difference between these two tectonic regimes that wasn't accounted for by the style-of-faulting factors. In fact, what little effect we saw indicated that ground motions in extensional regimes were possibly larger. However, John Anderson (USGS Workshop, Reno, NV, 2006) has disagreed with the assignment of extensional and non-extensional regimes to several California earthquakes in the NGA database based on the original assessment by Spudich et al. (1997, 1999). He suggests, for example, that earthquakes in the Mojave Desert (e.g., 1992 Landers and 1999 Hector Mine) should be classified as extensional. If this were to be confirmed, we are not sure what difference it would make in our assessment of extensional versus non-extensional tectonic regimes.[6]

Rather than look at the absolute value of ground motion, as was suggested in the question, we again look at the residuals for the earthquakes you have mentioned to see if there is

[6] In a subsequent investigation, Paul Spudich and Dave Boore determined that the 1992 Landers, 1999 Kocaeli, and 1999 Hector Mine earthquakes likely occurred in a strike-slip (non-extensional) stress regime.

a systematic bias in the predictions from our NGA model that is consistent with the statement in the question. Absolute values can be deceiving, since they do not take into account differences in predictor variables, such as magnitude and local soil conditions, between earthquakes. In Figure B.40 we plot the intra-event residuals for PGA versus rupture distance for the 1995 Kobe, 1992 Landers, 1999 Kocaeli, and 1987 Superstition Hills earthquakes over the full range of distances used in our model to see how well the model fits the data overall. Also shown on this plot is the adjusted baselines for these same events after accounting for the inter-event residuals (source term) and the additional bias caused by constraining the model to saturate when oversaturation was predicted. The negative adjusted baselines indicate underprediction by the model. A larger negative baseline implies a larger underprediction.

Looking at the adjusted baselines, Figure B.40 shows that all four events are underpredicted overall, with the Kobe and Superstition Hills events having the largest underprediction and the Landers and Kocaeli events having the largest underprediction. The other interesting observation is that PGA is underpredicted relative to other intra-event residuals for these four earthquakes between distances of around 65–125 km, where one might expect increased ground motions from crustal reflections. (This effect becomes negligible at longer periods). Our functional form does not allow for differences in geometrical attenuation from such reflections because of their complexity and variability with respect to period. Figure B.41 shows a similar plot for $R_{JB} \leq 20$ km. This plot extends to a larger distance than was suggested so that there would be enough recordings to make a meaningful comparison. In this distance range, the comparison is quite different than that over all distances. Comparing the intra-event residuals with the adjusted baselines, the Superstition Hills earthquake is clearly underpredicted, but the predictions for the other three earthquakes all appear to be relatively unbiased. Similar results are found for 0.2s spectral acceleration as shown in Figures B.42 and B.43.

If differences in stress drop were causing the differences noted in the question and observed in the residual plots for short-period ground motions, these differences should be diminished at longer periods. To test this hypothesis, we show the same residual plots as above for the 1.0 and 3.0s spectral accelerations in Figures B.44–B.47. Again, all of the events are underpredicted overall, but now the largest underprediction is for the Kobe earthquake for 1.0s period (Figure B.44) and the Landers earthquake for 3.0s period (Figure B.46), while the other events are all moderately underpredicted with the smallest underprediction occurring for the Kocaeli event. This ranking for the Kocaeli earthquake does not seem to support the idea that the short-period differences for this event are the result of an unusually low stress drop. At 3.0s, the Landers event is underpredicted at distances beyond about 130 km. Within 20 km, Kocaeli is overpredicted, Kobe is underpredicted, and the other two events are relatively unbiased compared to their adjusted baselines.

B.8.3 Conclusion

We did not find any significant difference in ground motions between extensional and non-extensional tectonic regimes based on an analysis of residuals after accounting for differences due to style of faulting (see Section B.1). Our residuals also indicate that all four events that

were mentioned in the question are underpredicted by our model, so the Kocaeli earthquake is not unique in this regard, nor does it appear to be an outlier. The Kobe earthquake has the largest underprediction in our model, which might be consistent with it occurring in a transpressional stress regime. However, it also had a relatively large hypocentral depth (17 km) and its rupture was buried, at least along its northern reaches where most of the recordings were located, which might have also contributed to this underprediction. At short periods, the Superstition Hills earthquake, which also had a buried rupture, is underpredicted by our model by about the same amount as the Kobe earthquake. Therefore, one might argue that the relative differences between the residuals for these four earthquakes could be explained by whether they had buried versus surface faulting rather than whether they were affected by regional differences in stress drop. We found this to be the case for reverse faults, but we believed that the data were too ambiguous to allow us to apply such a factor to strike-slip earthquakes at the present time.

Our analysis of residuals suggests that our results either do not support the observation that, for high frequencies, the spectral accelerations for close-in sites (<10 km JB distance) are far higher for Superstition Hills, Landers, and Kobe earthquakes than for the Kocaeli earthquake or that these differences have been reasonably captured in our model. Although we agree that there could be regional differences in stress drop and stress regime for strike slip earthquakes, and our residuals possibly support this, we also believe that this might be just as easily modeled by accounting for differences between buried versus surface faulting. Under the hypothesis that ground motions should be larger in transpressional stress regimes (presumably due to larger stress drops), large strike-slip earthquakes in California from the Big Bend north would be underpredicted by our model; whereas, under the hypothesis that ground motions are smaller for surface-faulting events, these earthquakes would be overpredicted by our model. By not specifically attempting to model one hypothesis over the other, our model allows for the possibility of both hypotheses with a corresponding increase in aleatory variability, which we believe reasonably reflects the uncertainty expressed within the scientific community.

Spudich, P., Fletcher, J., Hellweg, M., Boatwright, J., Sullivan, C., Joyner, W.B., Hanks, T.C., Boore, D.M., McGarr, A.F., Baker, L.M., and Lindh, A.G. (1997). SEA96: a new predictive relation for earthquake ground motions in extensional tectonic regimes. *Seism. Res. Lett.* **68**, 190–198.

Spudich, P., Joyner, W.B., Lindh, A.G., Boore, D.M., Margaris, B.M., and Fletcher, J.B. (1999). SEA99: a revised ground motion prediction relation for use in extensional tectonic regimes. *Bull. Seism. Soc. Am.* **89**, 1156–1170.

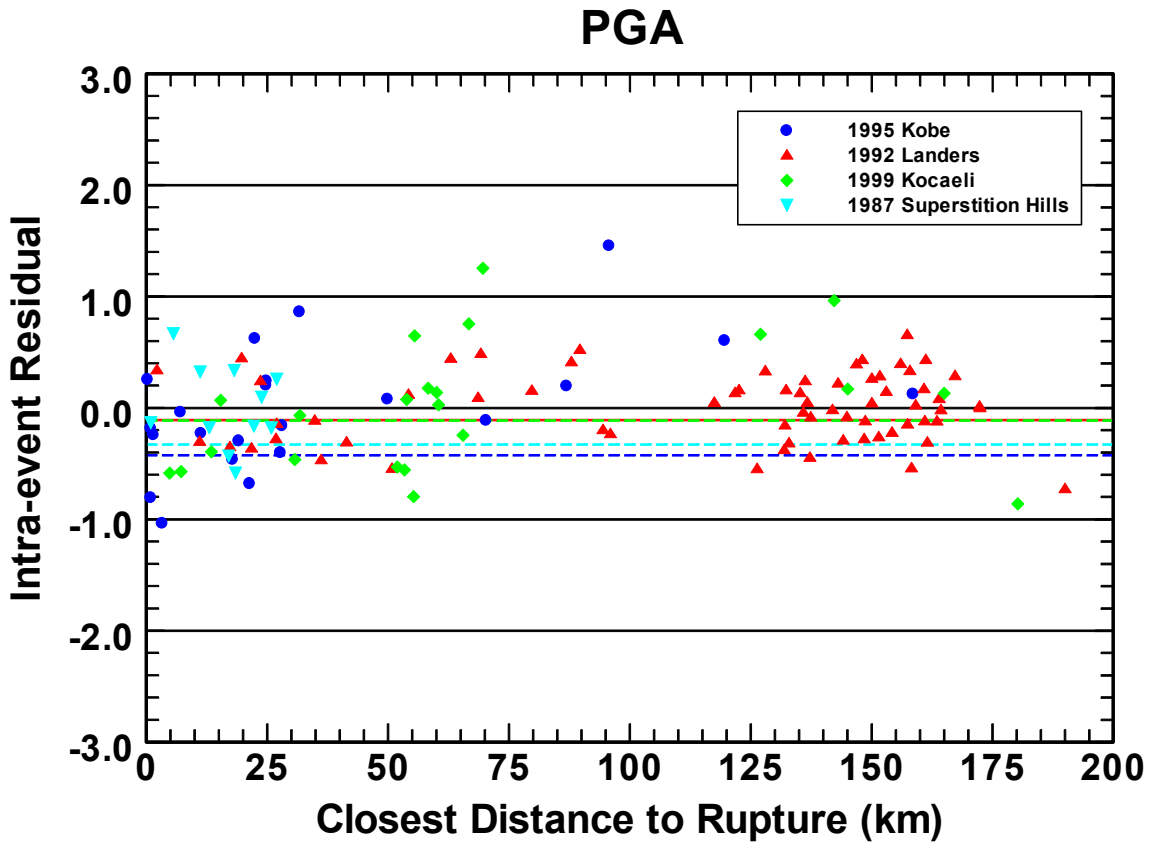

Fig. B.40 **Plot of the PGA intra-event residuals from the Campbell-Bozorgnia NGA model for the Kobe (blue circles), Landers (red triangles), Kocaeli (green diamonds), and Superstition Hills (cyan inverted triangles) earthquakes for $R_{RUP} \leq 200$ km. The horizontal dashed lines represent the adjusted baseline for these same earthquakes after accounting for the source term and the additional bias caused by disallowing oversaturation, where a negative value represents an underprediction by the model.**

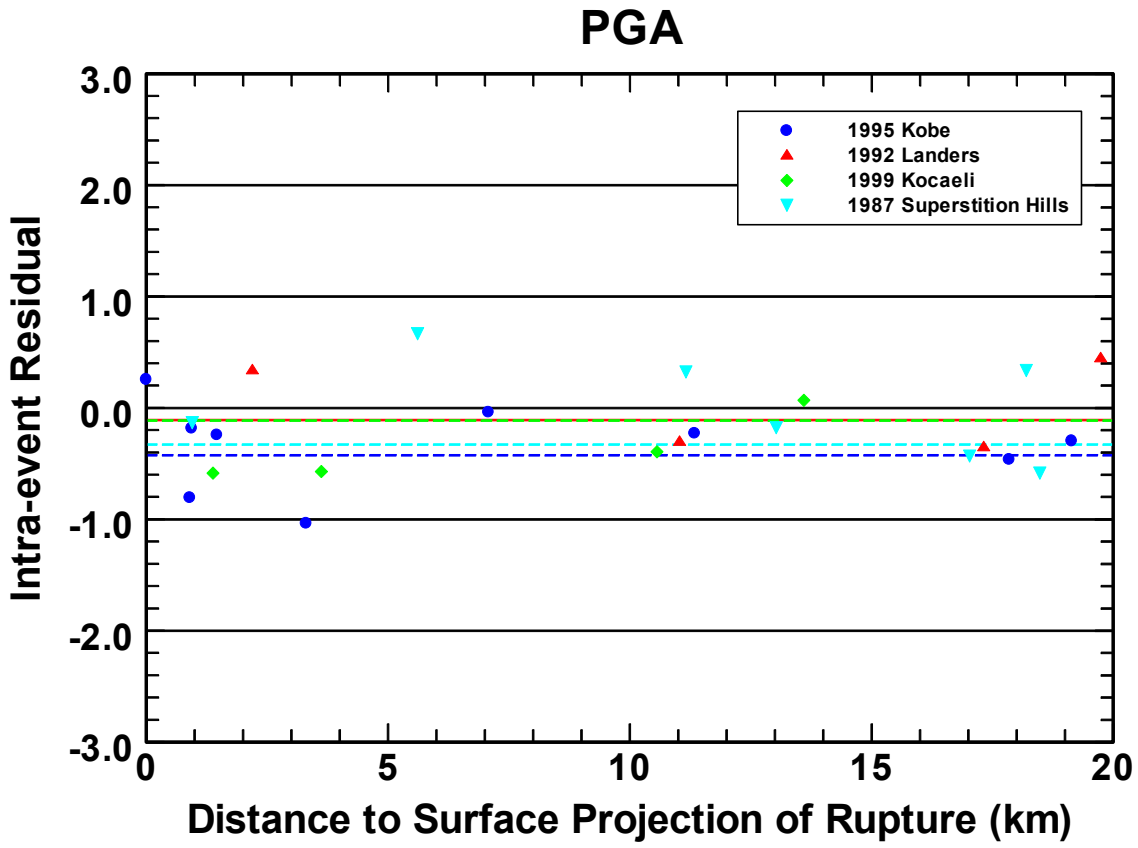

Fig. B.41 **Plot of the PGA intra-event residuals from the Campbell-Bozorgnia NGA model for the Kobe (blue circles), Landers (red triangles), Kocaeli (green diamonds), and Superstition Hills (cyan inverted triangles) earthquakes for $R_{JB} \leq 20$ km. The dashed lines are the same as in Figure B.40.**

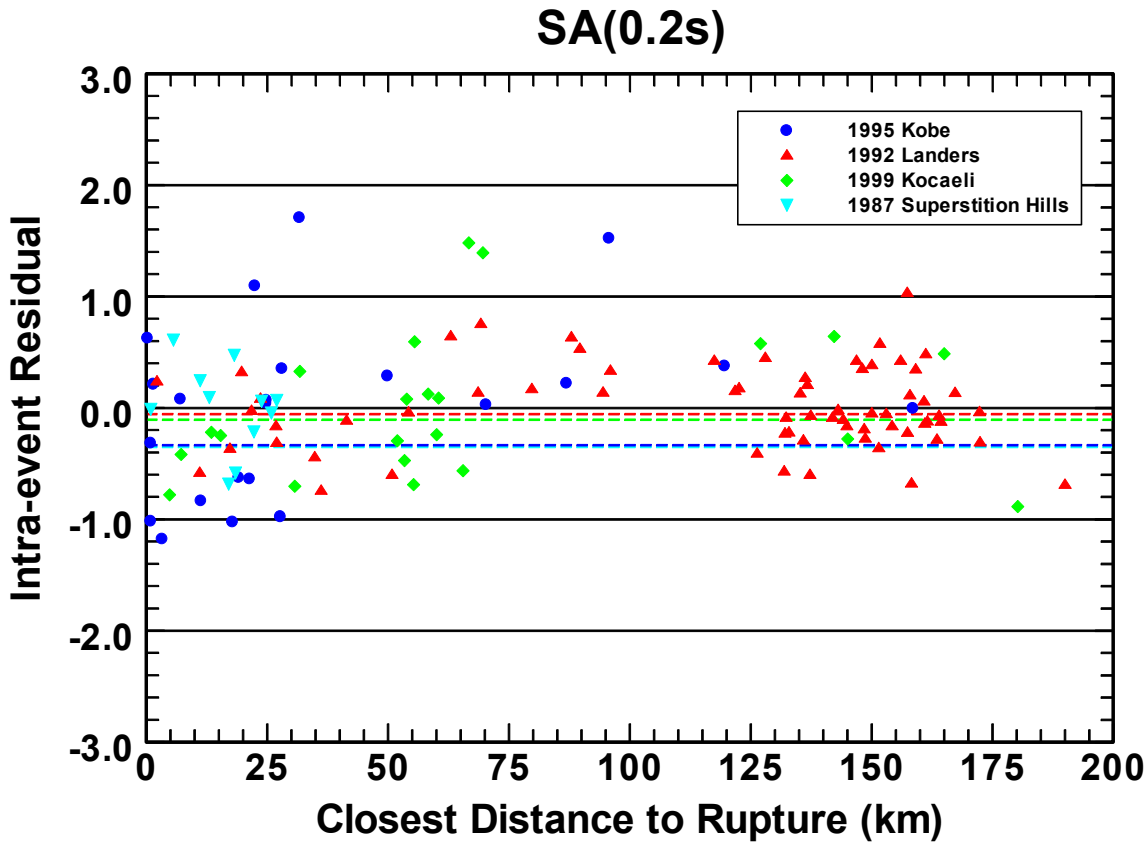

Fig. B.42 **Plot of the 0.2s spectral acceleration intra-event residuals from the Campbell-Bozorgnia NGA model for the Kobe (blue circles), Landers (red triangles), Kocaeli (green diamonds), and Superstition Hills (cyan inverted triangles) earthquakes for $R_{RUP} \leq 200$ km. The horizontal dashed lines represent the adjusted baseline for these same earthquakes after accounting for the source term and the additional bias caused by disallowing oversaturation, where a negative value represents an underprediction by the model.**

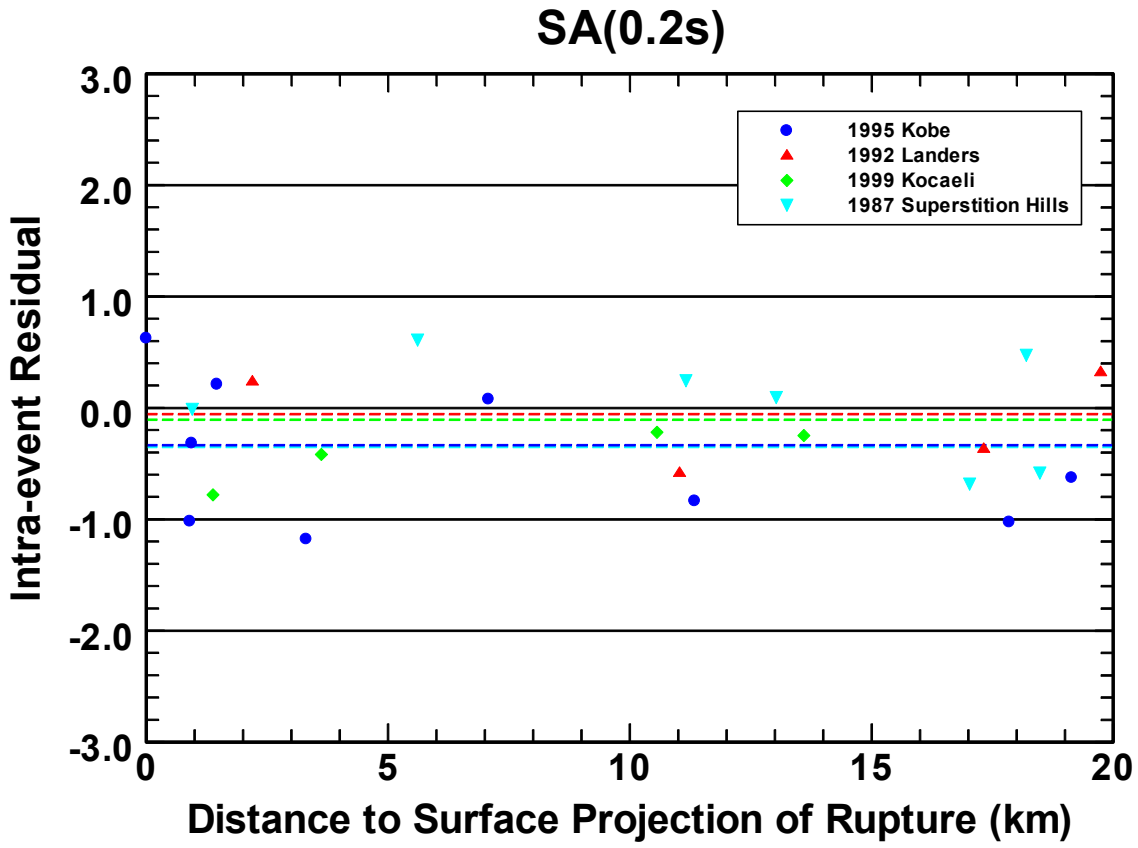

Fig. B.43 **Plot of the 0.2s spectral acceleration intra-event residuals from the Campbell-Bozorgnia NGA model for the Kobe (blue circles), Landers (red triangles), Kocaeli (green diamonds), and Superstition Hills (cyan inverted triangles) earthquakes for $R_{JB} \leq 20$ km. The dashed lines are the same as in Figure B.42.**

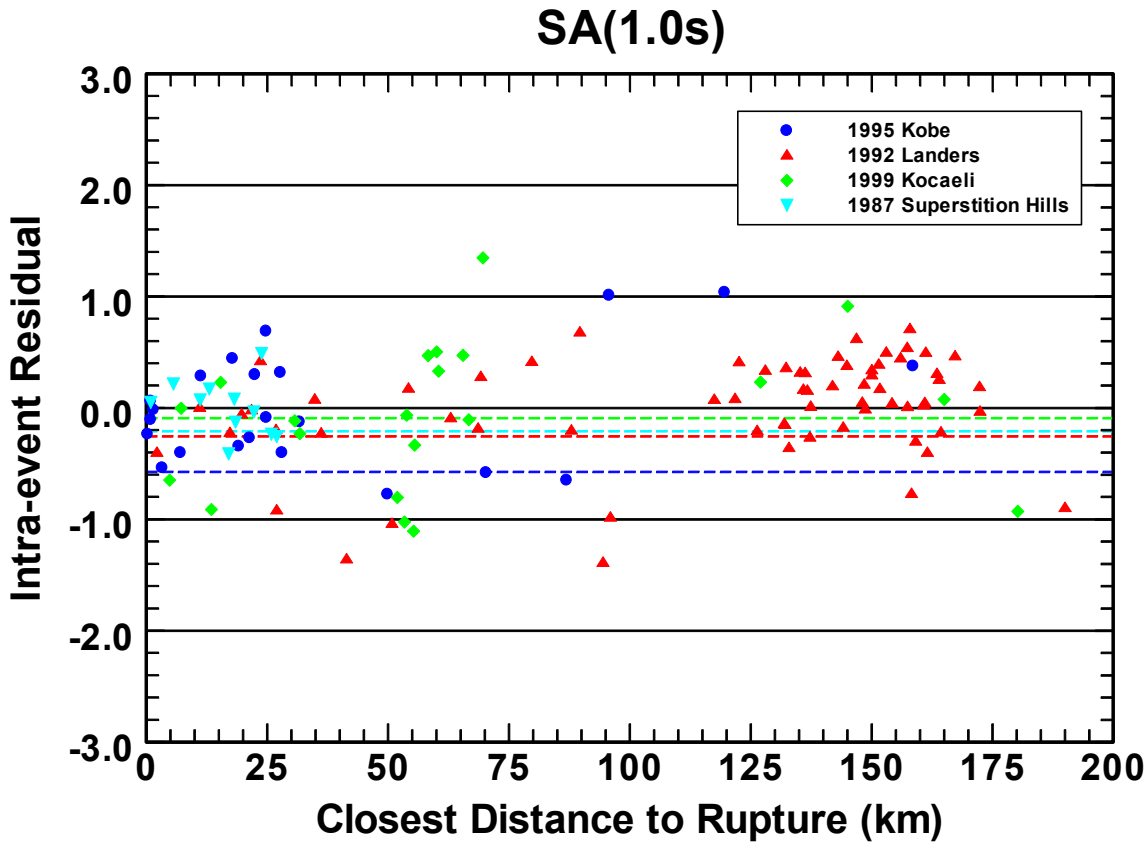

Fig. B.44 **Plot of the 1.0s spectral acceleration intra-event residuals from the Campbell-Bozorgnia NGA model for the Kobe (blue circles), Landers (red triangles), Kocaeli (green diamonds), and Superstition Hills (cyan inverted triangles) earthquakes for $R_{RUP} \leq 200$ km. The horizontal dashed lines represent the adjusted baseline for these same earthquakes after accounting for the source term and the additional bias caused by disallowing oversaturation, where a negative value represents an underprediction by the model.**

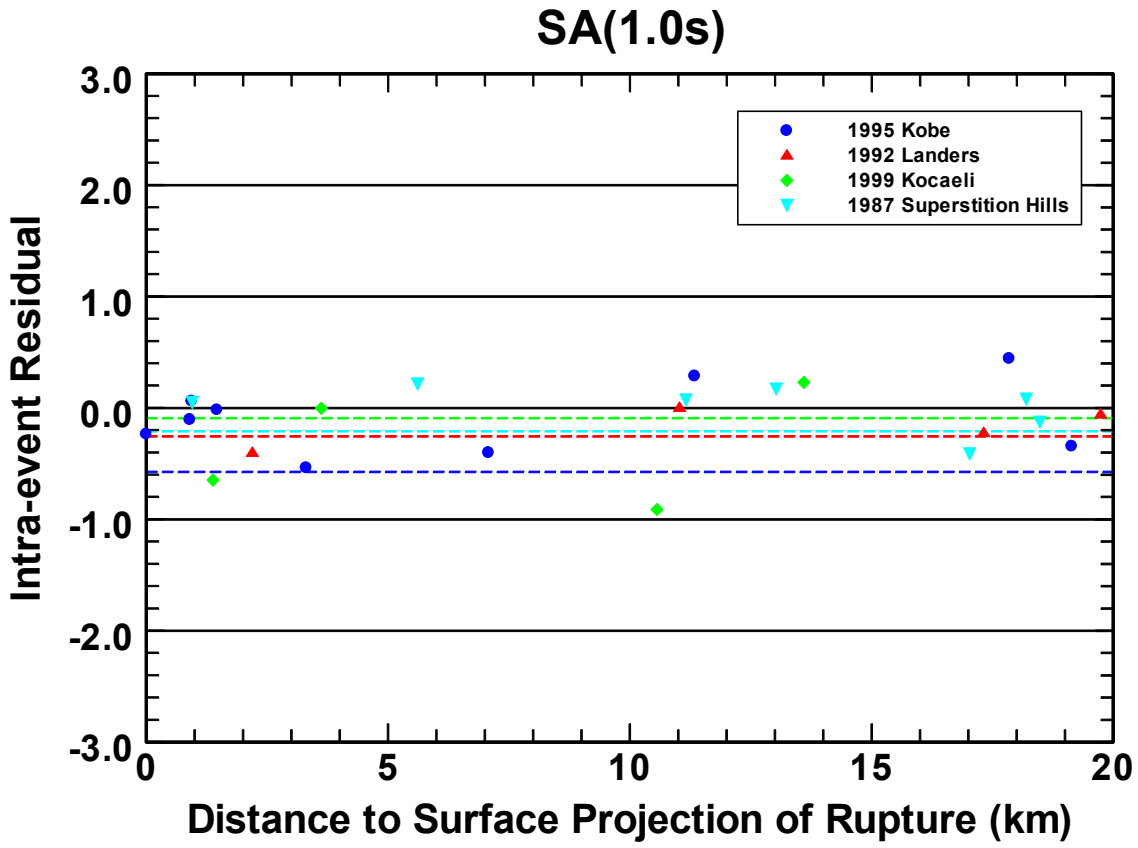

Fig. B.45 **Plot of the 1.0s spectral acceleration intra-event residuals from the Campbell-Bozorgnia NGA model for the Kobe (blue circles), Landers (red triangles), Kocaeli (green diamonds), and Superstition Hills (cyan inverted triangles) earthquakes for $R_{JB} \leq 20$ km. The dashed lines are the same as in Figure B.44.**

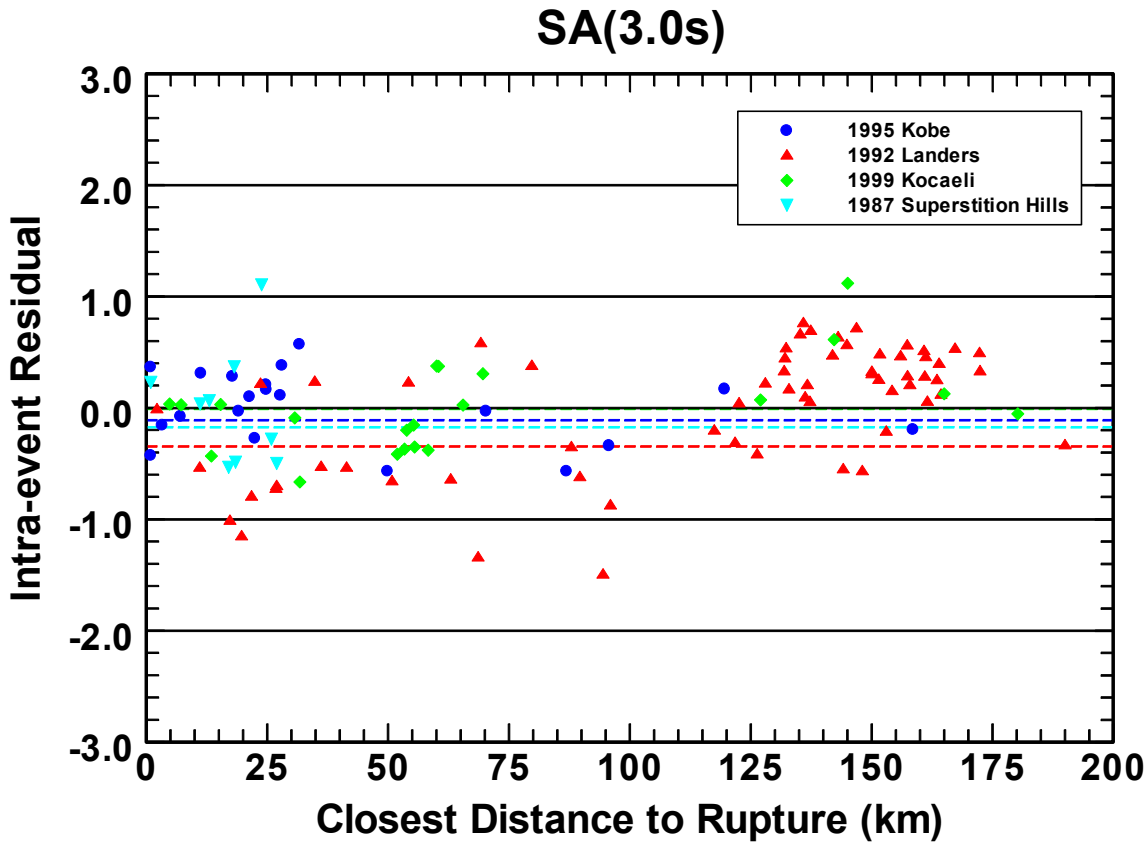

Fig. B.47 **Plot of the 3.0s spectral acceleration intra-event residuals from the Campbell-Bozorgnia NGA model for the Kobe (blue circles), Landers (red triangles), Kocaeli (green diamonds), and Superstition Hills (cyan inverted triangles) earthquakes for $R_{RUP} \leq 200$ km. The horizontal dashed lines represent the adjusted baseline for these same earthquakes after accounting for the source term and the additional bias caused by disallowing oversaturation, where a negative value represents an underprediction by the model.**

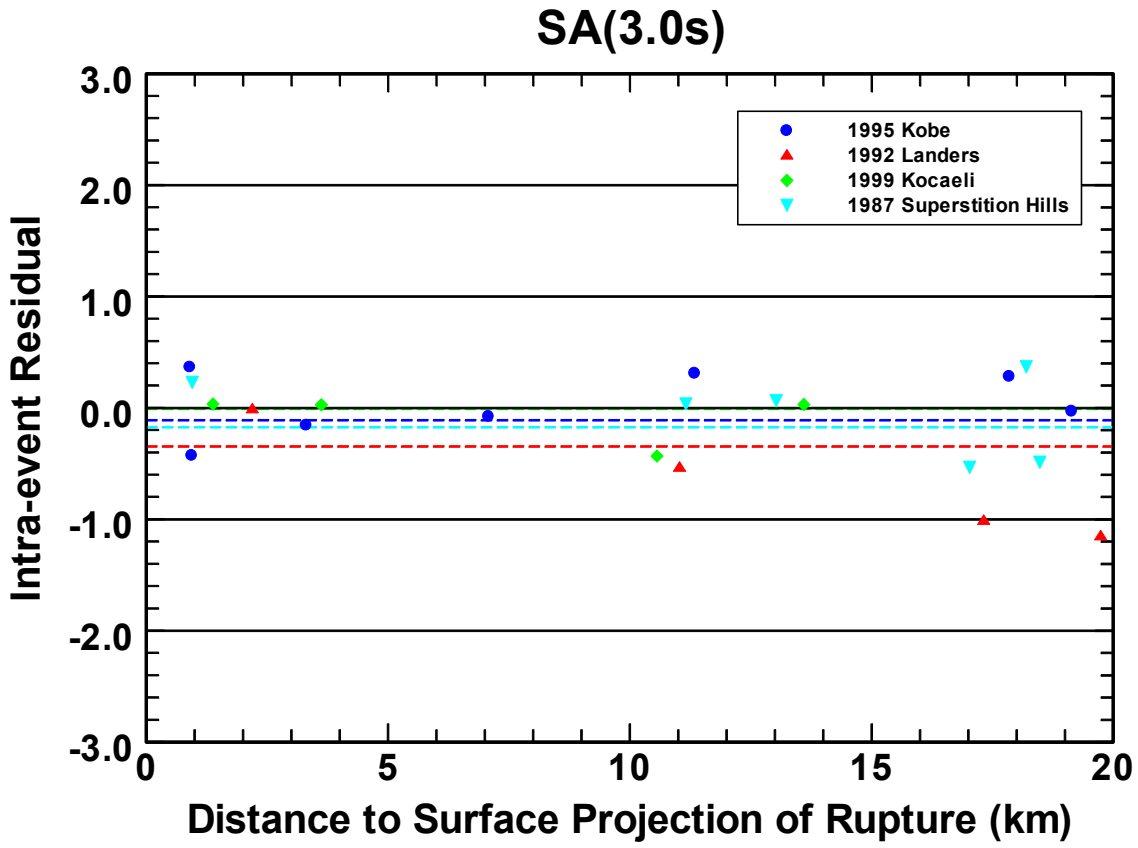

Fig. B.48 **Plot of the 3.0s spectral acceleration intra-event residuals from the Campbell-Bozorgnia NGA model for the Kobe (blue circles), Landers (red triangles), Kocaeli (green diamonds), and Superstition Hills (cyan inverted triangles) earthquakes for $R_{JB} \leq 20$ km. The dashed lines are the same as in Figure B.47.**

B.9 USGS QUESTION #9

Changes from previous attenuation relations. There are substantial differences in ground motions from moderate-sized (M6.5) earthquakes at distances of 15-30 km between the NGA relations and the previous relations from the same authors (using the same site conditions). Since there doesn't appear to be very much new data in this magnitude and distance range, why the large differences? An egregious example is Boore-Atkinson (2006) compared to Boore, Joyner and Fumal (1996) for 1 sec S.A. for R_{JB}=0 and M=6.5. There is about a factor of two decrease for BA (2006) compared to Boore et al. 1996. Why?

B.9.1 Comparison of NGA and 2003 Models

Figures 3 and 4 in the main body of our report show that the predictions of PGA from our previous model (CB03) (Campbell and Bozorgnia, 2003a) are very similar to those from our NGA model (CB06) for $V_{S30} = 760$ m/s (NEHRP BC site conditions) and $\mathbf{M} = 6.5$ at all distances of interest. This is largely due to two important properties of the CB03 model: (1) it had a factor for adjusting predictions from generic rock ($V_{S30} = 620$ m/s) to NEHRP BC site conditions, which avoided an overprediction of NEHRP BC ground motions and (2) it incorporated magnitude saturation, which was found to be an important property of the CB06 model based on a much larger dataset. Figures 11 and 12 in the main body of our report show similar results for 1.0s spectral acceleration. The biggest differences between the two models are in the predictions for magnitudes of 7.0 and above, for which there was a paucity of data in the previous database. This issue is addressed in the next section.

B.9.2 Differences in Magnitude and Distance Scaling for M > 7.0

The primary difference in the magnitude and distance scaling characteristics of the CB03 and CB06 models is at large magnitudes ($\mathbf{M} > 7.0$). Two factors cause this difference: (1) there was very little data to constrain this scaling in the previous model and (2) the previous model forced magnitude saturation while at the same time fixing the rate of attenuation to be independent of magnitude. This latter property caused the attenuation to be too flat in the critical 10–30 km distance range mentioned in the question and, as a result, forced too much magnitude scaling at large magnitudes. This was possible because of the lack of data in this magnitude and distance range in the previous database. The relatively large number of recordings for large magnitudes in the PEER database, especially at near-source distances, clearly indicated that we needed to change our functional form to accommodate an attenuation rate that was dependent on magnitude (flattening with increasing magnitude), thus leading to the large difference in the two models at large magnitudes and short distances.

To show that this revision in our NGA model is supported by the available data, please refer to Figures B.20–B.23 in Section B.2. These figures show the near-source intra-event residuals for our NGA model for PGA and PSA at periods of 0.2, 1.0 and 3.0s, respectively. There are no trends in these data that would indicate a bias in our predictions over the critical 15–30 km distance range mentioned in the question. Of course, this only proves that that the

attenuation rate is unbiased. There is still the issue of magnitude scaling, which can decrease or increase the predictions at all distances for a given magnitude. This issue is discussed at length in Section B.1 and will not be repeated here.

B.9.3 Conclusion

We find that the predictions of ground motion from our NGA (CB06) and previous (CB03) empirical ground motion models are similar for $\mathbf{M} = 6.5$ and $V_{S30} = 760$ m/s at all distances. This is due to two factors: (1) we incorporated magnitude saturation in our previous model as in our NGA model and (2) we provided a factor for adjusting ground motions from generic rock to NEHRP BC site conditions in our previous model. Furthermore, the intra-event residuals from our NGA model show that our revised functional form that predicts magnitude-dependent attenuation is supported by the NGA database, even though it leads to large differences between our NGA and previous models at $\mathbf{M} > 7.0$.

B.10 USGS QUESTION #10

Site Amplification. It appears that most of the NGA developers used a similar functional form for the site amplification. How much of the coefficients are derived from numerical modeling and how much are from actually fitting the data? Obviously, using the same functional forms can cause underestimation of the uncertainty.

All of the developers used V_{S30} for shallow site classification. We consider this to be a major advancement, because it allows an unambiguous use of the NGA ground motion models with the NEHRP site categories. This ambiguity has led to unintentional biases in the USGS national seismic hazard maps in the past. For all four models, the linear amplification is modeled as a linear function of the logarithm of V_{S30}. So the linear amplification does use the same functional form for all of the models. This functional form has been used successfully in both the United States and Japan by many authors to model linear site-response effects.

While all of the developers included nonlinearity in their models, they did so in different ways. Even those that used the same nonlinear site term found different linear site coefficients (see Section B.17). Therefore, in conclusion, we believe that the difference in nonlinear site terms and in linear site coefficients has not artificially constrained the degree of epistemic uncertainty reflected by the models.

B.11 USGS QUESTION #11

Unique aspects of Chi Chi mainshock. The fact that the Chi-Chi aftershocks do not show the same anomalously low high-frequency excitation in the near-source region (< 30 km) as the mainshock (Wang et al., Dec. 2004 BSSA) combined with the observation that regional and teleseismic spectra of the aftershocks and mainshock scale as expected for a constant stress drop model (Frankel, 2006, SSA annual meeting), indicates that there is a bias in the near-source recordings of the Chi-Chi earthquake. This may be due to the low accelerations near the north

end of the rupture and/or footwall effects described [in a previous question]. We have previously noted the possible bias introduced by a higher number of stations located near the north end of the rupture compared to the south end. It is worth noting that Kanno et al. (June 2006 BSSA) exclude the Chi Chi mainshock data from their new attenuation relations for Japan (which include some California data), citing propagation differences between Taiwan and Japan. The Kanno et al. (2006) relations appear to be significantly higher than the NGA ones, for large magnitudes and close-in distances.

There are four issues raised in this question: (1) that Wang et al. (2004) found anonymously low high-frequency (short-period) ground motions in the near-source region of the Chi-Chi mainshock as compared to its aftershocks, (2) that there might be a bias in the short-period ground motions near the fault because of low accelerations near the north end of the rupture and/or because of footwall effects, (3) that Kanno et al. (2006) excluded Chi-Chi mainshock data from their new empirical ground motion model for Japan, citing possible tectonic differences between Taiwan and Japan, and (4) that the Kanno et al. model appears to predict significantly higher ground motion than the NGA models at large magnitudes and close distances. Each of these issues is discussed below.

B.11.1 Results of Wang et al. (2004) Implying Differences Between Mainshock and Aftershocks

Wang et al. (2004) compared observed ground motions from the mainshock and five large aftershocks of the 1999 Chi-Chi (**M** 7.6) earthquake with predictions from four older empirical ground motion models. They concluded that the observed aftershock motions are in reasonable agreement with the predictions, particularly at distances of 10–30 km, which is in marked contrast to the motions from the mainshock, which are much lower than the predicted motions for periods less than 1.0s. They also concluded that the aftershock motions at distances of 10–30 km are somewhat lower than the predictions, suggesting that the ground motion possibly attenuates more rapidly in this region of Taiwan than it does in the areas represented by these older models.

We did not include Chi-Chi aftershocks in the development of our NGA model, so their specific behavior is not relevant with respect to our predictions. However, the relative difference between these aftershocks and the mainshock, especially at short periods, is potentially important and is addressed here. These authors' conclusions are based on comparing the residuals with respect to a set of older ground motion models, so all that these results really indicate is that the previous models are not consistent with the short-period magnitude scaling from these earthquakes, either because there is a problem with the magnitude scaling predicted by the models or because there is something different in the short-period behavior of the mainshock. So these results by themselves are equivocal for concluding whether the short-period ground motions from the Chi-Chi mainshock are unusually low with respect to other earthquakes of similar size.

Wang et al. also brought up the possibility that the ground motions might attenuate more rapidly in this part of Taiwan than they do in the areas it is compared with (primarily California). We have addressed that issue in Sections B.3, B.7 and B.9, where we show plots that indicate that there is no overall bias in the intra-event residuals with respect to distance in Taiwan (i.e., the Chi-Chi earthquake) or any of the other regions identified in these plots. There are, however, azimuthal differences in the Chi-Chi ground motions as discussed in the next section.

B.11.2 Bias in Short-Period Ground Motions Near the Fault

The question suggests that there might be a bias in the short-period ground motions from the Chi-Chi earthquake near the fault because of low accelerations near the north end of the rupture and/or because of footwall effects. The issue regarding footwall effects was addressed in Section B.7. Figures B.28–B.29 of that response show that there is no overall positive bias (underprediction) in PGA or 0.2s spectral acceleration with respect to distance. The only bias is a general overprediction of ground motions once the inter-event residual (source term) is taken into account. However, as Figures B.36 and B.36, there are relatively strong azimuthal effects that appear to be consistent with your observations. To better address these effects, we have re-plotted these figures over a shorter distance range of 0–40 km in Figures B.49 and B.50. For purposes of comparison, we also show similar plots for 1.0 and 3.0s spectral accelerations in Figures B.51 and B.52.

Figures B.49 and B.50 clearly show that short-period ground motions in the northern direction at distances of 30 km and less are overpredicted by our model, whereas those to the south are underpredicted by our model, relative to the Chi-Chi earthquake as a whole. This is consistent with the observation that short-period ground motions to the north are lower than those to the south. Interestingly, this effect fades out at 1.0s (Figure B.51) and the opposite effect occurs at 3.0s (Figure B.52). This shift from relatively low short-period ground motions to relatively high long-period ground motions to the north is consistent with both directivity (rupture was primarily to the north) and the increased fault displacement along the northern part of the rupture.

Given that the near-source biases mentioned in the question are confirmed by our residuals, the question remains whether they biased our near-source predictions. Again, we refer to the figures referenced in the previous section, which clearly show that there is no overall bias in our predictions at either near-source or far-source distances. This is due to the large number of recordings from this earthquake, which as a whole provide an unbiased estimate of ground-motion attenuation.

B.11.3 Decision by Kanno et al. (2006) to Exclude Chi-Chi Data

Kanno et al. (2006) chose to exclude recordings from the Chi-Chi earthquake, even though they included recordings from California, the United States, and Turkey, citing three different investigators suggestions that the short-period ground motions from this earthquake were anonymously low. They performed no independent analyses. They offered two reasons why this

might have been the case: (1) that Taiwan is located on a much-fractured continental margin and (2) that seismic wave propagation may be different than in other regions of the crust. We showed in the previous two sections that the second reason is not valid for our dataset. The first observation might be true, but that does not necessarily imply lower attenuation in Taiwan as compared to other active tectonic regions, again as demonstrated by our database.

The Kanno et al. model does appear to predict higher values of PGA than the NGA models for shallow earthquakes at large magnitudes and close distances. These estimates are generally consistent with those predicted by the previous U.S. models (e.g., see their Figure 12 for a comparison with the Boore et al., 1997, model). This is no surprise, since these authors used a traditional magnitude-dependent functional form with the parameter that controls the magnitude scaling at close distances (their e_1) fixed at a value of 0.5 based on previous studies. Furthermore, their magnitude scaling at large magnitudes is linear, whereas most of the recent models have used a quadratic relation, which predicts decreasing magnitude scaling with increasing magnitude at all distances.

By fixing e_1 and using linear magnitude scaling, these authors did not allow their large-magnitude data at either short or long distances to have much influence on the behavior of their model in this critical magnitude range. To show how this decision has biased their predictions, we refer the reader to their Figure 16c, which plots their inter-event residuals versus magnitude for the shallow events. This figure shows that events with magnitudes between 6.5 and 7.0 are generally underpredicted by their model, whereas those with magnitudes of 7.0 and greater (7 events, including 4 from California) are generally overpredicted by their model. A model that predicts less magnitude scaling for $\mathbf{M} > 6.5$, as our NGA model does, would likely reduce or eliminate this bias.

B.11.4 Conclusion

Based on the discussion provided in the previous sections, we conclude that the Chi-Chi earthquake has not biased the short-period predictions in our NGA model either at near-source or far-source distances. In fact, once the inter-event residuals are taken into account, our model generally overpredicts these short-period ground motions. That is not to say that there are not strong azimuthally dependent attenuation effects, only that there is sufficient data at all azimuths and distances to provide a relatively unbiased estimate of the overall rate of attenuation during this earthquake. Our results also show that overall attenuation during the Chi-Chi earthquake is consistent with our model as well as with the data we used from other regions.

Kanno, T., Narita, A., Morikawa, N., Fujiwara, H., and Fukushima, Y. (2006). A new attenuation relation for strong ground motion in Japan based on recorded data. *Bull. Seism. Soc. Am.* **96**, 879–897.

Wang, G.Q., Boore, D.M., Igel, H., and Zhou, X.Y. (2004). Comparisons of ground motions from five aftershocks of the 1999 Chi-Chi, Taiwan, earthquake with empirical predictions largely based on data from California. *Bull. Seism. Soc. Am.* **94**, 2198–2212.

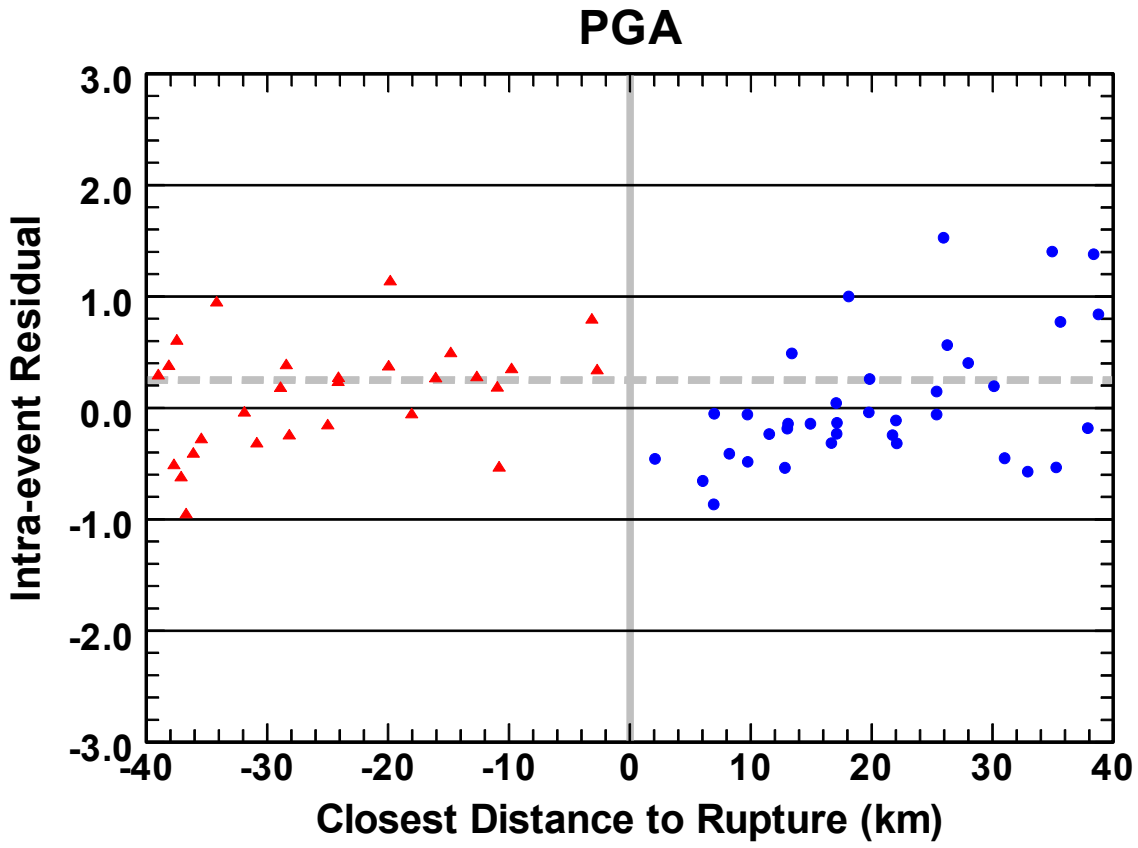

Fig. B.49 **Plot of the PGA intra-event residuals from the Campbell-Bozorgnia NGA model for the Chi-Chi mainshock. Recordings are identified as being off the edge of the fault to the north in the direction of rupture (blue circles) or off the edge of the fault to the south in the opposite direction of rupture (red triangles). Southern distances are plotted as negative values for clarity. The vertical solid grey line demarks the transition from the northern sites to the southern sites. The horizontal dashed grey line represents the adjusted baseline after accounting for the source term and the additional bias caused by disallowing oversaturation, where a positive value represents an overprediction by the model (in this case a significant overprediction).**

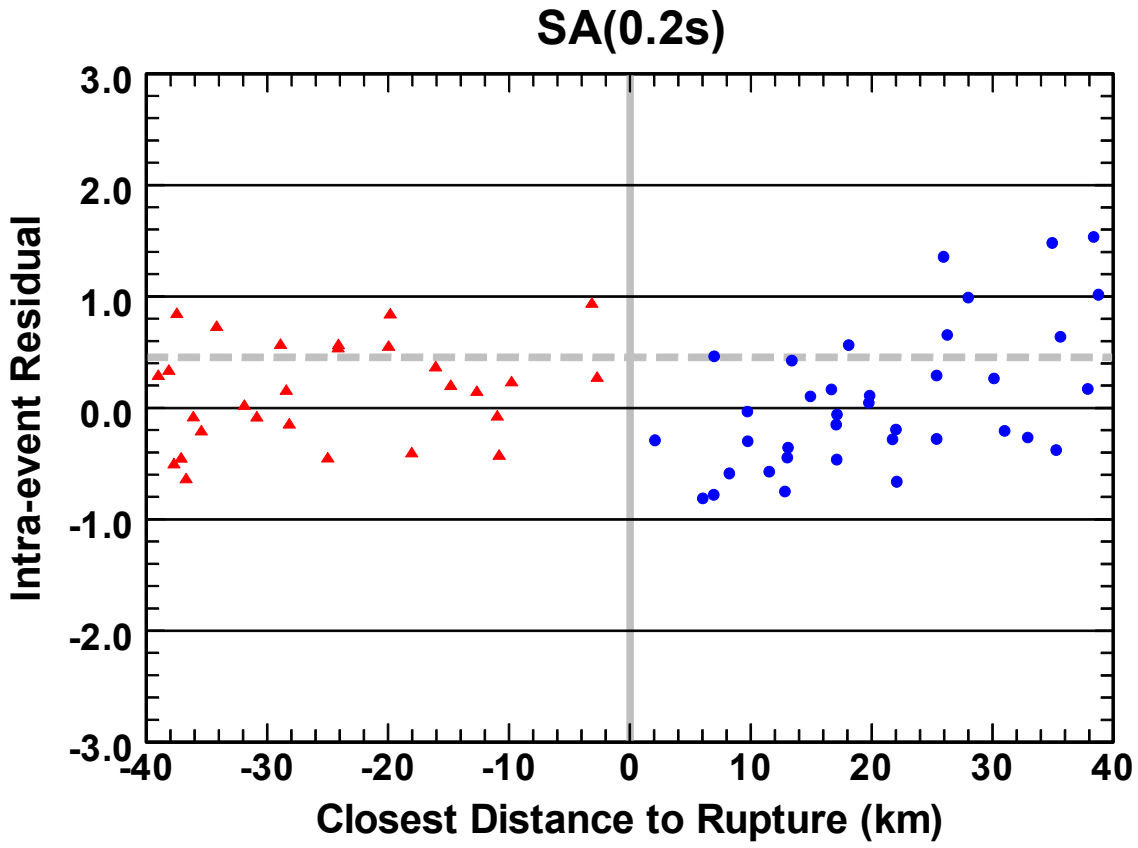

Fig. B.50 **Plot of the 0.2s spectral acceleration intra-event residuals from the Campbell-Bozorgnia NGA model for the Chi-Chi mainshock. The symbols and grey solid and dashed lines are the same as in Figure B.49.**

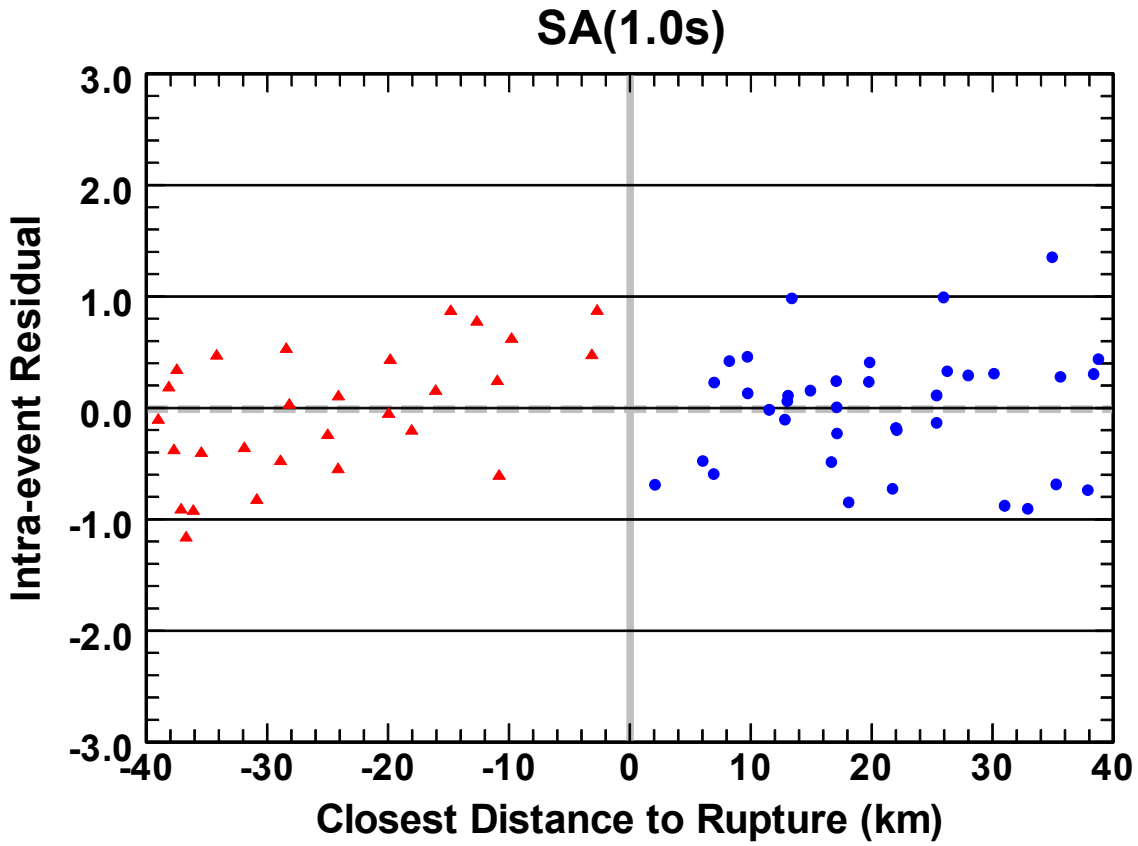

Fig. B.51 **Plot of the 1.0s spectral acceleration intra-event residuals from the Campbell-Bozorgnia NGA model for the Chi-Chi mainshock. The symbols and grey solid and dashed lines are the same as in Figure B.49.**

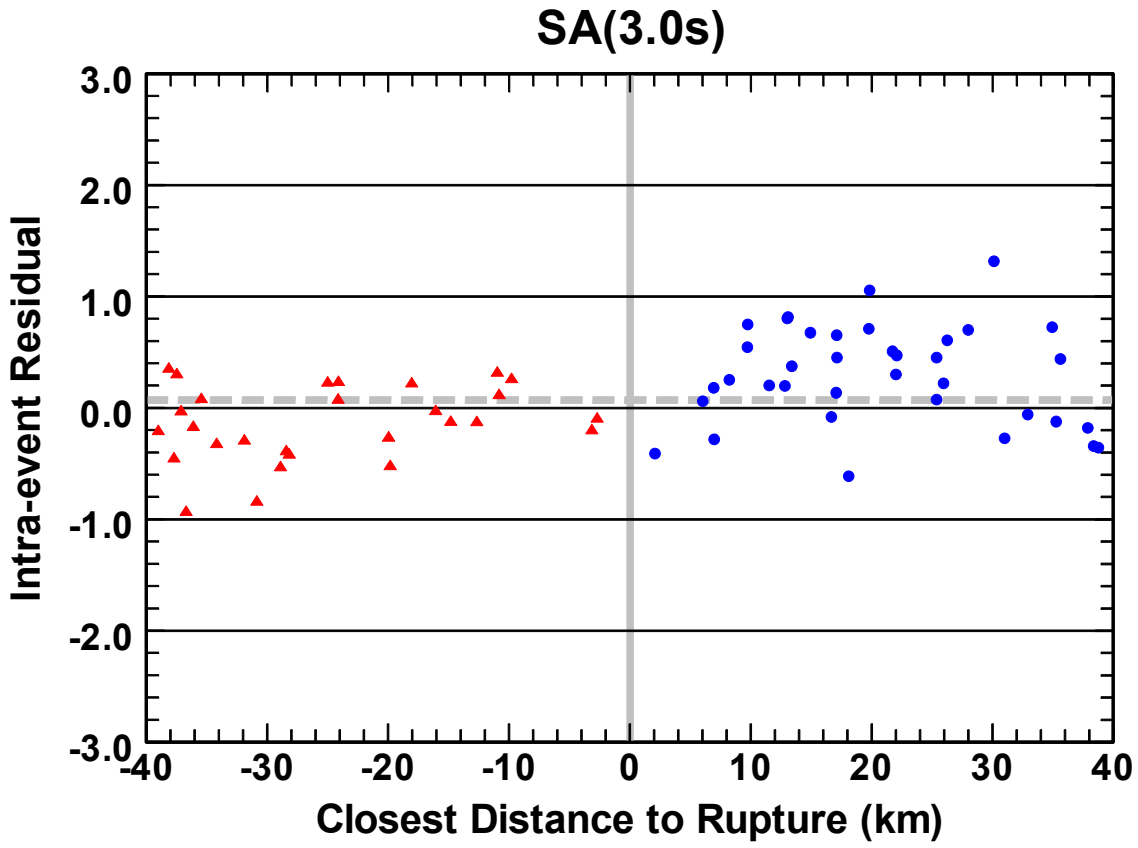

Fig. B.52 **Plot of the 3.0s spectral acceleration intra-event residuals from the Campbell-Bozorgnia NGA model for the Chi-Chi mainshock. The symbols and grey solid and dashed lines are the same as in Figure B.49.**

B.12 CGS QUESTION #1

What is the scientific rational for the upper limit of magnitudes: 8.0 for dip-slip and 8.5 for strike-slip? As far as we know, the upper limit on dip-slip faulty style is 7.6 Chi-Chi and for strike-slip it is 7.9 Denali (and Denali has only one record in the near-field).

In the past, published ground motion models often gave limits on the range of magnitudes for which the model was considered to be applicable based on the empirical data set used to derive the models, but these limits were generally ignored in the application of the models in PSHA. Since the users of the models (often people with no ground motion expertise) are going to extrapolate them to magnitudes outside the range of the empirical data, the PEER NGA Project decided that it would be better to have the model developers decide how their models should be extrapolated.

The specified upper limits on magnitude have nothing to do with the applicable limits of the data. In practice, the models will be applied to whatever magnitudes are included in the source characterization. Using the USGS WG02 model, the largest magnitudes for strike-slip earthquakes in Northern California are larger than **M** 8. For example, for rupture of all four segments of the northern San Andreas, the mean characteristic magnitude can be as large as 8.1. Including aleatory variability about this mean magnitude of 0.24 units leads to a **M** 8.34 earthquake. Therefore, if the WG02 source model is going to be used in a PSHA, ground motions are needed for strike-slip earthquakes up to **M** 8.34. This value was rounded to **M** 8.5 for the PEER NGA Project. For reverse earthquakes, reverse faults in California can have mean characteristic magnitudes in the high **M** 7 range. For example, the Little Salmon fault has a mean characteristic magnitude of 7.75. Again, including the aleatory variability leads to a magnitudes as large as 8.0.

We recognized that the empirical data would not constrain the ground motion models at these large magnitudes. To help the developers constrain the extrapolation to these very large magnitudes, suites of numerical simulations for rock site conditions were conducted based on 1-D kinematic models. The set of simulation exercises and a summary of the magnitude scaling resulting from these simulations are given in Somerville et al. (2006).

These simulations were not as useful as we had hoped because the resulting magnitude scaling was not consistent between the three groups that conducted the simulations (URS, Pacific Engineering, and UNR). Additional work is being conducted to improve the numerical simulations to address the short-comings from the NGA study, but this work is expected to take several years.

In conclusion, it should be the responsibility of the developers, not the users, to use the information provided during the PEER NGA Project and their expertise in ground motions to extrapolate their empirical models to the very large magnitudes demanded by the latest PSHA models.

Somerville, P., Collins, N., Graves, R., Pitarka, A., Silva, W., and Zeng, Y. (2006). Simulation of ground motion scaling characteristics for the NGA-E project. *In* Proceedings, Eighth National Conference on Earthquake Engineering, Paper No. 977.

B.13 CGS QUESTION #2

What is the justification for the upper and lower level of periods 0.01 to 10 sec (0.1 to 100 Hz)? All analog type instruments like SMA-1 have a limit of about 20 Hz (0.05 sec), and it is about 50 Hz for the new digital. For the long-period part, most data before Northridge were processed up to about 5 secs. Only starting with Hector Mine we can justify 10 sec as a cut-off.

As with the magnitude limits discussed in Section B.12, the specified limits on period have nothing to do with the applicable limits of the data. In practice, response spectra are required to cover very high frequencies (e.g., for equipment) and very long periods (e.g., for high rise buildings, bridges and tanks). If we only develop the ground motion models for periods that are well constrained by the empirical data, then these spectra will have to be extrapolated to high frequencies and long periods for individual projects. In the past, this extrapolation has been done in inconsistent ways. In many cases, the spectra are extrapolated by people without expertise in ground motions. Therefore, we decided that it would be better to have the NGA developers do the extrapolation to high frequencies and long periods.

To assist the NGA developers, the 1-D rock site simulations discussed in Section B.12 provided spectral values that covered the specified period range. In addition, scaling of long period spectra values based on 3-D basin simulations were also provided.

In conclusion, it should be the responsibility of the developers to use this information and their expertise in ground motions to extrapolate their empirical models to the high frequencies and long periods demanded by engineers.

In order to judge whether our model predicts reasonable spectral values at long periods, we plotted the displacement spectra predicted by our model out to 10s. Although the overall shape of the spectra looked reasonably good, we could see that the long-period spectral behavior at magnitudes less than around 6.5 were not in line with what one might expect from simple seismological theory. In order to better constrain the model at long periods and small magnitudes, we looked at the predicted displacement spectra from ground-motion simulations. Figure B.53 gives an example of the displacement spectra predicted by our model. The predictions above **M** 6.5 are generally constrained by the empirical data, so it is only the smaller magnitudes that have been constrained from seismological theory.

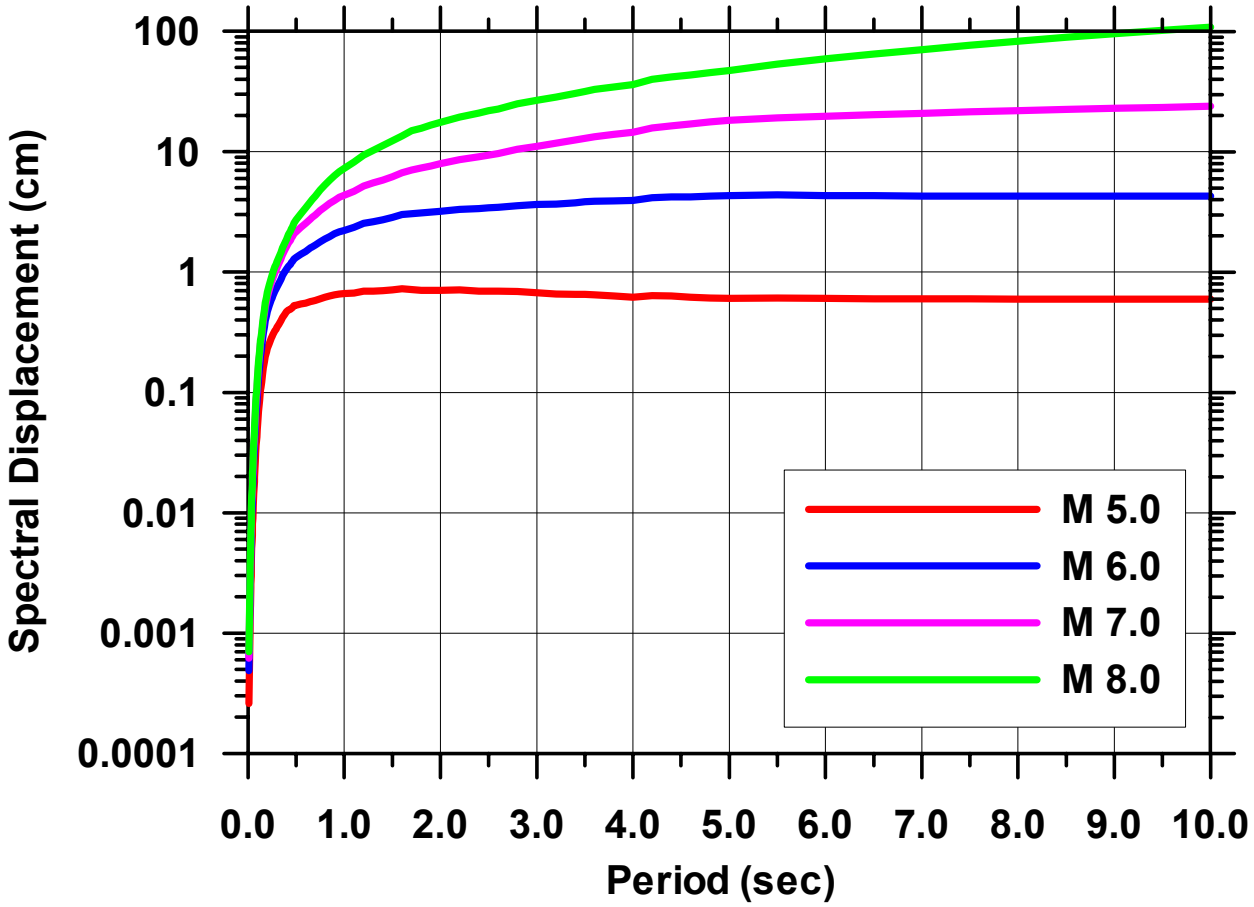

Fig. B.53 **Relative displacement spectra predicted by the Campbell-Bozorgnia NGA model for a distance of 10 km, NEHRP BC site conditions, and strike-slip faulting.**

B.14 CGS QUESTION #3

Strong motion data are biased toward larger motions at large distances, but data truncation at 60-80 km is really very restrictive. For example, it basically eliminates basin effect, which is extremely important in Southern California (Hector Mine, Landers). How can you justify applicability of the equations up to 200 km by using data set that practically doesn't have surface waves?

The 200 km upper limit on the distance has nothing to do with the applicable limits of the data. In practice, the ground motion models are used for large distances regardless of the limits of applicability that the developers may state. Since the ground motion models will be extrapolated to large distances, we decided that it would be better to have the NGA developers do the extrapolation to large distances. To assist the developers, 1-D rock simulations (as discussed in Section B.12) were provided out to distances of 200 km. The Green's functions for two of three sets of simulations include surface waves, but only for rock site conditions (e.g., no surface waves due to basin response).

In addition, an analysis of attenuation from network data (Boatwright, 2005) was provided that could be used to guide the extrapolation to large distances. Finally, the developers were provided recordings from digital accelerograms from several magnitude 5 earthquakes out to distances of several hundred kilometers that could be used to constrain the attenuation at large distances (Dave Boore, written communication, 2005).

A few developers opted to truncate the distance used to select the database at a value less than the required 200 km. However, those developers used additional data, such as broadband and other network data, to extrapolate their models to larger distances.

We were initially concerned that using data out to 200 km would result in a bias in our prediction of near-source ground motions. As a result, we first truncated the database at 60 km as in our 2003 model and performed our analysis. We then added the remaining data and repeated the analysis. The comparison showed that the near-source predictions were not significantly impacted by the more distant data. The largest effect was a much more moderate degree of oversaturation at large magnitudes and short distances when data from all distances were used. Since we chose not to allow oversaturation in our model, we thought that a database that minimized this behavior was preferable over one that did not. Of course, as suggested in this question, including such data also increased the number of recordings that contributed to our sediment depth (i.e., 3-D basin) term. One adverse impact of using the more distant data is our belief that our model might underpredict the amount of attenuation for the smaller earthquakes, but this only impacts ground motion of little engineering importance. This impact is due in part to the selectiveness of only processing earthquakes and/or recordings with the largest ground motions, especially for earthquakes with magnitudes less than around 6.0.

B.15 CGS QUESTION #4

What is the current thinking on large distance data with amplitudes below 0.5% g recorded at non-strong motion networks? It was a long discussion at a couple of meetings and justification for use of these data, and they are not even mentioned in the current reports?

The discussions you refer to centered on the validity of these ground motions, considering they potentially come from instruments whose response is flat to velocity rather than acceleration. Such data would require differentiation to obtain acceleration. None of the developers explicitly used such data in their regression analyses. In fact, including data other than that provided through the PEER database development team (the so-called "flatfile") was strictly forbidden. However, data other than that provided by the PEER NGA Project was used to various degrees by some developers to help constrain their models, which was allowed. We did not use any data other than that provided by the PEER NGA Project team (the so-called flatfile) in the development of our model, so the small-amplitude data you refer to did not influence our model.

B.16 CGS QUESTION #5

What is the seismological justification for using non-linearity in it current form? Is it in accordance to what is known about non-linearity in strong motion:

- *Non-linearity is only proven for amplitudes of ground motion higher than 20-30% g in some earthquakes. (Loma Prieta, Northridge, Chi-Chi), but does not show up for examples in records or Whittier Narrows (Beresnev, 2002).*
- *Non-linearity is a frequency dependent phenomenon shown to take place for frequencies 1.0-5.0 Hz (Field, 2000)*
- *Empirical results of Choi & Stewart (2005) for 5% damped response spectral acceleration show large degree of non-linearity for Vs30<180 m/s, rapidly decreasing with increasing Vs30.*

The developers used different approaches to modeling the nonlinearity. All of the approaches are consistent with what is "known" about nonlinear behavior in strong motion; however, what the developers consider to be "known" may be different between the different developers. In each case, the developers checked that the nonlinearity in their models is consistent with their selected subset of the empirical data. But these data are not sufficient to constrain the nonlinear soil behavior at large ground motions and soft sites, so most of the modelers reverted to modeling to some extent to define the models in this region.

Because NEHRP E sites can be subject to unique site-response characteristics, we have recommended that our model not be used for values of V_{S30} less than 180 m/sec, unless the user believes that his site will not be subject to such unique site-response characteristics.

B.17 CGS QUESTION #6

All three reports use Choi and Stewart (2005) for the site amplification effect but the coefficients for the linear part vary: it is 0.36 in B&A, 0.34 in C&B, and 0.48 in C&Y. Why is it so different if it is based on the same source?

Note that all of these coefficients are actually negative to accommodate a reference site velocity in the denominator of the site velocity term. Not all of the developers used Choi and Stewart (2005) for their site-amplification term as indicated in Section B.16, so one would not necessarily expect them to also have the same linear site term. This term will depend on the degree of nonlinearity predicted by the model, the reference site velocity, the selected database, and other factors.

The four models all determine the linear site term from the empirical data. Since the models use different empirical subsets, the linear terms will be different. For example, Chiou-Youngs and Abrahamson-Silva include the Chi-Chi aftershocks in the determination of the site response, but Boore-Atkinson and Campbell-Bozorgnia do not include these aftershocks. Given the large number of recordings from the Chi-Chi aftershocks, this data set difference could lead to a significant difference in the linear site terms.

Our linear soil coefficients of -0.34 and -0.73 for PGA and 1.0s spectral acceleration are very similar to the values of -0.37 and -0.70 originally derived by Boore et al. (1997). Although this doesn't prove our values are correct, it does imply that the non-linear site model we adopted from Walling and Abrahamson (2006) probably has not strongly biased our linear site term. We also checked our residuals and found, at least for NEHRP D and stiffer sites for which we consider our model valid, that our nonlinear site term removed the tendency for our linear model to overpredict short-period ground motions on NEHRP C and D sites at the largest observed values of PGA without underpredicting at smaller values of PGA.

PEER REPORTS

PEER reports are available from the National Information Service for Earthquake Engineering (NISEE). To order PEER reports, please contact the Pacific Earthquake Engineering Research Center, 1301 South 46th Street, Richmond, California 94804-4698. Tel.: (510) 665-3405; Fax: (510) 665-3420.

PEER 2007/02 *Campbell-Bozorgnia NGA Ground Motion Relations for the Geometric Mean Horizontal Component of Peak and Spectral Ground Motion Parameters.* Kenneth W. Campbell and Yousef Bozorgnia. May 2007.

PEER 2007/01 *Boore-Atkinson NGA Ground Motion Relations for the Geometric Mean Horizontal Component of Peak and Spectral Ground Motion Parameters.* David M. Boore and Gail M. Atkinson. May. May 2007.

PEER 2006/12 *Societal Implications of Performance-Based Earthquake Engineering.* Peter J. May. May 2007.

PEER 2006/11 *Probabilistic Seismic Demand Analysis Using Advanced Ground Motion Intensity Measures, Attenuation Relationships, and Near-Fault Effects.* Polsak Tothong and C. Allin Cornell. March 2007.

PEER 2006/10 *Application of the PEER PBEE Methodology to the I-880 Viaduct.* Sashi Kunnath. February 2007.

PEER 2006/09 *Quantifying Economic Losses from Travel Forgone Following a Large Metropolitan Earthquake.* James Moore, Sungbin Cho, Yue Yue Fan, and Stuart Werner. November 2006.

PEER 2006/08 *Vector-Valued Ground Motion Intensity Measures for Probabilistic Seismic Demand Analysis.* Jack W. Baker and C. Allin Cornell. October 2006.

PEER 2006/07 *Analytical Modeling of Reinforced Concrete Walls for Predicting Flexural and Coupled–Shear-Flexural Responses.* Kutay Orakcal, Loenardo M. Massone, and John W. Wallace. October 2006.

PEER 2006/06 *Nonlinear Analysis of a Soil-Drilled Pier System under Static and Dynamic Axial Loading.* Gang Wang and Nicholas Sitar. November 2006.

PEER 2006/05 *Advanced Seismic Assessment Guidelines.* Paolo Bazzurro, C. Allin Cornell, Charles Menun, Maziar Motahari, and Nicolas Luco. September 2006.

PEER 2006/04 *Probabilistic Seismic Evaluation of Reinforced Concrete Structural Components and Systems.* Tae Hyung Lee and Khalid M. Mosalam. August 2006.

PEER 2006/03 *Performance of Lifelines Subjected to Lateral Spreading.* Scott A. Ashford and Teerawut Juirnarongrit. July 2006.

PEER 2006/02 *Pacific Earthquake Engineering Research Center Highway Demonstration Project.* Anne Kiremidjian, James Moore, Yue Yue Fan, Nesrin Basoz, Ozgur Yazali, and Meredith Williams. April 2006.

PEER 2006/01 *Bracing Berkeley. A Guide to Seismic Safety on the UC Berkeley Campus.* Mary C. Comerio, Stephen Tobriner, and Ariane Fehrenkamp. January 2006.

PEER 2005/16 *Seismic Response and Reliability of Electrical Substation Equipment and Systems.* Junho Song, Armen Der Kiureghian, and Jerome L. Sackman. April 2006.

PEER 2005/15 *CPT-Based Probabilistic Assessment of Seismic Soil Liquefaction Initiation.* R. E. S. Moss, R. B. Seed, R. E. Kayen, J. P. Stewart, and A. Der Kiureghian. April 2006.

PEER 2005/14 *Workshop on Modeling of Nonlinear Cyclic Load-Deformation Behavior of Shallow Foundations.* Bruce L. Kutter, Geoffrey Martin, Tara Hutchinson, Chad Harden, Sivapalan Gajan, and Justin Phalen. March 2006.

PEER 2005/13 *Stochastic Characterization and Decision Bases under Time-Dependent Aftershock Risk in Performance-Based Earthquake Engineering.* Gee Liek Yeo and C. Allin Cornell. July 2005.

PEER 2005/12 *PEER Testbed Study on a Laboratory Building: Exercising Seismic Performance Assessment.* Mary C. Comerio, editor. November 2005.

PEER 2005/11 *Van Nuys Hotel Building Testbed Report: Exercising Seismic Performance Assessment.* Helmut Krawinkler, editor. October 2005.

PEER 2005/10 *First NEES/E-Defense Workshop on Collapse Simulation of Reinforced Concrete Building Structures.* September 2005.

PEER 2005/09 *Test Applications of Advanced Seismic Assessment Guidelines.* Joe Maffei, Karl Telleen, Danya Mohr, William Holmes, and Yuki Nakayama. August 2006.

PEER 2005/08 *Damage Accumulation in Lightly Confined Reinforced Concrete Bridge Columns.* R. Tyler Ranf, Jared M. Nelson, Zach Price, Marc O. Eberhard, and John F. Stanton. April 2006.

PEER 2005/07 *Experimental and Analytical Studies on the Seismic Response of Freestanding and Anchored Laboratory Equipment.* Dimitrios Konstantinidis and Nicos Makris. January 2005.

PEER 2005/06 *Global Collapse of Frame Structures under Seismic Excitations*. Luis F. Ibarra and Helmut Krawinkler. September 2005.

PEER 2005//05 *Performance Characterization of Bench- and Shelf-Mounted Equipment.* Samit Ray Chaudhuri and Tara C. Hutchinson. May 2006.

PEER 2005/04 *Numerical Modeling of the Nonlinear Cyclic Response of Shallow Foundations.* Chad Harden, Tara Hutchinson, Geoffrey R. Martin, and Bruce L. Kutter. August 2005.

PEER 2005/03 *A Taxonomy of Building Components for Performance-Based Earthquake Engineering.* Keith A. Porter. September 2005.

PEER 2005/02 *Fragility Basis for California Highway Overpass Bridge Seismic Decision Making*. Kevin R. Mackie and Bozidar Stojadinovic. June 2005.

PEER 2005/01 *Empirical Characterization of Site Conditions on Strong Ground Motion.* Jonathan P. Stewart, Yoojoong Choi, and Robert W. Graves. June 2005.

PEER 2004/09 *Electrical Substation Equipment Interaction: Experimental Rigid Conductor Studies.* Christopher Stearns and André Filiatrault. February 2005.

PEER 2004/08 *Seismic Qualification and Fragility Testing of Line Break 550-kV Disconnect Switches.* Shakhzod M. Takhirov, Gregory L. Fenves, and Eric Fujisaki. January 2005.

PEER 2004/07 *Ground Motions for Earthquake Simulator Qualification of Electrical Substation Equipment.* Shakhzod M. Takhirov, Gregory L. Fenves, Eric Fujisaki, and Don Clyde. January 2005.

PEER 2004/06 *Performance-Based Regulation and Regulatory Regimes.* Peter J. May and Chris Koski. September 2004.

PEER 2004/05 *Performance-Based Seismic Design Concepts and Implementation: Proceedings of an International Workshop.* Peter Fajfar and Helmut Krawinkler, editors. September 2004.

PEER 2004/04 *Seismic Performance of an Instrumented Tilt-up Wall Building.* James C. Anderson and Vitelmo V. Bertero. July 2004.

PEER 2004/03 *Evaluation and Application of Concrete Tilt-up Assessment Methodologies.* Timothy Graf and James O. Malley. October 2004.

PEER 2004/02 *Analytical Investigations of New Methods for Reducing Residual Displacements of Reinforced Concrete Bridge Columns.* Junichi Sakai and Stephen A. Mahin. August 2004.

PEER 2004/01 *Seismic Performance of Masonry Buildings and Design Implications.* Kerri Anne Taeko Tokoro, James C. Anderson, and Vitelmo V. Bertero. February 2004.

PEER 2003/18 *Performance Models for Flexural Damage in Reinforced Concrete Columns.* Michael Berry and Marc Eberhard. August 2003.

PEER 2003/17 *Predicting Earthquake Damage in Older Reinforced Concrete Beam-Column Joints.* Catherine Pagni and Laura Lowes. October 2004.

PEER 2003/16 *Seismic Demands for Performance-Based Design of Bridges.* Kevin Mackie and Božidar Stojadinovic. August 2003.

PEER 2003/15 *Seismic Demands for Nondeteriorating Frame Structures and Their Dependence on Ground Motions.* Ricardo Antonio Medina and Helmut Krawinkler. May 2004.

PEER 2003/14 *Finite Element Reliability and Sensitivity Methods for Performance-Based Earthquake Engineering.* Terje Haukaas and Armen Der Kiureghian. April 2004.

PEER 2003/13 *Effects of Connection Hysteretic Degradation on the Seismic Behavior of Steel Moment-Resisting Frames.* Janise E. Rodgers and Stephen A. Mahin. March 2004.

PEER 2003/12 *Implementation Manual for the Seismic Protection of Laboratory Contents: Format and Case Studies.* William T. Holmes and Mary C. Comerio. October 2003.

PEER 2003/11 *Fifth U.S.-Japan Workshop on Performance-Based Earthquake Engineering Methodology for Reinforced Concrete Building Structures.* February 2004.

PEER 2003/10 *A Beam-Column Joint Model for Simulating the Earthquake Response of Reinforced Concrete Frames.* Laura N. Lowes, Nilanjan Mitra, and Arash Altoontash. February 2004.

PEER 2003/09 *Sequencing Repairs after an Earthquake: An Economic Approach.* Marco Casari and Simon J. Wilkie. April 2004.

PEER 2003/08 *A Technical Framework for Probability-Based Demand and Capacity Factor Design (DCFD) Seismic Formats*. Fatemeh Jalayer and C. Allin Cornell. November 2003.

PEER 2003/07 *Uncertainty Specification and Propagation for Loss Estimation Using FOSM Methods.* Jack W. Baker and C. Allin Cornell. September 2003.

PEER 2003/06 *Performance of Circular Reinforced Concrete Bridge Columns under Bidirectional Earthquake Loading*. Mahmoud M. Hachem, Stephen A. Mahin, and Jack P. Moehle. February 2003.

PEER 2003/05 *Response Assessment for Building-Specific Loss Estimation.* Eduardo Miranda and Shahram Taghavi. September 2003.

PEER 2003/04 *Experimental Assessment of Columns with Short Lap Splices Subjected to Cyclic Loads*. Murat Melek, John W. Wallace, and Joel Conte. April 2003.

PEER 2003/03 *Probabilistic Response Assessment for Building-Specific Loss Estimation.* Eduardo Miranda and Hesameddin Aslani. September 2003.

PEER 2003/02 *Software Framework for Collaborative Development of Nonlinear Dynamic Analysis Program.* Jun Peng and Kincho H. Law. September 2003.

PEER 2003/01 *Shake Table Tests and Analytical Studies on the Gravity Load Collapse of Reinforced Concrete Frames.* Kenneth John Elwood and Jack P. Moehle. November 2003.

PEER 2002/24 *Performance of Beam to Column Bridge Joints Subjected to a Large Velocity Pulse.* Natalie Gibson, André Filiatrault, and Scott A. Ashford. April 2002.

PEER 2002/23 *Effects of Large Velocity Pulses on Reinforced Concrete Bridge Columns.* Greg L. Orozco and Scott A. Ashford. April 2002.

PEER 2002/22 *Characterization of Large Velocity Pulses for Laboratory Testing.* Kenneth E. Cox and Scott A. Ashford. April 2002.

PEER 2002/21 *Fourth U.S.-Japan Workshop on Performance-Based Earthquake Engineering Methodology for Reinforced Concrete Building Structures*. December 2002.

PEER 2002/20 *Barriers to Adoption and Implementation of PBEE Innovations.* Peter J. May. August 2002.

PEER 2002/19 *Economic-Engineered Integrated Models for Earthquakes: Socioeconomic Impacts.* Peter Gordon, James E. Moore II, and Harry W. Richardson. July 2002.

PEER 2002/18 *Assessment of Reinforced Concrete Building Exterior Joints with Substandard Details.* Chris P. Pantelides, Jon Hansen, Justin Nadauld, and Lawrence D. Reaveley. May 2002.

PEER 2002/17 *Structural Characterization and Seismic Response Analysis of a Highway Overcrossing Equipped with Elastomeric Bearings and Fluid Dampers: A Case Study.* Nicos Makris and Jian Zhang. November 2002.

PEER 2002/16 *Estimation of Uncertainty in Geotechnical Properties for Performance-Based Earthquake Engineering.* Allen L. Jones, Steven L. Kramer, and Pedro Arduino. December 2002.

PEER 2002/15 *Seismic Behavior of Bridge Columns Subjected to Various Loading Patterns.* Asadollah Esmaeily-Gh. and Yan Xiao. December 2002.

PEER 2002/14 *Inelastic Seismic Response of Extended Pile Shaft Supported Bridge Structures.* T.C. Hutchinson, R.W. Boulanger, Y.H. Chai, and I.M. Idriss. December 2002.

PEER 2002/13 *Probabilistic Models and Fragility Estimates for Bridge Components and Systems.* Paolo Gardoni, Armen Der Kiureghian, and Khalid M. Mosalam. June 2002.

PEER 2002/12 *Effects of Fault Dip and Slip Rake on Near-Source Ground Motions: Why Chi-Chi Was a Relatively Mild M7.6 Earthquake.* Brad T. Aagaard, John F. Hall, and Thomas H. Heaton. December 2002.

PEER 2002/11 *Analytical and Experimental Study of Fiber-Reinforced Strip Isolators*. James M. Kelly and Shakhzod M. Takhirov. September 2002.

PEER 2002/10 *Centrifuge Modeling of Settlement and Lateral Spreading with Comparisons to Numerical Analyses***.** Sivapalan Gajan and Bruce L. Kutter. January 2003.

PEER 2002/09 *Documentation and Analysis of Field Case Histories of Seismic Compression during the 1994 Northridge, California, Earthquake.* Jonathan P. Stewart, Patrick M. Smith, Daniel H. Whang, and Jonathan D. Bray. October 2002.

PEER 2002/08 *Component Testing, Stability Analysis and Characterization of Buckling-Restrained Unbonded Braces™*. Cameron Black, Nicos Makris, and Ian Aiken. September 2002.

PEER 2002/07 *Seismic Performance of Pile-Wharf Connections.* Charles W. Roeder, Robert Graff, Jennifer Soderstrom, and Jun Han Yoo. December 2001.

PEER 2002/06 *The Use of Benefit-Cost Analysis for Evaluation of Performance-Based Earthquake Engineering Decisions*. Richard O. Zerbe and Anthony Falit-Baiamonte. September 2001.

PEER 2002/05 *Guidelines, Specifications, and Seismic Performance Characterization of Nonstructural Building Components and Equipment*. André Filiatrault, Constantin Christopoulos, and Christopher Stearns. September 2001.

PEER 2002/04 *Consortium of Organizations for Strong-Motion Observation Systems and the Pacific Earthquake Engineering Research Center Lifelines Program: Invited Workshop on Archiving and Web Dissemination of Geotechnical Data, 4–5 October 2001*. September 2002.

PEER 2002/03 *Investigation of Sensitivity of Building Loss Estimates to Major Uncertain Variables for the Van Nuys Testbed.* Keith A. Porter, James L. Beck, and Rustem V. Shaikhutdinov. August 2002.

PEER 2002/02 *The Third U.S.-Japan Workshop on Performance-Based Earthquake Engineering Methodology for Reinforced Concrete Building Structures*. July 2002.

PEER 2002/01 *Nonstructural Loss Estimation: The UC Berkeley Case Study.* Mary C. Comerio and John C. Stallmeyer. December 2001.

PEER 2001/16 *Statistics of SDF-System Estimate of Roof Displacement for Pushover Analysis of Buildings.* Anil K. Chopra, Rakesh K. Goel, and Chatpan Chintanapakdee. December 2001.

PEER 2001/15 *Damage to Bridges during the 2001 Nisqually Earthquake.* R. Tyler Ranf, Marc O. Eberhard, and Michael P. Berry. November 2001.

PEER 2001/14 *Rocking Response of Equipment Anchored to a Base Foundation.* Nicos Makris and Cameron J. Black. September 2001.

PEER 2001/13 *Modeling Soil Liquefaction Hazards for Performance-Based Earthquake Engineering.* Steven L. Kramer and Ahmed-W. Elgamal. February 2001.

PEER 2001/12 *Development of Geotechnical Capabilities in OpenSees.* Boris Jeremi . September 2001.

PEER 2001/11 *Analytical and Experimental Study of Fiber-Reinforced Elastomeric Isolators*. James M. Kelly and Shakhzod M. Takhirov. September 2001.

PEER 2001/10 *Amplification Factors for Spectral Acceleration in Active Regions.* Jonathan P. Stewart, Andrew H. Liu, Yoojoong Choi, and Mehmet B. Baturay. December 2001.

PEER 2001/09 *Ground Motion Evaluation Procedures for Performance-Based Design.* Jonathan P. Stewart, Shyh-Jeng Chiou, Jonathan D. Bray, Robert W. Graves, Paul G. Somerville, and Norman A. Abrahamson. September 2001.

PEER 2001/08 *Experimental and Computational Evaluation of Reinforced Concrete Bridge Beam-Column Connections for Seismic Performance*. Clay J. Naito, Jack P. Moehle, and Khalid M. Mosalam. November 2001.

PEER 2001/07 *The Rocking Spectrum and the Shortcomings of Design Guidelines.* Nicos Makris and Dimitrios Konstantinidis. August 2001.

PEER 2001/06 *Development of an Electrical Substation Equipment Performance Database for Evaluation of Equipment Fragilities*. Thalia Agnanos. April 1999.

PEER 2001/05 *Stiffness Analysis of Fiber-Reinforced Elastomeric Isolators.* Hsiang-Chuan Tsai and James M. Kelly. May 2001.

PEER 2001/04 *Organizational and Societal Considerations for Performance-Based Earthquake Engineering.* Peter J. May. April 2001.

PEER 2001/03 *A Modal Pushover Analysis Procedure to Estimate Seismic Demands for Buildings: Theory and Preliminary Evaluation.* Anil K. Chopra and Rakesh K. Goel. January 2001.

PEER 2001/02 *Seismic Response Analysis of Highway Overcrossings Including Soil-Structure Interaction.* Jian Zhang and Nicos Makris. March 2001.

PEER 2001/01 *Experimental Study of Large Seismic Steel Beam-to-Column Connections.* Egor P. Popov and Shakhzod M. Takhirov. November 2000.

PEER 2000/10 *The Second U.S.-Japan Workshop on Performance-Based Earthquake Engineering Methodology for Reinforced Concrete Building Structures.* March 2000.

PEER 2000/09 *Structural Engineering Reconnaissance of the August 17, 1999 Earthquake: Kocaeli (Izmit), Turkey.* Halil Sezen, Kenneth J. Elwood, Andrew S. Whittaker, Khalid Mosalam, John J. Wallace, and John F. Stanton. December 2000.

PEER 2000/08 *Behavior of Reinforced Concrete Bridge Columns Having Varying Aspect Ratios and Varying Lengths of Confinement.* Anthony J. Calderone, Dawn E. Lehman, and Jack P. Moehle. January 2001.

PEER 2000/07 *Cover-Plate and Flange-Plate Reinforced Steel Moment-Resisting Connections.* Taejin Kim, Andrew S. Whittaker, Amir S. Gilani, Vitelmo V. Bertero, and Shakhzod M. Takhirov. September 2000.

PEER 2000/06 *Seismic Evaluation and Analysis of 230-kV Disconnect Switches.* Amir S. J. Gilani, Andrew S. Whittaker, Gregory L. Fenves, Chun-Hao Chen, Henry Ho, and Eric Fujisaki. July 2000.

PEER 2000/05 *Performance-Based Evaluation of Exterior Reinforced Concrete Building Joints for Seismic Excitation.* Chandra Clyde, Chris P. Pantelides, and Lawrence D. Reaveley. July 2000.

PEER 2000/04 *An Evaluation of Seismic Energy Demand: An Attenuation Approach.* Chung-Che Chou and Chia-Ming Uang. July 1999.

PEER 2000/03 *Framing Earthquake Retrofitting Decisions: The Case of Hillside Homes in Los Angeles.* Detlof von Winterfeldt, Nels Roselund, and Alicia Kitsuse. March 2000.

PEER 2000/02 *U.S.-Japan Workshop on the Effects of Near-Field Earthquake Shaking.* Andrew Whittaker, ed. July 2000.

PEER 2000/01 *Further Studies on Seismic Interaction in Interconnected Electrical Substation Equipment.* Armen Der Kiureghian, Kee-Jeung Hong, and Jerome L. Sackman. November 1999.

PEER 1999/14 *Seismic Evaluation and Retrofit of 230-kV Porcelain Transformer Bushings.* Amir S. Gilani, Andrew S. Whittaker, Gregory L. Fenves, and Eric Fujisaki. December 1999.

PEER 1999/13 *Building Vulnerability Studies: Modeling and Evaluation of Tilt-up and Steel Reinforced Concrete Buildings.* John W. Wallace, Jonathan P. Stewart, and Andrew S. Whittaker, editors. December 1999.

PEER 1999/12 *Rehabilitation of Nonductile RC Frame Building Using Encasement Plates and Energy-Dissipating Devices.* Mehrdad Sasani, Vitelmo V. Bertero, James C. Anderson. December 1999.

PEER 1999/11 *Performance Evaluation Database for Concrete Bridge Components and Systems under Simulated Seismic Loads.* Yael D. Hose and Frieder Seible. November 1999.

PEER 1999/10 *U.S.-Japan Workshop on Performance-Based Earthquake Engineering Methodology for Reinforced Concrete Building Structures.* December 1999.

PEER 1999/09 *Performance Improvement of Long Period Building Structures Subjected to Severe Pulse-Type Ground Motions.* James C. Anderson, Vitelmo V. Bertero, and Raul Bertero. October 1999.

PEER 1999/08 *Envelopes for Seismic Response Vectors.* Charles Menun and Armen Der Kiureghian. July 1999.

PEER 1999/07 *Documentation of Strengths and Weaknesses of Current Computer Analysis Methods for Seismic Performance of Reinforced Concrete Members.* William F. Cofer. November 1999.

PEER 1999/06 *Rocking Response and Overturning of Anchored Equipment under Seismic Excitations.* Nicos Makris and Jian Zhang. November 1999.

PEER 1999/05 *Seismic Evaluation of 550 kV Porcelain Transformer Bushings.* Amir S. Gilani, Andrew S. Whittaker, Gregory L. Fenves, and Eric Fujisaki. October 1999.

PEER 1999/04 *Adoption and Enforcement of Earthquake Risk-Reduction Measures.* Peter J. May, Raymond J. Burby, T. Jens Feeley, and Robert Wood.

PEER 1999/03 *Task 3 Characterization of Site Response General Site Categories.* Adrian Rodriguez-Marek, Jonathan D. Bray, and Norman Abrahamson. February 1999.

PEER 1999/02 *Capacity-Demand-Diagram Methods for Estimating Seismic Deformation of Inelastic Structures: SDF Systems.* Anil K. Chopra and Rakesh Goel. April 1999.

PEER 1999/01 *Interaction in Interconnected Electrical Substation Equipment Subjected to Earthquake Ground Motions.* Armen Der Kiureghian, Jerome L. Sackman, and Kee-Jeung Hong. February 1999.

PEER 1998/08 *Behavior and Failure Analysis of a Multiple-Frame Highway Bridge in the 1994 Northridge Earthquake.* Gregory L. Fenves and Michael Ellery. December 1998.

PEER 1998/07 *Empirical Evaluation of Inertial Soil-Structure Interaction Effects.* Jonathan P. Stewart, Raymond B. Seed, and Gregory L. Fenves. November 1998.

PEER 1998/06 *Effect of Damping Mechanisms on the Response of Seismic Isolated Structures.* Nicos Makris and Shih-Po Chang. November 1998.

PEER 1998/05 *Rocking Response and Overturning of Equipment under Horizontal Pulse-Type Motions.* Nicos Makris and Yiannis Roussos. October 1998.

PEER 1998/04 *Pacific Earthquake Engineering Research Invitational Workshop Proceedings, May 14–15, 1998: Defining the Links between Planning, Policy Analysis, Economics and Earthquake Engineering.* Mary Comerio and Peter Gordon. September 1998.

PEER 1998/03 *Repair/Upgrade Procedures for Welded Beam to Column Connections.* James C. Anderson and Xiaojing Duan. May 1998.

PEER 1998/02 *Seismic Evaluation of 196 kV Porcelain Transformer Bushings.* Amir S. Gilani, Juan W. Chavez, Gregory L. Fenves, and Andrew S. Whittaker. May 1998.

PEER 1998/01 *Seismic Performance of Well-Confined Concrete Bridge Columns.* Dawn E. Lehman and Jack P. Moehle. December 2000.